SCHOOL OF ENVIRONMENTAL SCIENCES

University of Venda

SYNTHESIS OF BIOPOLYMER-METAL OXIDE NANOPARTICLES REINFORCED COMPOSITES FOR FLUORIDE AND PATHOGENS REMOVAL IN GROUNDWATER

By

Ayinde, Wasiu Babatunde

Student No. 16023630

Promoter: Prof. Gitari W. M.

Co-promoter: Dr. Muchindu M.

A Ph.D. thesis submitted in fulfillment of the requirements for the degree of **Doctor of Philosophy**

Department of Ecology and Resource Management

August 2019

Declaration

I, Ayinde Wasiu Babatunde, hereby declare that "**Synthesis of biopolymer-metal oxide nanoparticles reinforced composites for fluoride and pathogens removal in groundwater**" is my own work in design and execution. It is being submitted for the degree of Doctor of Philosophy to the University of the Venda, South Africa. It has never been submitted for any degree or examination in any other University. All the sources I have used or quoted have been indicated and duly acknowledged by complete references.

Full Names: **Ayinde Wasiu Babatunde**

Signature: …… Date: ……...

Acknowledgments

All glory and adoration to God Almighty, the source of my life, the source of knowledge, wisdom, comfort, the most gracious, most merciful. To him belong whatever is in heaven and on earth and they do declare His Praises and Glory. He is the Exalted in Might, the wise; whose love and protection has sustained me through this sojourn.

I wish to express my sincere and profound gratitude to my promoter Professor Wilson Mugera Gitari, a distinguished scholar, for his very valuable guidance, dedication, invaluable suggestion and financial commitments throughout this research project. Prof., it is a privilege to work and serve under your supervision, you are worthy of emulation. Thank you. My special thanks also go to my co-promoter, Dr. Munkombwe Muchindu of Mintek, Johannesburg, for her expert advice, input, and direction as well as granting me the opportunities and accessibilities to Mintek material and characterization facilities.

My indebtedness also goes to my mentors (past and present): Prof. Drae E. O., Prof. Amidou Samie, Prof. James A. Smit, Dr. Segun A., and Dr. Oladoyinmbo F. O. for their support and encouragement and particularly setting and making this academic pathway a reality. Also, worth mentioning are Dr. Joshua Edokpayi, Dr. Alayande S. O., Mr. Olaleru A., and Mr. Ekanade K. I., your guidance and assistance in achieving this project has been remarkable.

The contribution(s) of both the academic and non-academic staffs in the Department of ERM and School of Environmental Sciences, Molecular Parasitology and Opportunistic Infections Program Research group (Ms. Murendeni and Ms. Arinao), Department of Microbiology, School of Mathematical and Natural Sciences, University of Venda for the success of this project is highly appreciated.

I would like to thank my postgraduate colleagues and Environmental Remediation and Nanoscience (EnViReN) Research Group members (Dr. Rabelani, Glynn (Rastaman), Murendeni (my super mentor), our daddy Mr. Obijole, Nsovo (Madam Shikwambana), Oses, Rhanzhu Novela (#2019), Lloyd, Humbe, Valentia, Rendani, Elisa, Lusani, Salphina, Tafadzwa, and all the honours students in the group), whose company I enjoyed most in the course of this program. You guys are the best group members one could ever seek. You guys are AWESOME.

Many thanks to my inestimable family, my sisters Mrs. Adeyemi T. S, Mrs.Ola-Bello Muinat, brother Mr. Ayinde Saheed O. (Lastborn) and my uncle, Mr. Adebayo S. May God continue to bless and guide you all through in all your endeavors.

Finally, this project will be incomplete if I fail to acknowledge the support, prayers, patience and advise of my lovely wife and mother of my beautiful children (Basith, Fuad and Ameerah (my princess)), Mrs. Ayinde Sandra Nkeiruka during the period of this program. I really appreciate all your efforts while away for this program. May God Almighty reward you in abundance and may you eat the fruits of all your efforts (AMEN). Thank you!!!!

The completion of this thesis may not have been possible without the financial support of USAID-PEER Cycle 6-Award No: AID-OAA-A-11-00012; National Research Foundation Grant No: 114726; University of Venda, South Africa (RPC grant Number: SES/17/ERM/03), Prof Gitari DHET Research incentive funds and Mintek, South Africa.

Dedication

This thesis is dedicated to the Almighty God who preserved my life through this sojourn. I also dedicate this work to my late parent Mr. and Mrs. Ayinde as well as my late sister Mrs. Abisogun Riskat. May their souls continue to rest in peace.

Project Summary

Groundwater has traditionally been perceived to be low in chemical species toxicity and microbiologically 'pure'. However, depending on the geological chemistry, formations and anthropogenic activities creating the frequent occurrence of microbiological contamination and excess toxic chemical constituents, the high quality of groundwater as a drinking water source can easily be compromised rendering it unsafe, thus, leading to severe waterborne epidemics. The rapid increase in fluoride and microbial contamination of groundwater have become a global problem to human health. Fluoride in its acceptable concentration in drinking water (< 1.5 mg/L); is known to be beneficial for human growth and development but becomes detrimental at higher concentrations (> 1.5 mg/L) leading to the prevalence of dental and crippling skeletal fluorosis. On the other hand, consumption of microbiologically contaminated water has led to many types of diseases including diarrhea, cholera, typhoid, dysentery and other serious illnesses often leading to millions of deaths annually worldwide. South Africa had experienced water-borne diseases epidemic in the recent past due to failing water treatment facilities in many parts of the country including rural areas. Fluorosis, diarrhea, and cholera are among the chronic health hazards affecting a large population in South Africa. Continuous outbreaks of water-related diseases have been at an unimaginable high level with a reported increase in death rate. The inefficiency of conventional water treatment plants to remove fluoride and disinfect these pathogens from the contaminated domestic and rural community has led to the development of many techniques. These include membrane filtration, ion-exchange, coagulation-precipitation, adsorption among others of which adsorption process proves to be a more significant technology for fluoride removal. Equally, the emergence of nanomaterials has also proved to be the natural answer to solve problems associated with microbes in water since these are absolute barriers to pathogens whose size exceeds most sorbent pore sizes. Also, materials from natural biopolymers or biomass can be utilized at an affordable cost as effective sorbent material for toxic chemical ions and pathogens removal from contaminated water. Consequently, extensive research works have been channeled into the development of more advanced low cost sustainable functionalized sorbent materials and technologies with multifunctional properties for effective water purification. The present study focused on the development of a functionalized chitosan-cellulose hybrid nanocomposite decorated with metal-metal oxides nanoparticles for simultaneous fluoride and microbial removal from groundwater. This was to increase the selectivity and disruption of such pollutants for effective groundwater purification technology.

The thesis is presented in nine chapters: (1) General introduction, problem statement, and motivation, research objectives, hypothesis and delimitations of the research are briefly discussed, (2) This chapter gives the literature review of occurrence and sources of fluoride, various fluoride removal techniques; sources, control measures and prevention of microbial pollution in groundwater; the importance of biosynthesis of nanomaterials as emerging novel water treatment adsorbents, the strength of Point-Of-Use as a means of water treatment, water treatment adsorbents synthesis and types of adsorbents with emphasis on hydroxyapatites and biopolymeric based sorbent materials, (3) Optimization of microwave-assisted synthesis of silver nanoparticle by *Citrus paradisi* peel extracts and its application against pathogenic water strain, (4) Biosynthesis of ultrasonically modified Ag-MgO nanocomposite and Its potential for antimicrobial activity, (5) Green synthesis of Ag/MgO nanoparticle modified nanohydroxyapatite and its potential for defluoridation and pathogen removal in groundwater (6) Green Synthesis of AgMgOnHaP nanoparticles supported on Chitosan matrix: defluoridation and antibacterial effects in groundwater, (7) Biosynthesis of nanofibrous cellulose decorated Ag-MgO-nanohydoxyapatite composite for fluoride and bacterial removal in groundwater, (8) Defluoridation and removal of pathogens from groundwater by hybrid

cross-linked biopolymeric matrix impregnated Ag-MgOnHaP nanocomposite (9) Conclusions and Recommendations. It is important to point out that Chapters 3 to 8 contains a collection of the research deliverables produced in forms of paper publications and manuscripts and are summarized in a systemic order of experimental protocol.

This first output (Chapter 3) of this study evaluated the optimization of a time-dependent microwave-assisted biosynthesis of silver nanoparticles using aqueous peel extracts of *Citrus paradisi* (Grapefruit red) as a reducing, stabilizing and capping agent with emphasis on its antibacterial property. Optical, structural and morphological properties of the synthesized *Citrus paradis*i peel extract silver nanoparticle (CPAgNp) were characterized using UV-visible spectrophotometer, transmission electron microscope (TEM), scanning electron microscope (SEM), energy dispersive spectroscopy (EDS), Brunauer–Emmett–Teller (BET) and X-ray diffractometer (XRD). The antimicrobial activity was evaluated using the well- and disc-diffusion as well as microdilution methods. Characteristic surface plasmon resonance (SPR) wavelength in the range of 420-440 nm at an optimized intensity growth rate typical of silver nanoparticles was obtained. Microwave irradiation accelerates the reaction medium within seconds of nucleation compared to conventional heating methods of synthesis. The influence of the reaction mixtures affected the SPR patterns on the different nucleation, stability and nanoparticle growth. The mixing ratio of 2:3 (*C. paradi*si peel extracts: 1 mM $AgNO_3$) was chosen as the optimum reaction mixing ratio relative to the bio-reduction intensity of SPR process contributing to the particle size growth of CPAgNps. The presence, interaction and shifting of the functional groups in the FT-IR spectra of biosynthesized CPAgNps indicated that bioactive compounds present in *C. paradisi* peel extract were responsible for the bio-reduction of the silver ion to silver nanoparticles. The electron micrographs of the synthesized CPAgNps showed a face-centered cubic (FCC) unit phase structure, spherically-shaped nanoparticles size of 14.84 ± 5 nm with a BET pore diameter of 14.31 nm. The use of biological material allowed the control of the size and stability of the nanoparticle but was obtained in low quantity. The *Citrus paradisi* peel extract mediated AgNp were found to possess a broad-spectrum antimicrobial activity against water-borne pathogenic microbes in the order: *Escherichia coli* > *Staphylococcus aureus* > Klebsiella *pneumonia*.

In Chapter 4, a synergistic bi-layered Ag-MgO nanocomposite from Ag and MgO precursor salts using a natural source from the waste product (citrus fruits outer cover) as a reducing and capping agent was successfully synthesized by a simple rapid, integrated bio-mediated microwave and ultrasonic methods. This was carried out to investigate the interfacial interaction and the encapsulated growth rate behind their combination in obtaining an enhanced antibacterial activity against common water fecal pathogen (*Escherichia coli*). The growth sequence, structural and morphology interface as well as the composition of the nanocomposite were examined and evaluated by the different characterization techniques. The respective potential application as an antimicrobial agent was evaluated and compared against *Escherichia coli*. The bio-mediated core-shell Ag-MgO nanocomposite showed characteristic synergetic UV-visible absorption bands at 290 nm for MgO nanoparticle and at around 440 nm for Ag nanoparticle, which moved to a lower wavelength of 380 nm in the composite. The shifting to a lower wavelength confirmed the reduction in the particle size as influenced by the growth rate optical property of biomolecular capped Ag-MgO nanocomposite from the phytochemical constituents in the peel extract of the *Citrus paradisi*. FTIR analysis further elaborated the role of the organic moieties in the *Citrus paradisi* extracts acting as the capping and stabilizing agent in the formation of the core-shell Ag-MgO nanocomposite. SEM analysis revealed an agglomeration of layered clustered particles, which was poly-dispersed while XRD showed the cubical crystal lattice network phase structure of the Ag-MgO nanocomposite. The TEM micrograph

showed a structurally uniform and spherical biosynthesized Ag-MgO nanocomposite with a diameter of about 20–100 nm with an average particle size of 11.92 nm. The bi-layered Ag-MgO nanocomposite exhibited a higher level broad-spectrum of antibacterial potential on *E. coli* with 22 mm zone of inhibition and MIC of 20 (µg/mL) in comparison with the Ag (9 mm; 40 µg/mL) and MgO (9 mm; 80 µg/mL) nanoparticles. The leaching and toxicity level of the time-dependent releases of metal ions indicates that the effluents contain a lower concentration of Ag and Mg ions as compared to World Health Organization permissible limit of < 100 ppb (Ag). The biosynthesized Ag-MgO nanocomposite exhibited an enhanced antibacterial activity synergistic effect against *E. coli* than Ag and MgO nanoparticles, thus, proving to be a potential disinfect material against common pathogens in water treatment.

Chapter 5 presented the biosynthesis, characterization, and assessment of simultaneous fluoride and pathogen removal potential in aqueous solutions of a multi-layered Ag-MgO/nanohydroxyapatite (Ag-MgOnHaP) composite. The successful incorporation of Ag-MgO into nanohydroxyapatite (Ag-MgOnHaP) sorbent via an in-situ solution-gelation (sol-gel) method was ascertained from UV-visible absorption spectrum bands at 290 and 440-378 nm typical of MgO and Ag nanoparticles combination in Ag-MgOnHaP composite. FTIR analysis showed the main surface functional groups involved to be –OH, C=N, carbonate and phosphate species on the backbone of Mg-O-Mg vibrational mode. The hydroxyl and amine groups indicated the interaction of a variety of metabolites components present in citrus peel extract as bio-reductive compounds associated with the Ag-MgO and also in fluoride ion exchange. SEM, TEM images and XRD analysis showed a well-dispersed discretely embedded layered-spherical Ag-MgOnHaP nanocomposite without any form of agglomeration after ultrasound exposure ranging in size from 20 to 100 nm with an average mean particle size diameter of 16.44 nm. The high purity of the synthesized Ag-MgOnHaP nanocomposite was confirmed by the presence Ag, Mg and O impregnated on the nanohydroxyapatite template from EDS spectrum analysis. Batch sorption studies using the nanocomposite under different experimental parameters were conducted and optimized. Equilibrium fluoride adsorption capacity of 2.146 mg/g at 298 K was recorded with more than 90% fluoride removal at optimized conditions of 60 min, 10 mg/L initial F^- concentration, 0.3 g/L dosage, and pH 6 at 250 rpm. pHpzc of Ag-MgOnHaP nanocomposite was established to be 8. The equilibrium data were best fitted to the Freundlich isotherm model and followed the pseudo-second-order kinetics model at room temperature. The presence of competing anions such as Cl^-, NO_3^-, does not have an impact on percentage fluoride uptake efficiency, but SO_4^{2-} and CO_3^{2-} reduce the F^- removal efficiency. Moreover, as the concentration of the co-anions increased, fluoride adsorption uptake decreases. The biosynthesized nanohydroxyapatite incorporated Ag/MgO nanoparticle adsorbent (Ag-MgOnHaP) showed strong antibacterial activity against *Escherichia coli* and *Klebsiella pneumonia* when compared to hydroxyapatite alone. The presence and interaction between the Ag, MgO nanoparticles with the respective bacterial genomes was suggested to have accounted for this bioactivity. The synthesized Ag-MgOnHaP sorbent was found to portray a better sorption capacity compared to other adsorbents of similar composition in the literature and could be successfully regenerated with 0.01 M NaOH with fluoride removal of 74.24% at the 4^{th} cycle of re-use.

The impregnation of metal-metal oxide nanoparticles on sustainable natural biopolymers from waste products was presented in Chapters 6, 7 and 8. The use of these sustainable natural biopolymers (chitosan and cellulose) was targeted with more emphasis on surface functionalization, improved structural diversity and improved specific surface area with the sole aim of increasing the adsorptive capacity of fluoride ions as well as antimicrobial properties. The selected polymers were chosen because of their biodegradability,

non-toxicity, renewability, selectivity and abundance in nature, which makes them promising starting materials for the purpose of sustainable water treatment.

Chapter 6 presents the successful sol-gel biosynthesis, characterization, potential application for fluoride and pathogens removal from aqueous solution using Ag-MgOnHaP embedded on a chitosan polymer backbone (AgMgOnHaP@CSn) sorbent material. The overall formation of the AgMgOnHaP@CSn nanocomposite from different surface functionalization precursors and phases were supported by the various characterization methods such as UV–vis spectroscopy, SEM-EDS, FTIR, TEM, and Brunauer–Emmett–Teller (BET) techniques. Batch fluoride sorption experiments were conducted to assess fluoride uptake efficiency through optimization of several operational parameters such as contact time, adsorbent dosage, initial pH and co-competing anions. The antimicrobial activity of the synthesized AgMgOnHaP@CSn nanocomposites was also determined. The presence and bio-reduction processes of both Ag and MgO chemical species due to the interaction and coordination of bonds within the bioactive functional species of the polymer matrix was confirmed by the emergence of a sharp peak appearing at around 290 nm to a broad plateau plasmon absorbance above 440 nm on the AgMgOnHaP@CSn nanocomposite. FTIR analysis further supported the presence of the main bioactive functional species to be –OH, $–NH_2$ $CO_3^{2–}$, PO_4^{3-}, Mg–O-Mg amongst other groups on the material surface. SEM and TEM displayed homogeneously dispersed particles within the aggregated biopolymeric composite with a diameter ranging between 5-30 µm. Pore sizes were observed to be in the micro-mesoporous range with an average size of about 35.36 nm and a pore diameter of 33.67 nm. The optimized conditions were as follows: 30 mins contact time, a dose of 0.25 g/50 mL, adsorbate concentration of 10 mg/L F-, initial pH 7 while adsorption capacity decreases with increase in temperature. AgMgOnHaP@CSn composite has a pHpzc value of ≈ 10.6 and the maximum sorption capacity was established to be 6.86 mg/g for 100 mg/L F- concentration at 303 K. The effect of co-existing anions was observed to be of the following order: $Cl^- < NO_3^- < SO_4^{2-} << CO_3^{2-}$. The fluoride sorption experimental data was well described by Langmuir adsorption isotherm while the sorption reaction mechanisms were diffusion-controlled and followed the pseudo-second-order sorption model. F- sorption process could best be described as a combination of ligand exchange, electrostatic attraction, and improved structural surface modification. The antimicrobial susceptibility analysis through the zone of inhibition (mean and standard deviation) showed the potency to pathogens of the following order: *Staphylococcus aureus* > *Escherichia coli*.

Chapter 7 gives an insight into the development of cellulose nanofibrous matrix (isolated from saw-dust) decorated with Ag-MgO-nanohydroxyapatite (CNF-AgMgOnHaP) and its application in fluoride and pathogen removal from contaminated water. The synthesized CNF-AgMgOnHaP, unlike the cellulose nanofiber, showed characteristic absorption bands in UV–vis spectroscopy between 270-290 nm typical of MgO together with a broad band around 420 nm associated with the characteristic of silver nanoparticles. FTIR spectrometry suggested the presence of nanohydroxyapatite (nHaP) and MgO species impregnation within the CNF matrix. SEM, TEM, XRD, and EDS analysis showed a well-established structural and morphological modifications between cellulose nanofiber alone, biosynthesized CNF-AgMgOnHaP and fluoride sorbed CNF-AgMgOnHaP nanocomposite. A granulated aggregation of micro-mesoporous particles with an improved BET surface area of 160.17 m^2/g was developed. Optimum fluoride sorption capacity was 8.71 mg/g for 100 mg/L F- solution at 303 K. F^- sorption capacities decreased as the operating temperatures increases. Optimum F- removal of 93 % was achieved at optimum conditions established: pH 5, solid/liquid ratio of 0.25 g/ 50 mL, 10 mg/L F^-, contact time 10 min, temperature 25 ± 3 °C and shaking speed of 250 rpm. Percent F^- removal decreased with increasing initial adsorbate concentration. The pHpzc

value of the CNF-AgMgOnHaP occurred at ≈ 4.7. Co-existing ions were observed to have an effect on the adsorption of F- in the following order: NO_3^- < Cl^- < SO_4^{2-} <<CO_3^{2-}. Equilibrium fluoride sorption onto the CNF-AgMgOnHaP was best described by non-linear Freundlich isotherm model across all the operating temperatures. The linear Dubinin-Radushkevvich (D-R) model for F- sorption energies were in the 3.54 – 4.08 kJ/mol across all operating temperature. This suggested the physical adsorption mechanism processes were involved in the F- uptake by the CNF-AgMgOnHaP sorbent. The overall kinetic results indicated that the mechanisms not only depend on the pseudo-second-order process but were also governed by mass transfer of the adsorbate molecules across the CNF-AgMgOnHaP surface. The thermodynamic parameters revealed that the sorption process of F- onto CNF-AgMgOnHaP was endothermic and spontaneous at the sorbent/solution interface. The regeneration-reuse study showed that the synthesized adsorbent can be reused for a maximum of 5 adsorption-desorption cycles using Na_2CO_3 and NaOH as regenerants. Overall surface chemistry by XPS, FTIR, EDS as well as sorption isotherm and kinetic models analysis suggested that both physical and chemical adsorption processes were involved in the fluoride uptake by CNF-AgMgOnHaP nanocomposite. The observed zone of inhibition demonstrated that CNF-AgMgOnHaP adsorbent possesses antibacterial activity against all the bacterial strains in the following order: *E. Coli* > *S. aureus* > *K. pneumonia*. The antibacterial potency increased with increasing sorbent concentration.

In chapter 8, Defluoridation and antimicrobial activity of synthesized cross-linked cellulose-chitosan impregnated with the developed nanomaterial (AgMgOnHap) are presented. The before and after fluoride sorption by the synthesized CECS@nHapAgMgO nanocomposites were characterized using several physical and chemical techniques which include, BET, SEM-EDS, TEM, XPS, XRD, and FTIR. The overall batch fluoride sorption processes and adsorption capacity through optimization of different experimental sorption parameters, sorption isotherms, and kinetic mechanisms as well as antibacterial potency were studied and reported. SEM and TEM analysis showed densely irregular multiple-layered structures, homogeneous deposition of the AgMgOnHaP on the polymeric matrices. Equilibrium fluoride sorption capacity on CECS@nHapAgMgO sorbents showed an increased affinity of 26.11 mg/g for 150 mg/L F- solution at 313 K.at optimized conditions of 40 min contact time, dosage of 0.3 g and pH of 5. The pH point of zero charge was found to be 7.27. The reaction pathway model sequence of fitness follows the order Pseudo first order < Elovich < Pseudo-second order kinetic model while intra-particle diffusion model and mass transfer of fluoride molecules from the external surface onto the improved pores of the adsorbent were found to be involved in the rate-controlling step. Although both non-linear Langmuir and Freundlich isotherms showed appropriate trends in the F- sorption process, the adsorption isotherm data were better fitted to the non-linear Freundlich isotherms models, suggesting stronger heterogeneous adsorption onto the active binding sites of the CECS@nHapAgMgO surface. The fluoride sorption was observed to be a favorable process across the operating temperatures. Temkin heat of sorption (B_T) and the mean free adsorption energy (E) of the D-R isotherm model was within the range of 0.68-3.39 J/mol and 1.58 -7.45 kJ/mol respectively. The fluoride sorption process was observed to be temperature-dependent; while adsorption capacities (Q_m) and Temkin heat of sorption (B_T) increased with increasing temperature, D-R Mean free sorption energy (E) decreased at higher temperatures. The thermodynamic analysis demonstrated that fluoride sorption on the CECS@nHapAgMgO surface was exothermic, feasible and spontaneously inclined with a decrease in the degree of randomness at the sorbate-sorbent interface. The influence of co-existing anions on fluoride removal exhibited the following trend Cl^-< NO_3^- <SO_4^{2-} << CO_3^{2-} <<HCO_3^-. The practical and economic viability, potential for regeneration showed its reusability up to 3 cycles with water and Na_2CO_3 as regenerants. The potential ability of CECS@nHapAgMgO to disinfect both gram-

positive and gram-negative water bacterial was confirmed by the zone of inhibition and Minimum Inhibitory Concentration (MIC) measurements. The observed values showed the inhibitory efficiency in the following order: *S. aureus* > *E. Coli* > *K. pneumonia* where the MIC values of 20 µg/mL were recorded for *S. aureus* and *E. Coli* respectively and 10 µg/mL for *K. pneumonia*. Lastly, the applicability of the sorbents was tested with a field water sample collected from a high fluoride borehole water from a local village (Lephalale Municipality of Limpopo province, South Africa). The before and after analysis showed the excellent potential of CECS@nHapAgMgO sorbent in removing fluoride.

In conclusion, the successful surface functionalization synthesis of these improved surface area hybrid nano-sorbents supported by the different morphological techniques was found to be effective in creating more surface-active binding sites for fluoride adsorption and disinfection of waterborne pathogens from aqueous solution. The originality of this developed sorbent lies firstly, in the ability to simultaneously remove both chemical and biological water pollutants; secondly, the use of biodegradable, eco-friendly and non-toxic abundance wastes raw materials to develop a water purification material and in solving waste management issues was a key factor towards environmental sustainability. Above all the developed materials were established to possess superior fluoride adsorption capacity when compared to other reported sorbent materials. Lastly, the project findings /innovation will contribute to Sustainable Development Goals (SDG) 3 and 6, aimed at improving clean water supply and health of the communities and the world at large.

However, the following recommendations were made following the findings from this study: 1) In order to increase the surface area to volume ratio, greater selectivity, porosity, and mechanical stability of the polymers as well as size-exclusion mechanism without a large energy penalty of the microbes and fluoride ion for effective water treatment, a more effective and an enhanced multifunctional, multi-layer nanofibrous hybrid sorbent through electrospinning techniques should be considered for future work, 2) More studies on the mode of actions and morphological changes in the pathogens leading to the cell death through the influence of the nanocomposites should be further explored, 3) Application of this advanced technology vis-à-vis other biomaterials to generate filter membrane towards efficient microbial removal and deflouridation is a great challenge worth looking at, 4) Lastly, materials developed in the present study should be modeled, tested and fabricated at the point of use for fluoride and pathogen removal at household level.

Academic Outputs

Conferences and workshops

- W. B. Ayinde; W. M. Gitari (2017) **Nano-synthesis of adsorbent as a means of sustainable water management (***BERGEN SUMMER RESEARCH SCHOOL (BSRS) 2017 on "Water management, Development Trajectories and the Modern World". Bergen, Norway 12 – 22 June 2017***)**
- W. B. Ayinde; W. M. Gitari and M. Munkombwe (2017). **Green Synthesis of Ultrasonically modified MgO-nanohydroxyapatite composite and its potential for simultaneous defluoridation and pathogen removal in groundwater** (*Paper presented at First Regional Conference and School on Climate Change, Water and Environmental Sanitation For Early Career Scientists Working in Africa, 28th – 31st August 2017 at Ghana Academy of Arts and Sciences Auditorium, Accra - Ghana*)
- W. B. Ayinde; W. M. Gitari; M. Munkombwe and Samie Amidou (2017). **Green Synthesis of Ag/MgO nanoparticle modified nanohydroxyapatite and its potential for defluoridation and pathogen removal in groundwater**. (*Paper presented at 18th WaterNet/WARFSA/GWP-SA Symposium on "Integrated Water Resources Development and Management: Innovative Technological Advances for Water Security in Eastern and Southern Africa", 25th to the 27th of October 2017 at Swakopmund Hotel and Entertainment Centre, Swakopmund, Namibia*)
- W. B. Ayinde; W. M. Gitari; M. Munkombwe and Samie Amidou (2018). **Green synthesis of ultrasonically modified Ag-MgO nanocomposite and its prospective antimicrobial activity.** (*Paper presented at 7th International Conference on Nanoscience and Nanotechnology in Africa (NanoAfrica2018), Salt Rock Hotel in Durban (South Africa) on 22 - 25 April 2018*.)
- Ayinde W. B, Gitari W. M, Munkombwe M, and Amidou Samie. **Biosynthesis of Ag-MgO-nanohydroxyapatite on nanofibrous cellulose for fluoride and bacterial removal in groundwater.** (*Paper presented at 1st International Conference on Sustainable Management of Natural Resources (ICSMNR 2018), Bolivia Lodge, Polokwane, Limpopo (South Africa) on 15 – 17 October 2018*)

Publications

- W.B. Ayinde, W.M. Gitari, M. Munkombwe, Samie Amidou. **Green synthesis of Ag/MgO nanoparticle modified nanohydroxyapatite and its potential for defluoridation and pathogen removal in groundwater,** Physics and Chemistry of the Earth, Parts A/B/C, 2018, ISSN 1474-7065, https://doi.org/10.1016/j.pce.2018.08.007.

- Wasiu B. Ayinde, Mugera W. Gitari, Munkombwe Muchindu, and Amidou Samie, **"Biosynthesis of Ultrasonically Modified Ag-MgO Nanocomposite and Its Potential for Antimicrobial Activity,"** Journal of Nanotechnology, vol. 2018, Article ID 9537454, 10 pages, 2018. https://doi.org/10.1155/2018/9537454.
- W. B. Ayinde; W. M. Gitari; M. Munkombwe and Samie Amidou (2019). **Optimization of microwave-assisted synthesis of silver nanoparticle by Citrus *paradisi* peel and its application against pathogenic water strain,** *Green Chemistry Letters and Review*, 12:3, 225-234. https://doi.org/10.1080/17518253.2019.1627427

Paper in Refereed Conference Proceedings

- Ayinde W. B, Gitari W. M, Munkombwe M, and Amidou Samie. **Biosynthesis of Ag-MgO-nanohydroxyapatite on nanofibrous cellulose for fluoride and bacterial removal in groundwater.** (*Proceeding in the 1st International Conference on Sustainable Management of Natural Resources (ICSMNR 2018), Bolivia Lodge, Polokwane, Limpopo (South Africa) on 15 – 17 October 2018*)

Publications submitted to journals (Under Review)

- W. B. Ayinde; W. M. Gitari; Samie Amidou; M. Munkombwe and James Smith (2019). **Green Synthesis of AgMgOnHaP nanoparticles supported on Chitosan matrix: defluoridation and antibacterial effects in groundwater (**Submitted to *Springer Environmental Science and Pollution Research*) **(Manuscript ID: ESPR-D-19-02543)**

Publications to be submitted to journals

- W. B. Ayinde; W. M. Gitari; Samie Amidou and James Smith (2019). **Biosynthesis of nanofibrous cellulose decorated Ag-MgO-nanohydroxyapatite composite for fluoride and bacterial removal in groundwater. (**Ready for submission to Journals of Biological Macromolecules**)**
- Ayinde W. B, Gitari W. M, Muchindu M, Samie Amidou, and James A. Smith (2019.) **Defluoridation and removal of pathogens from groundwater by hybrid cross-linked biopolymeric matrix impregnated Ag-MgOnHaP nanocomposite.** (Ready for submission to Journal of Applied Materials and Interface)
- W. B. Ayinde; W. M. Gitari; Samie Amidou; M. Munkombwe and James Smith (2019). **Comparative study of fluoride sorption and antimicrobial potentials by biopolymeric-metal oxide nanocomposite** (Draft).

Table of Contents

CHAPTER ONE

INTRODUCTION AND PROJECT RATIONALE

1.1 Background

Water is life and life without water is inevitable. According to the United Nations Children's Fund, "Universal access to safe drinking water is a fundamental need and human right". Moreover, the United Nations World Water Development Reports (WWAP, 2015) placed water at the core of its sustainable development. The sustainable development goals (SDG's) highlight the need to ensure water availability and its sustainable management for all by 2030. Its sub-theme emphasizes on the need to achieve universal and equitable access to safe and affordable drinking water for all. However, with rapid population growth, urbanization, demographic changes and increasing incidence of climatic change, water availability is on the decline and deterioration of water quality on the rise due to contaminated water sources in many parts of the world. Presently, 844 million people live without access to potable drinking water and more than 2.3 billion live without access to improved sanitation (WHO/UNICEF, 2017). Globally, increasing water scarcity (Fig. 1) is gradually coming up as a potential threat to food security, human health, and natural ecosystems with more than 50% of the world projected to experience this water shortage by the year 2050 (Shahin and Mady, 2014; Connor *et al*., 2017). Increased water scarcity has led to high cases of contaminated water resulting in millions of deaths across the globe with an estimated 829 000 water-related diseases deaths each year (WHO, 2016). In many parts of the world, most common sources of water resources contamination are caused majorly from naturally and anthropogenic chemically discharged pollutants (organic and inorganic) and waterborne pathogens.

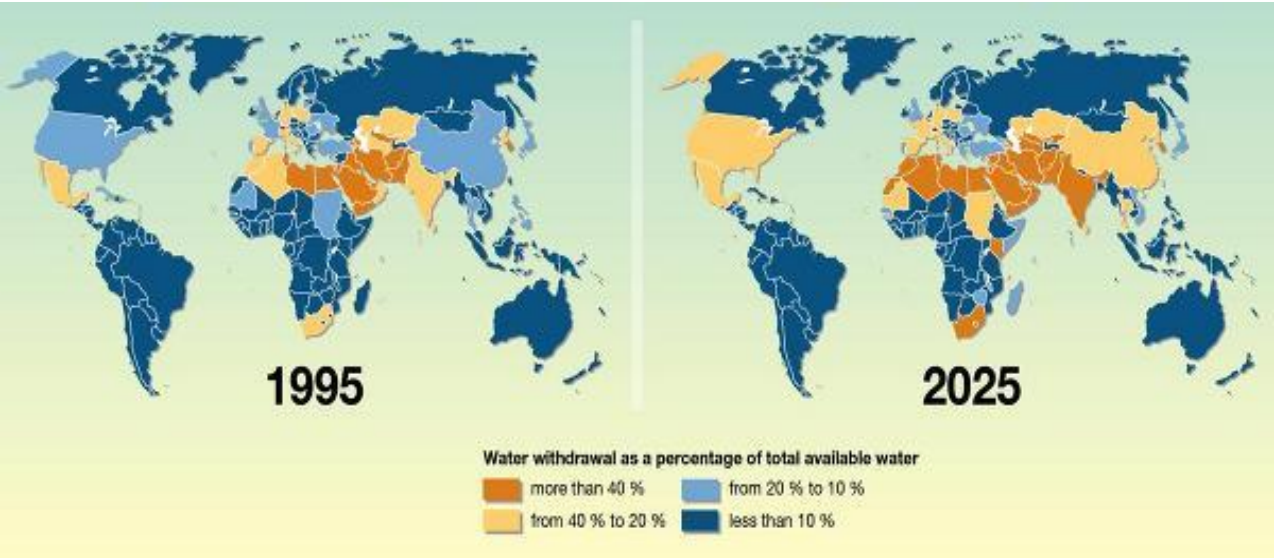

Fig. 1: Water scarcity as a global challenge (UNEP, 2008)

The usefulness and availability of water for a specific need is largely dependent on the quality standard and provision, thus, not all the waters are fit for consumption; hence, increasing reliance on other accessible alternative sources like surface and groundwater in reducing water demands. However, the quality of these water sources such as rivers and boreholes for domestic needs are being hampered due to the continuing rise in water contamination from waterborne pathogens and discharge of chemical pollutants. In many of the developing countries, rural community dwellers access polluted and contaminated water for their domestic purposes and use it directly without any treatment whatsoever. Moreover, not everyone has access to treated water and, where such is treated, the water still contains traces amount of pollutants, which may bio-accumulate with time and eventually become deadly to human health. A consequence of this is epidemic, an outbreak of diseases and eventual high mortality rate mostly among children (WHO/UNICEF JMP, 2015; 2017).

Fig. 2: Images of rural dwellers as they fetch polluted river water for direct drinking

According to the World Health Organization, re-use of wastewater, water recovery management, and purification of contaminated water through sustainable technologies is becoming an important strategy. The removal and means of reducing these contaminants to acceptable limit are immensely vital for the human and economic growth of any nation. Therefore, adequate managing, monitoring, and provision of safe domestic water resources remain a high developing priority. However, despite numerous intervention strategies and large public and private investments, many challenges continue to impede water availability worldwide especially in the developing countries. One of the key challenges associated with water needs and purification in developing countries due to economic constraints is high operational costs. There is, therefore, the needs to develop efficient, low-cost and appropriate water treatment technologies to reduce this menace for human survival.

1.2 Problem statement and Motivation

Water is an essential part of human existence and the provision of safe, potable drinking water adequate in quantity and acceptable quality is vital for human existence. In its press statement on "Obstacles faced by developing countries in meeting water, sanitation, and human settlements",

the United Nation identified developing countries as the weakest link in the global chain of sustainable development due to poverty, hunger, deteriorating environments and infectious diseases (Press Release: ENV/DEV/767). South Africa National Development Plan (2030) recognizes the fact that one of the approaches for a minimum standard of living by society is the provision of water and sanitation (NDP2030-SA, 2016). The lack of access to safe drinking water and the continuing increased in water-associated diseases as well as recurring freshwater shortages is of great public concern according to the World Health Organization. It is a recognized fact that the most important aspect of improving the health of people is to provide safe and clean water to communities in a rural area.

Based on the Falkenmark Water Stress Indicator (that calculates an index for a given area using various measures for water availability, water quality, water demand, water affordability, and service coverage.); South Africa is classified as a water-stressed country (Siebrits and Winter, 2013). Furthermore, the World Water Assessment Program places South Africa in the extreme risk category (Water Systems Analysis Group, 2012) and several reports have warned that South Africa faces a growing water-related environmental, economic and social crisis (Turton *et al*., 2006; Bond and Dugard, 2008). Many water treatments in South Africa are usually concentrated in urban areas while little or no effort exists in providing clean water treatment in rural communities. Where such exist, usually it is through a small water treatment plants (Momba *et al*., 2008) and the water quality parameters generally did not always meet the South African Guidelines for drinking water (DWAF, 1996) on such plants distribution. The lack of centralized treated water supply systems means most rural communities of most developing and sub-Saharan African countries rely on unsafe surface water and groundwater sources for their domestic water supply (Gitari *et al*., 2013). Thus, placing rural people at health risk to water contaminants. As a valuable alternative source of drinking water, groundwater is a key component of the water resources of South Africa. However, groundwater can become unsuitable for drinking due to the high dosage of naturally occurring and human-induced chemical and microbial pollution from pollutants (USGC, 2016; Fuller, 2012). These often resulted in acute and chronic health effects on the users with children the most vulnerable to a greater risk of strange water-related diseases resulting in preventable sudden deaths.

One of such contaminants associated with many aquifers depending on geology and chemistry is fluoride. The rapid increase in fluoride contamination of groundwater has become an unprecedented global problem to human health. Fluoride is not necessarily present in groundwater as a pollutant but a naturally occurring chemical species that generally leached into groundwater by slow dissolution of fluorine-based mineral rocks (García and Borgnino, 2015). Furthermore, the increasing amount of wastewater containing fluoride is being released from various engineering processes and anthropogenic activities (Miretzky and Cirelli, 2011). Fluoride concentration in the drinking water is considered to be of substantial significance from the perspectives of public health due to the serious threat to human health (Bhatnagar *et al*, 2011). Fluoride is known to be beneficial at concentrations < 1.5 mg/L but becomes detrimental at

concentrations > 1.5 mg/L (WHO, 2011). More than 200 million people across the globe face excess fluoride-related issues from drinking water, with high health effects and morbidity in several regions depending on the geographical and economic status (Ayoob *et al*., 2008; Mumtaz *et al*. 2015). The excessive ingestion of fluoride in drinking water depending upon the concentration and period of ingestion can cause dental or crippling skeletal fluorosis (Fig. 3 and 4), which are chronic diseases, manifested by mottling of teeth in mild cases, softening of bones and neurological damage in severe cases (Zhang *et al*., 2012). Other non-skeletal issues include neurological and thyroid dysfunction, cardiovascular and reproductive problems, etc.

Fig. 3: Severe dental fluorosis

Fig 4: Photographic evidence of severe skeletal fluorosis across the world.

In addition to chemical pollutants, the majority of global water pollution outbreaks are often associated with the consumption of microbiologically-infested water sources depending on the level of protection of the water. This is naturally caused by the presence of pathogenic microorganisms like *Escherichia Coli, Cryptosporidium sp., Klebsiella sp., Staphylococcus aureus, Vibrio cholerae,* etc. (Keyser, 1997; Bitton, 2014; WHO, 2016). The World Health Organization estimated at least 2 billion people consume a drinking water source contaminated with feces and this contributed to about 5 million water-related diseases and deaths annually (WHO, 2016). From these, diarrhea and cholera are currently responsible for about 90% of all deaths of children under five years in developing countries (WHO/UNICEF JMP, 2010).


Fig. 5: Water-related diseases by pathogenic organisms (Source: CNN)

In order to prevent and reduce the transmission of water-related diseases from these pollutants, removing fluoride and disinfecting these pathogens is a necessity for improved water quality and public health. Various water treatment techniques through the use of conventional and emerging methods have been applied towards the removal of fluoride and pathogens; based on the principle of sorption, precipitation, membrane filtration, coagulation, chlorination, ultraviolet (UV) irradiation etc. (Hijnen, 2006; Momba *et al.*, 2013; Gitari *et al*., 2013). However, these methods often create some drawbacks, which further compromise the quality of the water and adversely affects human health. These include the introduction of secondary pollutants, the formation of harmful carcinogenic disinfection byproducts (DBPs), low adsorption rate, the high cost of energy and operational cost, technical skills, etc. (Hijnen, 2006). These constraints generally make such technologies unsustainable for rural communities of most developing countries. There is, therefore, need to develop robust simple processes, cost-effective and sustainable separation technologies that can be recycled for small-scale towards efficient pathogenic microorganisms and fluoride removal from groundwater applicable in the rural areas to solving the lingering water and environmental problems.

South Africa had experienced water-borne diseases epidemic in the recent past due to failing water treatment facilities in rural areas and several other cities. Groundwater in some communities in Limpopo, Northwest, and Northern Cape are known to have fluoride concentrations >5mg/L (Gitari *et al*, 2016: WRC Report Project No: K5/2363//3-In press). Thus, the need to address and proffer a sustainable and effective solution to the causes of this infectious disease transmission and related fluoride content of groundwater used for domestic and drinking purposes, whose impact in the health of a local community in South Africa remains significant.

The World Health Organization reported appropriate technology options in water treatment to include both community-scale and household-scale point-of-use (POU) designs. Also, nanotechnological influence on the use of biomaterials loaded with nanoparticles is on the rise towards overcoming these water-related problems, especially at the P.O.U. but has not yet been felt in most developing nations. Hence, this proposed research is challenged by this unpalatable incidental phenomenon and therefore seeks to develop a sustainable advanced water treatment material for simultaneous fluoride and pathogen removal in groundwater. The focus is to ensure

that the developed adsorbent is more effective, eco-friendly, reusable and affordable towards the delivery of safe and clean water to rural communities at household-scale.

The study strategic approach is centered on the combination of positive attributes of providing the solution for a sustainable economic and ecologically viable multifunctional water purification techniques in a hybrid nanoparticle system containing sustainable natural polymeric materials from waste. Finally, it is expected that a more robust, effective and inexpensive water treatment technology would go a long way in addressing the root causes of diseases and poverty in South Africa and the rest of the developing nation as we combine particulate and adsorptive filtration through adsorption technology; suitable for POU application in homes.

1.3 Research objectives

The overall objective is to develop a novel multifunctional hybrid biopolymer-metal oxide nanoparticle reinforced composites that are envisaged to simultaneously remove fluoride and pathogens in groundwater for application in household water treatment devices.

The specific objectives of this proposed study were to:

1. Synthesize Ag and Ag-MgO nanomaterials using green methods and evaluate its antimicrobial potency.
2. Synthesize Ag/MgO/nanohydroxyapatite nanoparticles via modified bio-reduction techniques and test its application for fluoride and pathogen removal in groundwater.
3. Isolate and develop a multi-functional chitosan/cellulose nanofibrous composite membranes from biomass with surface modification of Ag/MgO/nanohydroxyapatite nanoparticles towards fluoride and pathogen removal in groundwater treatment.
4. Evaluate the physicochemical, surface chemistry and morphological properties of the synthesized materials and its modified chitosan/cellulose/n-Hap/Ag-MgO composites.
5. Test and optimize the fluoride sorption performances of the Ag/MgO/nanohydroxyapatite and the different modified biopolymeric supported adsorbent using batch experiments and evaluate their respective antimicrobial potency on a laboratory scale.
6. Investigate and compare the model kinetic, equilibrium isotherm, the thermodynamic and the adsorption mechanisms from experimental sorption data.
7. Determine the feasibility for simple regeneration potential of fluoride-sorbed adsorbents.

1.4 Hypothesis

Developed multifunctional hybrid biopolymer-metal oxide nanoparticles reinforced composites can effectively remove fluoride and waterborne pathogen simultaneously from groundwater.

1.5 Delimitations of the research

Excessive fluoride and biological related diseases are a worldwide problem despite the presence of other pollutants in groundwater. Several reports had clearly indicated that safe drinking water is still a dream in rural areas of the world including South Africa. There are several naturally occurring sorbent materials that have been reportedly used for defluoridation studies. This study uses naturally occurring and non-toxic precursors and polymers from biomass because of the advantage of the hydroxyl groups in its chemical structure which could easily exchange for fluoride ions in water as well as their availability, biodegradability, sustainability and stability in retaining nanoparticles. The concept of this research is tailored to the use of field fluoride-rich groundwater in some selected places in Limpopo Province; where preliminary fluoride analyses of the water from the commonly used boreholes showed its high fluoride content. This study, therefore, focused on defluoridation of fluoride-rich Lephalale groundwater in Limpopo Province. Thus, limiting the overall representative of all fluoride-rich groundwater in South Africa and the world in general. In addition, bacteria, protozoa, and viruses are the major pollutants of contaminated water by microbes. This research was only limited to the common pathogenic organisms with high fecal coliforms i. e. *Staphylococcus aureus, Escherichia coli, and Klebsiella pneumonia.*

References

Ayoob, S., Gupta, A.K., Bhat, V.T., 2008. A conceptual overview on sustainable technologies for the defluoridation of drinking water. Crit. Rev. Environ. Sci. Technol. 38, 401–470.

Bhatnagar, A., Kumar, E., Sillanpää, M., 2011. Fluoride removal from water by adsorption—a review. Chem. Eng. J. 171 (3), 811–840.

Bitton, G., 2014. Microbiology of Drinking Water: Production and Distribution. John Wiley & Sons

Bond, P. and Dugard, J., 2008. Water, human rights and social conflict: South African experiences. Law, Social Justice & Global Development, 1, pp.1-21.

CNN: http://www.cnn.com/2010/WORLD/americas/10/21/haiti.cholera/?hpt=Sbin

Connor, R., Renata, A., Ortigara, C., Koncagül, E., Uhlenbrook, S., Lamizana-Diallo, B.M., Zadeh, S.M., Qadir, M., Kjellén, M., Sjödin, J. and Hendry, S., 2017. The united nations world water development report 2017. wastewater: The untapped resource. The United Nations World Water Development Report.

Dankovich, T.A., Levine, J.S., Potgieter, N., Dillingham, R. and Smith, J.A., 2016. Inactivation of bacteria from contaminated streams in Limpopo, South Africa by silver-or copper-nanoparticle paper filters. Environmental science: water research & technology, 2(1), pp.85-96.

Department of Water Affairs and Forestry (DWAF), 1996 South African Water Quality Guidelines for Domestic Use (2nd edn.) Pretoria. 197 pp.

Fluorosis endemic https://www.hindustantimes.com/ranchi/relief-at-sight-for-fluorosis-endemic-village/story-BGzriSBS8LTZaGkNMjijjP.html

Fuller, T., 2006. Rural water supplies and water-quality issues. Healthy Housing Reference Manual 1–12.

García, M.G. and Borgnino, L., 2015. Fluoride in the Context of the Environment. Fluorine: Chemistry, analysis, function and effects, 3. http://dx.doi.org/10.1039/9781782628507-00003

Gitari W.M., Ngulube, T., Masindi, V., Gumbo, J.R. 2013. Defluoridation of groundwater using Fe3+-modified bentonite clay: Optimization of adsorption conditions, Desalin. Water Treat. 1–13, doi: 10.1080/ 19443994.2013.855669

Hijnen, W., Beerendonk, E. & Medema, G. J. 2006. Inactivation credit of UV radiation for viruses, bacteria and protozoan (oo)cysts in water: a review. Water Res. 40, 3–22.

Keyser, S. L., 1997. Microorganisms, Bacteria and Viruses. Retrieved from http://extoxnet.orst.edu/faqs/safedrink/microorg.htm on 14th of July, 2016.

Miretzky, P. and Cirelli, A.F., 2011. Fluoride removal from water by chitosan derivatives and composites: a review. Journal of Fluorine Chemistry, 132(4), pp.231-240.

Momba, M.N.B., Obi, C.L. and Thompson, P., 2008. Improving disinfection efficiency in small drinking water treatment plants. Water Research Commission.

Momba, M.N.B., 2013. Selection and Use of Home Water-treatment Systems and Devices: Report to the Water Research Commission. Water Research Commission.

Mumtaz, N., Pandey, G. and Labhasetwar, P.K., 2015. Global fluoride occurrence, available technologies for fluoride removal and electrolytic defluoridation: a review. Critical Reviews in Environmental Science and Technology, DOI: 10.1080/10643389.2015.1046768

National Planning Commission, 2013. National development plan vision 2030.

Press Release ENV/DEV/767. https://www.un.org/press/en/2004/envdev767.doc.htm

Shahin, H. and Mady, E., 2014. Nanocomposites Electrospun Nanofiber Membranes for Environmental Remediation. Materials, 7, pp.1017-1045.World Health Organization, 1996. Guidelines for drinking-water quality. Geneva: WHO, Vol: 2.

Siebrits, R. and Winter, K., 2013. Identifying and Prioritizing Water Research Questions for South Africa (No. 2170/1, p. 13). WRC Report.

Skeletal Fluorosis and Natural Fluoride In India: http://poisonpaste.com/skeletal-fluorosis.php

Turton, A., Schultz, C., Buckle, H., Kgomongoe, M., Malungani, T. and Drackner, M., 2006. Gold, scorched earth and water: the hydropolitics of Johannesburg. Water Resources Development, 22(2), pp.313-335.

UNEP (2008), Vital Water Graphics - An Overview of the State of the World's Fresh and Marine Waters. 2nd Edition. UNEP, Nairobi, Kenya. ISBN: 92-807-2236-0

USGC, 2016. Contaminants Found in Groundwater. Available online: http://water.usgs.gov/edu/groundwater-contaminants.html (accessed on July 2017)

WHO. 2003b. Emerging Issues in Water and Infectious Disease. World Health Organization, Geneva.

WHO, Guidelines for drinking water quality, fourth ed., World Health Organization, Geneva, 2011.

World Health Organization, 2016. Mortality and burden of disease from water and sanitation. Global Health Observatory (GHO) data.

WHO/UNICEF JMP (Joint Monitoring Programme for Water Supply and Sanitation). 2010. Improved sanitation coverage estimates (1980 - 2010). 20-22.

WHO/UNICEF JMP (Joint Monitoring Programme for Water Supply and Sanitation). 2010. JMP Rapid Assessment on Drinking-water Quality pilot report 2010. 8-10. http://www.un.org/waterforlifedecade/background.shtml.

WRC 2001 Distribution of Fluoride-Rich Groundwater in the Eastern and Mogwase Regions of the Northern and North-West Province. WRC Report No. 526/1/01 1.1 - 9.85 Pretoria.

World Health Organization and UNICEF Joint Monitoring Programme. (2017). Progress on Drinking Water and Sanitation, 2017 Update and MDG Assessment.

WWAP (United Nations World Water Assessment Programme). 2015. The United Nations World Water Development Report 2015: Water for a Sustainable World. Paris, UNESCO.

Zhang, G., He, Z. and Xu, W., 2012. A low-cost and high efficient zirconium-modified-Na-attapulgite adsorbent for fluoride removal from aqueous solutions. Chemical Engineering Journal, 183, pp.315-324.

CHAPTER TWO

LITERATURE REVIEW

2.1 Groundwater resources as an alternative source of water

Water is a constant factor in human life. Water scarcity has already been identified as a global challenge with increased adverse effects on all populations (WHO-UNICEF, 2017). The essentiality of clean, portable and easily accessible water that is free of toxic chemicals and pathogens to human health cannot be over-emphasized. Water from the public water-treatment systems aimed at preventing and protecting people found in such areas from such contaminants are often less reliable in terms of supplying the required water quality. Globally, groundwater is an important natural source of water supplies and accounts for approximately one-third of all available freshwater resources (UNESCO 1999; 2009). Many communities in most parts of the world rely on groundwater for their domestic needs and source of drinking water. This is mainly due to it being naturally well protected by overlying soil and sediment layers, which act as effective mechanical and biological filters, thus, providing a natural clean-up water system free of contaminants with minimal treatment (Steffen and Christian, 2011). However, nowadays as a results of geogenic and anthropogenic processes, climatic and demographic variations as well as unhygienic sanitation systems, the quality of this naturally generated groundwater is being compromised from increased chemical compositions and microbiological pollutants (Pedley *et al*., 1997; 2006; Steffen and Christian, 2011; Thole, 2013). Among the naturally and anthropogenic deposited inorganic chemical species include fluoride, arsenic, iron, lead, nitrate, sulfate, trace and heavy metals, while bacterial, virus and protozoans are the major causes of microbiological origin. Controlling and removing these pollutants from affected contaminated water will go a long way in improving the quality of groundwater, hence minimizing the health risks associated with human existence for sustainable water management.

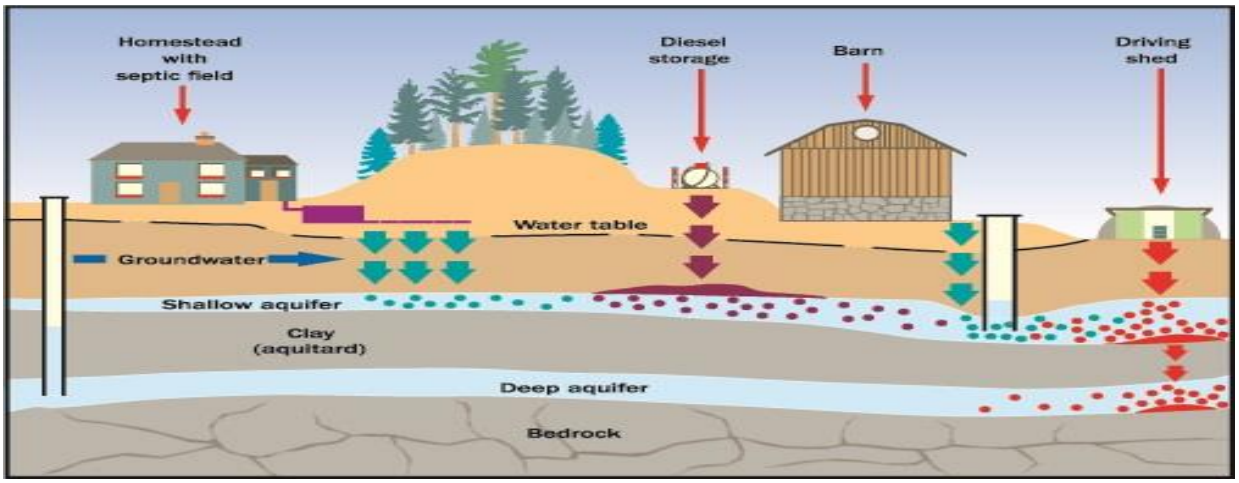

Fig 2.1. Pathways to groundwater contamination (Simpson, 2015).

2.2. Groundwater and Microbial Pollution: Sources, Control Measures, and Prevention

Microorganisms exist and are found everywhere in the natural environment. Generally, groundwater is perceived to be free of microbiological and biological properties in because it is protected by overlaying geological layers and vertical transport times, which makes it difficult for microbial organisms to survive and exists in such aquifers (Tufenkji and Emelko, 2011; Steffen and Christian, 2011). However, the risks of groundwater and drinking water contamination are becoming increasingly higher at an alarming rate because of many anthropogenic activities including on-site sanitation systems, landfills, effluent from wastewater treatment plants, leaking sewers, etc. (Gerba, 1988; Sampat, 2000; Wikipedia contributors. 2019).

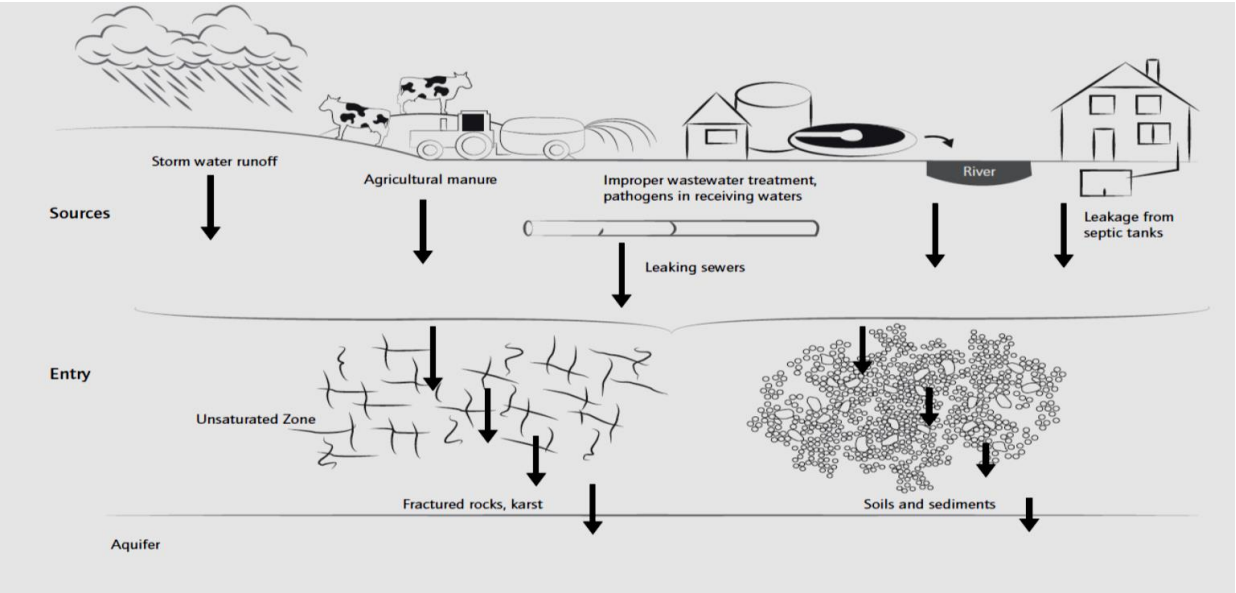

Fig. 2.2. Major sources of microbial pollutants to groundwater (Steffen and Christian, 2011)

Waterborne diseases due to the heavy presence of pathogenic microbes and viruses have been reported worldwide and pose a possible health threat to these communities associated with such water resources (WHO, 2004; Pedley and Howard, 1997, WHO-UNICEF, 2011). The major health risks associated with groundwater is from microbiological origins derived from human and animal feces. The most common microbial contaminant of public health concern in drinking water is caused by bacteria, protozoa, and viruses. These include *Cryptosporidium* spp. (stomach cramps, etc. – no treatment), *Giardia Lamblia* (beaver disease – no treatment), *Escherichia Coli* (an indicator of the presence of potentially harmful bacteria), *Salmonella* spp. and *Klebsiella pneumonia* (Typhoid fever), *Entamoeba Histolytica* (gastrointestinal disease), *Shigella Virus* (Hepatitis virus) (Keyser, 1997). These are all serious disease-causing pathogens that are common in water and have resulted into small and huge endemic outbreaks especially developing countries with the high rate of death related to microbial diseases (Steffen and Christian, 2011; WHO, 2011, WHO-UNICEF, 2017). South Africa has experienced water-borne diseases epidemic in the recent

past due to failing water treatment facilities in many parts, most especially in rural areas of the country (DHA, 2007; 2009). Therefore, negative environmental factor on the bacteriological quality of domestic water supplies remains a colossal problem. Bacterial infections are a major cause of chronic infections and mortality. Hence, World Health Organization and South African National Standard (SANS 241) sets the permissible portable water standard to contain less than one *E. coli* per 100ml, fecal (0 cfu/100ml) and total fecal coliforms (0.5 cfu/100ml) respectively of drinking water (WHO, 2003b; SANS, 241, 2006).

Table 2.1. Pathogens found in groundwater (Keyser, 1997; Steffen and Christian, 2011).

PATHOGEN	MAJOR DISEASES	SOURCES
Bacteria		
Escherichia coli	Gastroenteritis, Haemolytic Uraemic Syndrome (enterotoxic *E. coli*)	Human faeces
Salmonella spp.	Enterocolitis, endocarditis, meningitis, pericarditis, reactive arthritis, pneumonia	Human and animal faeces
Shigella spp.	Gastroenteritis, dysentery, reactive arthritis	Human faeces
Campylobacter jejuni	Gastroenteritis, Guillain-Barré syndrome	Human and animal faeces
Yersinia spp.	Diarrhoea, reactive arthritis	Human and animal faeces
Vibrio cholerae	Cholera	Human faeces and freshwater zooplankton
Legionella spp.	Pneumonia (Legionnaires' disease)	Thermally enriched water
Pseudomonas aeruginosa	Pneumonia, urinary tract infections, bacteremia	Soil and water
Mycobacterium spp.	Pulmonary disease, skin and soft tissue disease	Soil and water

Protecting groundwater resources against pollution demands preventing pollution to the recharge areas and preventing direct disposal of pollutants into the aquifer. (Alföldi, 1986; Kačaroğlu, 1999). Measures for the protection of groundwater against pollution are designed to prevent pollution, to eliminate its consequences, to preserve and improve the quality of the groundwater (Kačaroğlu, 1999). The purification of water disinfection against pathogen entry by use of traditional methods such as chlorination, boiling and ultraviolet (UV) irradiation is rapidly becoming a major challenge due to the formation and release of harmful carcinogenic disinfection by-products (DBPs) and utilization of high amounts of energy (Hijnen *et al*., 2006; Chlorine Chemistry Council and American Chemistry Council, 2006). A systematic review of point of use disinfection treatments found that after a year of implementation, chlorine, chlorine coagulant and solar disinfection (SODIS) has not been effective in reducing water-related diseases (Hunter 2009). Advanced physical methods (like reverse osmosis or ultrafiltration) are the safest and most efficient but largely limited to industrialized countries due to high investment costs. (Jens Lange *et al*, (2016). These advanced current technologies are not yet enough to address contaminated

groundwater due to cost implication, especially in rural areas. Here prevention through safe and hygienic handling is the most practical solution.

2.3. Fluoride in Groundwater: Occurrence and Health implication

Fluorine is a univalent poisonous gaseous halogen and the lightest, electronegative as well as most chemically reactive of all elements in the periodic table, hence possess a strong affinity to acquire a negative charge and form anionic fluoride (F^-) in solution (Tressaud, 2006a). Fluoride is a common naturally occurring constituent and contaminant found in groundwater resources. It is naturally connected to various types of rocks minerals and geological processes due to weathering and leaching of fluoride-bearing minerals from rocks and sediments (Jha *et al*., 2013; García and Borgnino, 2015). The main fluoride-bearing minerals include fluorapatite [$3Ca_3(PO_4)2Ca(F,Cl_2)$], cryolite (Na_3AlF_6), sellaite (MgF_2), and fluorspar (CaF_2) (García and Borgnino, 2015). These minerals are nearly insoluble in water and can only release fluoride ions when the conditions of temperature, pH, anion-exchange, among others, favor their dissolution in water resources (Gosh *et al*., 2013). Fluoride concentration varies depending on the water source, and high concentrations of fluoride in water are associated with underground sources (Nanyaro *et al*., 1984; García and Borgnino, 2015). Seawater typically contains about 1 mg/L while rivers and lakes generally exhibit concentrations of less than 0.5 mg/L (WHO, 2004). The concentrations of fluoride in surface waters generally are hardly beyond 0.3 mg/L except in isolated cases. Fluoride ion occurs in groundwater when the aquifer conditions favor their leaching or high fluoride-containing effluents are discharged to the water bodies from industries (Mohapatra *et al.*, 2009). As a result of these factors, the fluoride concentrations in groundwater in the globally range from 0.01 to 48 mg/L (Mumtaz *et al*., 2015). Some of the main factors controlling the concentrations of fluoride in groundwater and other waters resources are listed below (Ncube 2002; Brunt *et al*., 2004).

- Temperature
- residence times in the aquifers
- Presence or absence of complexing and precipitating ions
- The solubility of fluoride-bearing minerals
- The anion exchange capacity of aquifer materials (OH^- or F^-)
- Type of geological formations
- Chemical composition of groundwater as shown in Eq 2.1 and 2.2

$$CaF_2 + Na_2CO_3 \rightarrow CaCO_3 + 2Na^+ + 2F^- \quad \text{.....2.1}$$

$$CaF_2 + 2NaHCO_3 \rightarrow CaCO_3 + 2Na^+ + 2F^- + H_2O + CO_2 \quad \text{.....2.2}$$

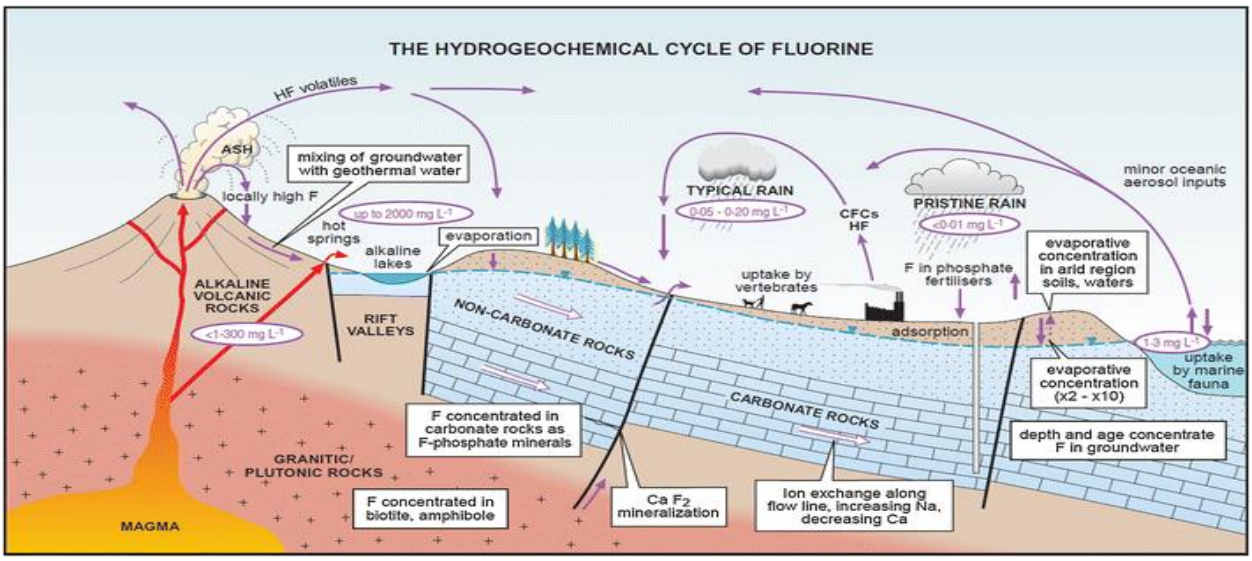

Fig. 2.3. Fluorine hydrogeochemical cycle (Yeşilnacar *et al*., 2016)

The rapid increase in fluoride contamination of groundwater has become a recurring global problem to human health. Generally, as an important source of drinking water, groundwater is a major source of human intake of fluoride. Globally, over 200 million people across 27 nations face issues of excess fluoride greater than 1.5 mg/L in drinking water, the intensity and severity of which varies with the environmental settings in terms of their geographical and economic status (WHO, 2004; Mumtaz *et al*., 2015). The problem of high concentrations of fluoride in groundwater sources has now become one of the most important toxicological and geo-environmental issues in many parts of the world such as India, Turkey, China, Kenya, Ethiopia Tanzania, South Africa, etc. (Agrawal *et al.*, 1997; Ncube, and Schutte, 2005, Fawell *et al*., 2006; Ayoob *et al*., 2006; Bailey *et al*., 2010; Thole, 2013).

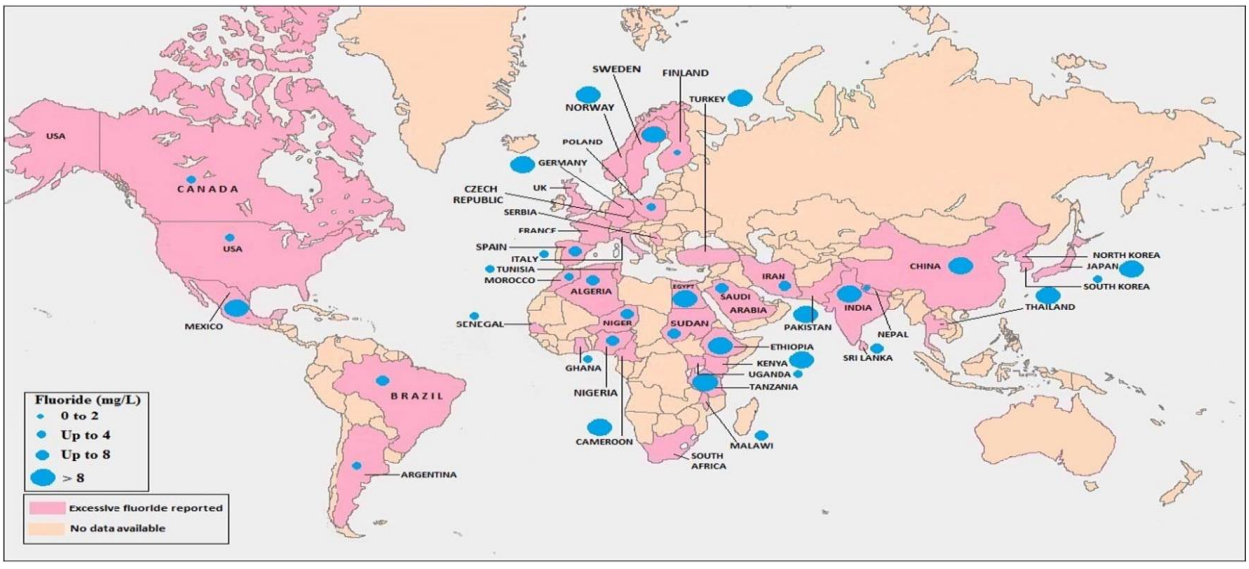

Fig. 2.4. Global fluoride distribution (Source: UNICEF)

High fluoride levels occur in groundwaters in some parts and the Republic of South Africa. Ncube and Schutte (2002) observe that high F- in South African groundwater is mainly found in areas underlain by sedimentary rocks, granites, metamorphic and volcanic rocks. McCaffrey (1993) calculated groundwater distribution maps from the South Africa National Groundwater Database in the early 1990s and observed that large areas of the country are subject to F- concentrations in groundwater in excess of 1.5 mg/ℓ (Fig 2.5). Boreholes in some communities in Limpopo, Northwest, and Northern Cape are known to have fluoride concentrations >5mg/L (Odiyo and Makungo, 2012; Gitari *et al*., 2017).

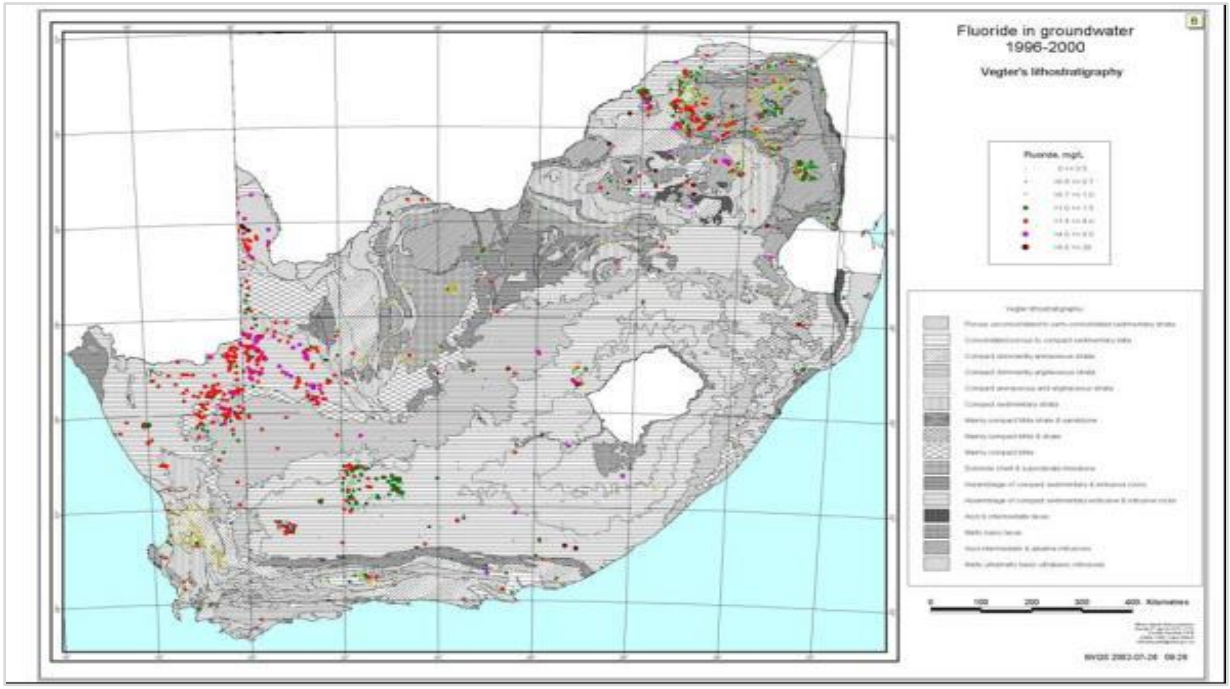

Fig. 2.5. Fluoride occurrence in groundwater in South Africa (Ncube and Schuttle, 2005).

2.3.1. Fluoride and its health effect

The World Health Organization gives guidelines for the concentration of fluoride in drinking water recommending it should be in the range 0.5 – 1.5 mg/L. Fluoride, when consumed at less than 0.5 mg/L, produces chronic physiological effects like dental caries, lack of formation of dental enamel, and deficiency of mineralization of bones, especially in children (Jha *et al*., 2013). The concentration of fluoride at about 0.7 mg/L is beneficial in drinking water as an essential component for normal mineralization of bones and formation of dental enamel but harmful once it exceeds 1.5 mg/L leading to dental or skeletal fluorosis. (Bell and Ludwig, 1970; WHO, 2011). According to Rošin-Grget and Linčir (2001), fluoride reacts with the dental caries and phosphate minerals in the body in form of apatite either as iso-ionic exchange of F^- for OH^- in apatite (Eq. 2.3), crystal growth of fluorapatite from supersaturated solutions (Eq. 2.4) and apatite dissolution with CaF_2 formation (Eq. 2.5).

$$Ca_{10}(PO_4)_6(OH)_2 + 2\,F^- \Rightarrow Ca_{10}(PO_4)6F_2 + 2\,OH^- \quad \text{.....2.3}$$

$$10\ Ca^{2+} + 6\ PO_4^{3-} + 2\ F^- \Rightarrow Ca_{10}(PO_4)6F_2) \quad \text{.....2.4}$$

$$Ca_{10}(PO_4)_6(OH)_2 + 20F^- \Rightarrow 10\ CaF_2 + 6PO_4^{3-} + 2OH^- \quad \text{.....2.5}$$

Eq. 2.3 and 2.4 may occur during long-term exposure to low fluoride levels in the solution, while Eq. 2.5 occurs in chronic fluoride concentrations consumption (Rošin-Grget and Linčir, 2001). This form of exchange between F- and OH- occurs due to structurally isoelectronic, with both ions possessing comparable ionic radius, which makes it easier to exchange mechanisms. Table 2.1 summarizes the different health risk associated with prolonged ingestion of fluoride. These include discolored teeth, deformed bones and dental fluorosis, crippling skeletal fluorosis, skeletal cancer, and neurotoxicological effects, etc. (Mjengera and Mkongo, 2003; Harrison, 2004; Ayoob and Gupta, 2006; Choi *et al*., 2012).

Table 2.2. Health effects of fluoride concentration in water

Fluoride concentration (mg/ L)	Effect on health
<0.5	Dental caries
0.5-1.5	Promotes dental health and prevents dental caries
1.5-4	Mottling of teeth, Dental fluorosis, arthritis
>>5	Dental and crippling skeletal fluorosis, neurological damage, Increases risk of Alzheimer's disease, osteosclerosis, thyroid disorder, kidney damage, cancer, Gastroenteritis, renal diseases, and other skeletal abnormalities

2.4. Defluoridation Techniques in Groundwater

It is important to know that due to the differences in the water quality across the globe, the possibility of one problem solution capturing all situations cannot be achieved. Therefore, the modifications of the design of efficient molecular mechanisms for water purification largely depends on different removal techniques. Several defuoridation technologies have been developed and adopted in many parts of the world. Ayoob *et al*. (2006) and Mohapatra *et al*. (2009) greatly reviewed different technologies for the defluoridation of drinking water with each having its own merits and demerits. Such technique includes precipitation, ion exchange, reverse osmosis, electrodialysis and adsorption (Fan *et al*, 2003, Fawell *et al*., 2006; Thole, 2013). These techniques depend on the fluoride ions concentration, existing treatment processes, treatment costs, handling of residuals and versatility of the given technique (Onyango and Matsuda, 2006; Bhatnagar *et al*., 2011). Moreover, the application of some of these methods may be impractical due to economic constraints or may be insufficient to meet strict regulatory requirements that make them unpractical for developing countries. Traditional approaches for the removal of such trace contaminants lead to further ecological damage in terms of waste generated and often leads to the introduction of

secondary hazardous products or products which are difficult to treat (Gavrilescu, 2004; Pradeep and Anshup, 2009). Some of the traditional techniques of removing fluoride from groundwater and drinking water are briefly discussed below:

2.4.1. Precipitation – Coagulation Method

Precipitation – coagulation is a widely known defluoridation method. It is a method which is based on the addition of chemicals (coagulants and aids) to water and the subsequent formation of insoluble fluoride precipitates. The general mechanisms are shown Eq. 2.6 and 2.7),

$$nAl^{3+}{}_{(aq)} + (3n-m)\ OH^{-}{}_{(aq)} + MF^{-}{}_{(aq)} \rightarrow A\ln Fm(OH)3n-m_{(s)} \quad \text{.....2.6}$$

$$Al_n(OH)_{3n(s)} + mF^{-}{}_{(aq)} \rightarrow Al_nF_m(OH)_{3n-m(s)} + mOH^{-}{}_{(aq)} \quad \text{.....2.7}$$

A typical example is the Nalgonda technique developed in India, which makes use of both lime and alum for the removal of fluoride from water and bleaching powder as a disinfectant to raw water by rapid mixing, flocculation, sedimentation, and filtration (Eswar and Devaraj, 2011). Generally, in this technique co-precipitation chemicals like aluminum sulfate and lime is usually added periodically in batch to treat water in fluoride removal (Thole, 2013). Lime and alum sludge are the most commonly used coagulants while iron (III), activated alumina has also been widely investigated (Ghorai and Pant, 2005; Tressaud, 2006b; Meenakshi and Maheshwari, 2006). The coagulation-precipitation technique for defluoridation is cost-effective, can be used at domestic and community levels, no regeneration of media, design, and construction is simple, least disposal problems and no electricity is needed to power the unit. However, some demerit of using this technique include low fluoride removal capacity and high residual introduction of aluminum concentration (> permissible limit) in the treated water, which can lead to serious health risks (Nayak, 2002; Meenakshi and Maheshwari, 2006; Ayoob *et al*., 2008).

2.4.2. Ion-exchange Technique

Ion exchange methods is another important means of removing excess amounts of fluoride from drinking water. Ion exchange usually occurs throughout a polymeric solid, the solid being of gel-type, which dissolves some fluid-phase solvent, or truly porous (LeVan, 1997). Synthetic chemical materials, such as anion and cation exchange resins have been used for various defluoridation processes. In this method, a strongly basic anion-exchange, cation/chelating type resins have been employed for sorption of fluoride. A typical example of an ion-exchange mechanism, where fluoride ions replace the chloride ions of the resin is shown according to Eq 2.8;

$$Matrix - NR_3{}^{+}Cl^{-} + F^{-} \rightarrow Matrix - NR_3{}^{+}F^{-} + Cl^{-} \quad \text{.....2.8}$$

Some of the different exchange resins that have been used under this technique include aminomethylphosphonic acid-type ion exchanger, quarternary ammonium selective ion-exchange resin, metal(III)-loaded amberlite resins and metal loaded cation exchangers (Popat *et al*., 1994; Zhang 2002; Luo and Inoue, 2004; Meenakshi and Viswanathan, 2009). The defluoridation technology has the advantage of being able to remove (90-95) % fluoride from water. But, its high handling cost, couples with specialized disposal system of fluoride and can only treat water with a very low pH makes the use a constraint, especially in rural communities.

2.4.3. Overview of Membrane Science and Technology as a means of Water Purification

Membrane technology is a generic term for a number of different, very characteristic separation processes and have proven viable in water purification with decades of productive use and are now competing for conventional techniques (Baker, 2004; Lee *et al*., 2016). Membrane separation process is based on the presence of semi-permeable membranes and the key property that is exploited is the ability of a membrane to control the permeation rate of a chemical species freely, while hindering permeation of other components on their physical and/or chemical properties (Beck *et al*, 1992; Baker, 2004; Lee *et al*., 2016). Membranes are being used more and more often for the creation of process water from groundwater, surface water or wastewater. A number of materials constitute membranes, with ceramic, polymers and sintered metals being the most common types of membranes. Whereas ceramic and sintered metals are normally found in industrial applications, polymeric membranes are becoming a common tool for drinking water treatment and municipal applications (Beck *et al*., 1992; Lee *et al*., 2016). Membrane processes are designed to carry out physical or physicochemical separations. Membranes can be generally classified into three groups: inorganic, polymeric or biological membranes. These three types of membranes differ significantly in their structure and functionality (Peter-Varbanets *et al*., 2009; Lee *et al*., 2016). The main force of membrane technology is the fact that it works without the addition of chemicals, with a relatively low energy use, easy and well-arranged process conductions (Baker, 2004; Ayoob *et al*., 2008; Lee *et al*., 2016). In addition, membrane processes generate a high-water quality with easy maintenance, low chemical sludge effluent, and excellent separation efficiency and stationary parts with compact modular construction (Lee *et al*., 2016). However, these processes are relatively expensive to install, operate and prone to fouling, scaling, or membrane degradation (Ayoob *et al*., 2008).

2.4.3.1. Membrane Filtration

Membrane filtration operates on the principle of particle separation based on pore size and pore size distribution (Joseph *et al.*, 1999). Membrane filtration can be used as an alternative for flocculation, sediment purification, adsorption (sand filters and active carbon filters, ion exchangers), extraction and distillation techniques (Lenntech, 2016). Membrane filtration can be divided up into nanofiltration (NF), Reverse Osmosis (RO or hyperfiltration) and electrodialysis (ED). This technique has been applied industrially in fields ranging from medicine to the chemical

industries in the removal of inorganic ions minerals, volatile organic compounds fluoride, and other chemical contaminants as well as microbial pollutants from drinking water supplies (Dach, 2008).

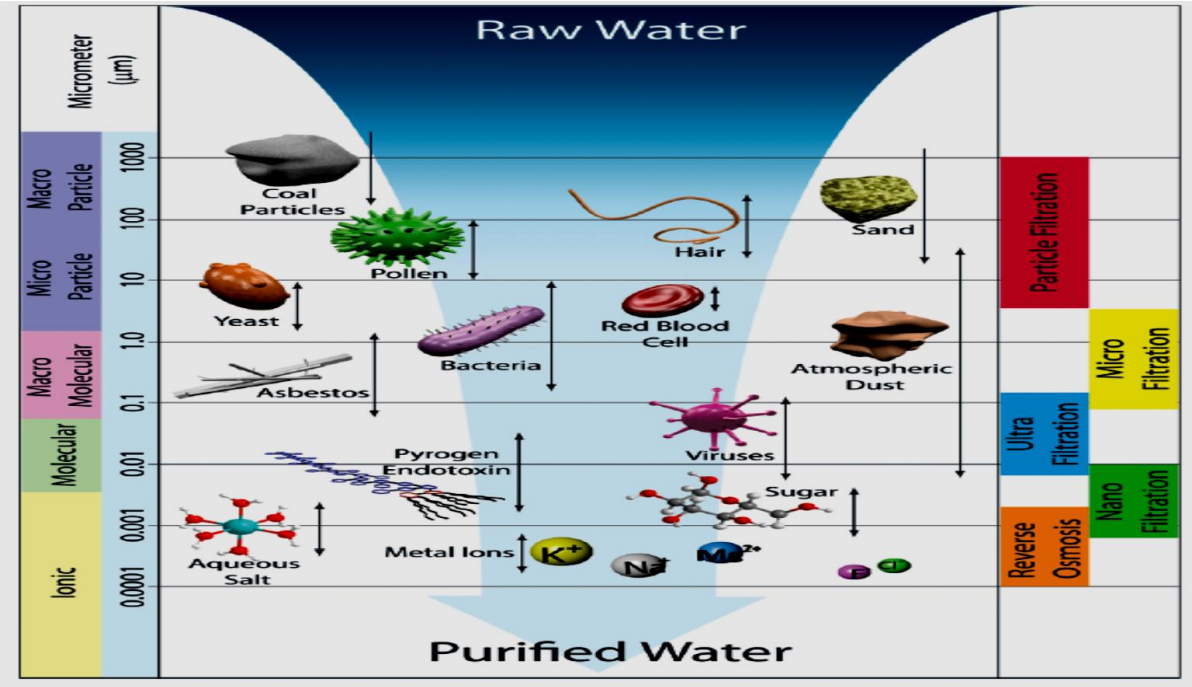

Fig. 2.6. Membrane filtration spectrum (Lee *et al*., 2016)

Reverse osmosis (RO) is a physical process in which the contaminants are removed by applying pressure on the feed water to direct it through a semi-permeable membrane. In reverse osmosis, the hydraulic pressure is exerted on one side of the semi-permeable membrane which forces the water across the membrane to overcome the natural osmotic pressure leaving the contaminant behind (Dach, 2008). The relative size of the pollutants left behind depends on the pressure exerted on the membrane. Reverse osmosis systems are used to purify water and remove salts and other impurities from the tap and brackish water. This process is capable of rejecting bacteria, sugars, proteins, particles, dyes, and other dissolved constituents. Recently, RO membrane process has been utilized in removing fluoride water as a preferred alternative for providing safe drinking water without posing the problems associated with other conventional methods (Hu and Dickson, 2006; Ayoob *et al.*, 2008; Babu *et al*., 2011).

NF is a pressure-driven process with properties in between reverse osmosis (RO) and ultrafiltration (UF), in which the contaminants are removed by a water-permeable membrane. NF membranes have typically 1-2 nm diameter pores, that is, larger than the size of hydrated ions, hence making their selectivity depends on a combination of steric and charge interactions, which allow removing hardness ions and reducing the concentration of monovalent ions such as fluoride. (Farsi *et al.*, 2017: Moran Ayala *et al*., 2018). Over the last decades the use of NF in water defluoridation has

been utilized with promising results at laboratory and pilot scale (Nasr *et al*., 2013; Xi *et al*., 2014; Boussouga *et al*., 2017: Moran Ayala *et al*., 2018)

Electrodialysis also uses membranes, but unlike RO and NF, the salt ions are deliberately carried through the membranes rather than using a membrane to retain the solutes, leaving behind the freshwater (Simons, 1993; Singh *et al*., 2016). In ED, the membrane pores are much less restrictive than those for NF and the solute can be driven through by either the Donnan effect or electric field (Adeloju *et al*., 1998; Szymczyk et al. 2006; Santos *et al*., 2009; Singh *et al*., 2016). Banasiak and Schafer, (2009) reported that about 70–75% reduction can be achieved through electro-dialysis at neutral solution pH.

Defluoridation by membrane filtration techniques have been reported to be effective with about 45 to 98 % of efficiencies, requires no chemicals, can effectively remove other chemical and microbial pollutants (Huiliang *et al*., 1987; Szymczyk and Fievet 2005; Ndiaye *et al*. 2005; Bason *et al*. 2006; Sehn, 2008; Babu *et al*., 2011; Shen *et al*., 2016; Owusu-Agyeman *et al*., 2017). Tahaikt et al. (2007) and Elazhar et al., (2013), established the performance of nanofiltration and electrodialysis through pilot plant study with improved removal percentages. However, generally the drawback is such that the membranes are very complicated, highly energy-intensive and expensive, sensitive to pH and temperature, addition of mineral is required after treatment, units are also subject to chemical attacks, plugging, fouling by particulate matter and concentrated and large quantity of wastes and membrane degradation (Ayoob *et al*., 2008; Babu *et al*., 2011, Singh *et al*., 2016).

2.5. Adsorption Technology in Fluoride removal

Adsorption is defined as a process that occurs when a gas or liquid solute (adsorptive) accumulates on the surface of a solid or a liquid (adsorbent), forming a molecular, ionic, or atomic film (Ruthven, 1984; Worch, 2012). This technique, among various other methods, has been employed to a broader extent for water treatment for more than 100 years and is still offers satisfactory results. Fig 2.6 shows the general concept in adsorption techniques.

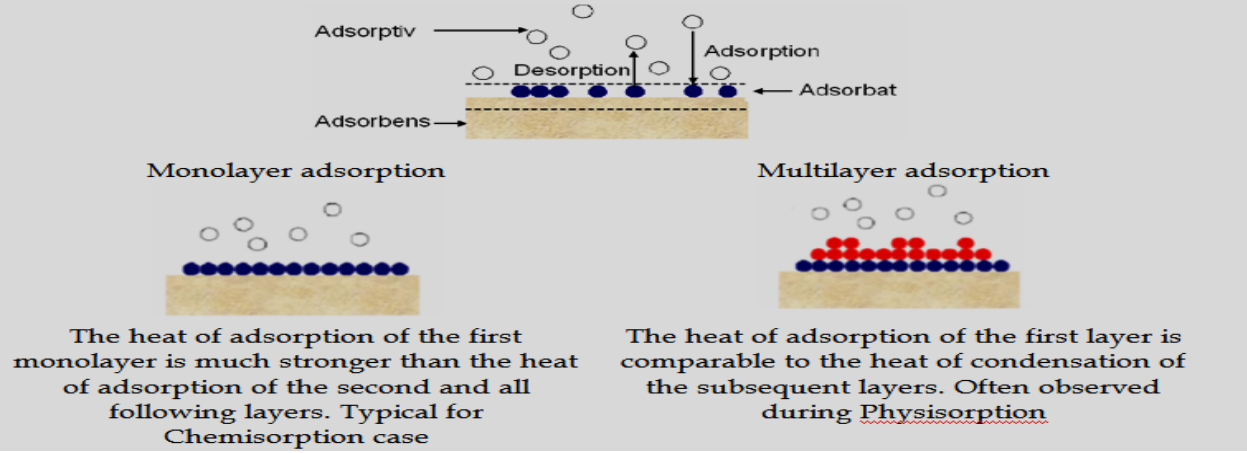

Fig. 2.7. Typical adsorption process (Christmann, 2010)

Since the adsorption techniques is a surface process, the surface area of the adsorbent is of great importance for the extent of adsorption and therefore a key quality parameter (Worch, 2012). The choice of particle size is made by considering the following factors: the ease of mass transfer from the fluid to the surface, creation of as much interfacial surface area as possible and reduction of antiparticle diffusion path length, all of which favour smaller particles; and maintenance of a low pressure drop, which favours larger particles (Jimmy, *et al*., 1997; LeVan, 1997; Worch, 2012).

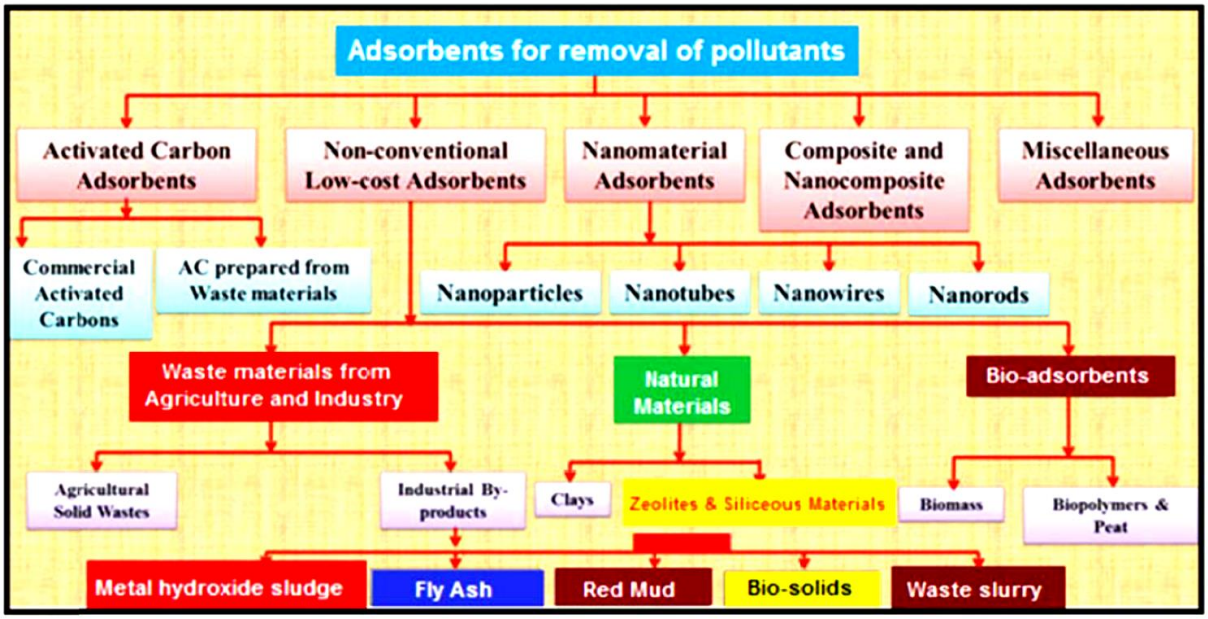

Fig. 2.8. Types of adsorbents in water purification (Raval *et al*., 2016)

Adsorption utilization in removing fluoride and other chemical pollutants has been extensively reported in terms of cost, simplicity of design and operation, economic and environmental considerations, provision of low-cost adsorbents, which can effectively remove F around the neutral pH of drinking water. (Mohapatra *et al*., 2009; Bhatnagar *et al*., 2011; Loganathan *et al*., 2013; Gitari *et al*., 2013; 2017).

According to Worsh, (2012) and Loganathan *et al*., (2013), based on the type of adsorbent, surface mechanisms may affect the adsorbate/adsorbent interaction. The following mechanisms may govern the fluoride uptake in any adsorption process:

- Van der Waals forces (outer-sphere surface complexation,
- Ion exchange (outer-sphere surface complexation),
- Hydrogen bonding (H-bonding) (inner-sphere surface complexation),
- Ligand exchange (inner-sphere surface complexation), and
- Chemical modification of the adsorbent surface.

Generally, several developed adsorbents have shown the ability to exhibit the highest adsorption capacities. The criteria for the selection of suitable adsorbents include adsorption capacity, cost of

the medium, ease of operation, potential for reuse and possibility of regeneration. The most widely used adsorbents are activated alumina and activated carbon.

A different defluoridation technique which uses activated alumina, carbon, bone, among others, with a removal efficiency between 85-95% have been reported (Farrah, *et al*., 1987; Meenakshi and Maheshwari, 2006; Ayoob, *et al*., 2008; Camacho *et al*., 2010). However, factors such as the quality of source materials, hardness and surface loading, high sensitivity to solution pH, poor integrity, needs pre-treatment and introduction of secondary pollutants has made it unsuitable for water treatment (Meenakshi and Maheshwari, 2006; Ayoob *et al*., 2008). Moreover, the use of activated charcoal produces a very poor fluoride adsorption capacity which is only effective at pH less than 3.0 (Mckee and Johnston, 1934). (Janardhana *et al*., 2006). Therefore, in order to overcome this constraint, various modifications on the overall improvement of these adsorbents have been established. This includes alumina coated with manganese dioxide (Maliyekkal, *et al*., 2006 Gadhari *et al*., 2010; Sanghavi and Srivastava, 2010), iron-based materials (Streat *et al*., 2008), calcium-based sorbent materials (Jain *et al*., 2009), carbon-based materials (Zhu *et al*., 2008; Ma *et al*., 2009), metal oxides/hydroxides/oxyhydroxides as well as clay and soil-based systems (Lou et al., 2012; Dandan Tang 2016 ; Gitari *et al*., 2013; 2016). Also, several low-cost natural adsorbent materials (Fig 2.7), in addition to other engineered adsorbent materials used in fluoride removal from water by adsorption and their adsorption properties have been extensively established and reported (Gupta et al., 2009; Worch, 2012 ; Bhatnagar *et al*., 2011; Loganathan *et al*., 2013; Thole, 2013).

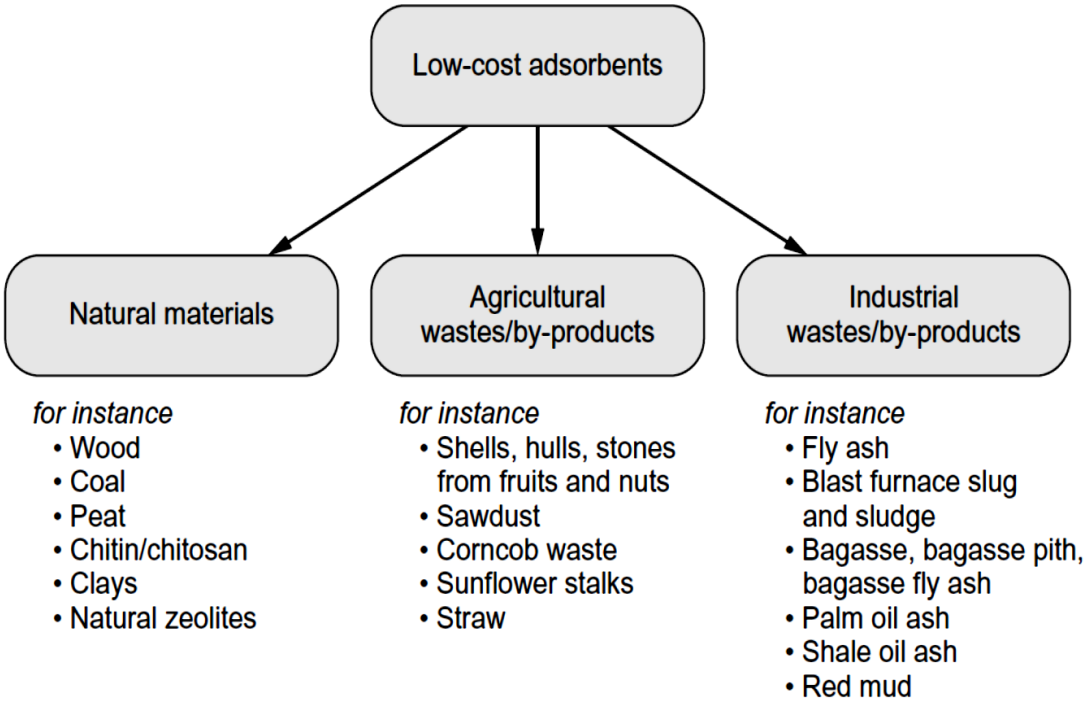

Fig. 2.9. Natural and low-cost adsorbent for defluoridation (Worsh, 2012)

2.6. Nanotechnology and water purification: Nanomaterials as an adsorbent

Nanotechnology is increasingly being identified as an area of science and technology that could play a role in addressing some of the shortcomings of conventional water treatment methods. The rapid development in nanotechnology has propelled significant interest in the environmental applications of nanomaterials and is one key area that cannot be ignored. Nanotechnology is the engineering and art of manipulating matter at the nanoscale (1-100 nm). Nanotechnology has the potential to provide a long-term solution of water quality, availability and viability of water resources, such that nanotechnology-based materials could lead to cheaper, more durable and more efficient water treatment technologies that can meet the needs of developing countries (Choi, 2005 Agarwal *et al*., 2010). In particular, it potential to revolutionize century-old conventional water treatment processes through the use of advanced filtration materials which makes it possible for greater water reuse, decontamination, water management and other treatments (Morones, 2005; Rajan 2011; Bhati 2017). Nanotechnology is the answer to reducing costs, improve efficiency and propose new functionality products and systems as a promising technology in water and wastewater worldwide (Twardowski, 2007). Nanomaterials are excellent adsorbents, catalysts, and sensors due to their large specific surface area and high reactivity (Chen and Chatterjee, 2013; Dhillon *et al*., 215; Lu and Astruc, 2018). In the past decade, nanomaterials have received substantial attention and efforts from the academic and industrial world, because of its distinct properties at the nanoscale. Nano-porous or nanocomposite materials as a subset of nanomaterials could be natural or synthetic, organic or inorganic and hybrid materials and possess a set of unique properties above all other materials. This includes large specific surface-volume ratio, high interior surface area, exclusive size sieving, and shape selectivity, control over pores' size, nanoscale space confinement, and specific gas/fluid permeability as well as having the ability to modify chemical and physical characteristics of materials, thus having a direct impact on its adsorption properties (Rabovsky, 1995; Li *et al.*, 2012; Figoli *et al*., 2017).

Water treatment with nanomaterials is considered capable of meeting many objectives such as inorganic heavy metals, organic contaminants and microorganisms and for removing by-product formation and showed promise as a cost-effective means of meeting new standards (Savage *et al*., 2005, Clasen *et al*., 2007 Cloete *et al*., 2010; Hotze and Lowry, 2010)

Nanocomposite materials can be classified, according to their dispersed matrix and dispersed phase materials. Among different nanocomposites, polymer-based nanocomposite, a class of hybrid materials composed of the organic polymer matrix in which inorganic particles with nanoscale dimension are embedded, have become a prominent area of research and development (Savage, and Diallo, 2005; Ebrahimi, 2012). Many efforts have been made in the last two decades using novel nanotechnology and nanoscience knowledge in order to get nanomaterials with determined functionality (Ebrahimi, 2012)

Recently, several reports from researchers have tested many materials towards defluoridation such as carbon-zirconium nanoparticles (Velazquez-Jimenez *et al.*, 2014), The use of inorganic carbon base network like graphene (because of its numerous novel properties, such as large surface area, unique thermal and mechanical properties), is on the increase towards defluoridation. Barathi *et al*. (2014b) report a typical example, where the fluoride removal capacity with the support of graphene oxide–aluminum oxyhydroxide was established with a maximum defluoridation capacity of 51.42 mg/g. These high sorption capacities for metal ions can be of great use in the reduction of toxic metals ions in groundwater and this can be enhanced through the use of polymer matrix with metal as support for effective removal of these ions.

2.7. Green synthesis: Metals and Metal oxides nanoparticle in water purification

The technological revolution in nanoscale science and nanotechnology suggest that many of the issues involving water quality could be resolved or greatly improve using nanomaterials with significantly novel and improved physical, chemical and biological properties (Savage and Diallo, 2005; Sundrarajan *et al*., 2012; Wani and Shah, 2012). Nanoparticles are one of the important building blocks with lengths that range from 1-100 nm in two or three dimensions in the fabrication of nanomaterials (Al *et al*., 2008). The basic properties, extremely small size and high surface area to volume ratio of nanoparticles provide better kinetics for the adsorption of target contaminants from aqueous solutions. Nanoparticles can be made of materials of diverse chemical nature, the most common being metals, metal oxides, silicates, non-oxide ceramics, polymers, organics, carbon and biomolecules (Sharma *et al*., 2009). Metal ions present in aqueous solution in water is of vital health concern, especially in the case of toxic chemicals. However, for some Fe, Ag, TiO_2, ZnO, and CeO_2 derived materials, the solubility of the species concerned is low, and therefore the ionic concentration is not beyond the permissible limits (Pradeep and Anshup, 2009). This serves as an important factor in designing water quality applications materials. As the water, in general, is contaminated with several ionic species, the nature of the metal ion can be different from case-to-case (Pradeep and Anshup, 2009). Hence, nanoparticles are expected to play a crucial role in water purification (Stoimenov, 2002). Nanoparticles can also be designed and synthesized to act as either separation or reaction media for pollutants. Several types of research have ventured into the use of nanomaterials in the purification of surface water, groundwater, and industrial wastewater streams with the expectation that they can be used to kill harmful organisms, repair body tissue, in water quality improvement and to cure disease (Dhermendra *et al*., 2008; Figoli *et al*., 2017).

Out of all kinds of nanoparticles, the metallic nanoparticles, including gold, silver, iron, zinc and noble metals as well as metal oxide nanoparticles, have shown great promise in terms of biomedical and water treatment applications, not only due to their large surface area to volume ratio but also because they exhibit different bioactivities (Albrecht *et al.*, 2006; Jaina *et al.*, 2009). The resurgence of promotion of silver (as colloidal silver) as an alternative medicine treatment has

been on the rise. It has been reported that silver nanoparticles (SNPs) are non-toxic to humans but inhibits the growth of bacteria, virus and other eukaryotic microorganisms (Jeong *et al*., 2005).

Metal oxide nanoparticles such as ZnO, MgO, and CaO had also been investigated as inorganic antibacterial agents (Roselli *et al*., 2003; Stoimenov *et al*., 2002; Shi *et al*., 2012; Tang *et al*., 2012). MgO is an exceptionally important inorganic material with a wide bandgap, which is used in catalyst, toxic-waste remediation agent, or as an additive in refractory, adsorbent, etc. (Liang and Gay, 1986; Al-Gaashani *et al*., 2012). Stoimenov *et al*. (2002) showed that MgO nanoparticles and magnesium (Mg) nanoparticles are very effective biocides against Gram-positive and Gram-negative bacteria (*Escherichia coli* and *Bacillus megaterium*) and bacterial spores (*Bacillus subtillus*). Due to drawbacks in conventional water purification, there is an increased demand for effective disinfectants due to the emergence of multiple-resistant microorganisms and the harmful disinfection byproducts produced by conventional disinfectants (Li *et al.*, 2008; Ruparelia *et al.* 2008; Figoli *et al*., 2017). Classically physical and chemical methods have been employed in synthesizing nanoparticles and these methods are costly, toxic and non-ecofriendly but in recent times, scientists are looking forward to low cost, non-toxic and eco-friendly synthetic methods (Parvulescu *et al.*, 2010). However, methods to provide stable nanoparticle dispersions that resist aggregation in biological media and have high oxidation resistance are significant. It is also desirable to employ natural and renewable reagents during synthesis because of the higher potential for biocompatibility exists, which may eliminate the need for extensive post-synthesis purification or surface modification as compared to conventional synthesis procedures that use known cytotoxic compounds (Leonov *et al*., 2008; Boca and Astilean, 2010)

2.8. Chitosan, Cellulose composite materials as a means of water purification

Nature has beautifully incorporated several molecular technologies in different living bodies (Pradeep *et al*., 2009), a typical example are biopolymers. Cellulose and chitosan are among the most abundant biopolymers on earth; they are natural, renewable, environmentally benign, cost-efficient, non–toxic, biodegradable and biocompatible (Crini and Badot, 2008; Muzzarelli, 2012; Li *et al*., 2015). Since adsorption relative to the conventional methods of water purification using low–cost adsorbents/materials have become an attractive choice, these biopolymers present an interesting option (Kalia and Avérous, 2011).

Chitosan (Fig. 2.10) with a chemical structure of 1-4-linked-2-amino-2- deoxy-b-D-glucopyranose is a biodegradable and biocompatible polycation acquired from chitin, the second most abundant polysaccharide after cellulose (Gandhi *et al.*, 2010). Chitosan originates from exoskeletons of crustacean shells like crabs, shrimps, crawfish, and cell walls of fungi as well as cuticles of insects has the ability to fix a great range of heavy metals and radionuclides from wastewaters in comparison to other polysaccharides (Guibal, 2004; Kyzas *et al.*, 2009; Jayakumar *et al.*, 2011; Muzzarelli, 2012). The characterization of chitosan as a promising material in adsorption techniques is attributed to its properties such as macromolecular structure, hydrophilicity, biocompatibility, biodegradability, non-toxicity, low-cost and presence of very reactive amino

(-NH_2) and Hydroxyl (-OH) groups in its backbone. The metals uptakes ensured due to a large number of these reactive functional groups by interacting with various metallic species through chelation or ion exchange mechanism (Sureshkumar *et al*., 2010). There is also inherent antibacterial activities, and metal-binding properties in aqueous beds (Varma *et al*., 2004; Kyzas et al, 2009; Muzzarelli, 2012), which makes its applicable to many fields (Zhang *et al*., 2010; Chen et al 2011). Chitosan (CS-based) ENMs were used because of its intrinsic antibacterial properties and biocompatibility as next-generation filters for antibacterial water filtration applications and defluoridation (Helander *et al*., 2001; Miretzky and Cirelli, 2011) Studies have shown the adsorptive removal of heavy metals and dyes utilizing cellulose– and chitosan-based materials (O'Connell *et al*., 2008; Ahmad *et al*., 2015)

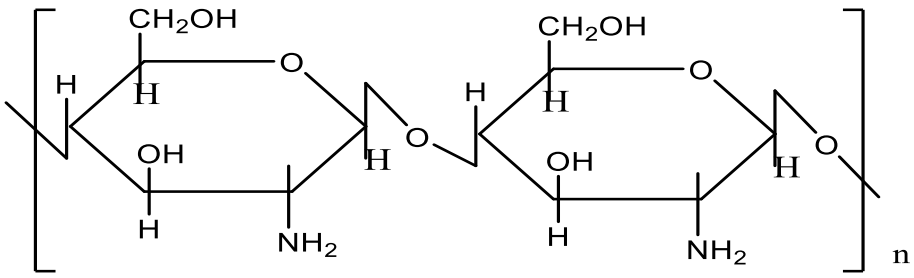

Fig. 2.10. Chitosan chemical structure

The use of chitosan composites and derivatives for removing fluoride ions, heavy metals and dyes in wastewater treatment are attributed to its modifiable functional groups present in its chemical structure backbone. In addition to many attractive features such as the high adsorption capacity and the fact that chitosan is obtained from natural raw sources (crustacean shell waste), an environmentally friendly material of low cost, opposed to petroleum-based materials (Elsabee *et al*., 2012).

Several methods have been used to modify natural chitosan either physically or chemically in order to improve the adsorption capacity, antibacterial as well as to enhance their metal-binding abilities (Zhang, 2007). Ultrasonically zirconium loaded cellulose and zirconium entrapped chitosan/silica gel composite (Barathi *et al*., 2014; Prabhu and Meenakshi, 2014) were all proved as promising materials for defluoridation. Electropositive multivalent metals incorporated to chitosan beads has been established to be effective in fluoride uptakes, Viswanathan and Meenakshi, (2009) developed Ce (III) encapsulated chitosan polymeric matrix with a removal efficiency of 9 at pH of 7. An eco-magnetic nano-hydroxyapatite chitosan composite Fe_3O_4@n-HApCS for enhanced fluoride sorption was reported by Pandi, and Viswanathan, 2015 composite
The maximum removal of fluoride at pH 3.0 was 4.77 mg/g. Another use of various chitosan and its derivatives for fluoride sorption has been reported by Miretzky and Cirelli, 2011. Chitosan can also act as a reducing agent to produce AgNPs from $AgNO_3$. Improved mechanical properties and superior inhibition of bacterial growth have been observed for porous CS–silver nanocomposite

films (Vimala *et al.*, 2010). The enhanced antibacterial activity of the CS–Ag–ZnO composite has also been demonstrated (Li *et al.*, 2010). An *et al*. (2009) reported that the addition of $AgNO_3$ to a CS/PEO solution, as a silver rendering component. Due to F strong affinity for electropositive, the use of chitosan loaded with multivalent metal ions like Al (III), Zr(IV), Ce(IV), Fe(III), and La(III) have been employed for fluoride removal (Kamble *et al.*, 2017). Today the development of chitosan-based nanomaterials and nanocomposites is of a great scope to exploit the unique.

Cellulose (Fig. 2.11) is the most abundant renewable biopolymer on earth and is a very promising raw material available at low cost to synthesize an adsorbent for defluoridation. The structure of cellulose gives a characteristic property of hydrophilicity, chirality, and degradability. Chemical reactivity is largely a function of the high donor reactivity of the OH groups (Sundaram *et al*., 2009). Pure cellulose has very few applications compared to the diversity of applications of its modified form (Sundaram *et al.*, 2008). Therefore, chemical modifications increase its adsorption capacity for heavy metals in aqueous and non-aqueous media (Sundarama *et al.*, 2009). Surface functionalization of nanocellulose has shown outstanding adsorption performance towards water contaminants because of their large removal efficiency and the spontaneous decontamination of water pollutants (Sharma *et al*., 2009; Omer *et al.*, 2013). Potential applications of cellulose and chitosan nanoparticles/composites are numerous, and a comprehensive review was reported especially in wastewater treatment (Sharon Olivera *et al*., 2016; Grishkewich *et al*., 2017).

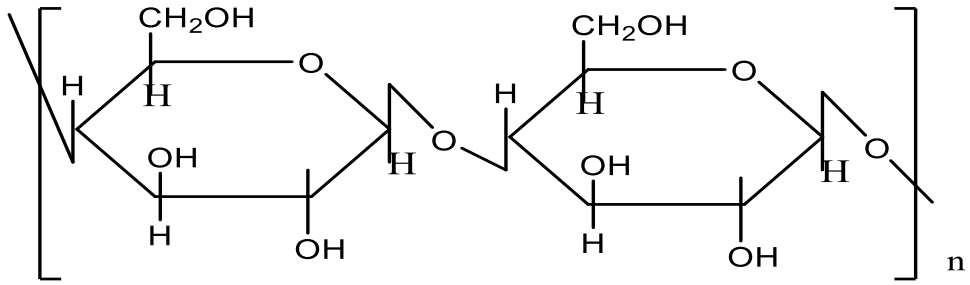

Fig. 2.11. Chemical structure of cellulose

Cellulose and cellulosic-based materials with different adsorption performances of fluoride have received increasingly significant attention. Cellulose modified with poly (N, N-dimethyl aminoethyl methacrylate) (PDMAEMA) was reported with an 8.59 mg/g for fluoride removal (Tian *et al*., 2011). Zhao *et al*. (2008) developed a Fe (III)-loaded ligand exchange cotton cellulose with an adsorption capacity of 8.59 mg/g. Other reported output has shown the successful use of cellulose-based materials in defluoridation (Anirudhan *et al*., 2010; Barathi *et al*., 2013; Wang, *et al*., 2014).

2.9. Hydroxyapatite application in defluoridation

Hydroxyapatite [HAp, $Ca_{10}(PO_4)_6(OH)_2$] is a naturally occurring inorganic mineral made up of calcium and phosphate and is found in human bones. Hydroxyapatite can be synthesized via several methods such as wet chemical deposition, biomimetic deposition, sol-gel route (wet-chemical precipitation) or electrodeposition (Poinern *et al.*, 2011). Hydroxyapatite synthesis as shown from several studies via wet-chemical route can be improved by power ultrasound (Gao *et al*., 2009). Different mineral materials such as hydroxyapatite, binary metal oxides, magnesia, hydrotalcite, alumina, rare earth metals, etc. have been supported on chitosan resulting in inorganic composites with high fluoride removal capacity (Sundaram et al, 2008; 2009). The ultrasonically assisted synthesis of hydroxyapatite was successfully used in the production of nanostructured hydroxyapatite at high-quality standard (Poinern *et al.*, 2011; Kanno *et al*., 2014; Pandi and Viswanathan, 2015). The ultrasonic route allows producing nano-crystalline hydroxyapatite as well as modified particles, e.g. core-shell nanospheres, and composites (Ferraz *et al.*, 2004). It has been proved as a good adsorbent because of the low cost, availability and high defluoridation capacity (Sundaram *et al.*, 2008; 2009). It has been reported that the nanosilver– and silver zeolite– or silver hydroxyapatite–CS composites provide increased mechanical strength and water barrier properties (Rhim *et al.*, 2006; Saravanan, 2011). Also Yu *et al*. (2013), successfully demonstrated how a cellulosic composite material can be prepared as an adsorbent for efficient removal of fluoride from drinking water; where the presence of cellulose facilitates the formation of nano-size hydroxyapatite and the interact binding sites between cellulose and HA exists in cellulose-HA nanocomposites.

It is vital to note that the choice of the selected metal-metal oxides is quite important due to the fact that they contribute a critical role in water treatment, the synergistic effects could be driven by on a suitable bio-polymeric substrates matrix. Biopolymers selection as support is quite important because it has a large surface area on which nanoparticles can be loaded efficiently and effectively as well as in playing an important role in water purification. It is assumed that all components work systematically and synergistically to remove a variety of fluorides and pathogens from drinking water through surface functionalization. Hence, the present study focuses on the fabrication of Chitosan/Cellulose, loaded with Ag/MgO NPs and nanohydroxyapatite, for effective defluoridation and microbial removal in groundwater.

To our knowledge, this is the first study, which will investigate different aspects of chitosan/cellulose nanocomposite containing metal-metal oxides nanoparticles and nanohydroxyapatite combinations to be utilized in water microbial elimination and defluoridation through adsorption and ion exchange mechanisms. The anticipated output of this project will be the availability of a green simple, cheap and robust technology for drinking water purification which will be available and most affordable.

References

Abdul Khalil. H.P.S, Saurabh, C.K., Adnan, A.S., Fazita, M.N., Syakir, M.I., Davoudpour, Y., Rafatullah, M., Abdullah, C.K., Haafiz, M.K.M. and Dungani, R., 2016. A review on chitosan-cellulose blends and nanocellulose reinforced chitosan biocomposites: Properties and their applications. Carbohydrate polymers, 150, pp.216-226.

Adeloju, S.B., Young, T.M., Jagner, D. and Batley, G.E., 1998. Anodic stripping potentiometric determination of antimony on a combined electrode. Analyst, 123(9), pp.1871-1874.

Agarwal, A. and Joshi, H., 2010. Application of nanotechnology in the remediation of contaminated groundwater: a short review. Recent Research in Science and Technology, 2(6).

Agrawal, V., Vaish, A.K. and Vaish, P., 1997. Groundwater quality: focus on fluoride and fluorosis in Rajasthan. Current Science, 73(9), pp.743-746.

Albrecht, M. A., Evans, C. W and Raston, C. L. (2006). Green Chem., 8, 417–432

Alföldi, L., 986, 'Groundwater Protection inrous, Fractured and Karstic Aquifer Systems (General report)', in symposium on Groundwater Protection Areas (19th Congress of IAH),Proceedings, Novinar Publ. House, Czechoslavakia, vol. XIX, part 2, pp 89–103

Alicia Godlove,. 2016. Groundwater Pollution: Causes and Prevention. https://info.esg.adec-innovations.com/blog/groundwater-pollution-causes-and-prevention

An, J., Zhang, H., Zhang, J., Zhao, Y., and Yuan, X., 2009. Preparation and antibacterial activity of chitosan/poly(ethylene oxide) membranes containing silver nanoparticles. Colloid PolymSci 287:1425–1434.

Anirudhan, T.S. and Suchithra, P.S., 2010. Synthesis and characterization of iron (III)-coordinated amine-modified poly (glycidylmethacrylate)-grafted densified cellulose and its applicability in defluoridation from industry effluents. Industrial & Engineering Chemistry Research, 49(23), pp.12254-12262.

Ayoob, S. and Gupta, A.K., 2006. Fluoride in drinking water: a review on the status and stress effects. Critical Reviews in Environmental Science and Technology, 36(6), pp.433-487.

Ayoob, S., Gupta, A.K., Bhat, V.T., 2008. A conceptual overview on sustainable technologies for the defluoridation of drinking water. Crit. Rev. Environ. Sci. Technol. 38, 401–470.

Banasiak, L.J. and Schäfer, A.I., 2009. Removal of boron, fluoride and nitrate by electrodialysis in the presence of organic matter. Journal of Membrane Science, 334(1-2), pp.101-109.

Babu, C.A., Sujish, D., Murugappa, M.S., Mohanakrishnan, G., Kalyanasundaram, P. and Raj, B., 2011. A comprehensive treatment method for defluoridation of drinking water.

Baker R. W., 2004. Membrane Technology and Applications John Wiley & Sons, Ltd ISBN: 0-470-85445-6.

Bansiwal, A., Pillewan, P., Biniwale, R.B. and Rayalu, S.S., 2010. Copper oxide incorporated mesoporous alumina for defluoridation of drinking water. Microporous and Mesoporous Materials, 129(1-2), pp.54-61.

Barathi, M., Kumar, A.S.K., and Rajesh, N., 2013. Efficacy of novel Al–Zr impregnated cellulose adsorbent prepared using microwave irradiation for the facile defluoridation of water. Journal of Environmental Chemical Engineering, 1(4), pp.1325-1335.

Basheer, A.A., 2018. New generation nano-adsorbents for the removal of emerging contaminants in water. Journal of Molecular Liquids, 261, pp.583-593.

Bason, S., Ben-David, A., Oren, Y., Freger, V., 2006. Characterization of ion transport in the active layer of RO and NF polyamide membranes. Desalination 199, 31–33.

Beck, J.S., Vartuli, J.C., Roth, W.J., Leonowicz, M.E., Kresge, C.T., Schmitt, K.D., Chu, C.T.W., Olson, D.H., Sheppard, E.W., McCullen, S.B. and Higgins, J.B., 1992. A new family of mesoporous molecular sieves prepared with liquid crystal templates. Journal of the American Chemical Society, 114(27), pp.10834-10843.

Bell, M.C. and Ludwig, T.G., 1970. The supply of fluoride to man: ingestion from water, fluorides and human health, WHO Monograph series 59. World Health Organization, Geneva.

Bhatnagar, A., Kumar, E., Sillanpää, M., 2011. Fluoride removal from water by adsorption—a review. Chem. Eng. J. 171 (3), 811–840.

Bhati, M. and Rai, R., 2017. Nanotechnology and water purification: Indian know-how and challenges. Environmental Science and Pollution Research, 24(30), pp.23423-23435.

Boussouga, Y.A., and Lhassani, A., 2017. Modeling of fluoride retention in nanofiltration and reverse osmosis membranes for single and binary salt mixtures. Desalination Water Treat., 95, pp.162-169.

Brunt, R., Vasak, L. and Griffioen, J., 2004. Fluoride in groundwater: probability of occurrence of excessive concentration on global scale. IGRAC.

Camacho, L.M., Torres, A., Saha, D., Deng, S., 2010. Adsorption equilibrium and kinetics of fluoride ion sol–gel-derived activated alumina adsorbents. J. Colloid Interface Sci. 349, 307–313

Chen, A. and Chatterjee, S., 2013. Nanomaterials based electrochemical sensors for biomedical applications. Chemical Society Reviews, 42(12), pp.5425-5438.

Choi, A.L., Sun, G., Zhang, Y. and Grandjean, P., 2012. Developmental fluoride neurotoxicity: a systematic review and meta-analysis. Environmental health perspectives, 120(10), pp.1362-1368.

Christmann K. 2010. Adsorption. Lecture Series 2010/2011: "Modern Methods in Heterogeneous Catalysis Research", Institut für Chemie und Biochemie, Freie Universität, Berlin, Available: http://www.fhierlin.mpg.de/acnew/department/pages/teaching/pages/teaching__wintersemester__2010_2011/klaus_christmann__adsorption__101105.pdf

Clasen, T., Schmidt, W., Rabie, T., Roberts, I., and Cairncross, S. 2007. Interventions to improve water quality for preventing diarrhea: a systematic review and meta-analysis British Medical Journal, doi:10.1136/bmj.39118.489931.BE.

Cloete, T.E., De Kwaadsteniet, M. and Botes, M. eds., 2010. Nanotechnology in water treatment applications. Horizon Scientific Press.

Chlorine Chemistry Council and American Chemistry Council (2006) Drinking Water Chlorination: A Review of Disinfection Practices and Issues. Water conditioning and purification international p.68.

Dach, H., 2008. Comparison of nanofiltration and reverse osmosis processes for a selective desalination of brackish water feeds (Doctoral dissertation, Université d'Angers).

Department of Health (DHA). 2009. National Department of Health Issues: Cholera. Archive of cholera updates. Jan 2009: https://mg.co.za/article/2009-01-14-cholera-death-toll-in-south-africa-rises

Department of Health (DHA). 2005. Diarrhea and Typhoid outbreak in Delmas under control. November, 2007. https://mg.co.za/article/2007-11-02-diarrhoea-in-delmas-affects-150-people

Dhermendra, K., Tiwari, J., Behari and Prasenjit Sen., 2008. Application of Nanoparticles in Waste Water Treatment.World Applied Sciences Journal 3 (3): 417-433. ISSN 1818-4952.© IDOSI Publications.

Dhillon, A., Nair, M., Bhargava, S.K. and Kumar, D., 2015. Excellent fluoride decontamination and antibacterial efficacy of Fe–Ca–Zr hybrid metal oxide nanomaterial. Journal of colloid and interface science, 457, pp.289-297.

Ebrahimi, F. ed., 2012. Nanocomposites: New trends and developments. BoD–Books on Demand

Edmunds WM, Smedley PL (2005) Fluoride in natural waters. In: Selinus O, Alloway B, Centeno JA, Finkelman RB, Fuge R, Lindh U, Smedley PL (eds) Essentials of medical geology, Springer, The Netherlands, p 301–330

Elazhar, F., Tahaikt, M., Zouahri, A., Taky, M., Hafsi, M. and Elmidaoui, A., 2013. Defluoridation of Moroccan groundwater by nanofiltration and electrodialysis: performances and cost comparison. World Appl Sci J, 22(6), p.844.

Eswar, P. and Devaraj, C.G., 2011. Water defluoridation: Field studies in India. Indian Journal of Dental Advancements, 3(2), pp.526-33.

Fan, X., Parker, D.J. and Smith, M.D., 2003. Adsorption kinetics of fluoride on low-cost materials. Water Research, 37(20), pp.4929-4937.

Farrah, H., Slavek, J., and Pickering, W.F., 1987. Fluoride interactions with hydrous aluminum oxides and alumina. Soil Research, 25(1), pp.55-69.

Farsi, A., Malvache, C., De Bartolis, O., Magnacca, G., Kristensen, P.K., Christensen, M.L. and Boffa, V., 2017. Design and fabrication of silica-based nanofiltration membranes for water desalination and detoxification. Microporous and Mesoporous Materials, 237, pp.117-126.

Fawell, J., Bailey, K., Chilton, J., Dahi, E., Fewtrell, L., Magara, Y. 2006. Fluoride in drinking water. IWA Publishing, London, 4-81.

Ferraz, M. P., Monteiro, F. J., and Manuel, C. M. (2004). "Hydroxyapatite nanoparticles: A review of preparation methodologies". Journal of applied biomaterials & biomechanics: JABB 2 (2): 74–80. PMID 20803440.

Figoli, A., Dorraji, M.S.S. and Amani-Ghadim, A.R., 2017. Application of nanotechnology in drinking water purification. In Water Purification (pp. 119-167). Academic Press.

Gadhari, N.S., Sanghavi, B.J., Karna, S.P. and Srivastava, A.K., 2010. Potentiometric stripping analysis of bismuth-based on carbon paste electrode modified with crypt and [2.2. 1] and multiwalled carbon nanotubes. Electrochimica Acta, 56(2), pp.627-635.

Gao, S., Sun, R., Wei, Z. G., Zhao, H. Y., Li, H. X., and Hu, F., 2009. Size-dependent defluoridation properties of synthetic hydroxyapatite. Journal of Fluorine Chemistry, 130(6), 550–556.

García, M.G. and Borgnino, L., 2015. Fluoride in the context of the environment. Fluorine: Chemistry, analysis, function and effects, 3.

Gavrilescu, M., 2004. Removal of heavy metals from the environment by biosorption. Engineering in Life Sciences, 4(3), pp.219-232.

Gerba, C.P., 1988. Methods for virus sampling and analysis of groundwater. In Ground-Water Contamination: Field Methods. ASTM International

Ghorai, S. and Pant, K.K., 2005. Equilibrium, kinetics and breakthrough studies for adsorption of fluoride on activated alumina. Separation and purification technology, 42(3), pp.265-271.

Gitari, W.M., Izuagie, A.A. and Gumbo, J.R., 2017. Synthesis, characterization and batch assessment of groundwater fluoride removal capacity of tri-metal Mg/Ce/Mn oxide-modified diatomaceous earth. Arabian Journal of Chemistry.

Ghosh, A., Mukherjee, K., Ghosh, S.K. and Saha, B., 2013. Sources and toxicity of fluoride in the environment. Research on Chemical Intermediates, 39(7), pp.2881-2915.

Grishkewich, N., Mohammed, N., Tang, J. and Tam, K.C., 2017. Recent advances in the application of cellulose nanocrystals. Current Opinion in Colloid & Interface Science, 29, pp.32-45.

Gupta, V.K., Carrott, P.J.M., Ribeiro Carrott, M.M.L. and Suhas, 2009. Low-cost adsorbents: growing approach to wastewater treatment—a review. Critical Reviews in Environmental Science and Technology, 39(10), pp.783-842.

Harrison, P.T., 2005. Fluoride in water: a UK perspective. Journal of fluorine chemistry, 126(11-12), pp.1448-1456.

Harrison, R.M. ed., 2015. Pollution: causes, effects, and control. Royal Society of Chemistry.

Hijnen, W., Beerendonk, E. & Medema, G. J. 2006. Inactivation credit of UV radiation for viruses, bacteria and protozoan (oo)cysts in water: a review. Water Res. 40, 3–22.

Hotze, E.M., Phenrat, T., and Lowry, G.V., 2010. Nanoparticle aggregation: challenges to understanding transport and reactivity in the environment. Journal of environmental quality, 39(6), pp.1909-1924.

Hu, K., Dickson, J.M., 2006. Nanofiltration membrane performance on fluoride removal from water. J. Membr. Sci. 279, 529–538.

Huiliang, H., Jagner, D. and Renman, L., 1987. Flow constant-current stripping analysis for antimony (III) and antimony (V) with gold fibre working electrodes: application to natural waters. Analytica chimica acta, 202, pp.123-129.

Hunter P. R., 2009. Household Water Treatment in Developing Countries: Comparing Different Intervention Types Using Meta- Regression. Environ. Sci. Technol.; 43(23): 8991-8997.

Izuagie, A.A., Gitari, W.M., and Gumbo, J.R., 2016. Synthesis and performance evaluation of Al/Fe oxide coated diatomaceous earth in groundwater defluoridation: towards fluorosis mitigation. Journal of Environmental Science and Health, Part A, 51(10), pp.810-824.

Jain, S. and Jayaram, R.V., 2009. Removal of fluoride from contaminated drinking water using unmodified and aluminum hydroxide impregnated blue limestone waste. Separation Science and Technology, 44(6), pp.1436-1451.

Jens Lange, Tineke Materne, Jörg Grüner., 2016. Do low-cost ceramic water filters improve water security in rural South Africa? Drink. Water Eng. Sci. Discuss., doi: 10.5194/dwes-2016-6

Jha, S.K., Singh, R.K., Damodaran, T., Mishra, V.K., Sharma, D.K. and Rai, D., 2013. Fluoride in groundwater: toxicological exposure and remedies. Journal of Toxicology and Environmental Health, Part B, 16(1), pp.52-66.

Joseph Cotruvo, Gunther F. Craun, and Nancy Hearne (1999). Providing Safe Drinking Water in Small Systems: Technology, Operations, and Economics. CRC Press, 1999 pg 241. ISBN156670393X, 9781566703932

Kačaroğlu, F., 1999. Review of groundwater pollution and protection in karst areas. Water, Air, and Soil Pollution, 113(1-4), pp.337-356. Review of groundwater pollution and protection in karst areas. Water, Air, and Soil Pollution, 113(1-4), pp.337-356.

Kalia, S., and Avérous, L., 2011. Biopolymers: biomedical and environmentalapplications. John Wiley & Sons.

Kamble, S.P., Jagtap, S., Labhsetwar, N.K., Thakare, D., Godfrey, S., Devotta, S. and Rayalu, S.S., 2007. Defluoridation of drinking water using chitin, chitosan, and lanthanum-modified chitosan. Chemical Engineering Journal, 129(1-3), pp.173-180.

Kanmani, P., Aravind, J., Kamaraj, M., Sureshbabu, P. and Karthikeyan, S., 2017. Environmental applications of chitosan and cellulosic biopolymers: A comprehensive outlook. Bioresource technology, 242, pp.295-303.

Kanno, C.M., Sanders, R.L., Flynn, S.M., Lessard, G. and Myneni, S.C., 2014. Novel apatite-based sorbent for defluoridation: synthesis and sorption characteristics of nano-micro-crystalline hydroxyapatite-coated-limestone. Environmental science & technology, 48(10), pp.5798-5807.

Keyser, S. L., 1997 Microorganisms, Bacteria and Viruses June 1997. Retrieved from http://extoxnet.orst.edu/faqs/safedrink/microorg.htm on 14th of July, 2016.

Krauss, S., Griebler, C., and Deutsche Akademie der Technikwissenschaften, 2011. Pathogenic microorganisms and viruses in groundwater. Acatech. UNESCO (1999): World Water Resources at the Beginning of the 21st Century. CD version, UNESCO, Paris.

Lee, K.Y., Jeong, L., Kang, Y.O., Lee, S.J. and Park, W.H., 2009. Electrospinning of polysaccharides for regenerative medicine. Advanced drug delivery reviews, 61(12), pp.1020-1032.

Lee, A., Elam, J.W. and Darling, S.B., 2016. Membrane materials for water purification: design, development, and application. Environmental Science: Water Research & Technology, 2(1), pp.17-42.

LeChevallier, M.W. and Au, K.K., 2004. Water treatment and pathogen control. IWA publishing.

Lenntech Membrane Technology. 2016. Retrieved on 15th of July, 2016: http://www.lenntech.com/membrane-technology.htm

LeVan, M.D., Carta, G. and Yon, C.M., 1997. Adsorption and ion exchange. Energy, 16, p.17.

Li, L., Ndoni, S., Jonsson, G. E., and Vigild, M. E., 2012. Nanoporous Polymers for Membrane Applications. Kgs.Lyngby: Technical University of Denmark, Department of Chemical Engineering.

Liang, S.H. and Gay, I.D., 1986. A 13C solid-state NMR study of the chemisorption and decomposition of ethanol on MgO. Journal of Catalysis, 101(2), pp.293-300.

Loganathan, P., Vigneswaran, S., Kandasamy, J. and Naidu, R., 2013. Defluoridation of drinking water using adsorption processes. Journal of Hazardous materials, 248, pp.1-19.

Lu, F. and Astruc, D., 2018. Nanomaterials for removal of toxic elements from water. Coordination Chemistry Reviews, 356, pp.147-164.

Luo, F. and Inoue, K., 2004. The removal of fluoride ion by using metal (III)-loaded Amberlite resins. Solvent extraction and ion exchange, 22(2), pp.305-322.

Ma, Y., Wang, S.G., Fan, M., Gong, W.X. and Gao, B.Y., 2009. Characteristics and defluoridation performance of granular activated carbons coated with manganese oxides. Journal of hazardous materials, 168(2-3), pp.1140-1146.

Maliyekkal, S.M., Sharma, A.K., and Philip, L., 2006. Manganese-oxide-coated alumina: a promising sorbent for defluoridation of water. Water Research, 40(19), pp.3497-3506.

McCaffrey, L. P. and Willis J. P., 1993. Distribution of fluoride-rich groundwater in the eastern parts of Bophuthatswana, relationship to bedrock and soils and constraints on drinking water supplies: a preliminary report. Africa Needs Ground Water. An International Ground Water Convention. 1 1-8.

Meenakshi S.K., and Maheshwari R.C., 2006. Fluoride in drinking water and its removal. Journal of Hazardous materials, 137(1), pp.456-463.

Miretzky, P. and Cirelli, A.F., 2011. Fluoride removal from water by chitosan derivatives and composites: a review. Journal of Fluorine Chemistry, 132(4), pp.231-240.

Mjengera, H. and Mkongo, G., 2003. Appropriate deflouridation technology for use in fluorotic areas in Tanzania. Physics and Chemistry of the Earth, Parts A/B/C, 28(20-27), pp.1097-1104.

Mohapatra, M., Anand, S., Mishra, B.K., Giles, D.E. and Singh, P., 2009. Review of fluoride removal from drinking water. Journal of environmental management, 91(1), pp.67-77.

Moran Ayala, L.I., Paquet, M., Janowska, K., Jamard, P., Quist-Jensen, C.A., Bosio, G.N., Mártire, D.O., Fabbri, D. and Boffa, V., 2018. Water defluoridation: nanofiltration vs membrane distillation. Industrial & Engineering Chemistry Research, 57(43), pp.14740-14748

Morones, J.R., Elechiguerra, J.L., Camacho, A., Holt, K., Kouri, J.B., Ramírez, J.T. and Yacaman, M.J., 2005. The bactericidal effect of silver nanoparticles. Nanotechnology, 16(10), p.2346.

Mumtaz, N., Pandey, G. and Labhasetwar, P.K., 2015. Global fluoride occurrence, available technologies for fluoride removal and electrolytic defluoridation: a review. Critical Reviews in Environmental Science and Technology, DOI: 10.1080/10643389.2015.1046768

Muzzarelli, R. 2012. Nanochitins and nanochitosans: Paving the way to eco-friendly and energy-saving exploitation of marine resources. PolymerScience: A Comprehensive Reference, 10, 153–164.

Nasr, A.B., Charcosset, C., Amar, R.B. and Walha, K., 2013. Defluoridation of water by nanofiltration. Journal of Fluorine Chemistry, 150, pp.92-97.

Nanyaro, J.T., Aswathanarayana, U., Mungure, J.S. and Lahermo, P.W., 1984. A geochemical model for the abnormal fluoride concentrations in waters in parts of northern Tanzania. Journal of African Earth Sciences (1983), 2(2), pp.129-140.

Nayak, P., 2002. Aluminum: impacts and disease. Environmental Research, 89(2), pp.101-115.

Ndiaye PI, et al. Desalination. 2005. 173. 25–32p.

Ncube, E.J., 2002. The distribution of fluoride in South African Groundwater and the impact thereof on dental health. MSc Dissertation. Water Utilization. University of Pretoria, South Africa.

Ncube, E.J. and Schutte, C.F., 2005. The occurrence of fluoride in South African groundwater: A water quality and health problem. Water SA, 31(1), pp.35-40.

Odiyo, J.O., and Makungo, R., 2012. Fluoride concentrations in groundwater and impact on human health in Siloam Village, Limpopo Province, South Africa. Water SA, 38(5), pp.731-736.

Onyango, M.S., and Matsuda, H., 2006. Fluoride removal from water using adsorption technique. Advances in fluorine science, 2, pp.1-48.

Owusu-Agyeman, I., Jeihanipour, A., Luxbacher, T. and Schäfer, A.I., 2017. Implications of humic acid, inorganic carbon, and speciation on fluoride retention mechanisms in nanofiltration and reverse osmosis. Journal of Membrane Science, 528, pp.82-94.

Pandi, K. and Viswanathan, N., 2015. In situ fabrication of magnetic iron oxide over nano-hydroxyapatite gelatin eco-polymeric composite for defluoridation studies. Journal of Chemical & Engineering Data, 61(1), pp.571-578.

Peter-Varbanets, M., Zurbrügg, C., Swartz, C. and Pronk, W., 2009. Decentralized systems for potable water and the potential of membrane technology. Water Research, 43(2), pp.245-265.

Pedley, S. and Howard, G., 1997. The public health implications of microbiological contamination of groundwater. Quarterly Journal of Engineering Geology and Hydrogeology, 30(2), pp.179-188.

Pedley, S., Yates, M., Schijven, J.F., West, J. and Howard, G., 2006. Pathogens: health relevance, transport, and attenuation (No. 3, pp. 49-80). World Health Organization.

Popat, K.M., Anand, P.S. and Dasare, B.D., 1994. Selective removal of fluoride ions from water by the aluminum form of the aminomethylphosphonic acid-type ion exchanger. Reactive polymers, 23(1), pp.23-32.

Pradeep, T., 2009. Noble metal nanoparticles for water purification: a critical review. Thin solid films, 517(24), pp.6441-6478.

Rabovsky, J., 1995. Biogenic amorphous silica. Scandinavian journal of work, environment & health, 21, pp.108-110.

Rajan, C.S., 2011. Nanotechnology in groundwater remediation. International Journal of Environmental Science and Development, 2(3), p.182.

Raval, N.P., Shah, P.U., Shah, N.K., 2016. Adsorptive removal of nickel (II) ions from aqueous environment: A review. J. Environ. Manage. 179, 1 – 20.

Rhim, J.-W., Hong, S.-I., Park, H.-M. and Ng, P. Y. W. (2006) Preparation and characterization of chitosan-based nanocomposite films with antimicrobial activity, J. Agric. Food Chem. 54, 5814–5822.

Rošin-Grget, K. and Linčir, I., 2001. Current concept on the anticaries fluoride mechanism of the action. Collegium antropologicum, 25(2), pp.703-712.

Ruthven, D.M., 1984. Principles of adsorption and adsorption processes. John Wiley & Sons.

Sampat, P., 2000. Deep Trouble - The Hidden Threat of Groundwater Pollution. World Watch Paper 154.

SANS, 241. 2006. South African National Standard. Drinking water-Drinking water. Published by Standard South Africa, a division of SABS. www.stanza.co.za. ISBN 0-626-17752-9.

Sanghavi, B.J. and Srivastava, A.K., 2010. Simultaneous voltammetric determination of acetaminophen, aspirin, and caffeine using an in situ surfactant-modified multiwalled carbon nanotube paste electrode. Electrochimica Acta, 55(28), pp.8638-8648.

Santos, V.S., Santos, W.D.J.R., Kubota, L.T. and Tarley, C.R.T., 2009. Speciation of Sb (III) and Sb (V) in meglumine antimoniate pharmaceutical formulations by PSA using carbon nanotube electrode. Journal of pharmaceutical and biomedical analysis, 50(2), pp.151-157.

Savage, N. and Diallo, M.S., 2005. Nanomaterials and water purification: opportunities and challenges. Journal of Nanoparticle Research, 7(4-5), pp.331-342.

Sehn, P., 2008. Fluoride removal with extra low energy reverse osmosis membranes: three years of large scale field experience in Finland. Desalination, 223(1-3), pp.73-84.

Sharma, V.K.; Yngard, R.A., and Lin, Y., 2009. Silver nanoparticles: Green synthesis and their antimicrobial activities. Adv. Colloid Interface Sci., 145, 83–96.

Shen, J., Richards, B.S., and Schäfer, A.I., 2016. Renewable energy powered membrane technology: Case study of St. Dorcas borehole in Tanzania demonstrating fluoride removal via nanofiltration/reverse osmosis. Separation and Purification Technology, 170, pp.445-452.

Simons, R., 1993. Trace element removal from ash dam waters by nanofiltration and diffusion dialysis. Desalination, 89(3), pp.325-341.

Singh, J., Singh, P., and Singh, A., 2016. Fluoride ions vs removal technologies: a study. Arabian Journal of Chemistry, 9(6), pp.815-824.

Simpson H. 2015. Groundwater — An Important Rural Resource Protecting the Quality of Groundwater Supplies; Factsheet 15-045: AGDEX 716/552: http://www.omafra.gov.on.ca/english/engineer/facts/15-045.htm

Stoimenov, P.K., Klinger, R.L., Marchin, G.L. and Klabunde, K.J., 2002. Metal oxide nanoparticles as bactericidal agents. Langmuir, 18(17), pp.6679-6686.

Streat, M., Hellgardt, K. and Newton, N.L.R., 2008. Hydrous ferric oxide as an adsorbent in water treatment: Part 3: Batch and mini-column adsorption of arsenic, phosphorus, fluorine and cadmium ions. Process safety and environmental protection, 86(1), pp.21-30.

Sundaram C. S., Viswanathan, N., Meenakshi, S., 2008. Uptake of fluoride by nanohydroxyapatite/ chitosan, a bioinorganic composite, Bioresour. Technol. 99 8226–8230.

Sundrarajan, M., Suresh, J. and Gandhi, R. R., 2012. A comparative study on antibacterial properties of MgO nanoparticles prepared under different calcination temperature. Digest Journal of Nanomaterials and Biostructures, 7, 983-989.

Szymczyk, A., Fievet, P., 2005. Investigating transport properties of nanofiltration membranes by means of a steric, electric and dielectric exclusion model. J. Membr. Sci. 252, 77–88.

Swain, S.K., Mishra, S., Patnaik, T., Patel, R.K., Jha, U. and Dey, R.K., 2012. Fluoride removal performance of a new hybrid sorbent of Zr (IV)–ethylenediamine. Chemical Engineering Journal, 184, pp.72-81.

Tang, D. and Zhang, G., 2016. Efficient removal of fluoride by hierarchical Ce–Fe bimetal oxides adsorbent: thermodynamics, kinetics, and mechanism. Chemical Engineering Journal, 283, pp.721-729.

Tahaikt, M., El Habbani, R., Haddou, A.A., Achary, I., Amor, Z., Taky, M., Alami, A., Boughriba, A., Hafsi, M. and Elmidaoui, A., 2007. Fluoride removal from groundwater by nanofiltration. Desalination, 212(1-3), pp.46-53.

Thakur, V.K. and Voicu, S.I., 2016. Recent advances in cellulose and chitosan-based membranes for water purification: a concise review. Carbohydrate polymers, 146, pp.148-165.

Thole, B., 2013. Groundwater contamination with fluoride and potential fluoride removal technologies for East and Southern Africa. In Perspectives in Water Pollution. IntechOpen.

Tian, Y., Wu, M., Liu, R., Wang, D., Lin, X., Liu, W., Ma, L., Li, Y. and Huang, Y., 2011. Modified native cellulose fibers—A novel efficient adsorbent for both fluoride and arsenic. Journal of hazardous materials, 185(1), pp.93-100.

Tokunaga, S., Haron, M.J., Wasay, S.A., Wong, K.F., Laosangthum, K. and Uchiumi, A., 1995. Removal of fluoride ions from aqueous solutions by multivalent metal compounds. International journal of environmental studies, 48(1), pp.17-28.

Tressaud, A. ed., 2006a. Fluorine and the environment: atmospheric chemistry, emissions & lithosphere (Vol. 1). Elsevier.

Tressaud, A., 2006b. Advances in Fluorine Science, Fluorine and the Environment, Agrochemicals, Archaeology. Green Chemistry & Water, 2.

Tufenkji, N. and Emelko, M.B., 2011. Groundwater Pollution: Impacts on Human Health: Fate and Transport of Microbial Contaminants. Encyclopedia of Environmental Health, J. Nriagu, Ed., Elsevier Publishing Inc.

Twardowski, T.E., 2007. Introduction to nanocomposite materials: properties, processing, characterization. DEStech Publications, Inc.

UNESCO. 2009. The United Nations World Water Development Report 3 - Water in a Changing World. UN Educ. Sci. Cult. Organ. Paris/New York: UNESCO/Berghahn Books.

Varma, A. J., Deshpande, S.V., and Kennedy J.F., 2004. Carbohydr. Polym. 55 77–93.

Viswanathan, N. and Meenakshi, S., 2009. Role of metal ion incorporation in ion exchange resin on the selectivity of fluoride. Journal of hazardous materials, 162(2-3), pp.920-930.

Wang, J., Lin, X., Luo, X. and Long, Y., 2014. A sorbent of carboxymethyl cellulose loaded with zirconium for the removal of fluoride from aqueous solution. Chemical Engineering Journal, 252, pp.415-422.

Wikipedia contributors. 2019, March 18 Groundwater pollution. In Wikipedia, The Free Encyclopedia. Retrieved 11:46, May 3, 2019, from https://en.wikipedia.org/w/index.php?title=Groundwater_pollution&oldid=888356565

WHO. 2003b. Emerging Issues in Water and Infectious Disease. World Health Organization, Geneva.

World Health Organization, 2004. Guidelines for drinking-water quality (Vol. 1). World Health Organization.

WHO, 2011. Guidelines for drinking-water quality. WHO chronicle, 38(4), pp.104-8.World Health Organization, Geneva, 2011.

World Health Organization, 2016. Mortality and burden of disease from water and sanitation. Global Health Observatory (GHO) data.

WHO/UNICEF JMP (Joint Monitoring Programme for Water Supply and Sanitation). 2011. Improved sanitation coverage estimates (1980 - 2010). 20-22.

World Health Organization and UNICEF Joint Monitoring Programme. (2017). Progress on Drinking Water and Sanitation, 2017 Update and MDG Assessment.

Worch, E., 2012. Adsorption technology in water treatment: fundamentals, processes, and modeling. Walter de Gruyter.

Xi, B., Wang, X., Liu, W., Xia, X., Li, D., He, L., Wang, H., Sun, W., Yang, T. and Tao, W., 2014. Fluoride and Arsenic Removal by Nanofiltration Technology from Groundwater in Rural Areas of China: Performances with Membrane Optimization. Separation Science and Technology, 49(17), pp.2642-2649.

Yeşilnacar, M.İ., Yetiş, A.D., Dülgergil, Ç.T., Kumral, M., Atasoy, A.D., Doğan, T.R., Tekiner, S.İ., Bayhan, İ. and Aydoğdu, M., 2016. Geomedical assessment of an area having high-fluoride groundwater in southeastern Turkey. Environmental Earth Sciences, 75(2), p.162 .https://doi.org/10.1007/s12665-015-5002-6

Zhang, S., Wu, K. and Hu, S., 2002. Voltammetric determination of diethylstilbestrol at carbon paste electrode using cetylpyridine bromide as medium. Talanta, 58(4), pp.747-754.

Zhao, Y., Li, X., Liu, L. and Chen, F., 2008. Fluoride removal by Fe (III)-loaded ligand exchange cotton cellulose adsorbent from drinking water. Carbohydrate Polymers, 72(1), pp.144-150.

Zhu, S., Fan, L., Liu, X., Shi, L., Li, H., Han, S. and Xu, G., 2008. Determination of concentrated hydrogen peroxide at single-walled carbon nanohorn paste electrode. Electrochemistry Communications, 10(5), pp.695-698.

CHAPTER THREE

OPTIMIZATION OF MICROWAVE-ASSISTED SYNTHESIS OF SILVER NANOPARTICLE BY *CITRUS PARADISI* PEEL AND ITS APPLICATION AGAINST PATHOGENIC WATER STRAIN

Introduction

This chapter addresses the optimization of microwave-assisted synthesis of silver nanoparticles using *Citrus paradisi* peel extracts as a bioreductant and stabilizing agent and its application for bacterial disinfection against selected water strains. This work is presented as a publication that is under review in Green Chemistry Letters and Reviews journal by Taylor and Francis.

W. B. Ayinde; W. M. Gitari; M. Munkombwe and Samie Amidou (2019). **Optimization of microwave-assisted synthesis of silver nanoparticle by *Citrus paradisi* peel and its application against pathogenic water strain**, *Green Chemistry Letters and Reviews 12:3, 225-234,* *https://doi.org/10.1080/17518253.2019.1627427*

Optimization of microwave-assisted synthesis of silver nanoparticle by *Citrus paradisi* peel and its application against pathogenic water strain

Ayinde W. B[a], Gitari W. M[a*], and Samie Amidou[b]

[a]*Environmental Remediation and Nanoscience (EnviReN), Department of Ecology and Resource Management, School of Environmental Sciences. University of Venda, South Africa.* [b]*Molecular Parasitology and Opportunistic Infections Program, Department of Microbiology, School of Mathematical and Natural Sciences, University of Venda.*

Correspondence email : mugera.gitari@univen.ac.za Tel. +27 159628572

Abstract

This study focuses on time-dependent microwave-assisted biosynthesis of silver nanoparticles using aqueous peel extracts of *Citrus paradisi* as a reducing, stabilizing and capping agent with emphasis on its antibacterial property. Optical, structural and morphological properties of the synthesized *Citrus paradisi* peel extract silver nanoparticle (CPAgNp) were characterized using UV-visible spectrophotometer, transmission electron microscope (TEM), scanning electron microscope (SEM), energy dispersive spectroscopy (EDS), Brunauer–Emmett–Teller (BET) and X-ray diffractometer (XRD). The antimicrobial activity was evaluated using the well- and disc-diffusion methods. Characteristic surface plasmon resonance (SPR) wavelength in the range of 420-440 nm at an optimized intensity growth rate typical of silver nanoparticles was obtained. The synthesized CPAgNp are spherical in shape having the size range of 14.84 ± 5 nm and possessing fcc unit phase structure. The *Citrus paradisi* peel extract mediated AgNp were found to possess a broad-spectrum antimicrobial activity against water-borne pathogenic microbes.

Keywords: Biosynthesis, silver nanoparticle, *Citrus paradisi* peel extracts, antibacterial activity.

3.1 Introduction

In the last decades, efforts are aiming at developing environmental benign, efficient, new energy transfer methods and cost-effective route in the synthesis of nanomaterial paramount for the survival of human life, environmental protection and recovery. The application of nanomaterials has been rapidly gaining importance in a number of areas such as environmental health, biomedical sciences, and water purification among other biotechnological applications (1-2).

The importance of choosing a proper synthetic route in designing nanostructured materials has been a driving force for the development of new methodologies for several decades (3). Moreover, the need for an efficient, sustainable and conservation of energy methods to process chemical reactions has led to the search for an alternative power source over conventional heating routes in recent times. Microwave-assisted synthesis methods provide a much faster way not only to prepare materials but also to create smaller particulate materials, thus contributing to energy savings and satisfying the demands for more environmentally benign materials and procedures (4).

In nano-structuring of material; the size, shape, stability, as well as application of the nanomaterials during synthesis, depends upon the choice of the reductants, capping and stabilizing agent. The use of material of biological entities in the formation of nanomaterial with significantly novel, improved structural and biological properties are progressively associated with modern developments in the field of material and nanoscience. Currently, plant-mediated synthesis of nanoparticles is fast gaining interest due to the vast distribution of plants and plant-parts extracts consisting of a wide range of metabolites, which favorably contributes to the exceptional stability and overall property of these materials in their area of applications (5-6).

Several reports had elucidated the choice of silver as the metal of choice among the noble metals due to its broad-spectrum antibacterial properties at very low concentrations, good biocompatibility in potential applications in the field of biological systems, medicine, water purification, industrial processes and many sectors of life (6-11). Researchers have documented successful biosynthetic routes for silver nanoparticle using wide varieties of plant extracts over other methods because of its reliability, eco-friendliness, and reproducibility as well as in preventing agglomeration of the nanoparticles without interfering with their biomedical activities (6; 12). Furthermore, it has also been reported that the different phytochemicals of polyol, nitrogen-containing and water-soluble heterocyclic plant constituents in these plants play a significant role in the reduction and stabilization of silver nanoparticles free from toxic chemicals (13-14).

Citrus is one of the major commercial fruit crops that is widely consumed both as fresh fruit or juice and most often the peel is discarded. This represents a huge waste, which often creates harmful effects on the environment. However, this is sometimes seen as an economic loss because

citrus peels have been reported to possess the highest amounts of polyphenolic compounds, ascorbic acid, flavonoids, etc. compared to other segments of the fruits, these phytochemical components are responsible for various bioactivities properties, including antioxidant, antiproliferation, anti-fungal, antibacterial and antiviral activities (15-19).

This work focuses on the biosynthesis of silver nanoparticles using *C. paradisi* peel extracts as a reductant, stabilizing and capping supportive agent. The biosynthesized material undergoes microwave irradiation as a heating medium to generate a porous nanoparticle structure. The growth rate optimization phenomenon and surface morphologies of the silver nanoparticle were evaluated and reported. The as-synthesized nanoparticle was studied for their antibacterial activity against *Escherichia coli, Staphylococcus aureus, and Klebsiella pneumonia*.

3.2 Materials and methods

Chemicals used were of analytical reagent grade. $AgNO_3$ used was purchased from Rochelle chemicals, South Africa and used directly without further purification. Deionized water from a Millipore water (18.2 MΩ/cm) was used for the preparation and dilution of standards throughout the experiment.

3.2.1 Preparation of *Citrus paradisi* peel extract

The fruit peels of *Citrus paradisi* (Grapefruit red) were removed, cleaned thoroughly using ultrapure (18.2 MΩ/cm) water to remove any dust particles adhering to the surface and cut into small pieces. 30 g of the peel was added to 100 mL of ultrapure water and boiled for 20 minutes at 70 °C. The extract was cooled and filtered through Whatmann No.1 filter paper and stored at 4 °C for further use in the subsequent experiments.

3.2.2 Microwave-assisted synthesis of Silver Nanoparticles using *Citrus paradisi* Peel extract (CPAgNp)

Biosynthesized Silver nanoparticles (AgNp) was obtained via microwave-assisted sol-gel method. In a typical experiment, 20 mL of the filtrate of the *Citrus paradisi* peel was added to 80 mL of 1mM $AgNO_3$ in 250 mL Erlenmeyer flasks at the ratio (1:4 v/v) for the reduction of Ag^+ to Ag^0. The mixture was then placed on a turntable domestic microwave oven (Russell Hobbs 20L (RHEM 21L)) operating at a power of 700 W and frequency 2450 MHz at different time interval (30-150) seconds for complete bio-reduction. The formation of silver nanoparticle (AgNp) was monitored using UV-Vis. Spectrophotometer (220 – 600 nm). The solution was centrifuged at 6000 rpm for 15 min and washed with ultrapure water (18.2 MΩ/cm) severally to remove any residue. The obtained nanoparticle was subjected to oven-drying at 40°C for 1 hr to obtain the CPAgNp. The procedure was repeated at a different mixing ratio (*C. paradisi* Peel extracts/1 mM $AgNO_3$) (1:4,

2:3, 3:2, 1:1 and 4:1) for optimization of the nucleation intensity of the nanoparticle. Time-resolved absorption spectra of the UV–Vis spectroscopy was used in monitoring the periodic bioprocess growth kinetics of AgNp through color variation. The silver nanoparticles obtained were characterized.

3.2.3 Characterization of the biosynthesized silver nanoparticle (CPAgNp)

The synthesized silver nanoparticle absorption range was monitored using UV-Visible Spectrophotometers (SPECTROstar Nano/ BMG LABTECH). Fourier transforms infrared (FTIR-ATR) spectra was recorded using Bruker: ALPHA FT-IR Spectrophotometer (4000 - 400 cm-1). The determination of the crystalline phases present in materials was identified by X-ray diffraction (X'Pert Pro, Cu-K radiation, wavelength 1.54443Å). Surface morphology examination and particle distribution analysis of the nanoparticles were characterized using SEM with an FEI Nova NanoSEM 230 with the field emission gun equipped with an Oxford Xmax SDD detector operating at an accelerating voltage of 20Kv for the EDS detector (Oxford X-Max with INCA software). Transmission electron microscopy (TEM) image was taken using an FEI Tecnai20 equipped with a LaB6 emitter, operating at 200 kV and fitted with a Gatan Tridiem GIF with a 2kX2k CCD camera. Images were collected using the Digital Micrograph suite of programs in relation to size and shape. The surface area, pore area and pore volume of the synthesized nanoparticle were measured using nitrogen adsorption Brunauer–Emmett–Teller (BET) surface area and porosity analyzer (Micromeritics ASAP2020). The adsorption-desorption plots were used to calculate the specific surface area.

3.2.4 Antibacterial Evaluation of the Nanoparticles

The bacterial resistance of the biosynthesized Ag nanoparticle was determined from the observed zone of inhibition (mm) using the standard Agar-Well disc diffusion methods (Kirby Bauer disk diffusion test) and Microdilution assay. The indicator strains used were Escherichia coli (ATCC 35218), Staphylococcus aureus (ATCC 33591) and a clinical isolate of Klebsiella pneumonia. Bacterial suspensions were prepared with the turbidity of 0.5 McFarland. Wells with a diameter of 6 mm were cut using a sterile cork-borer and filled with 50 µL 1 mg/ml of CPAgNPs solution on the Macconkey nutrient agar plates already inoculated with the bacterial cell suspension (50 µL). Plates were incubated at 37°C for 24 h. After incubation, the growth inhibition zone diameters were measured in millimeter (mm) and compared. Minimum inhibitory concentration (MIC) of biosynthesized Ag was also determined by using a 96-well microtitre plate broth-dilution method as described by Samie *et al*. (20).

To determine the release of silver ions in solution, 1 mg/ml of the biosynthesized CPAgNPs was left to stand at room temperature for 3 h. At different time intervals, the suspension was collected

and filtered through a membrane filter. The concentrations of Ag ions in the filtrate (20 µL) were measured on a PinAAcle 900T Atomic Absorption Spectrometers (AAS, PerkinElmer Inc).

3.3 Results and Discussion

3.3.1 Physicochemical and mineralogical characterization of Ag nanoparticles

3.3.1.1 UV-Visible analysis

Understanding the growth rate of the biosynthesized silver nanoparticles towards integration into a specific application is critical for optimizing performance. Fig. 3.1 (a, b, c, d, and e) show the different mixing ratio (*C. paradisi* peel extracts: 1 mM $AgNO_3$) bio-reduction process obtained from the time-resolved UV–Visible analysis. The first evidence in the formation of CPAgNPs from the silver ion precursor ($AgNO_3$) is obtained from the color variation of the reaction mixture as the reaction time increases. As shown in the photographic representations (Figs. 3.1 (a-e), the nucleation and growth of the CPAgNps displayed an outright bio=reduction property within 30 sec of reaction with plasmon resonance bands between the wavelength range of 390 to 470 nm across the different time intervals. The color variations from pale yellow to brown were observed across the different reaction mixing ratio upon microwave irradiation. The final color deepened with an increase in time of reaction. The changes associated with these color variations are due to characteristic vibrations due to changes in electronic energy levels, which arise from the coupling between the electron clouds on the CPAgNps surface with the incident electromagnetic radiation typical of the surface plasmon resonance phenomenon (21-23). Furthermore, reports showed that an absorption band can exhibit a shift towards either the red end (increase in wavelength) or the blue end (decrease in wavelength) of an absorption spectrum depending on the particle size, shape, state of aggregation and the surrounding dielectric medium (24-25). As shown in the optical bands, increasing the volume of CP extracts and the silver nitrate solution increases both the yield and the concentration of reductant in the reaction mixture, consequently shifting the bands and affecting the formation as well as the CPAgNPs sizes (26). Both band shifts were observed across the spectra as the time increases with respect to the mixing solution ratios. Spectra in Figs. 3.1 (d) and 1e show broader resonance bands with a maximum shift in absorption maxima observed in 1: 4 ratio at 470 nm. Consequently, the more the time of exposure, the more the bandwidth and increase in absorption maxima resulting in polydispersity and size increment of the CPAgNPs (27-28). In addition, the bio-reduction process leading to the formation of CPAgNPs occurred due to the availability and interaction of the phytochemical constituents in C. *paradisi* peel extracts creating the capping and stability effects on the synthesized nanoparticles from aggregation (12; 29).

Finally, a significant improvement in the overall rate through a bio-reduction process of CPAgNPs is observed during the interaction between the reaction mixture and the microwave heating method. Contrary to the conventional heating method at ambient temperature, exposing the reaction mixture to microwave irradiation accelerates the reaction medium providing lower energy usage, uniform nucleation and growth conditions for nanoparticles (30-31). In addition, the rapid heating created by the irradiation facilitates ease of releasing the phytochemical constituents in the peel through the disruption of the cell wall into the reaction mixture (29).

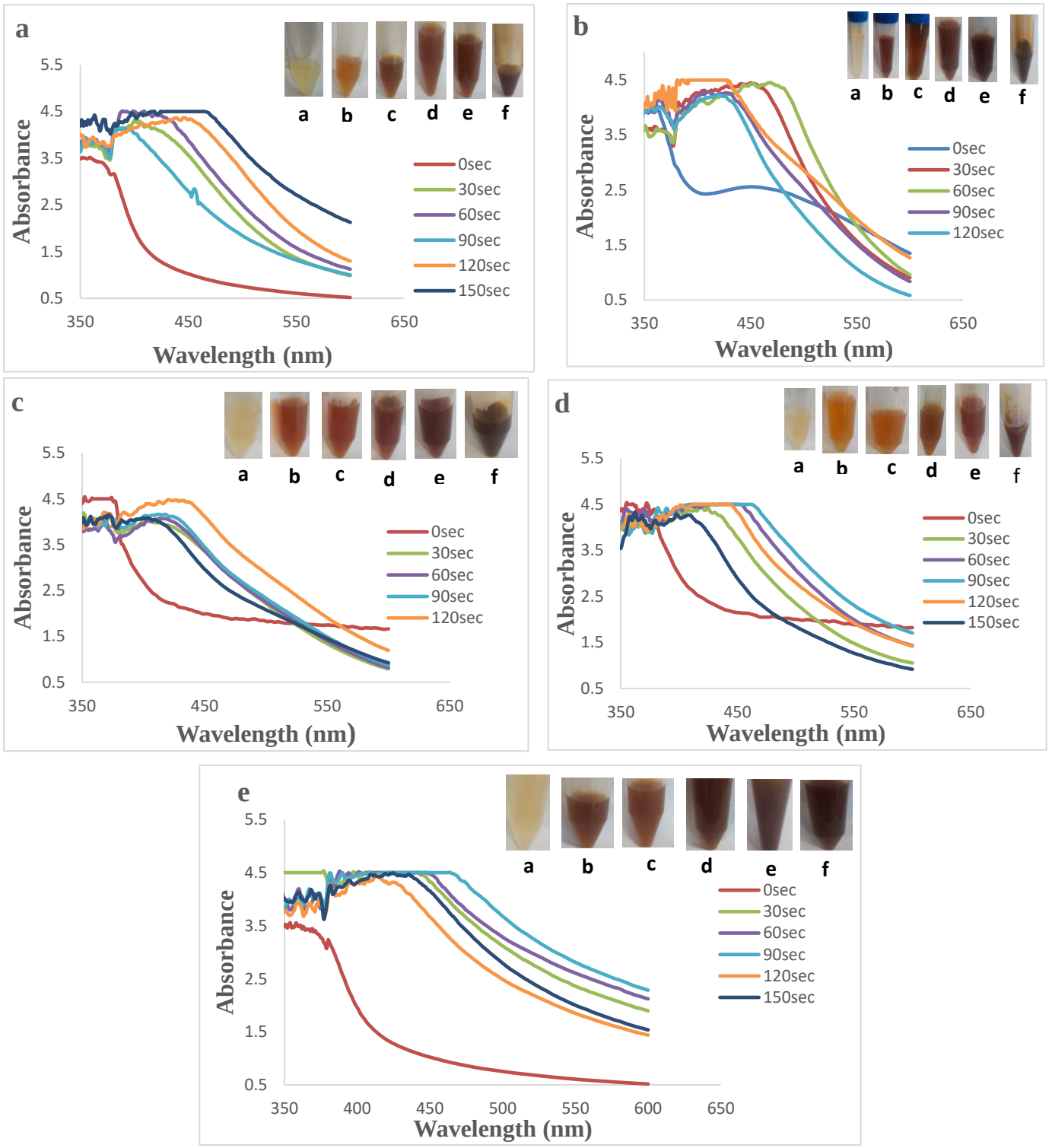

Fig. 3. 1. UV–Visible spectra and photographic representation of silver nanoparticle synthesis by aqueous extract of *C. Paradisi* peel extract at mixing ratio (a) 1:1; (b) 3:2; (c) 2:3; (d) 4:1; (e) 1:4 at different time interval.

Furthermore, the surface plasmon intensity relative to the maximum reaction time of microwave exposure for all the bio-reduction process across the different reaction mixture ratios from the respective UV–Vis graph was monitored and is shown in Fig. 3. 2. The influence of the reaction mixtures is observed to affect the SPR patterns on the different nucleation, stability and nanoparticle growth using the microwave-induced method. As shown in the graph, a rapid growth rate of CPAgNPs occurred in mixing ratio 1:1, 3:2, 4:1 and 1:4 with maximum intensity at the reaction time of 60 sec. The fast particle growth may have been attributed to the *C. paradisi* peel extracts possessing optimum phytochemical agents for the bio-reduction (12). However, the optimized mixing ratio at 2:3 exhibited a steady growth synthesis of CPAgNPs with the highest plasmon intensity at 120 secs with significance growth control on the size of the particles. Although this occurred at a higher time, the steady and slow growth may be attributed to strong interactions between the *C. paradisi* peel biomolecules and the growing isotropic silver particles as it is time-dependent as well as the dependency of the surface plasmon resonance on interparticle interactions (32-34). Conclusively, increasing the volumes of both the $AgNO_3$ and CP peel extracts ultimately increases bio-reduction of more silver ions on the surface of the particles leading to the formation of a stable CPAgNp. Therefore, the mixing ratio of 2:3 was chosen as the optimum reaction mixing ratio relative to the bio-reduction process contributing to the particle size growth of CPAgNps.

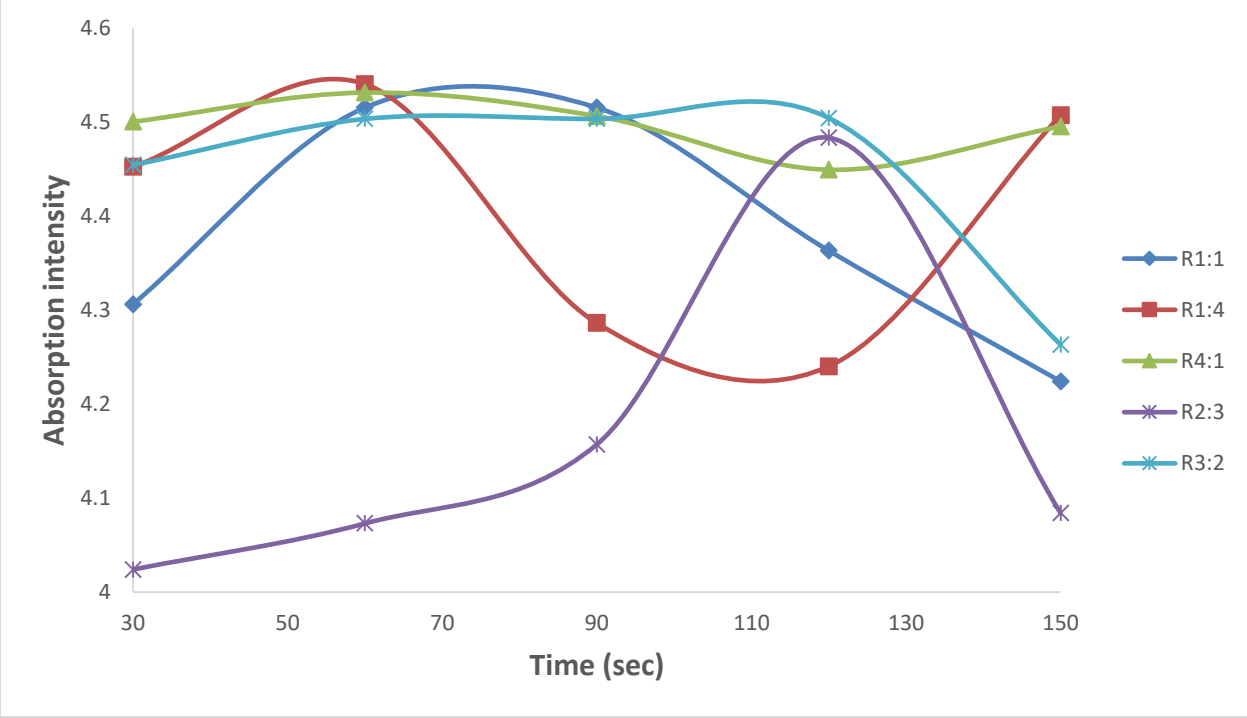

Fig. 3.2. Plots of the intensity of SPR band against reaction time for silver nanoparticles as obtained from various mixing ratio of *C. paradisi* peel extracts.

3.3.1.2 Fourier-Transform Infrared Spectroscopy

FTIR spectroscopic study of the green synthesized Ag nanoparticle (CPAgNp) was obtained to show the interaction of the different phytochemical constituents of the C. paradisi peel extract with the nanoparticle. Fig. 3.3 shows the comparative FTIR spectra of the aqueous extract of the peel and CPAgNp. In the spectrum, the broader band appearing in the range 3282-3300 cm^{-1} is attributed to the stretching vibrations of the –OH group, N–H stretch of various metabolites present in the peel extract in form of an alcohol, N–H stretch of 1° and 2° amines or amides, carboxylic acid, ester and ether (35). The broadness and shapes of these bands in both spectra depend on the hydrogen bonding systems interacting with the phytochemicals resulting in the formation of the nanoparticles through bio-reduction stages. The sharp peaks observed between 2915 cm^{-1} and 2850 cm^{-1} in the spectra could be assigned to the symmetric and asymmetric C–H stretching vibrations of methyl, methylene, and methoxy groups (36-37). The presence of C=O is found in both spectrums at around 1662 cm^{-1} in the extracts which shifted to 1626 cm^{-1} in the CPAgNps. This may be attributed to the presence of carboxylate ion and an amide functional group. In both spectra, different characteristic sharp peaks were also observed between 1538 and 1377 cm^{-1} which may be assigned to the -C=C in the aromatic rings, asymmetric stretching (C-N) mode in addition to the bending vibrations of the methyl and methylene groups of fatty acids. The C-O-C, C-C and carboxylic group (C–O) stretching vibrations were identified at 1238, 1156 and 1032 cm^{-1} band respectively (35). The presence, interaction and shifting of the above bands in *C. paradisi* peel extract indicate that bioactive compounds are presumed to act as reducing, capping and stabilizing agents of silver ions to the biosynthesized CPAgNps.

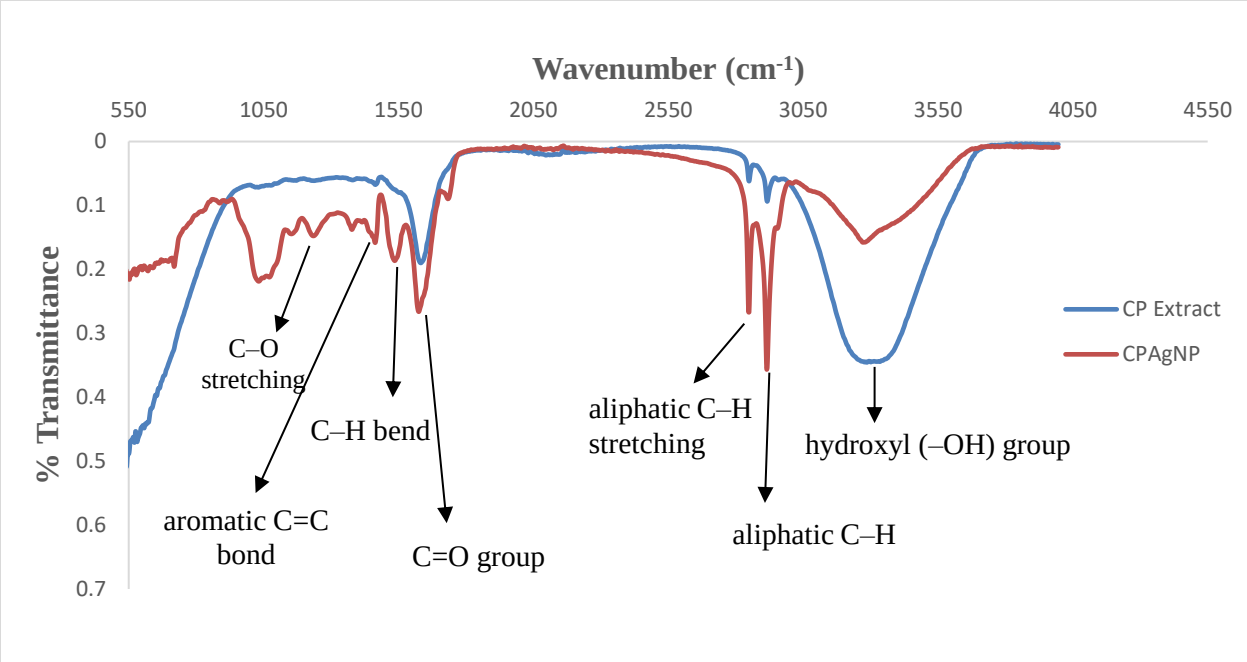

Fig. 3.3. FTIR spectra of C. *paradisi* peel extracts and CPAgNp.

3.3.1.3 Surface morphological analysis

The shape, size and overall surface morphology of the synthesized silver nanoparticles using *Citrus paradisi* peel extracts (CPAgNps) were examined using scanning electron microscopy (SEM) and transmission electron microscopy (TEM) analysis. The SEM micrograph (Fig. 3.4 (a) showed traces of congregation and polydispersity on the synthesized CPAgNps. The observed array of biomass could be attributed to the presence of the plant phytochemicals responsible for the bio-reducing and capping the nanoparticles resulting in their stabilization. The TEM micrograph (x100 nm) with the histogram image (inset)(Fig. 3.4 (b) together with the corresponding surface interactive 3D Image (x20 nm) (Fig. 3.4 (c) reveal the particles by their morphological size and circularity. As shown in Fig 4b, the CPAgNp are homogeneous, well dispersed and majorly small and sphere-like in shape with an average particle size of 14.84 ± 5 nm. The energy dispersive X-ray spectroscopy (EDS) (Fig. 3.4 (d) revealed absorption peak showing the presence of typical elemental silver around 3 keV without any form of impurity.

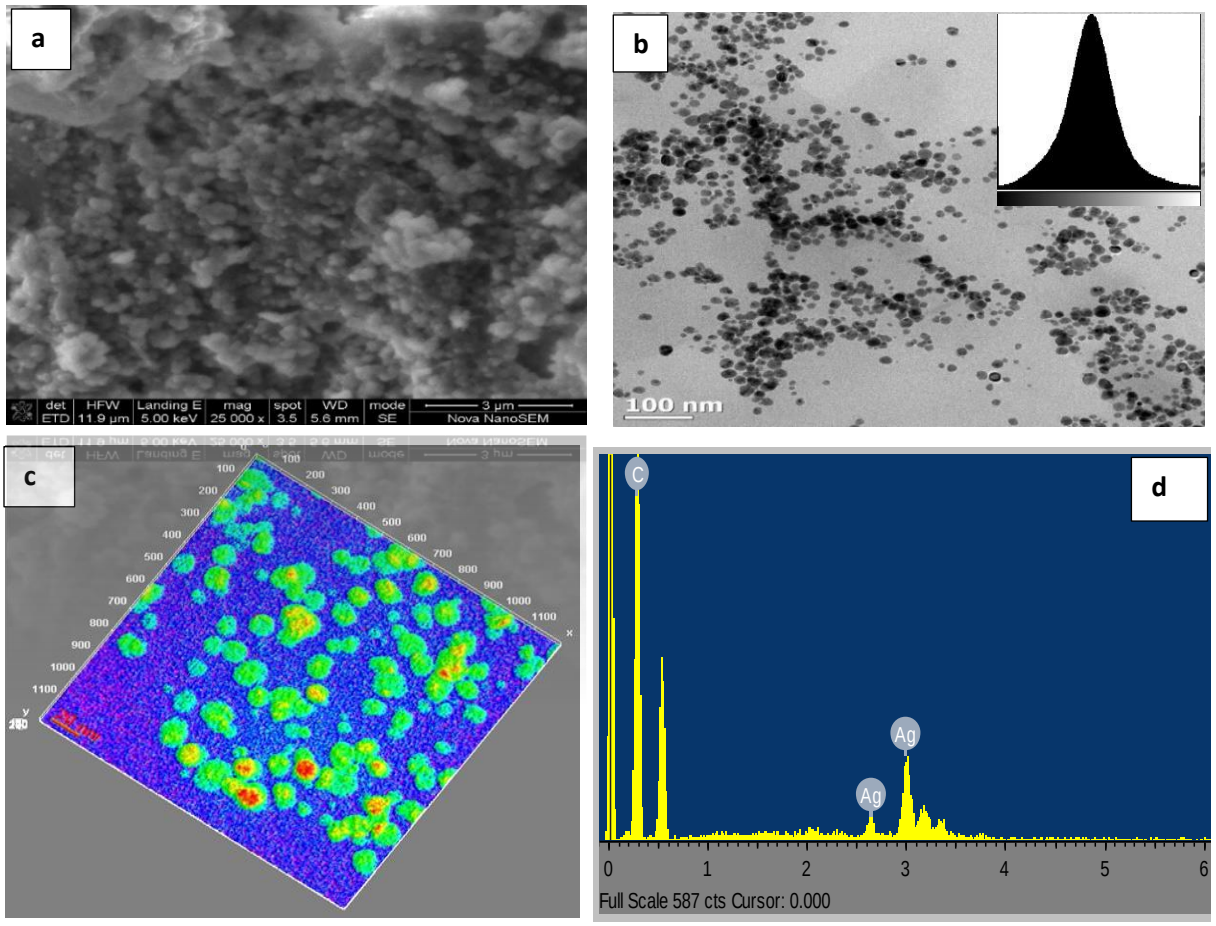

Fig. 3.4. (a) SEM image ; (b) and (c) TEM with corresponding Surface interactive 3D Image; (d) EDX of CPAgNp (2:3) from *C. paradisi* aqueous peel extracts.

3.3.1.4 XRD study

The crystalline phase of the CPAgNp was analyzed through the XRD spectroscopy as shown in Fig. 3.5 and Table 3.1. XRD pattern of CPAgNp showed major diffraction peaks at 38.26°, 44.47° and 64.71°, 77.76 ° and 81.91 ° which indexed the planes (1 1 1), (2 0 0), (2 2 0), (3 1 1) and (2 2 2) respectively typical of a cubical crystal system with an Fm-3m space group face-centered silver (38-39). The lattice constant calculated from the observed pattern was a = 4.0710 Å (calculated density 10.62 g/cm^3) matched with the database Cross-References code ICSD: 064996. The X-ray diffraction studies clearly indicate that the silver nanoparticles synthesized from *C. paradisi* peel extract are crystalline in nature.

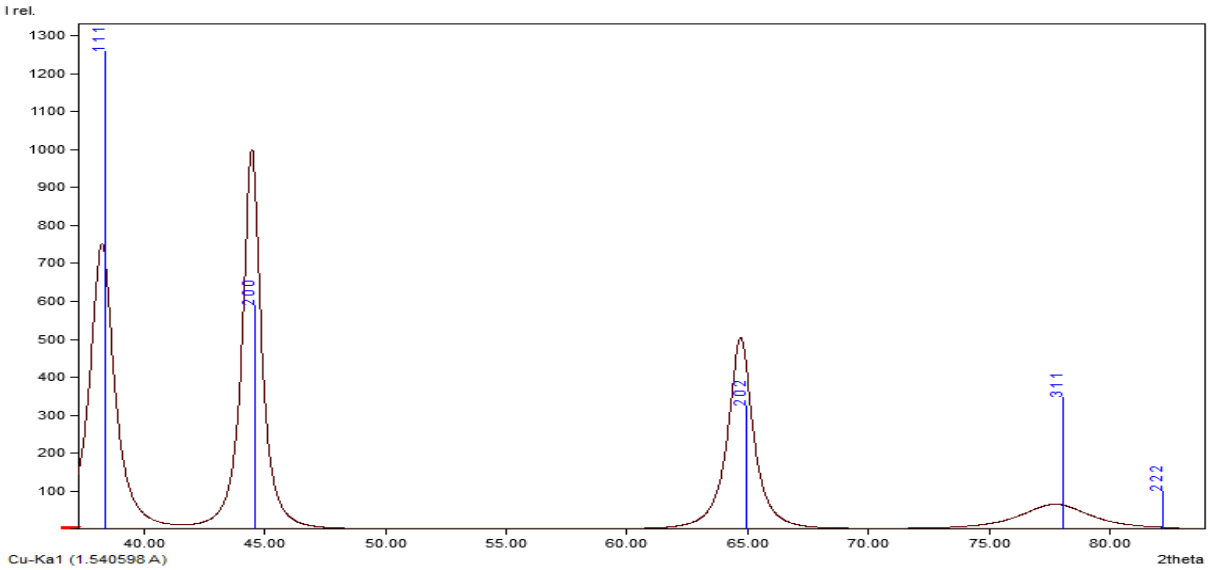

Fig. 3.5. XRD pattern of the silver nanoparticle synthesized from an aqueous extract of *C. paradisi* peel

Table 3.1: XRD data of CPAgNp

No.	2theta [°]	d [Å]	FWHM	I/I0
1	38.26	2.3504	1.0706	1000
2	44.47	2.0355	0.8029	1329.42
3	64.71	1.4393	1.0706	671.56
4	77.74	1.2274	3.2118	87.8
5	81.91	1.1752	6.1	0.36

3.3.1.5 Brunauer–Emmett–Teller (BET) surface area and porosity analysis

Table 3.2 shows the results of the BET specific surface areas, pore volume and pore width measurements of the optimized CPAgNp (2:3) at an ambient temperature of 22 °C. As shown in the table, the particle size obtained from the BET conforms to TEM result. Furthermore, the N_2 adsorption-desorption and pore size distribution isotherm curve of the CPAgNp (Fig. 3.6) classified the isotherm to be type IV with the obtained P/P^o within the range 0.5-1.0 (40-41). This is a typical characterization of mesoporous materials; therefore, the biosynthesized CPAgNp is mesoporous in nature with a BET pore diameter of 14.313 nm.

Table 3. 2. BET Surface analysis parameters of CPAgNp (2:3)

Parameters	**Quantity**		
	Area (m^2/g)	**Volume (cm^3/g)**	**Pore (nm)**
Single point surface area at P/Po = 0.199747844	0.1224		
BET Surface Area	0.1274		
Single point adsorption total pore volume of pores		0.000456	
Adsorption average pore width (4V/A by BET)			14.31302

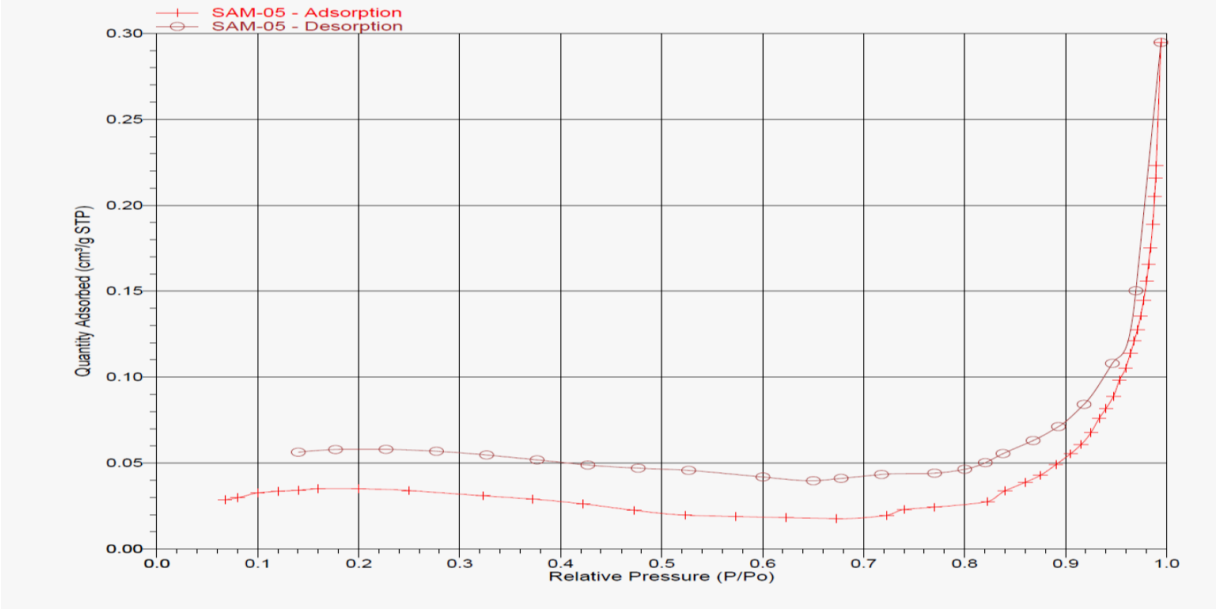

Fig. 3.6. N_2 adsorption-desorption and pore size distribution isotherms of CPAgNPs

3.4 Antimicrobial properties

The antimicrobial activity of CPAgNPs was examined by the well-diffusion and Microdilution assay method against both the Gram-positive bacterium of *Staphylococcus aureus* (ATCC 33591) and the Gram-negative bacteria of *Escherichia coli* (ATCC 35218) as well as *Klebsiella pneumonia* respectively. Table 3.3 summarized the comparative zone of inhibition and the viability to different concentration surrounding the CPAgNPs against all the test bacteria. As shown, it is evident from the results, that CPAgNPs possessed the ability to inhibit the growth of these pathogenic waterborne bacteria with maximum inhibition against Gram-negative *E. coli* (13 mm) in comparison to *Klebsiella pneumoniae* (4) and Gram-positive *S. aureus* (9 mm). It is important to note that the susceptibility of these bacterial to CPAgNp was subject to different concentration. Minimum Inhibitory Concentration (MIC) values of 20, 40 and 40 µg/mL of CPAgNp was recorded for *S. aureus* and *Klebsiella pneumonia* and *E. coli* respectively (Table 3). Studies have shown that the toxicity effects at different MICs values depend on the type of bacterial strains, precursor concentration, methods of preparation and the capping agents (42- 44).

As illustrated in Fig. 3.7, the time-dependent releases of metal ions from *C. paradisi* peel extracts biosynthesized Ag nanoparticle was also examined. It was observed that the Ag ions release was affected by time and rate of dissolution; metal ions release increases as time progresses. The concentration at the highest time interval (Ag ion (2.7 ppb) is lower than the observed minimum inhibitory concentration (MIC) (Table 3.3). These results suggested that MIC value does not correlate with the mode of action of the antimicrobial activity of CPAgNPs and the release of these metal ions against the bacteria.

Although there is controversy about the antibacterial mechanism of silver nanoparticles, ability in producing intracellular reactive oxygen species ROS production (45-46), contact action, size, as well as the reducing and capping agents used in the synthesis route (12; 47) between the nanoparticles and cells are widely believed to be some of the main factors responsible for the antibacterial activity. Consequently, these factors were considered as prominent agents that contributed to the potency of CPAgNPs targetting multiple sites in the bacterial cell leading to their inactivation.

Table 3.3. Antibacterial activity of CPAgNPs

Strains	Inhibited zone (mm)	MIC (µg/mL)
K. pneumonia	4	40
S. aureus	9	20
E. Coli	13	40

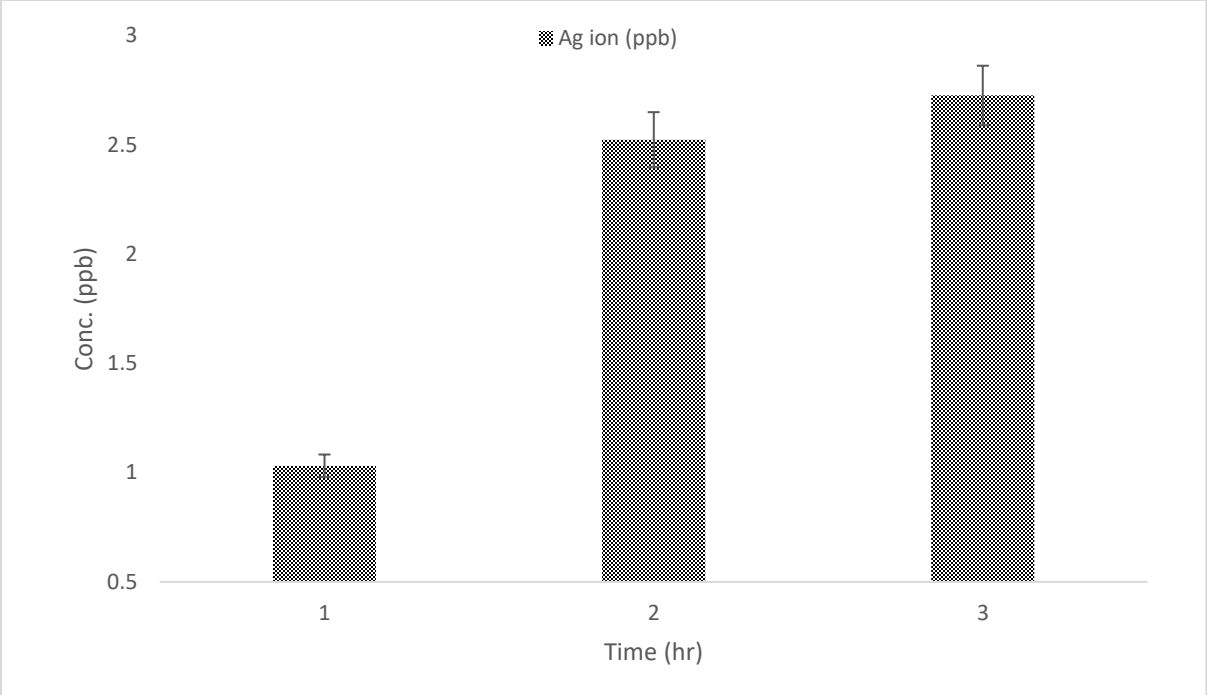

Fig. 3.7. Time-dependent silver ions release from biosynthesized CPAgNPs.

3.5 Conclusion

This study demonstrated the successful rapid green synthesis of an eco-friendly, cost-effective AgNPs using aqueous peel extract of *Citrus paradisi* and its antibacterial potency against some pathogenic water strains. The optical properties showed the participation of the metabolites in the peel extracts to be responsible for the bioreduction process with a steady growth rate at an optimized mixing ration of 2:3 through the bioreduction process. The CPAgNp morphological analysis suggests a spherical, cubical crystalline phase with an average size of 14.84 nm without any impurity was obtained. The CPAgNp demonstrated potential antibacterial potency against common gram-positive and gram-negative water pathogens.

Conflicts of interest

The authors declare no conflicts of interest.

Acknowledgment

Authors would like to acknowledge financial support from University of Venda, South Africa (RPC grant Number: SES/17/ERM/03) and Prof. Gitari DHET Research Incentive funds.

References

(1) Ananya, S.; Bharat, A.; Makwana. *Am. J. Nanosci. Nanotechnol.* **2014,** *4,* 84-92.
(2) Soloviev. A.; Mikhail. D. J. *Nanobiotechnol.* **2007,** 5 (11), 62-78.
(3) Jin Ho Bang; Kenneth S. Suslick. *Adv. Mater.* **2010,** *22,* 1039–1059.
(4) Genuino, H.; Huang, H.; Njagi, E.; Stafford, L.; Suib, S. L. *Handb. Green Chem.* **2012,** *8,* 217–244.
(5) Kulkarni N.; Muddapur, U. *J. Nanotechnol.* **2014,** 1–8.
(6) Ahmed, S.; Ahmad, M.; Swami, B. L.; Ikram, S. J. *Adv. Res.* **2016,** 7 (1), 17-28.
(7) Jaina, D.; Daimab, H.B.; Kachhwahaa, Sumita, B.S.; Kotharia, B. *Dig. J. Nanomater. Biostruct.* **2009,** *4,* 723–727.
(8) El-Kheshen A.A.; Gad El-Rab S.F. *Der. Pharma Chemical.* **2012,** 4 (1), 53-65.
(9) Jain P.; Pradeep T. *Biotechnol. Bioengg.* **2005,** *90,* 59-63.
(10) Lorna Fewtrell. *Aberystwyth University, Aberystwyth*. **2014.**
(11) Babu, R.; Zhang, J.; Beckman, E.J.; Virji, M.; Pasculle, W.A.; Wells, A. *Biomaterials.* **2006,** 27 (24), 4304–4314.
(12) Kuppusamy, P.; Yusoff, M. M.; Maniam, G.P.; Govindan, N. *Saudi Pharm. J.* **2016,** 24 (4), 473-484.
(13) Dare, E.O.; Oseghale, C.O.; Labulo, A.H.; Adesuji, E.T.; Elemike, E.E.; Onwuka, J. C.; Bamgbose, J.T. *J. Nanostruct Chem.* **2015,** 5 (1), 85-94.
(14) Leela, A.; Vivekanandan, M. *Afr. J. Biotech.* **2008,** *7,* 3162.
(15) Manthey, J.A.; Grohman, K. J. *Agric. Food Chem.* **2001,** *49,* 3268–3273.
(16) Gorinstein, S.; Martın-Belloso, O.; Park, Y. S.; Haruenkit, R.; Lojek, A.; Ciz, M Caspi, A.; Libman, I.; Trakhtenberg, S. *Food Chem.* **2001,** *74,* 309–315.
(17) Yusof, S.; Mohd Ghazali, H.; Swee King, G. *Food Chem.* **1990,** *37,* 113–121.
(18) Aruoma, O.I.; Landes, B.; Ramful-Baboolall, D.; Bourdon, E., Neergheen-Bhujun, V.; Wagner, K.H; Bahorun, T. *Prev. Med.* **2012,** S12–S16.
(19) Dillard, C. J.; German, J. B. *J. Sci. Food Agric.* **2000,** *80,* 1744–1756.
(20) Samie A; Obi C. L.; Bessong P. O.; Namrita L. *Afri. J. Biotech.* **2005,** 4 (12), 1443-1451.
(21) Bohren, C.F.; Huffman, D. R. Absorption and scattering of light by small particles. John Wiley & Sons: New York, 2008.
(22) Link, S.; El-Sayed, M. A. *Annual review of chemistry physical.* **2003,** 54 (1), 331-366.
(23) Krishnaraj, C.; Jagan, E. G.; Rajasekar, S.; Selvakumar, P.; Kalaichelvan, P. T.; Mohan, N. *Colloids and Surfaces B: Biointerfaces.* **2010**, 76 (1), 50-56.
(24) Smitha, S.L.; Nissamudeen, K.M.; Philip, D.; Gopchandran, K.G. *Spectrochim. Acta A.* **2008,** 71 (1), 186-190.
(25) Hao, E.; Schatz, G. C. *J. Phys. Chem.* **2014,** *120,* 357-366.
(26) Prathna, T.C.; Chandrasekaran, N.; Raichur, A.M.; Mukherjee, A. *Colloids and Surfaces B: Biointerfaces.* **2011,** *82,* 152–159.
(27) Ponarulselvam, S.; Panneerselvam, C.; Murugan, K.; Aarthi, N.; Kalimuthu, K.; Thangamani, S. *Asian Pac. J. Trop. Med.* **2012,** *2,* 574–580.

(28) He, R.X.; Liang, R.; Peng, P.; Zhou, Y.N. *J. Nanopart. Res.* **2017,** 19 (8), p. 267.
(29) Sökmen, M.; Alomar, S.Y.; Albay, C.; Serdar, G. *J. Alloys Compd.* **2017,** *725*, 190-198.
(30) Siby Joseph; Mathew B. *Res. J. Recent Sci.* **2013,** *3*, 185-191.
(31) Meng, L.Y.; Wang, B.; Ma, M.G.; Lin, K.L. *Materials Today Chemistry*. **2016,** *1*, 63-83.
(32) Huang, J.; Li, Q.; Sun, D.; Lu, Y.; Su, Y.; Yang, X.; Wang, H.; Wang, Y.; Shao, W.; He, N.; Hong, J.; Chen, C. *Nanotechnology*. **2007,** 18 (10), 105104.
(33) Su, K.H.; Wei, Q.H.; Zhang, X.; Mock, J.J., Smith, D. R.; Schultz, S. *Nano letters.* **2003,** 3 (8),1087-1090.
(34) Jain, P.K.; Huang, X.; El-Sayed, I.H.; El-Sayed, M.A. *Plasmonics.* **2007.** 2 (3), 107-118.
(35) Kalsi, P.S. Spectroscopy of Organic Compounds; *New Age International: New Delhi,* **2007.**
(36) Li, J.; Barron, A.R. *OpenStax-CNX module: m3 4660.* **2010.**
(37) Kumar, B.; Smita, K.; Cumbal, L.; Debut, A. *J. Saudi Chem. Soc.* **2014,** 18 (4), 364–369.
(38) Owen, E.A.; Williams, G.I. *J. Sci. Instrum.* **1954,** 31 (2), 49.
(39) Zuas, O.; Hamim, N.; Sampora, Y. *Materials Letters.* **2014,** *123*, 156-159.
(40) Hwang, N.; Barron, A.R. *The Connexions project.* **2011,** 1-11.
(41) Ma, J.; Wang, L.; Wu, Y.; Dong, X.; Ma, Q.; Qiao, C.; Zhang, Q.; Zhang, J. *Materials Transactions*. **2014,** 55 (12), 1900-1902.
(42) Velazquez-Meza, M.E.; Hernández-Salgado, M.; Sánchez-Alemán, M.A. *Microb. Drug Resist.* **2015,** 21 (4), 367-372.
(43) Mittal, J.; Jain, R.; Sharma, M.M. *Adv. Nat. Sci: Nanosci. Nanotechnol.* **2017,** 8 (2), 025011.
(44) Gong, P.; Li, H.; He, X.; Wang, K.; Hu, J.; Tan, W.; Zhang, S.; Yang, X. *Nanotechnology.* **2007,** 18 (28), 285604
(45) Durán, N.; Durán, M.; de Jesus, M.B.; Seabra, A.B.; Fávaro, W.J.; Nakazato, G. *Nanomedicine: Nanotechnology, Biology and Medicine.* **2016,** 12 (3), 789–799.
(46) Quinteros, M.A.; Aristizábal, V.C.; Dalmasso, P.R.; Paraje, M.G.; Páez, P.L. *Toxicol. In Vitro.* **2016,** *36*, 216-223.
(47) Raghupathi K.R.; Koodali R.T.; Manna A. C. *Langmuir.* **2011,** 27 (7), 4020–4028.

CHAPTER FOUR

BIOSYNTHESIS OF ULTRASONICALLY MODIFIED Ag-MgO NANOCOMPOSITE AND ITS POTENTIAL FOR ANTIMICROBIAL ACTIVITY

Introduction

This chapter focuses on the biosynthesis of ultrasonically modified Ag-MgO nanocomposite and its potential application as an antimicrobial agent against common waterborne pathogenic strain.The main work in this chapter was published in the Journal of Nanotechnology by Hindawi.

Ayinde W.B., Gitari W.M., Munkombwe M., Amidou S., 2018. **Biosynthesis of Ultrasonically Modified Ag-MgO Nanocomposite and Its Potential for Antimicrobial Activit**y. *J Nanotechnol* 2018. https://doi.org/10.1155/2018/9537454

Biosynthesis of ultrasonically modified Ag-MgO nanocomposite and its potential for antimicrobial activity

Ayinde B. Wasiu[a*]; Gitari W. Mugera[a]; Munkombwe Muchindu[b] and Samie Amidou[c]

[a]Environmental Remediation and Water Pollution Chemistry Group (ERWPCG), Department of Ecology and Resource Management, School of Environmental Sciences. University of Venda, Private Bag X5050, Thohoyandou, 0950, Limpopo Province, South Africa. Emails: twasiu33@gmail.com (W.B. Ayinde); mugera.gitari@univen.ac.za (W.M. Gitari)

[b]Mintek, South Africa, Advanced Materials Division (Nanotechnology Innovation Centre). MunkombweM@mintek.co.za

[c]Molecular Parasitology and Opportunistic Infections Program, Department of Microbiology, School of Mathematical and Natural Sciences. University of Venda. Email: samie.amidou@univen.ac.za

Correspondence should be addressed to Ayinde B. Wasiu; twasiu33@gmail.com

Abstract

This study reports a green synthesis route for a bi-layered Ag-MgO nanocomposite using aqueous peel extract of *Citrus paradisi* (grapefruit red) under an accelerated uniform heating technique and its antibacterial potency against *Escherichia coli*. Surface modifications and composition of the nanocomposite were examined using a UV-visible spectrophotometer, Transmission Electron Microscopy (TEM), X-ray diffraction (XRD), Fourier Transform Infrared (FTIR) spectroscopy and Scanning Electron Microscopy (SEM) equipped with an Energy Dispersive X-ray (EDX) analyzer. The efficiencies of the as-synthesized Ag-MgO nanocomposite against *Escherichia coli* were examined. The synthesized Ag-MgO nanocomposite showed characteristic synergetic bands at 290 nm for MgO nanoparticle and at around 440 nm for Ag nanoparticle which blue-shifted to 380 nm in the composite. A spherically dispersed nanocomposite with cubical crystal lattice network with a diameter of about 20–100 nm comprising Ag nanoparticle embedded within MgO nanoparticles was obtained. The nanocomposite produced stronger antibacterial activity against *Escherichia coli* as compared to MgO nanoparticle, indicating a higher interaction between Ag and MgO ion. The nanocomposite was successfully synthesized via an efficient modified method by bio-reductive agents with an improved synergistic antibacterial property towards water purification.

Keywords: Green synthesis; *Citrus paradisi*; core-shell nanocomposite; antibacterial activity

4.1 Introduction

Waterborne epidemics associated with high fecal contamination by pathogenic microbes are a worldwide problem. The treatment of infectious water-related diseases is becoming a threat to human existence because of the increase in some high resistance to the causative microbial agent. The consequence is a potential public health threat due to an epidemic outbreak of diseases often associated with microbiological contamination resulting in increasing number of death across the globe, mostly among children [1]. Water disinfection through the use of conventional methods such as chlorination and ultraviolet (UV) irradiation is rapidly becoming a major challenge due to the formation of harmful carcinogenic disinfection byproducts (DBPs) [2-3]. The development of inorganic nanoparticles with improved physicochemical and biological properties from the biosynthesized route is on the rise due to the growing need to develop environmentally benign technologies in material synthesis against infectious organisms. Generally, with the efforts to reduce generated hazardous waste, green synthesis and chemical processes are progressively integrating with modern developments in science and industry [4]. Researchers are exploiting the introduction of eco-friendly materials towards the development of a novel improved antibacterial resistance nanomaterials against multidrug-resistant human pathogens like *Escherichia coli*. *E.coli* is one of the deadly contaminants in drinking water. The non-toxicity and environmental compatibility of biosynthesis agents, especially from various plant-derived extracts or components make them reliable biosynthesis agents for metal and metal oxides nanoparticle synthesis [5-7].

Among the metallic and metal oxides nanoparticles, Silver (Ag) and Magnesium Oxide (MgO) nanoparticles have been extensively reported to possess broad-spectrum antibacterial activities [8-11]. Silver nanoparticles are undoubtedly the most widely used inorganic nanoparticles with tremendous applications in the field of highly sensitive biomolecular detection and antibacterial activities [12-14]. MgO nanoparticles, on the other hand, have recently received greater attention because of its vast applications in biomedical, catalysis and as absorbents [15-17]. However, based on the antibacterial properties of MgO nanoparticles having less potent bactericidal effect in comparison to silver-based antibacterial agents; efforts are now being channeled into the development of composite materials to exert strong synergistic antibacterial activity against infectious pathogens through chemical methods [9; 18-19]. However, the use of such chemicals in nano-synthesized biomedical materials has been a major concern due to their high cost, toxic nature, production of non-ecofriendly byproducts and nonbiodegradable stabilizing agents posing a danger to the environment and human beings [20-22].

To address this shortcoming, successive biosynthetic approaches using plant extracts have been explored and reported [23, 24]. The plant-based approaches have many advantages over chemical methods. According to previous investigations, the polyol components and the water-soluble heterocyclic components in these plants play a significant role in the reduction of metallic ions. They have proven to be effective capping and stabilizing agents for the nanoparticles with widespread technological and medicinal applications [25-26]. Silver and magnesium oxide nanoparticles have been synthesized using various plant extracts. The use of different biodiversity

plants extract has been extensively reported and reviewed for silver nanoparticles [8]. Furthermore, MgO nanoparticles have been successfully synthesized through different plant species extract including *Swertia chirayaita* leaf extract [16], *Clitoria ternatea* [28], and *Emblica officinalis* fruit extracts [29].

The peel of some fruits contains considerable amounts of minerals and vitamins, especially in citrus fruits. Previous studies have shown the presence of higher contents of phenolic, flavonoids as well as other valuable secondary plant metabolites and essential oils in fruit peel than another segment of citrus [30-32]. These metabolites are reported to account for various bioactivities including antibacterial and antioxidant properties. [33, 34]. In addition to the eco-friendly application of these components in synthesizing nanoparticles, efforts are now focusing on identifying different novel energy transfer assisted methods such as microwave [35] and ultrasound [36] capable of providing efficient uniform heating distribution in the formation of stable and sustainable biomedical nanocomposite materials with improved physicochemical properties.

In this present study, *Citrus paradisi* (Grapefruit red) peel extract was used via an efficient heating medium towards its bio-reducing, stabilization and capping ability in the formation of Ag-MgO nanocomposites. A detailed formation, characterization and *E. Coli* inactivation of the Ag-MgO nanocomposite was evaluated and reported. The novelty of this work is based on the fact that to the best our knowledge, the use of aqueous *C. paradisi* peel extracts in biosynthesizing Ag-MgO and testing of its antibacterial activity have not been reported.

4.2 Materials and Methods

All chemicals were of analytical reagent grade. $Mg(NO_3)_2.6H_2O$, $AgNO_3$, NaOH and other chemicals used were purchased from Rochelle chemicals, South Africa and used directly without further purification. Deionized water from a Millipore water (18.2 MΩ/cm) was used for the preparation and dilution of standards throughout the experiment.

4.2.1 Preparation of *Citrus paradisi* peel extracts

The fruit peels of *Citrus paradisi* (Grapefruit red) were removed, cleaned thoroughly using ultrapure (18.2 MΩ/cm) water to remove any dust particles adhering to the surface and cut into small pieces. 30g of the peel was added to 100 mL of Ultrapure water and boiled for 20 minutes at 70 °C. The extract was cooled and filtered through Whatman No.1 filter paper and stored at 4 °C for further use.

4.2.2 Microwave-assisted synthesis of Silver Nanoparticles using *Citrus paradisi* Peel Extract

Biosynthesized Silver nanoparticles (AgNps) were first obtained via microwave-assisted sol-gel method. In a typical experiment, 40 mL of the filtrate of the citrus peel was added to 60 mL of 1mM silver nitrate ($AgNO_3$) in 250 mL Erlenmeyer flasks at the ratio (2:3 v/v) for the reduction of Ag^+ to Ag^0. The mixture was then placed on a turntable domestic microwave oven (Russell

Hobbs 20L (RHEM 21L)) operating at a power of 700W and frequency 2450 MHz at a different time interval of (30, 60, 90, 120 and 150) seconds for complete bio-reduction. The formation of Silver nanoparticles (AgNps) was monitored using UV-vis. Spectrophotometer over the wavelength range (220 – 600 nm). Time-resolved absorption spectra of the UV–vis spectroscopy was used in monitoring the periodic bioprocess growth kinetics of AgNps through color variation. The synthesized nanoparticle was used for subsequent experiments.

4.2.3 Synthesis of Ag-MgO Nanocomposite

Ag-MgO nanoparticles were synthesized by seed growth via bio-reduction route through precipitation method at room temperature using a natural mild reducing agent (aqueous *Citrus paradisi* peel extracts) in the presence of the metallic precursors. (0.1M) (Mg $(NO_3)_2.6H_2O$) and 1×10^{-3} M $AgNO_3$ were used as the precursors of MgO and Ag respectively.

In a typical experimental procedure, Ag-MgO composite was obtained from an already optimized microwave-assisted aqueous mixture of *C. paradisi* peel extracts/1 mM $AgNO_3$ (2:3 v/v %). 80 ml of this solution was mixed with 20 mL (0.1M) (Mg $(NO_3)_2.6H_2O$) under continuous stirring (2 h) at room temperature with 2 mL of 0.1M NaOH solution added dropwise until complete precipitation was achieved. The composite solution was thereafter subjected to ultrasonic irradiation controlled at 100% amplitude (0.5 cycles) for 30 min. The product obtained was centrifuged (4500 rpm) for 30 min, filtered and freeze-dried.

4.2.4. Physicochemical and Mineralogical Characterization of Synthesized Nanocomposite

The synthesized Ag and Ag-MgO nanomaterials absorption range were monitored using UV-Visible Spectrophotometers (SPECTROstar Nano/ BMG LABTECH). Surface morphology of the nanoparticles was characterized using SEM with an FEI Nova NanoSEM 230 with the field emission gun equipped with an Oxford Xmax SDD detector operating at an accelerating voltage of 20Kv for the EDS detector (Oxford X-Max with INCA software). Bruker: ALPHA FT-IR Spectrophotometer was used to obtain the FTIR spectra (4000 - 400 cm^{-1}). The determination of the crystalline phases present in the materials was identified by X-ray diffraction (X'Pert Pro, Cu-K radiation, wavelength 1.54443Å). Transmission electron microscopy (TEM) image was taken using an FEI Tecnai20 equipped with a LaB6 emitter, operating at 200 kV and fitted with a Gatan Tridiem GIF with a 2kX2k CCD camera. Images were collected using the Digital Micrograph suite of programs in relation to size and shape.

4.2.5 Antibacterial Evaluation of the Crude Extract and Nanoparticles

The bacterial resistance of the biosynthesized Ag-MgO nanocomposite and MgO was determined from the observed zone of inhibition (mm) using the standard Agar-Well disc diffusion methods (Kirby Bauer disk diffusion test) and Microdilution assay. The indicator strain used is Escherichia *coli (ATCC 35218).* Bacterial suspensions were prepared with the turbidity of 0.5 McFarland. 50 µL (1 mg/mL) of MgO and Ag-MgO solution was impregnated on a cellulose nitrate sterile filter paper (pore size 0.45µm) and allowed to dry at room temperature for 3hr and placed on the Macconkey nutrient agar plates already inoculated with the bacterial cell suspension. The plates were incubated

at 37°C for 24 h and the diameter of the zone of growth inhibition around the sample was measured in millimeter (mm) and compared. The measured zones of inhibition were used to determine the antibacterial activities of the nanocomposite. Minimum inhibitory concentration (MIC) of biosynthesized Ag-MgO was also determined using the microtiter broth-dilution method as described by Samie et al. [37].

4.2.6 Release of silver and magnesium ions

To determine the release of silver and magnesium ions in solution, 1 mg/ml of the biosynthesized Ag-MgO was left to stand at room temperature for 3 h. At different time intervals, the suspension was collected and filtered through a membrane filter (pore size 0.45 μm (47 mm)). The concentrations of Ag-Mg ions in the filtrate (20 μL) were measured on a PinAAcle 900T Atomic Absorption Spectrometers (AAS, PerkinElmer Inc).

4.3 Results and Discussion

4.3.1 Physicochemical and mineralogical characterization of Ag-MgO-nanocomposite

4.3.1.1 UV-Visible analysis

Figures 4.1 and 4.2 show the UV–visible absorbance spectra for the Ag nanoparticle and Ag-MgO nanocomposite. The successful bio-reduction formation of AgNps by aqueous extract of *C. paradisi* peel extracts at mixing ratio 2:3 by volume at a different time interval ranging between 0-150 secs under microwave irradiation is indicated by a change in the color of the reaction solution from light yellow to dark brown (Fig. 4.1). AgNps were observed at intervals of (0–150 secs) with a characteristic surface plasmon vibrations band ranging between 410 - 440 nm appearing at approximately 30 secs of the reaction nucleation and onset of growth. The absorption peak intensity gradually increases with the increase of irradiation time with some overlapping plasmon bands with the formation of more AgNps evidently the same sizes which may be due to the stabilizing effect of the *C. paradisi* peel extract biomolecule. The intensity of the peaks indicated that *C. paradisi* peel extracts enhanced the bio-reduction process of Ag^{+} with the continual formation of AgNps up to the 150 secs with little variation in the absorption maxima. In general, the morphology of the nanoparticles is greatly influenced by the surface plasmon resonance, due to the mutual vibration of electrons of metal nanoparticles in resonance with lightwave serving as the basis for measuring adsorption of material onto the surface of metal nanoparticles [38, 39]. Furthermore, the use of microwave is vital in the development of this nanoparticle because it is eco-friendly in nature, provides rapid and even heating of the reaction medium, thus offering uniform nucleation and growth conditions for nanoparticles within the short reaction time unlike the traditional external heating methods [40].

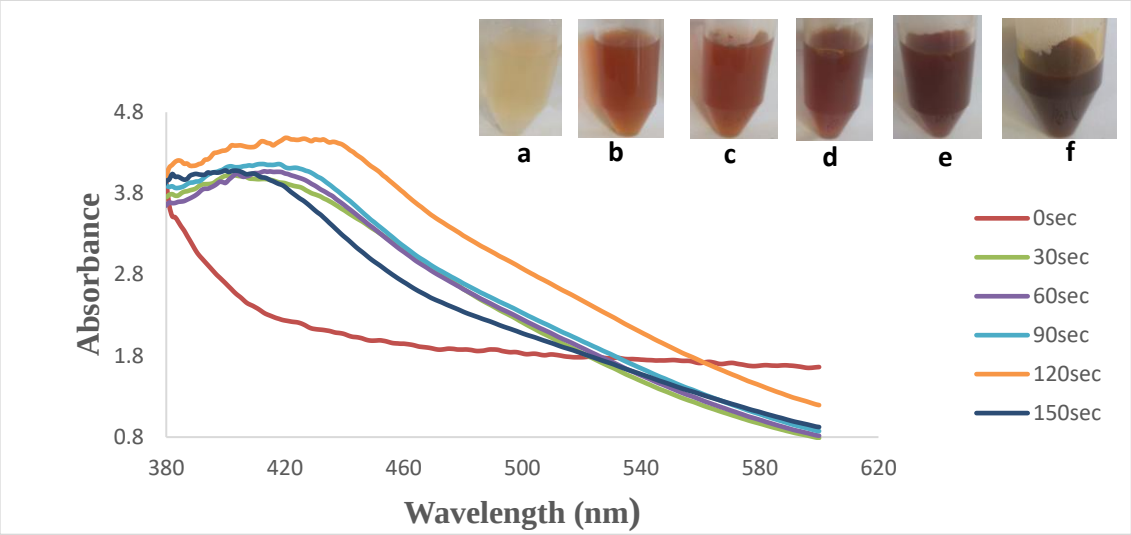

Fig. 4.1. UV–Visible spectra and photographic representation of silver nanoparticle biosynthesized by using aqueous *C. paradisi* peel extract at mixing ratio 2:3 at different time intervals.

Fig. 4.2 depicts an absorption spectrum of the synthesized biogenic Ag-MgO nanocomposite. As shown in the spectrum, two different distinct peaks were observed. A prominent intense band is observed in the low UV region at 290 nm typical of MgO together with a broad band at 378nm associated with AgNPs. It is observed that the incorporation of MgO onto the Ag layer resulted in a blue shift in the peak of AgNps from 440 nm to 378nm. This shifting is attributed to its particle size, which depends on nucleation and growth mechanism based on the excitation of plasmon resonance or inter-band transition, particularly on the size effect [13]. This clearly indicates the reduction in the particle size resulting from the optical property of biomolecular-capped Ag-MgO nanocomposite. Furthermore, the sizes of the composites were affected upon ultrasound exposure due to the cavitational collapse phenomenon resulting in an interparticle collision, thus, affecting the physicochemical properties of the composite in relation to the incident frequency of the sonicator [41, 42]. It can be established that the availability and impacts of the phytochemicals in *C. paradisi* peel extracts were responsible for the rate of bio-reduction leading to the formation of the composites.

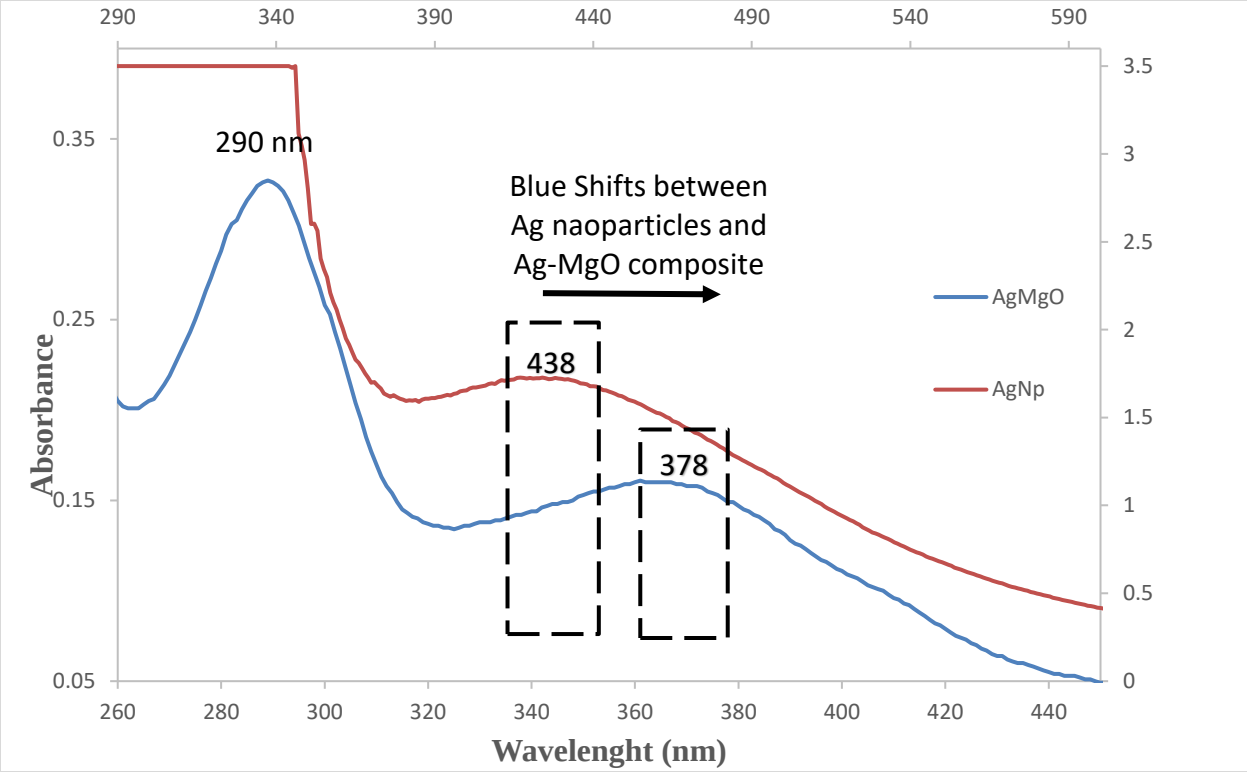

Fig. 4.2. UV–Visible spectra of biomolecular capped Ag-MgO nanocomposite.

4.3.1.2 FTIR analysis

The functional groups of the various metabolites present in the *C. paradisi* peel extract responsible for the bio-reduction, capping and stabilizing the Ag-MgO nanocomposite were identified between the 4000 and 500 cm^{-1} of the FTIR region. Fig. 4.3 shows the comparative FTIR spectra of as-synthesized Ag (CPAgNp) and Ag-MgO (CPAgMgO) from aqueous *C. paradisi* peel extract. In the CPAgNps spectrum, a strong band centred at around 3282 cm^{-1} resulting from the stretching vibrations of the hydroxyl (–OH), N–H stretch of various metabolites present in the peel extract in form of an alcohol, N–H stretch of 1° and 2° amines or amides, carboxylic acid, ester and ether [39]. These peaks shifted to a higher and broader frequency range of 3440-3200 cm^{-1} in intensity on binding with the MgO in CPAgMgO nanocomposite. The sharp peaks observed at 2915 cm^{-1} and 2849 cm^{-1} in CPAgNps which disappeared in CPAgMgO spectrum could be assigned to the symmetric and asymmetric C–H stretching vibrations of methyl, methylene, and methoxy groups [43, 44]. The presence of C=O is found in both spectrums at 1734 cm^{-1} and 1625 cm^{-1} for CPAgNps which shifted to 1626 cm^{-1} in the composite. This may be attributed to the presence of carboxylate ion and an amide group. In both spectra, different characteristic sharp peaks were also observed between 1538 and 1377 cm^{-1} which may be assigned to the -C=C in the aromatic rings, asymmetric stretching (C-N) mode in addition to the bending vibrations of the methyl and methylene groups of fatty acids. The C-O-C, C-C and carboxylic group (C–O) stretching vibrations were identified at 1238, 1156 and 1032 cm^{-1} band respectively. The absorption peaks in the region between 487–677 cm^{-1} are attributed to Mg–O-Mg compounds [45, 46] and from the spectrum of CPAgMgO it shows Mg-O-Mg deformation of the Mg-O absorption band at 540 cm^{-1} [47]. The

presence and interaction of the above bands in *C. paradisi* peel extracts indicate that the bioactive compounds were presumed to act as reducing, capping and stabilizing agents for the biosynthesized Ag-MgO nanocomposite.

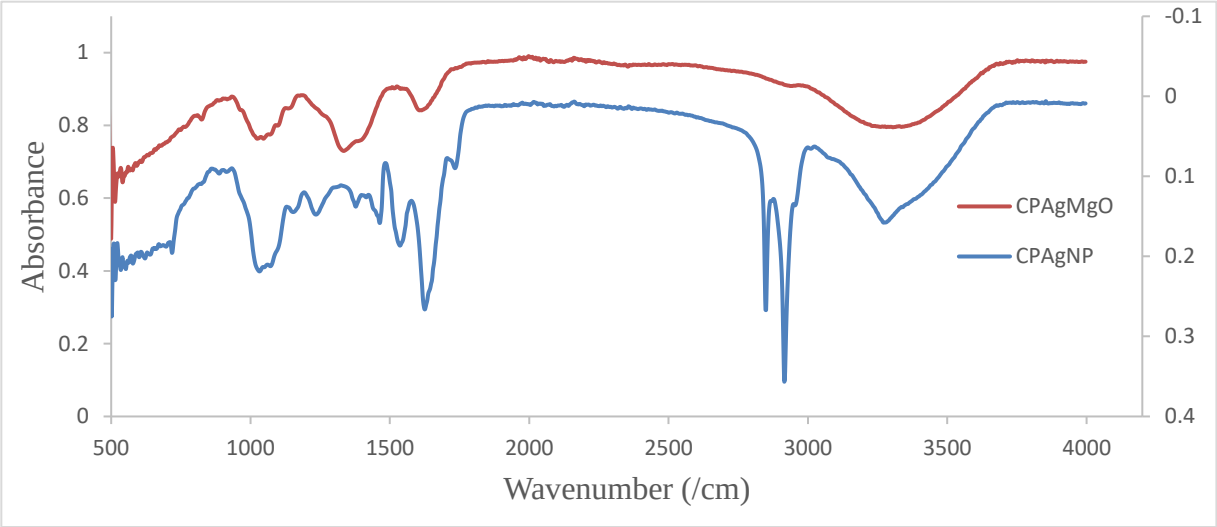

Fig. 4.3. Comparative FTIR spectra of bio-synthesized Ag and Ag-MgO nanomaterial

4.3.1.3 Surface morphology

The resulting morphological characteristics images (SEM and TEM) with associated EDAX spectra for the bio-synthesized Ag and Ag-MgO nanomaterials using the peel extract of *C. paradisi* are shown in Figures 4. 4 and 4.5. SEM micrograph of AgNps (Fig. 4.4a) shows a well spherically and uniformly dispersed nanoparticles, whereas the AgMgO composite nanoparticles image (Fig. 4.4b) displayed an agglomeration of layered clustered particles. It is poly-dispersed and crystalline in nature. The corresponding elemental compositions suggesting the formation of the AgNps and Ag-MgO nanocomposite are depicted in Fig. 4.4(b) and 4.4(d) respectively. The observed agglomeration in the composite may be due to higher amounts of organic moieties acting as the capping and stabilizing agent in the biomass of the *C. paradisi* peel extracts. In addition, the polarity and electrostatic attraction of the attached MgO nanoparticles in the composite may also result in the aggregation [48].

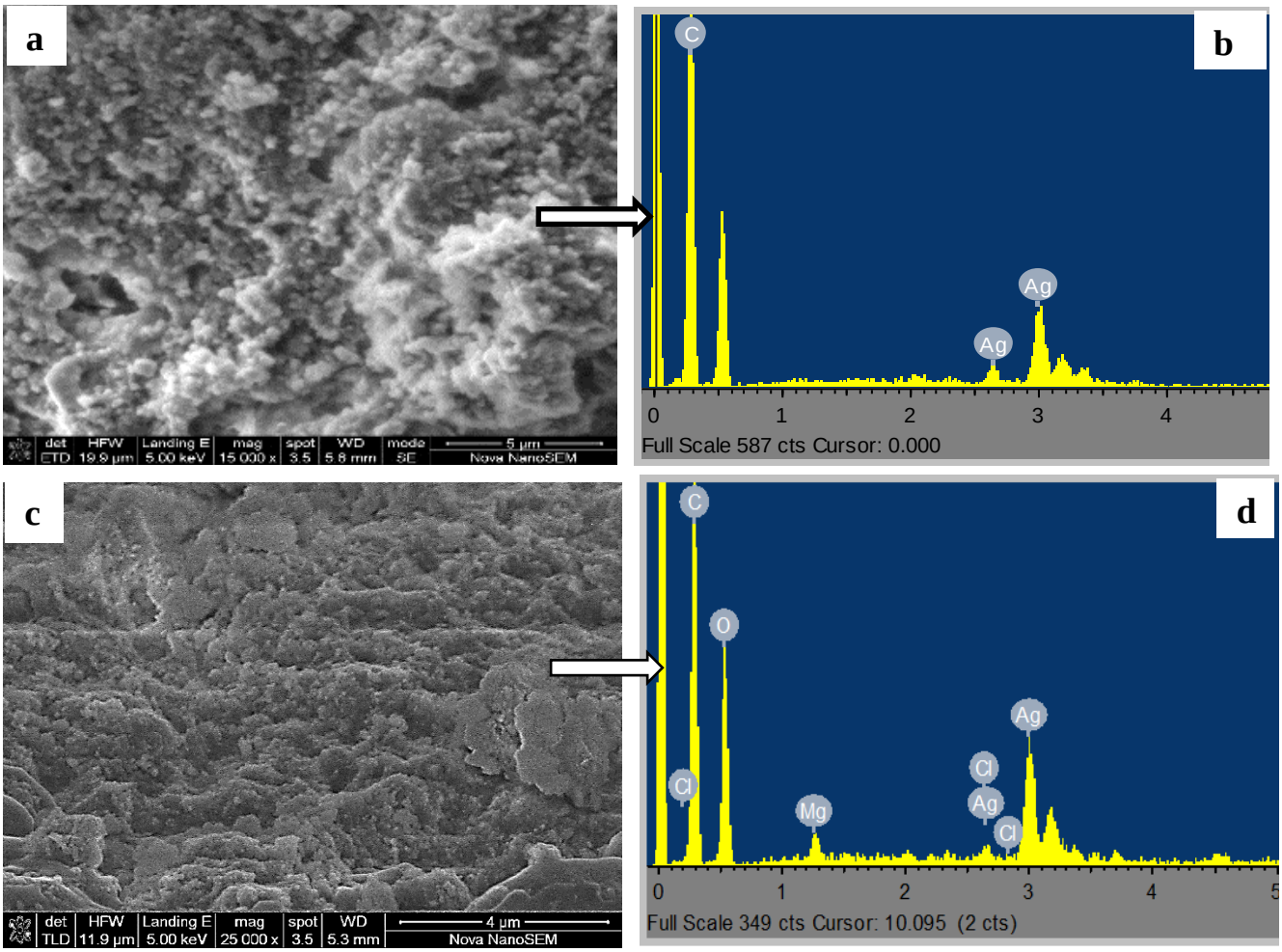

Fig. 4.4. SEM images of biosynthesized (a) AgNps; (b) EDAX spectra of AgNps; (c) Ag-MgO nanocomposite; (d) EDAX spectra of Ag-MgO nanocomposite.

Fig. 4.5 shows the morphology, shape and particle size distribution of the biosynthesized AgNPs and Ag-MgO nanomaterial through the TEM micrograph. The TEM images (Fig. 4.5(a)-4.5(c)) of *C. paradisi* peel extract mediated synthesized AgNps and Ag-MgO composite clearly show that the particles are uniformly dispersed and mostly spherical in shape with a particle size of 14.84 nm and 11.92 nm respectively. Figures 4.5(b) and 4.5(c) revealed the stabilization and distribution of the embedded-layered core-shell interaction between the Ag and MgO in the biosynthesized composite. The spherical shaped-like appearance and the sizes are well in line with the shape of the UV-Visible plasmon resonance band established during the cavitation process at high intensities of exposure resulting in the conversion of larger particle sizes to smaller sizes. The images from the different scale bar (Fig. 4.5(b) and (c)) clearly show the embedment of the bi-lateral core-shell interaction.

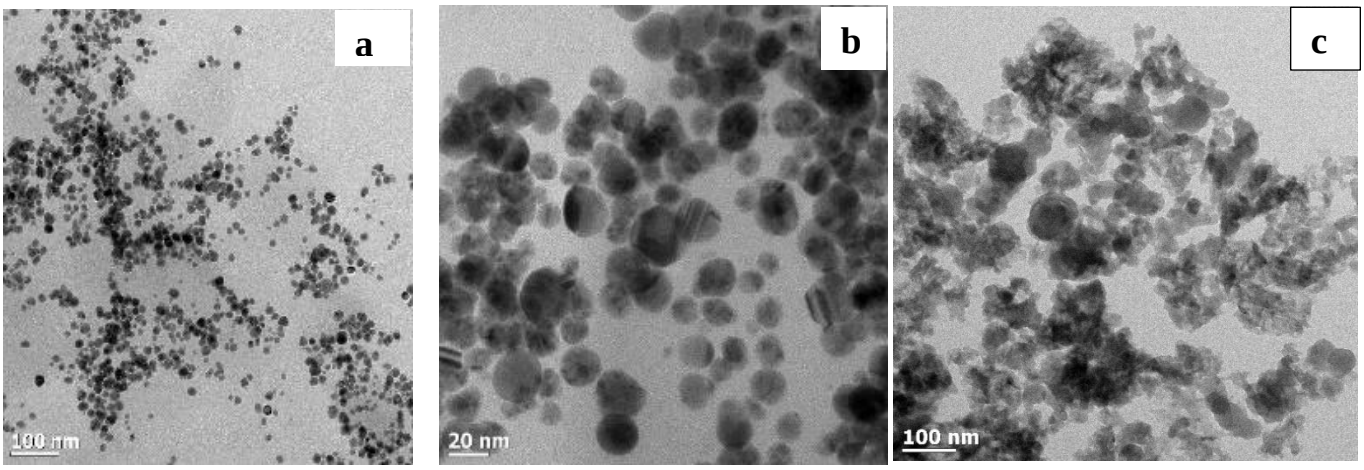

Fig. 4.5. TEM micrograph (a) AgNps; (b) Scale bar Ag-MgO nanocomposite image at 20 nm; (c) Ag-MgO at 100 nm

4.3.1.4 XRD pattern

The X-ray diffraction pattern of Ag-MgO nanocomposite, MgO and Ag nanoparticles synthesized using aqueous *C. paradisi* peel extracts over a range of 20-80° using Cu Kα radiation with its corresponding peak lists is shown in Fig. 4.6. The nanocomposite material showed major predominant consistent reflection peaks at 2θ values between the range (20-80 °) differently indexed to {111}, {200}, {202}, {311}, and {222} assigned to cubical crystal planes of Ag (reference code: 96-901-2962); together with an extended reflection labelled pattern {420} associated to cubical system phase of MgO (reference code: 96-901-3264) which shifted to a higher prominent 2θ value deposited on Ag-MgO plane lattice interaction. Silver-magnesium (0.8/0.2) planer lattice (reference code: 96-150-9046) was also detected, thus, providing confirmation of the composite nature of the material with a cubical crystal lattice network.

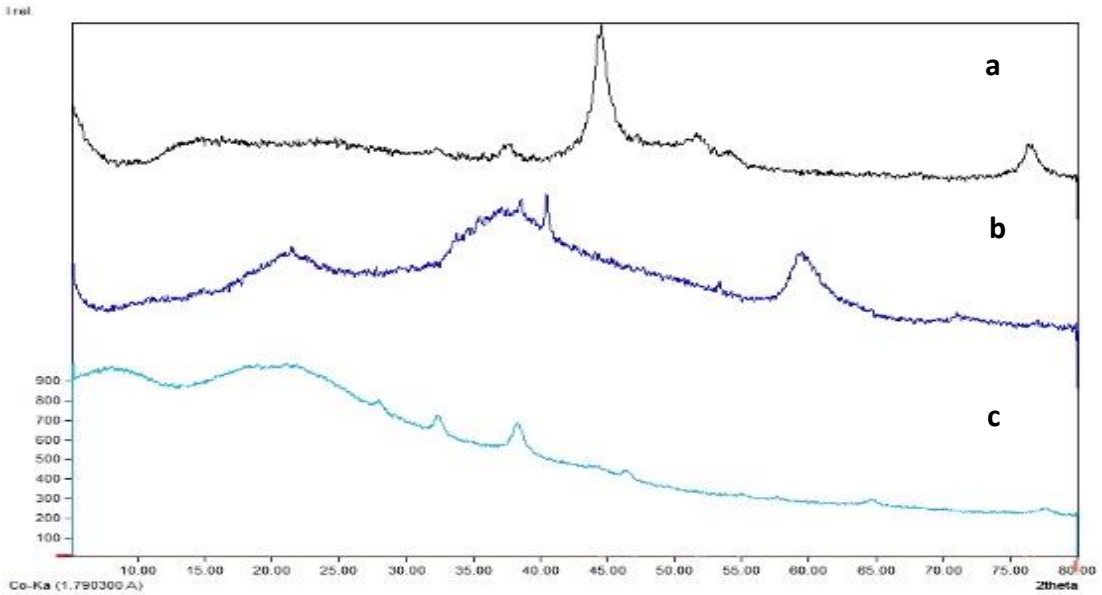

Fig. 4.6. XRD diffractogram of biosynthesized (a) Ag-MgO nanocomposite; (b) MgO; (c) Ag.

4.4 Antibacterial activity

The agar well diffusion and minimum inhibitory concentration experiments were carried out on MgO nanoparticle and Ag-MgO nanocomposite to perform a qualitative antimicrobial screening. Clear inhibition zones of varying diameter appeared against the Gram-negative bacteria *Escherichia coli* from both nanoparticles with Ag-MgO showing a wider antibacterial activity on the bacterial strain as shown in Fig. 4.7. Ag-MgO composite exhibited a higher level of antibacterial potential on *E. coli* with 22 mm zone of inhibition in comparison to the Ag and MgO nanoparticle (Table 4.1). In addition to visual readings from the agar well, the viability of *E. coli* was subjected to different concentration of the nanocomposite. As shown in Table 4.1, Minimum Inhibitory Concentration (MIC) values of 80, 40 and 20 μg/mL were recorded for MgO, Ag and Ag-MgO respectively. The lowest concentration at which the composite showed growth inhibition was recorded as the minimum inhibitory concentration. Studies have shown that the toxicity effects at different MICs values depend on the type of bacterial strains, precursor concentration, methods of preparation and the capping agents [49-51].

Although the inactivation mechanism of action of nanoparticles against microbes has been a major debate, studies have shown that bacterial inactivation appears to be driven by the toxicity of release of metal ions as well as the generation of intracellular reactive oxygen species (ROS) upon exposure of the bacterial cells to such nanomaterials amongst other factors [52-55]. Consequently, antimicrobial potency of any material will depend on the ability to disrupt the microbial cell membrane damaging its membrane properties, permeability and the collapsing of its respiration functions resulting in the cell death [29].

As illustrated in Fig. 4.8, the time-dependent releases of metal ions from *C. paradisi* peel extracts biosynthesized Ag-MgO nanocomposite was examined. Both Ag and Mg ions release were affected by time and rate of dissolution; metal ions release increases as the time progresses (Fig. 4.8). Although the release of Mg ions is in higher concentration than the Ag ion throughout the process, both concentrations at the highest time interval (Ag ion (2.7 ppb) and Mg ions (1027 ppb)) are lower than the observed minimum inhibitory concentration (MIC) (Table 4.1). These results suggested that MIC value does not correlate with the mode of action of the antimicrobial activity of Ag-MgO composite and the released of these metal ions against *Escherichia coli*. Consequently, there is a possibility that the bacterial susceptibility of this Ag-MgO nanocomposite, do not only rely on the interaction of metal ions with the cell wall structures of Gram-negative bacteria genome but are also dependent on the solution pH, cellular enzymes and biochemical events in producing intracellular reactive oxygen species (ROS) from the composite surface [15, 56, 57]. Furthermore, other factors that may be associated with microbial cell death by this nanocomposite could be attributed to its sizes, structure, and surface properties of the composite since smaller particles with larger surface area possess the affinity for interaction, giving more bactericidal effect than the larger particles [15; 58]. Moreover, the Ag-MgO nanocomposite antibacterial activity may also depend on the reducing and capping agents used in the synthesis route [59]. Therefore, the *C.*

paradisi peel extracts used in the synthesis of Ag-MgO may have contributed to the antimicrobial activity due to the different functional phytochemical species in the peel segment, which account for the bioactivity [32; 60].

Table 4.1. Antibacterial activity

Methods	MgO	Ag	Ag-MgO
Well diffusion assay (mm)	9	14	22
MIC (µg/mL)	80	40	20

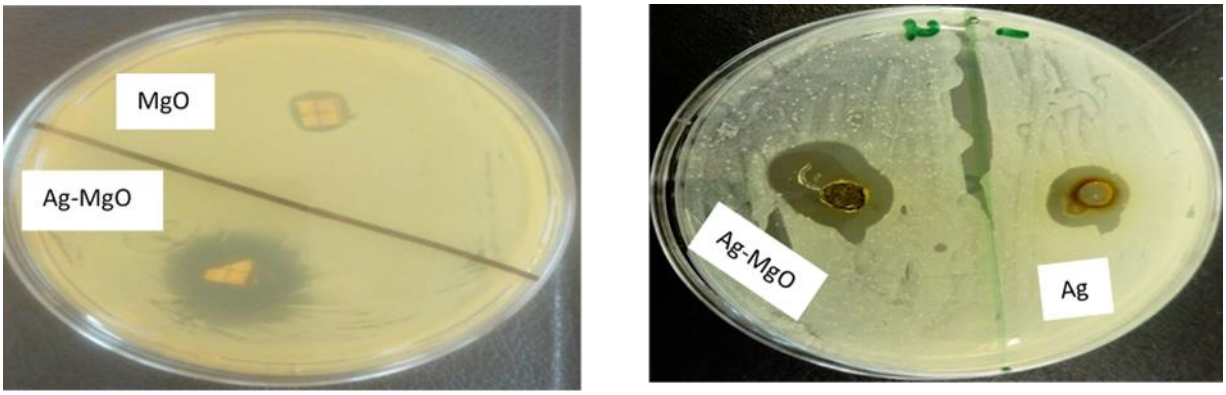

Fig. 4.7. Antibacterial activity of biosynthesized Ag, MgO and Ag-MgO against *E. Coli*

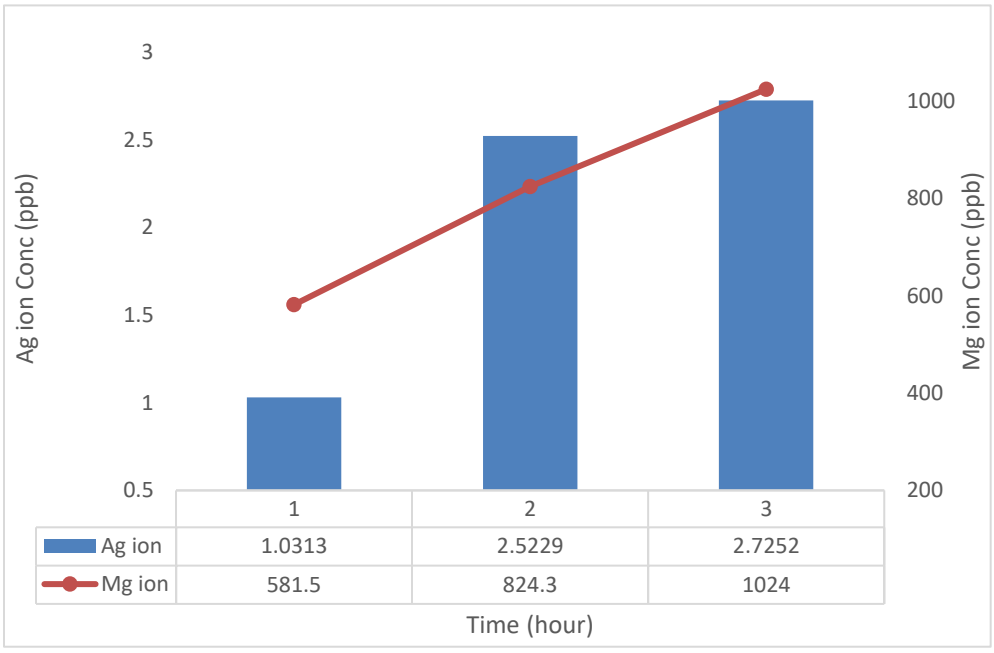

Fig. 4.8. Time-dependent metal ions release from biosynthesized Ag-MgO nanocomposite.

4.5 Conclusion

This study integrates bio-mediated microwave and ultrasonic simple and rapid synthetic methods using an aqueous peel extract of *Citrus paradisi* fruit as the reducing, capping and stabilizing agent for synthesis of Ag-MgO-nanocomposite. The presence of the phytochemicals in the extract was responsible for the rate of bio-reduction leading to the formation of the composites, thus, serving as an alternative to chemical and physical synthesis route. Surface Plasmon Resonance nucleation growth of AgNps was observed at 410 and 440 nm upon microwave exposure, which shifted to 378 nm band upon integrating with MgO shell, which displayed an absorption band at 290 nm confirming the presence of a bi-layered Ag-MgO core-shell synergy. Surface modifications and composition of the nanocomposite showed a spherical and uniformly distributed nanocomposite with an average crystalline size of 11.92 nm. The biosynthesized Ag-MgO nanocomposite exhibited an enhanced antibacterial activity than MgO nanoparticles proving as a potential material against common pathogens in water treatment.

Conflicts of interest

The authors declare no conflicts of interest.

Acknowledgment

Authors would like to acknowledge financial support from USAID-PEER Cycle 6-Award No: AID-OAA-A-11-00012; National Research Foundation Grant No: 114726; University of Venda, South Africa (RPC grant Number: SES/17/ERM/03), Prof Gitari DHET Research incentive funds and Mintek, South Africa.

References

1. WHO/UNICEF JMP (Joint Monitoring Programme for Water Supply and Sanitation). 2010. JMP Rapid Assessment on Drinking-water Quality pilot report 2010. 8-10.
2. Hijnen, W., Beerendonk, E. & Medema, G. J. 2006. Inactivation credit of UV radiation for viruses, bacteria and protozoan (oo)cysts in water: a review. Water Res. 40, 3–22.
3. Emelita Asuncion S. Dimapilis, Ching-Shan Hsu, Rose Marie O. Mendoza, Ming-Chun Lu, 2018. Zinc oxide nanoparticles for water disinfection, Sustainable Environment Research, Volume 28, Issue 2, Pages 47-56. https://doi.org/10.1016/j.serj.2017.10.001.
4. Sharma, V.K.; Yngard, R.A. and Lin, Y. (2009). Silver nanoparticles: Green synthesis and their antimicrobial activities. Adv. Colloid Interface Sci., 145, 83–96.
5. H.J. Lee, S.J. Yeo, S.H. Jeong, (2003) Antibacterial effect of nanosized silver colloidal solution on textile fabrics, J. Mater. Sci. 38 2199–2204.
6. Prathna T, Mukherjee A, Raichur AM, Mathew L, Chandrasekaran N (2010) Biomimetic synthesis of nanoparticles: science, technology & applicability. INTECH Open Access Publisher, Rijeka

7. J.L. Gardea Torresdey, G.L. Parsons, Formation and growth of Au nanoparticles inside live Alfalfa, Plant. Nano Lett. 2 (4) (2002) 397–401.
8. Muhammad Rafique, Iqra Sadaf, M. Shahid Rafique & M. Bilal Tahir. (2016). A review on green synthesis of silver nanoparticles and their applications, Artificial Cells, Nanomedicine, and Biotechnology, DOI: 10.1080/21691401.2016.1241792
9. Xiwei Zhu, Dan Wu, Wei Wang, Fatang Tan, Po Keung Wong, Xinyun Wang, Xiaolin et al. (2016). Highly effective antibacterial activity and synergistic effect of Ag-MgO nanocomposite against Escherichia coli, In Journal of Alloys and Compounds, Volume 684 , Pages 282-290, ISSN 0925-8388.
10. Tang, Zhen-Xing, & Lv, Bin-Feng. (2014). MgO nanoparticles as antibacterial agent: preparation and activity. Brazilian Journal of Chemical Engineering, 31(3), 591-601. https://dx.doi.org/10.1590/0104-6632.20140313s00002813
11. A. Monzavi, S. Eshraghi, R. Hashemian, F. Momen-Heravi (2015). In vitro and ex vivo antimicrobial efficacy of nano-MgO in the elimination of endodontic pathogens, Clin. Oral. Investig. 19 349e356.
12. Schultz, S., Smith, D.R., Mock, J.J., Schultz, D.A. (2000). Single-target molecule detection with nonbleaching multicolor optical immunolabels. Proc. Natl. Acad. Sci. 97, 996–1001
13. Krishnaraj C., E.G. Jagan, S.Rajasekar, P. Selvakumar, P.T. Kalaichelvan, N. Mohan, (2010). Synthesis of silver nanoparticles using Acalypha indica leaf extracts and its antibacterial activity against water-borne pathogens, Colloids Surf. B 76 50–56.
14. Franci G, Falanga A, Galdiero S, Palomba L, Rai M, Morelli G, Galdiero M. (2015). Silver nanoparticles as potential antibacterial agents. Molecules;20:8856–74.
15. Leung YH, Ng A, Xu X, Shen Z, Gethings LA, Wong MT, Chan C, Guo MY, Ng YH, Djuris˘ic´ AB (2014) Mechanisms of antibacterial activity of MgO: non-ROS mediated toxicity of MgO nanoparticles towards Escherichia coli. Small 10(6):1171–1183
16. Sharma G, Jasuja N.D. (2016) Phytoassisted synthesis of magnesium oxide nanoparticles by Swertia chirayaita. JTUSCI 11(3):471–477
17. Rashmi R. Devi , Iohborlang M. Umlong , Prasanta K. Raul , Bodhaditya Das , Saumen Banerjee and Lokendra Singh. (2014). Defluoridation of water using nano-magnesium oxide, Journal of Experimental Nanoscience, 9:5, 512-524, DOI: 10.1080/17458080.2012.675522
18. Cai, Y., Wu, D., Zhu, X., Wang, W., Tan, F., Chen, J., Qiao, X. and Qiu, X., 2017. Sol-gel preparation of Ag-doped MgO nanoparticles with high efficiency for bacterial inactivation. Ceramics International, 43(1), pp.1066-1072.
19. Cai, Y., Li, C., Wu, D., Wang, W., Tan, F., Wang, X., Wong, P.K. and Qiao, X., 2017. Highly active MgO nanoparticles for simultaneous bacterial inactivation and heavy metal removal from aqueous solution. Chemical Engineering Journal, 312, pp.158-166.
20. Kharissova O.V., Dias H.R., Kharisov B.I., Pe´rez BO, Pe´rez V.M.J. (2013) The greener synthesis of nanoparticles. Trends Biotechnol 31(4):240–248

21. G. Singhal, R. Bhavesh, K. Kasariya, A. Ranjan, Sharma. (2011). Biosynthesis of silver nanoparticles using Ocimum sanctum (Tulsi) leaf extract and screening its antimicrobial activity, J. Nanopart. Res. 13 2981–2988
22. Nadagouda, M.N., Hoag, G., Collins, J. and Varma, R.S. (2009) Green synthesis of Au nanostructures at room temperature using biodegradable plant surfactants. Crystal Growth and Design, 9, 4979–4983.
23. M. Shah, D. Fawcett, S. Sharma, S.K. Tripathy, G.E.J. Poinern (2015). Green synthesis of metallic nanoparticles via biological entities, Materials 8 7278–7308.
24. John Sushma, N., Prathyusha, D., Swathi, G. et al. Appl Nanosci (2016) 6: 437. https://doi.org/10.1007/s13204-015-0455-1
25. Arangasamy, L.; Munusamy, V.; Afr. J. Biotech. (2008), 7, 3162.
26. Genuino, H., Huang, H., Njagi, E., Stafford, L. and Suib, S. L. (2012). A Review of Green Synthesis of Nanophase Inorganic Materials for Green Chemistry Applications. Handbook of Green Chemistry. 8:8:217–244Dare, E.O., Oseghale, C.O., Labulo, A.H. et al. J Nanostruct Chem (2015) 5: 85. https://doi.org/10.1007/s40097-014-0139-5
27. E. O. Dare, C. O. Oseghale, A. H. Labulo et al., "Green synthesis and growth kinetics of nanosilver under biodiversified plant extracts influence," Journal of Nanostructure in Chemistry, vol. 5, no. 1, pp. 85–94, 2015.
28. John S N and Prathyusha D 2016 Facile approach to synthesize magnesium oxide NPs by using Clitoria ternatea-characterization and in vitro antioxidant studies Appl. Nanosci. 6, 895
29. Ramanujam, Kalimuthan & Sundrarajan, Mahalingam. (2014). Antibacterial effects of biosynthesized MgO nanoparticles using ethanolic fruit extract of Emblica officinalis. Journal of Photochemistry and Photobiology B: Biology. 141. 10.1016/j.jphotobiol.2014.09.011.
30. Yusof, S., Mohd Ghazali, H., & Swee King, G. (1990). Naringin content in local citrus fruits. Food Chemistry, 37, 113–121.
31. Andrea V, Nadia N, Teresa RM and Andrea A: Analysis of some Italian lemon liquors (*Limoncello*). *Journal of Agricultural Food Chemistry* 2003; 51(17): 4978-4983.
32. Gorinstein, S., Martın-Belloso, O., Park, Y. S., Haruenkit, R., Lojek, A., Ciz, M., et al. (2001). Comparison of some biochemical characteristics of different citrus fruits. Food Chemistry, 74, 309–315.
33. Dillard, C. J., & German, J. B. (2000). Phytochemicals: nutraceuticals and human health. Journal of the Science of Food and Agriculture, 80, 1744–1756
34. Jayaprakasha GK., Girennavar B and Patil BS: Radical scavenging activities of RioRed grapefruits and Sour orange fruit extracts in different *in vitro* model systems. *Journal of Bioresource Technology* 2008; 99 (10): 4484-4494.
35. S. Horikoshi, N. Serpone (Eds.), Microwaves in Nanoparticle Synthesis–Fundamentals and Applications, Wiley-VCH Verlag GmbH, Weinheim, Germany (2013)

36. Babu S.G., Neppolian B., Ashokkumar M. (2015) Ultrasound-Assisted Synthesis of Nanoparticles for Energy and Environmental Applications. In: Ashokkumar M. (eds) Handbook of Ultrasonics and Sonochemistry. Springer, Singapore
37. Samie A, Obi C. L., Bessong P. O., Namrita L. (2005). Activity profiles of fourteen selected medicinal plants from Rural Venda communities in South Africa against fifteen clinical bacterial species. Afri. J. Biotech. 4 (12):1443-1451
38. Elemike Elias Emeka, Oseghale Charles Ojiefoh, Chuku Aleruchi, Labulo Ayomide Hassan, Owoseni Mojisola Christiana, Mfon Rebecca et al. (2014) Evaluation of antibacterial activities of silver nanoparticles green-synthesized using pineapple leaf (Ananas comosus), Micron, Volume 57, Pages 1-5, ISSN 0968-4328. https://doi.org/10.1016/j.micron.2013.09.003.
39. Anandalakshmi, K., Venugobal, J. & Ramasamy, V. Appl Nanosci (2016) 6: 399. https://doi.org/10.1007/s13204-015-0449-z
40. L.-Y. Meng et al. The progress of microwave-assisted hydrothermal method in the synthesis of functional nanomaterials Materials Today Chemistry 1-2 (2016) 63-83
41. Santos, H.M., Lodeiro C., J.L. Capello-Martinez, the Power of Ultrasound, in: J.L. Capello-Martinez (Eds.), Ultrasound in Chemistry: Analytical Applications, 2009. Wiley - Vch Verlag GmbH & Co. KGaA, Weinheim, pp. 1–15.
42. Sawant S.S., A.C. Anil, V. Krishnamurthy, C. Gaonkar, J. Kolwalkar, L. Khandeparker, D. Desai, A.V. Mahulkar, V.V. Ranade, A.B. Pandit, 2008. Effect of hydrodynamic cavitation on zooplankton: a tool for disinfection, Biochem. Eng. J. 42 320–328.
43. Li J, Barron AR (2010) Fourier transform infrared spectroscopy of metal ligand complexes. OpenStax-CNX module: m3 4660
44. B. Kumar, K. Smita, L. Cumbal, and A. Debut, "Biogenic synthesis of iron oxide nanoparticles for 2-arylbenzimidazole fabrication," Journal of Saudi Chemical Society, vol. 18, no. 4, pp. 364–369, 2014.
45. Gowdhami Marquis, Balagurunathan Ramasamy, Sarkar Banwarilal, Ayyasamy Pudukadu Munusamy, (2016). Evaluation of antibacterial activity of plant mediated CaO nanoparticles using Cissus quadrangularis extract, Journal of Photochemistry and Photobiology B: Biology, Volume 155, Pages 28-33, ISSN 1011-1344, https://doi.org/10.1016/j.jphotobiol.2015.12.013.
46. Wang, W., Qiao, X. and Chen, J., 2008. The role of acetic acid in magnesium oxide preparation via chemical precipitation. Journal of the American Ceramic Society, 91(5), pp.1697-1699.
47. Balamurugan S, Ashna L, Parthiban P (2014) Synthesis of nanocrystalline MgO particles by combustion followed by annealing method using hexamine as a fuel. J Nano Tech 6:1–6. doi:10. 1155/2014/841803
48. T. Ponnaiah, A. Ramasamy, Synthesis of hierarchical structured MgO by sol-gel method, J. Nano. Bull. 2 (2) (2013). 130-106.

49. Velazquez-Meza, M.E., Hernández-Salgado, M. and Sánchez-Alemán, M.A., 2015. Evaluation of the antimicrobial activity of a super oxidized solution in clinical isolates. Microbial Drug Resistance, 21(4), pp.367-372.
50. Mittal, J., Jain, R. and Sharma, M.M., 2017. Phytofabrication of silver nanoparticles using aqueous leaf extract of Xanthium strumerium L. and their bactericidal efficacy. Advances in Natural Sciences: Nanoscience and Nanotechnology, 8(2), p.025011.
51. Gong, P., Li, H., He, X., Wang, K., Hu, J., Tan, W., Zhang, S. and Yang, X., 2007. Preparation and antibacterial activity of Fe3O4@ Ag nanoparticles. Nanotechnology, 18(28), p.285604
52. Park, H.J., Kim, J.Y., Kim, J., Lee, J.H., Hahn, J.S., Gu, M.B. and Yoon, J., 2009. Silver-ion-mediated reactive oxygen species generation affecting bactericidal activity. Water research, 43(4), pp.1027-1032.
53. Zhang, W., Yao, Y., Sullivan, N. and Chen, Y., 2011. Modeling the primary size effects of citrate-coated silver nanoparticles on their ion release kinetics. Environmental science & technology, 45(10), pp.4422-4428.
54. Horie, M., Fujita, K., Kato, H., Endoh, S., Nishio, K., Komaba, L.K., Nakamura, A., Miyauchi, A., Kinugasa, S., Hagihara, Y. and Niki, E., 2012. Association of the physical and chemical properties and the cytotoxicity of metal oxide nanoparticles: metal ion release, adsorption ability and specific surface area. Metallomics, 4(4), pp.350-360.
55. Krishnamoorthy, K., Moon, J.Y., Hyun, H.B., Cho, S.K. and Kim, S.J., 2012. Mechanistic investigation on the toxicity of MgO nanoparticles toward cancer cells. Journal of materials chemistry, 22(47), pp.24610-24617.
56. N. Durán, M. Durán, M. Bispo de Jesús, A.B. Seabra, W.J. Fávaro, G. Nakazato. Nanomedicine: NBM 12 (2016) 789–799.
57. Krishnamoorthy, K., Manivannan, G., Kim, S.J. et al. (2012). J Nanopart Res 14: 1063. https://doi.org/10.1007/s11051-012-1063-6
58. Raghupathi KR, Koodali RT, Manna AC. (2011). Size-dependent bacterial growth inhibition and mechanism of antibacterial activity of zinc oxide nanoparticles. Langmuir 27:4020–4028
59. Kuppusamy, P., Yusoff, M.M., Maniam, G.P. and Govindan, N., 2016. Biosynthesis of metallic nanoparticles using plant derivatives and their new avenues in pharmacological applications–An updated report. Saudi Pharmaceutical Journal, 24(4), pp.473-484.
60. Aromal, S.A. and Philip, D., 2012. Green synthesis of gold nanoparticles using Trigonella foenum-graecum and its size-dependent catalytic activity. Spectrochimica Acta Part A: Molecular and Biomolecular Spectroscopy, 97, pp.1-5.

CHAPTER FIVE

GREEN SYNTHESIS OF Ag/MgO NANOPARTICLE MODIFIED NANOHYDROXYAPATITE AND ITS POTENTIAL FOR DEFLUORIDATION AND PATHOGEN REMOVAL IN GROUNDWATER.

Introduction

This chapter addresses the Green Synthesis of Ag/MgO nanoparticle incorporated into nanohydroxyapatite.Its potential for defluoridation and pathogen removal in groundwater was explored and discussed. The main part of this chapter was published as an article in Physics and Chemistry of the Earth Parts A/B/C journal by Elsevier.

Ayinde W.B., Gitari W.M., Munkombwe M, Amidou S., 2018. **Green synthesis of Ag/MgO nanoparticle modified nanohydroxyapatite and its potential for defluoridation and pathogen removal in groundwater.** Physics and Chemistry of the Earth Parts A/B/C, 107, pp.25-37. https://doi.org/10.1016/j.pce.2018.08.007

Green Synthesis of Ag/MgO nanoparticle modified nanohydroxyapatite and its potential for defluoridation and pathogen removal in groundwater

Ayinde W. B. [a*], Gitari W. M. [a], Munkombwe M. [b], Samie Amidou [c]

[a]Environmental Remediation and Water Pollution Chemistry Group (ERWPCG), Department of Ecology and Resource Management, University of Venda, Thohoyandou, South Africa.

[b]Mintek, South Africa, Advanced Materials Division (Nanotechnology Innovation Centre).

[c]Molecular Parasitology and Opportunistic Infections Program, Department of Microbiology, School of Mathematical and Natural Sciences. University of Venda.

Corresponding author. Tel. +27 838734688, email: twasiu33@gmail.com

Abstract

The paper presents a facile green method of synthesizing a multi-functional 3-layered Ag-MgO/nanohydroxyapatite (Ag-MgOnHaP) composite via a combined microwave and ultrasonically modified methods with emphasis on simultaneous pathogens and fluoride removal in groundwater. The reduction of Ag and MgO ions by aqueous *Citrus paradisi* peel extracts was utilized for the impregnation Ag-MgO nanoparticles on the adsorbent surface. Ag-MgOnHaP composite morphological structures were characterized by UV-Visible spectroscopy, Fourier Transform Infrared (FT-IR) spectroscopy, scanning electron microscopy (SEM), energy dispersive-X-ray spectroscopy (EDS), X-ray diffraction (XRD), and transmission electron microscopy (TEM) analysis. Batch sorption studies using the nanocomposite under different experimental parameters were investigated to determine its adsorption capacity. The antibacterial activity of the adsorbent against *Escherichia coli* and *Klebsiella pneumonia* in water was also evaluated. The results showed the successful synthesis of the core-shell Ag-MgOnHaP composite with the presence of an optical intense absorption band at 290 nm together with a blue-shifted broad band of 378 nm typical of MgO and Ag nanoparticles. Ultrasound irradiation in synthesis resulted in the improved production of spherically smaller particle sizes of 16.44 nm. The optimum adsorption capacity of 2.146 mg/g at 298 K was recorded with more than 90% fluoride removal at 0.3g dosage. Maximum adsorption was achieved at pH 6. The sorption process fitted well to the Freundlich isotherm model and follows the pseudo-second-order kinetics at room temperature. The overall results showed not only the potential ability of the nanocomposite toward fluoride removal but also recorded strong antibacterial activity against *E. coli and K. pneumonia*.

Keywords: antimicrobial activity; *Citrus paradise;* core-shell nanocomposite; defluoridation

5.1 Introduction

The international health and environmental care organizations have been confronted with challenges of water quality and scarcity in the last decades (WHO/UNICEF, 2010). Water scarcity is gradually becoming a potential threat to food security, human health, and natural ecosystems with more than 50% of the world projected to experience this water shortage by the year 2025 (Shahin and Mady, 2014). Waterborne epidemics and excessive fluoride-related diseases are a worldwide problem despite the presence of other inorganic pollutants in surface and groundwater. According to the World Health Organization reports, 844 million people lack basic drinking-water service, with about 3.4 million people, mostly children, die annually from water-related diseases, especially in developing countries (WHO/UNICEF, 2017; 2010; WHO, 2000). A study by Johri *et al*. (2014) observed that 41.5% of urban and 60% of rural households were using contaminated water in Africa. The lack of improved water sources has reduced the proportion in the population that has reliable access to safe drinking water; therefore, increasing the risk of exposure to excessive divalent cations, monovalent anions as well as microbiologically contaminated water leading to potential water-related epidemics (Ben Nasr 2013; Bain *et al*. 2011; Hunter *et al*. 2010). The essentiality of clean, potable water free of toxic chemicals and pathogens to human health cannot be over-emphasized. Consequently, overcoming these challenges in sustainable water supply and treatments represents important opportunities to enhance public health for universal and equitable access to safe and affordable drinking water (WHO/UNICEF, 2017; Hunter *et al*. 2010).

The most appropriate and widely used source of drinking water for many rural communities in Sub-Saharan Africa and other developing countries is groundwater (Gitari *et al*. 2013). However, groundwater can become unsuitable for drinking due to the high concentration of naturally occurring and human-induced chemical species as well as microbial pollution (USGC, 2016; Fuller, 2006; Snson *et al*. 1999). Fluoride is one of the major inorganic geological contaminants in groundwater resources with its concentration ranging from 0.01 to 48 mg/L globally (Cai *et al*. 2016; Mumtaz *et al*. 2015). Fluoride epidemics in drinking water have been a global problem with over 200 million people suffering from high health effects and morbidity in a number of regions (Mumtaz *et al*. 2015; Chai *et al*. 2013). The main occurrence of fluoride is as fluorapatite [$3Ca_3(PO_4)2Ca(F, Cl_2)$], cryolite (Na_3AlF_6), sellaite (MgF_2), and fluorspar (CaF_2). These fluoride-rich minerals can release fluoride ions into groundwater when the conditions of temperature, pH, anion-exchange, among others, favor their dissolution (Gosh *et al*. 2013; Mohapatra *et al*. 2009). The presence of fluoride in small quantity (about 0.7 mg/L) is beneficial in drinking water as an essential component for normal mineralization of bones and formation of dental enamel as well as in the protection of teeth against tooth decay (Loganathan, *et al*. 2013; Bell and Ludwig, 1970). However, in excess of the recommended limit of 1.5 mg/L, it can be detrimental to human health, leading to dental or crippling skeletal fluorosis (Ramesh *et al*. 2017; WHO, 2011). In addition to fluoride epidemics, the majority of acute water-related diseases are often associated with microbiological contamination. Groundwater has traditionally been the water source less susceptible to contamination by human pathogens associated with surface water and generally

perceived as being microbiologically 'pure' (Pedley and Howard, 1997). However, the high quality of groundwater as a drinking water source can easily be compromised based on the ability of the soils and other underlying geological formations with a large subsurface residence or retention time, thereby creating the frequent occurrence of microbiological contamination. (Tufenkji and Emelko 2011; UK Groundwater Forum 2011). Therefore, the control of microbiological and inorganic pollutants is of paramount importance with standard guidelines to reduce water-related deaths worldwide (WHO, 2011; Pedley and Howard, 1997).

The inefficiency of conventional water treatment methods to filter and disinfect these pathogens and remove toxic chemical species from groundwater has forced scientists and engineers to look into new sustainable and innovative technologies, which utilize simple, eco-friendly and inexpensive technology for the supply of potable water. The techniques towards such removals are based on the principle of sorption as well as chemically-cell death by disrupting the cell walls of the microbes, especially at the point of use (Dankovich *et al*. 2016). Different technologies for the defluoridation of drinking water had been reported where such methods depended on fluoride ion concentration, existing treatment processes, treatment costs, handling of residuals and versatility of the given techniques (Mohapatra *et al*. 2009; Ayoob *et al*. 2008). Such techniques include precipitation, reverse osmosis, electrodialysis, ion exchange, nanofiltration and adsorption (Dhillon *et al*. 2015; Fan *et al*, 2003). Among these various physicochemical processes, the most suitable and commonly used because of its effectiveness, energy-saving, simplicity in small water resource layout is adsorption (Bhatnagar et al. 2011; Onyango and Matsuda, 2006). Furthermore, conventional water disinfection treatments are rapidly becoming a major challenge due to the formation of harmful carcinogenic disinfection byproducts (Dimapilis *et al*. 2017; Richardson, 2003).

Several reports have shown the efficient removal of fluoride from water (Subbaiah Muthu Prabu *et al*. 2017; Loganathan 2013; Kim and der Bruggen 2010; Sundaram 2008, 2009) as well as the inactivation of various micro-organisms (Garmasheva *et al*. 2016; Muhammad *et al*. 2016; Dhillon et al. 2015; Tang et al. 2014) using different materials. However, the development of a hybrid material targeting these two pollutants for purification of water has not been fully exploited. Nanoscience and nanotechnology multifunctional materials have been found relevant in environmental applications recently as an alternative method to conventional water treatment. These nanomaterials possess a significantly novel, and an overall improved physicochemical and biological properties (Sundrarajan *et al*. 2012; Shannon *et al*. 2008). Nanotechnological influence on the use and designing of nanostructured materials with an appropriate synthetic route has increased in response to solving water-related problems. This has been the driving force for the development of new methodologies with improved removal efficiencies for several decades (Jin and Kenneth, 2010). Thus, serving as an important factor in the overall designing of water quality application of materials towards separation, water disinfection where several ionic species, the nature of the metal ion as well as microbial control can be different from case-to-case in controlling human loss (Pradeep and Anshup, 2009; Li *et al*. 2008;). Therefore, creating methods to

effectively, efficiently and economically defluoridate drinking water and pathogenic organisms for human consumption is important through the development of multifunctional adsorbents.

Hence this study focuses on the green synthesis, characterization and application of reusable Ag-MgO loaded on nanohydroxyapatite composite via a natural bio-reductive, capping and a stabilizing agent (aqueous *C. paradisi* peel extracts) for simultaneous defluoridation and pathogen removal from groundwater. Batch studies on the different adsorption parameters as it affects defluoridation capacity of the adsorbent were considered and optimized. The sorption experimental data were fitted with different isotherm and kinetic models to establish the adsorption process and their efficiencies. Ag, MgO, nanohydroxyapatite was chosen because of their successful potential applications in trapping and removal of toxic metal species and anion, defluoridation as well as the abilities of Ag and MgO nanoparticles possessing antibacterial properties (Rajeshkumar and Bharath 2017; Rashmi *et al*. 2014; Tang *et al*. 2014; Gopi *et al*. 2012; Poinern *et al*. 2011; Kousalya *et al*. 2010). The novelty of this work is centered on the fact that no study has reported the synthesis of these nanocomposites through the aid of bio-reductive, stabilizing and capping agent (aqueous *C. paradisi* peel extracts) and their application for simultaneous microbial removal and defluoridation of groundwater. Therefore, the objectives of this work were: to synthesize and evaluate physicochemical and mineralogical properties of nanohydroxyapatite embedded with Ag-MgO nanoparticles from the aqueous *Citrus paradisi* peel, to determine the maximum fluoride adsorption capacity of the nanocomposite using different influencing conditions in batch studies together with the corresponding kinetics and equilibrium studies. Furthermore, the nanocomposite was examined towards its antibacterial activity against *E. coli* and *K. pneumonia* from groundwater.

5.2 Materials and Methods

All chemicals were of analytical reagent grade. $Ca(NO_3)_2.4H_2O$, KH_2PO_4, $Mg(NO_3)_2.6H_2O$, $AgNO_3$, NaF, NaOH and other chemicals used were purchased from Rochelle chemicals, South Africa and used directly without further purification. Deionized water from a Millipore water (18.2 MΩ/cm) was used in the preparation and dilution of standards throughout the experiment.

5.2.1 Preparation of *Citrus paradisi* peel extract

The fruit peels of *Citrus paradisi* (Grapefruit red) were removed, cleaned thoroughly using ultrapure (18.2 MΩ/cm) water to remove any dust particles adhering to the surface and cut into small pieces. 30g of the peel was added to 100 mL of Ultrapure water and boiled for 20 minutes at 70 °C. The extract was cooled and filtered through Whatman No.1 filter paper and stored at 4 °C for further use.

5.2.2 Microwave-assisted synthesis of Silver Nanoparticles using *Citrus paradisi* Peel Extract

In a typical experiment, 40 mL of the filtrate of the citrus peel was added to 60 mL of 1mM silver nitrate ($AgNO_3$) in 250 mL Erlenmeyer flasks at the ratio (2:3 v/v) for the reduction of Ag^+ to Ag^0. The mixture was then placed on a turntable domestic microwave oven (Russell Hobbs 20L (RHEM

21L)) operating at a power of 700W and frequency 2450 MHz at a different time interval (30-150 secs) for the complete bio-reduction. The formation of silver nanoparticles (AgNPs) was monitored using UV-vis. Spectrophotometer (300–600 nm range). Time-resolved absorption spectra of the UV–Vis spectroscopy was used in monitoring the periodic bioprocess growth kinetics of AgNPs through color variation. The synthesized nanoparticles were used in the subsequent experiments.

5.2.3 Synthesis of Ag-MgO-nanohydroxyapatite nanocomposite

Modified functionalized nanohydroxyapatite bound to Ag-MgO nanoparticles was synthesized using a combination of procedures (Sushma *et al*, 2016; Poinern *et al*. 2011). The experimental procedure entails seed growth via bio-reduction and precipitation method at room temperature using a natural mild natural reducing agent (aqueous *C. paradisi* peel extracts) in the presence of other metallic precursors.

Briefly, a homogeneous aqueous mixture of bio-reduced Ag-MgO nanoparticles using a natural reductant agent was obtained from an optimized microwave-assisted aqueous mixture of *C. Paradisi* Peel extracts/1 mM $AgNO_3$ (2:3 v/v %) mixed with 20 mL 0.1M ($Mg(NO_3)_2.6H_2O$) under continuous stirring for 2 hr at room temperature with 2 mL 0.2M NaOH solution added dropwise until a complete precipitation was achieved. The Ag-MgO mixture thus obtained was added to 40 mL 0.32 M $Ca(NO_3)_2 \cdot 4H_2O$ and 60 mL of 0.19 M KH_2PO_4 solution (Ca/P at 1.67) under continuous stirring. Subsequently, NH_4OH (25%) was added dropwise to adjust the pH value to 9, and the solution was stirred for another 2 hr. During the mixing process; the pH value was continually checked and maintained at 9 (using NH_4OH). The composite solution was thereafter subjected to ultrasound agitation at 100% amplitude (0.5 cycles) for 1 hr. The product obtained after the sonication was filtered and dried at 40 ◦C in an oven for 24 hr before being ground into a fine powder.

5.2.4 Physicochemical and mineralogical characterization of synthesized nanocomposite

The synthesized Ag-MgO embedded on nanohydroxyapatite was initially characterized using UV-Visible Spectrophotometers (SPECTROstar Nano/ BMG LABTECH). The surface morphology of the nano-adsorbent composite was characterized using SEM with an FEI Nova NanoSEM 230 with the field emission gun equipped with an Oxford Xmax SDD detector operating at an accelerating voltage of 20Kv for the EDS detector (Oxford X-Max with INCA software). Bruker: ALPHA FT-IR Spectrophotometer was used to obtain the FTIR spectra (4000-400 cm^{-1}). The determination of the crystalline phases present in materials was identified by X-ray diffraction (X'Pert Pro, Cu-K radiation, wavelength 1.54443Å). Transmission electron microscopy (TEM) images were taken using a FEI Tecnai20 equipped with a LaB6 emitter, operating at 200 kV and fitted with a Gatan Tridiem GIF with a 2kX2k CCD camera. Images were collected using the Digital Micrograph suite of programs in relation to size and shape. F^- and pH measurements of the fluoride in the supernatants were determined using a fluoride ion-selective electrode (9609 BNWP Orion, USA) coupled to an ISE/pH/EC electrode (Thermo SCIENTIFIC-ORION VERSA STAR Advanced Electrochemistry meter fluoride ion-selective electrode) calibrated with four fluoride

standards containing TISAB III at the volume ratio of 1:10 as in the case of the samples. The pHpzc was evaluated using solid addition method as described by Gitari et al. (2017). UP400S (400W at 24 kHz power control, amplitude 20-100% ultrasonic device with ultrasonic horn H14) from Hielscher Ultrasonics was used for sonicating the reaction mixtures.

5.2.5 Batch Fluoride adsorption experiments

The capacity of Ag-MgO-nanohydroxyapatite to defluoridate groundwater was evaluated through the batch experiment. Several parameters were optimized, these included contact time, pH, adsorbent dose, initial adsorbate concentration. A 1000 mg/L standard stock solution of fluoride was prepared by dissolving 2.210 g NaF into 1000 mL of ultrapure water at ambient condition. The desired fluoride solution was prepared by appropriate dilution of the standard stock solution. Batch adsorption experiments were carried out by mixing 0.225 g of Ag-MgO-nanohydroxyapatite with 50mL of 10 mg/LF^- solution. The mixture was shaken thoroughly using a reciprocating shaker (STUART SSL2) at 250 RPM. The solution was then centrifuged at 2000 RPM for 10 minutes and filtered. The residual fluoride ion concentration was determined.

The effect of co-existing anions on the defluoridation efficiency of the adsorbent was evaluated at different anion concentration between 5 - 30 mg/L each mixed with 10 mg/L fluoride solution. The adsorption isotherm experiments were conducted by varying the initial fluoride concentrations between 2–15 mg/L. Adsorption isotherms and kinetic models were adopted and used to model adsorption data. All the experiments were conducted in duplicate, and the mean of the results computed. Equations 1 and 2 were used to determine the adsorption capacity, q (mg/g) and percentage fluoride removal of the adsorbent.

$$q = (C_0 - C_e) \times \frac{V}{w} \qquad (1)$$

Where: Co is the initial F- concentration (mg/L); Ce is the F- concentrations at equilibrium (mg/L); V is the volume of solution (L) and m mass of the adsorbent (g)

$$\% \text{ removal} = \frac{(C_0 - C_e)}{C_0} \times 100 \qquad (2)$$

Where: Co is initial fluoride ion concentration and Ce is equilibrium fluoride ion concentration.

5.2.6 Antibacterial Evaluation of the Nanocomposites

Bacterial resistance and efficacy of the synthesized Ag-MgOnHaP composite and nHaP were determined from the observed zone of inhibition (mm) using the standard Agar-Well disc diffusion methods (Kirby Bauer disk diffusion test). The culture was inoculated by the spread plate method. The indicator strains used were the clinical isolates of *Escherichia coli and Klebsiella pneumonia.* 50 µL of Ag-MgOnHaP solution was impregnated on a cellulose nitrate sterile filter paper (pore size 0.45µm) and allowed to dry at room temperature for 3hr and placed on the already prepared bacterial cell suspension evenly spread on the Macconkey nutrient agar plates (Prepared as recommended by the manufacturer) using a sterile spreader. The plates were incubated at 37°C for

24 h and the diameter of the zone of growth inhibition below and around the sample was measured and compared. The measured zones of inhibition were used to determine the efficiency of the antibacterial activities of the nanocomposite.

5.3 Results and Discussion

5.3.1 Physicochemical and mineralogical characterization of Ag-MgO-nanohydroxyapatite

5.3.1.1 UV-Visible analysis

Figure 5.1 (a) shows the microwave assisted-time dependent UV-Visible absorption spectrum of synthesized silver nanoparticles (AgNPs) using *C. paradisi* peel extracts as the bio-reductive, capping and stabilizing agent. The first significant evidence in the formation of AgNPs is obtained from the color variation of the reaction mixture. A color variation from light yellow to dark brown was observed after 30 secs of microwave irradiation of the reaction nucleation and onset growth across 150 secs. The final color deepened with an increase in time. This may due to the excitation of localized surface plasmon resonance typical of all noble metals due to changes in their electronic energy levels with a direct impact on its size and polydispersity. (He *et al*. 2017; Veerasamy *et al*. 2011). The UV-Visible spectrum showed a characteristic surface plasma absorption band maximum of 440 nm, indicating the formation of silver nanoparticles from *C. paradisi* peel extracts (Rayhaneh *et al*. 2015). Although biosynthesis of nanoparticles can be achieved under ambient conditions, such a process requires considerable time, thus, the microwave-assisted methods serve as an alternative route in achieving the synthesized AgNps because it provides shorter reaction time, lower energy consumption, and better yields of the nanoparticle (Joseph and Mathew, 2013).

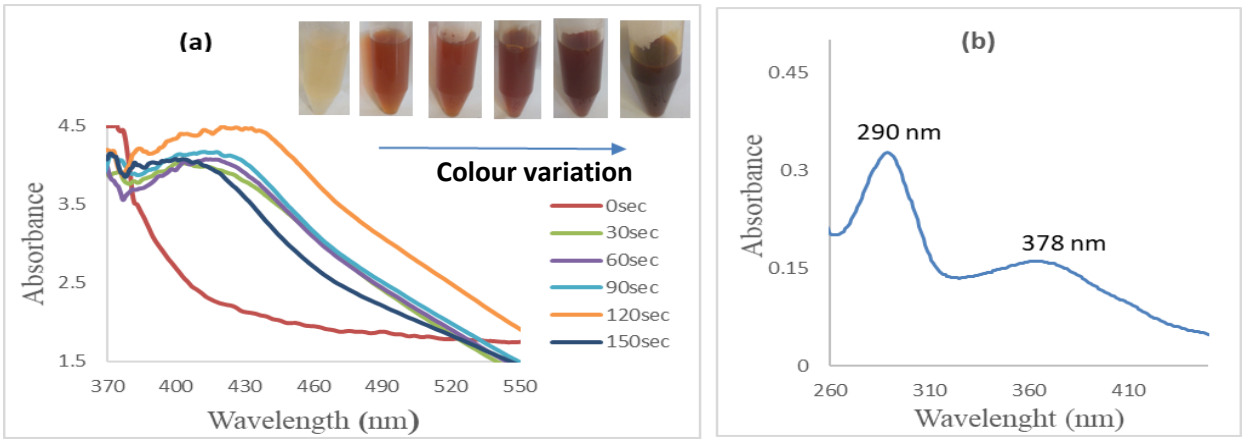

Fig. 5.1. UV-Visible absorbance spectra of synthesized (a) AgNps (b) Ag-MgO nanocomposite by *C. paradisi* peel extract.

Fig. 5.1 (b) depicts an absorption spectrum of the synthesized biogenic Ag-MgO loaded onto nanohydroxyapatite composite. As shown in the spectrum, two different distinct peaks were observed. A prominent intense band absorbed at 290 nm typical of MgO together with a broad band at 378 nm associated with AgNPs. It is observed that the incorporation of MgO onto the Ag

layer resulted in the blue shift in the peak from 440 nm (Fig. 5.1 (a)) to 378 nm. This shifting is attributed to its particle size, which depends on nucleation and growth mechanism based on the excitation of plasmon resonance or inter-band transition, particularly on the size effect (Krishnaraj *et al*. 2010). This clearly indicates the reduction in the particle size resulting from the optical property of biomolecular-capped silver nanoparticles. It can be established that the availability and interaction of the phytochemical components in *C. paradisi* peel extracts was responsible for the rate of bio-reduction leading towards the formation of the Ag-MgO composites (Kuppusamy *et al*. 2016; Aromal and Philip, 2012).

5.3.1.2 FTIR spectroscopy

Fig. 5.2 shows the FTIR spectrum of synthesized Ag-MgO particles loaded on nanohydroxyapatite composite after 1hr of ultrasound irradiation. The peaks observed at 3290 cm^{-1}; between 2000 - 2380 cm^{-1} and 1638-1645 cm^{-1} indicates the existence of –OH stretching vibration, C=N and alkyne group as well as vibrations bond of an amine I group, phenolic group, and H_2O molecules respectively (Sathiya and Akilandeswari, 2014; Kalsi, 2007). These may be due to the presence of a variety of metabolites components present in citrus peel extract as bio-reductive compounds associated with the Ag-MgO nanoparticles synthesis (Dar et al. 2016; Gorinstein et al. 2004). The associated peaks at 1035 and 563 cm^{-1} arise as evidence of the phosphate asymmetric stretching and bending vibrations respectively in the nanohydroxyapatite phase. Vibration bending mode of transverse and longitudinal optical frequency relating to PO_4^{3-} falls within the range 500-620cm^{-1} of the spectral region (Poralan *et al*. 2015). The absorption peaks in the region below 487–677 cm^{-1} are allotted to Mg-O-Mg compounds (Balamurugan *et al*. 2014). Therefore, the peak at 559 cm^{-1} may be attributed to the Mg–O stretching vibration in Mg $(OH)_2$. The peaks around 1352 to 1466 cm^{-1} are attributed to the vibrational mode of carbonate species on the backbone (Jevtić et al. 2008), thus, indicating the overall formation of the Ag-MgOnHaP composite.

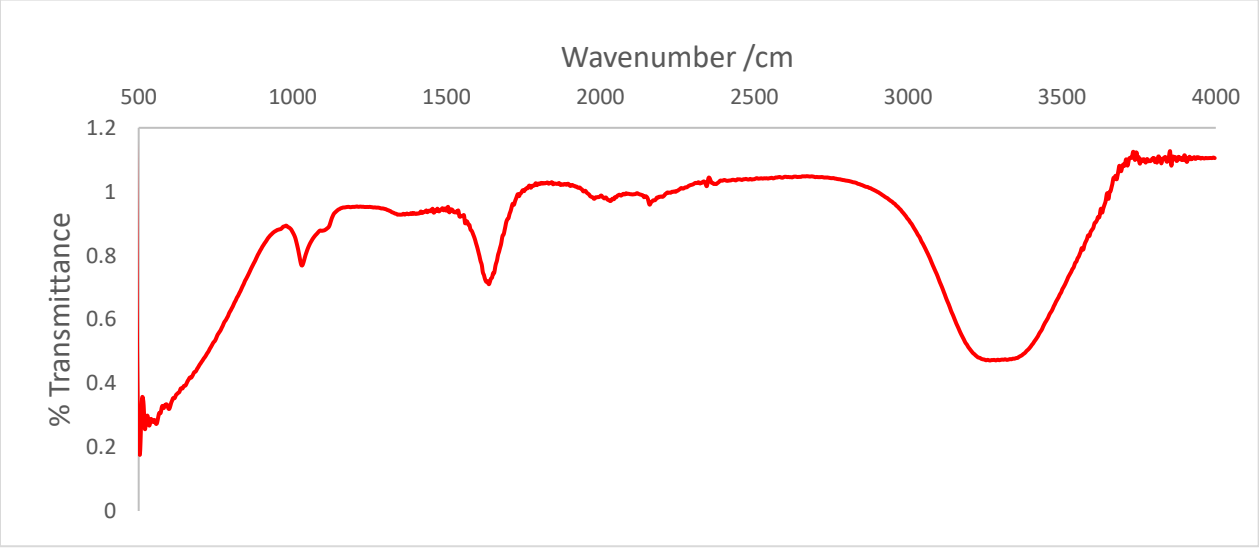

Fig. 5.2. FTIR spectra of Ag-MgOnHaP composite from *C. paradisi* peel extract

5.3.1.3 Surface morphology

Fig. 5.3 (a-e) show the surface morphologies from SEM and TEM micrographs of the Ag-MgOnHAP composite before and after ultra-sonication. SEM images in Figs. 3a and b, show the changes on the surfaces of the composites before and after 1hr ultrasound irradiation. Fig. 3a revealed irregular flake-like shapes in dimension, but upon ultrasound exposure, highly fine discrete spherical shapes were observed. The sizes of the composites were affected upon ultrasound exposure due to the cavitational collapse phenomenon resulting in an interparticle collision, thus, affecting the physicochemical properties of the composite in relation to the incident frequency of the sonicator (Santos *et al*. 2009; Sawant *et al*. 2008). Therefore, the route of synthesis through ultrasonication evidently serves as an efficient, uniform heating distribution and a means of controlling the overall structural phase of a stable nanocomposite with improved physicochemical properties.

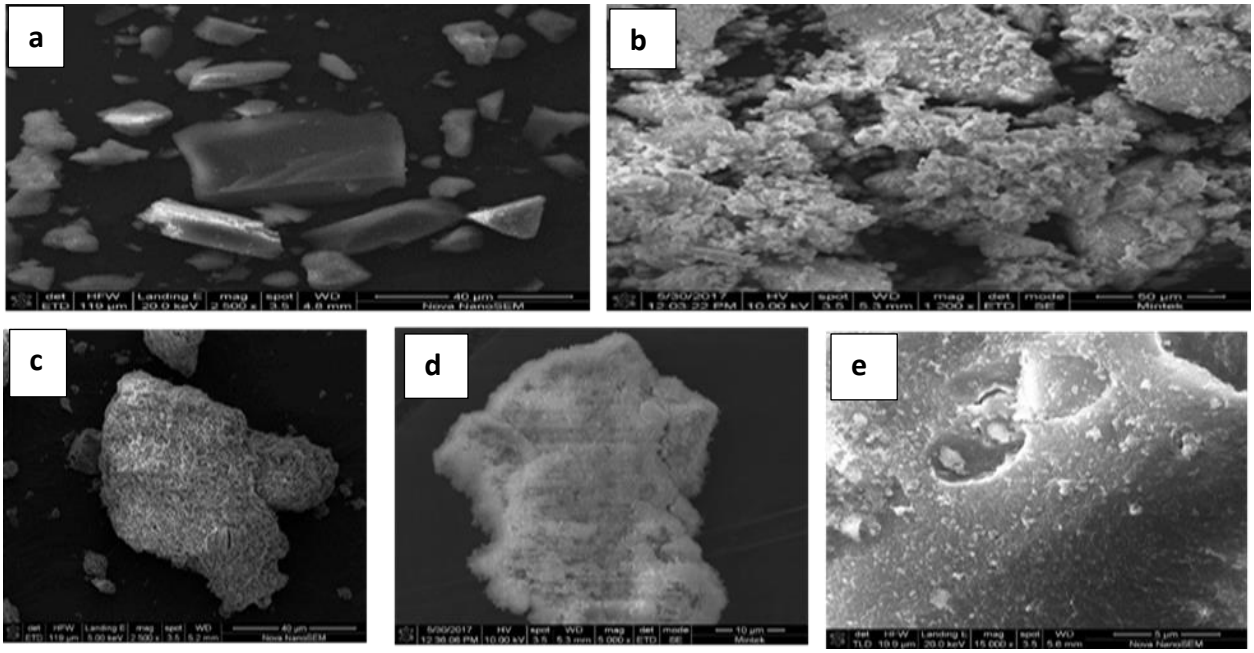

Fig. 5.3. SEM Ag-MgOnHaP (a) before sonication; (b) after 1hr sonication; (c) after 1hr sonication (x 2500) (d) after 1hr sonication (x 5000) (e) after 1hr sonication (x 15000)

Further morphological and microstructure analysis was achieved through TEM. Figure 5.4 (a) depicts the TEM micrograph of silver nanoparticles synthesized by *C. paradisi* peel extract thus confirming its spherical shape with the particle sizes at 14.84 nm. Fig. 5.4 (b) displayed an elongated rod-like shape with a particle size of 40.35 nm of the composite before ultrasound irradiation. A well-dispersed discretely embedded layered-spherical Ag-MgOnHaP nanocomposite without any form of agglomeration was observed after ultrasound exposure ranging in size from 20-100 nm with an average mean particle size diameter of 16.44 nm as shown in Fig. 5.4 (d). The improved surface morphology is established during the cavitation process at high intensities of exposure resulting in the conversion of larger particle sizes to smaller sizes.

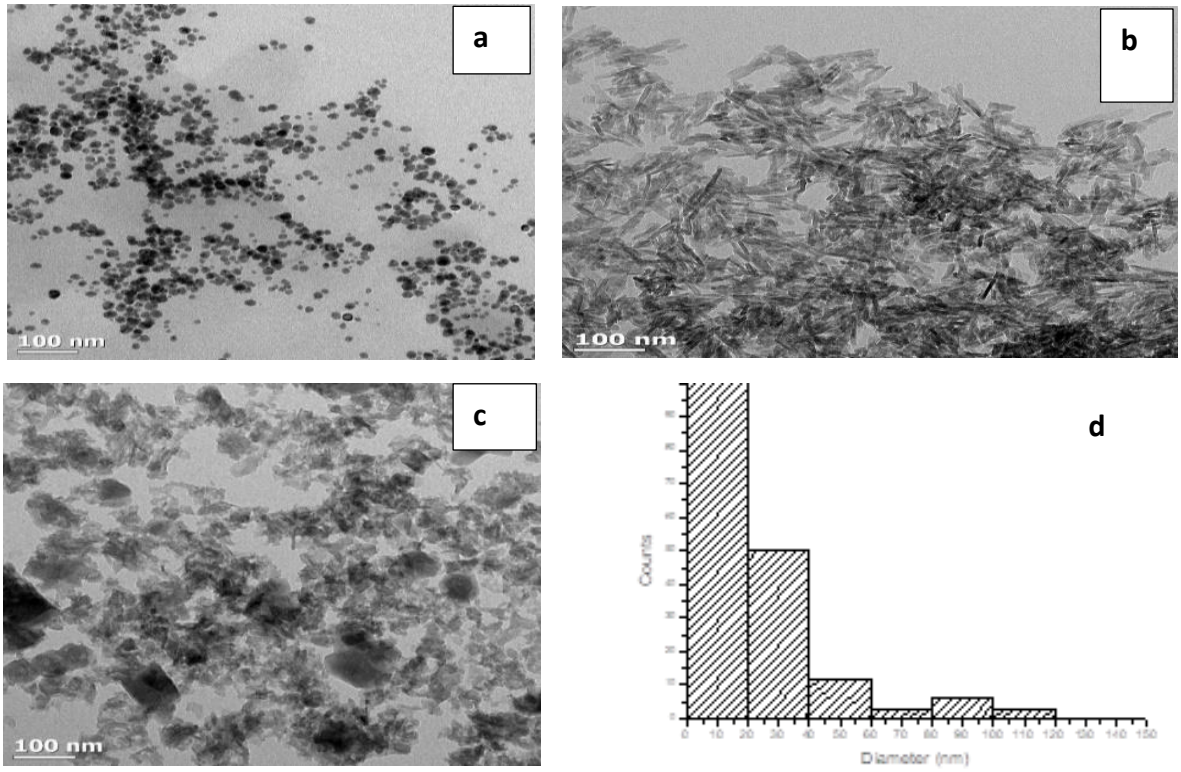

Fig. 5.4. TEM (a) AgNPs from *C. paradisi* peel (b) Ag-MgOnHaP before ultrasound exposure (c) Ag-MgOnHap after ultrasound irradiation (d) Ag-MgO particle size distribution.

The presence of the metal ions on the nano-hydroxyapatite was supported by the EDAX spectra (Fig. 5.5). The different elemental species (both quantitatively and qualitatively) in Ag-MgOnHap composite with their corresponding peaks as shown in the spectra, thus confirmed, the presence of Ag, Mg and O impregnated on the nHaP template. The low quantity of Ag species can be attributed to the low concentration of its precursor used during its biosynthesis.

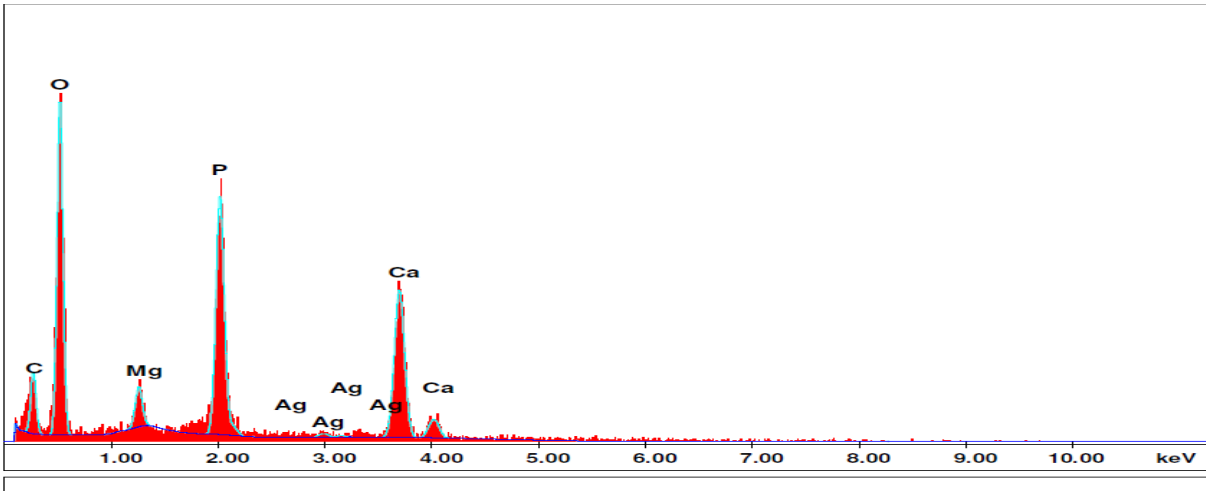

Fig. 5.5. EDAX spectra showing the different components in Ag-MgOnHap composite

5.3.1.4 XRD studies

Figure 5.6 presents the XRD spectrum of the Ag-MgOnHaP adsorbent. The spectrum has diffraction peaks for (002) and (112) at an intensities 61.4 (a. u.) (2θ = 25.880) and 54.9 (a. u.) (2θ = 32.196) in agreement with the reference model (JCPDF no. 00-064-0738) typical of hydroxyapatite (Veselinović *et al*. 2010; Wilson *et al*. 1999) in terms of the position, strong intensities, and shapes of the peaks. Other secondary phases apart from the nHaP were identified which are related to the Ag-MgO phase structures at 22.862, 38.180, 40.448 and 46.703° corresponding to lattice planes (111), (200), (220), (221) and (222) respectively, indicating a composite layered material. Different unassigned peaks were observed, ranging from 49 to 80° that may correspond to citric acid hydrate (JCPDF 00-015-0985) (Genevieve *et al*. 2014) on the surface of the composite with the use of aqueous *C. paradisi* peel extract.

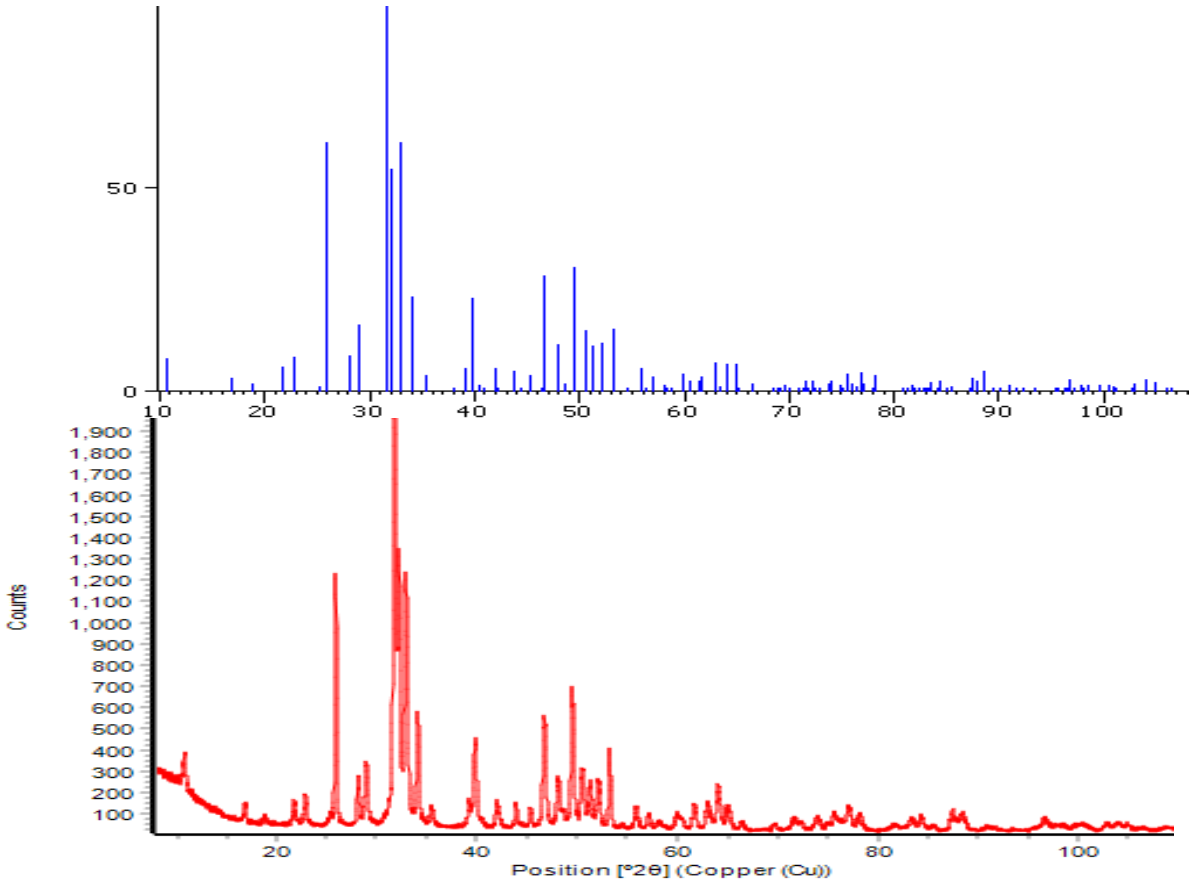

Fig. 5. 6. XRD patterns of Ag-MgOnHaP nanocomposites.

5.3.2 Batch adsorption Studies of Ag-MgOnHaP nanocomposites

5.3.2.1 Effect of Contact time on fluoride adsorption and adsorption kinetics

Variation of percentage fluoride removal at different contact time by Ag-MgOnHap composite at an initial fluoride concentration of 10 mg/L at 250 rpm is presented in Figure 5.7.

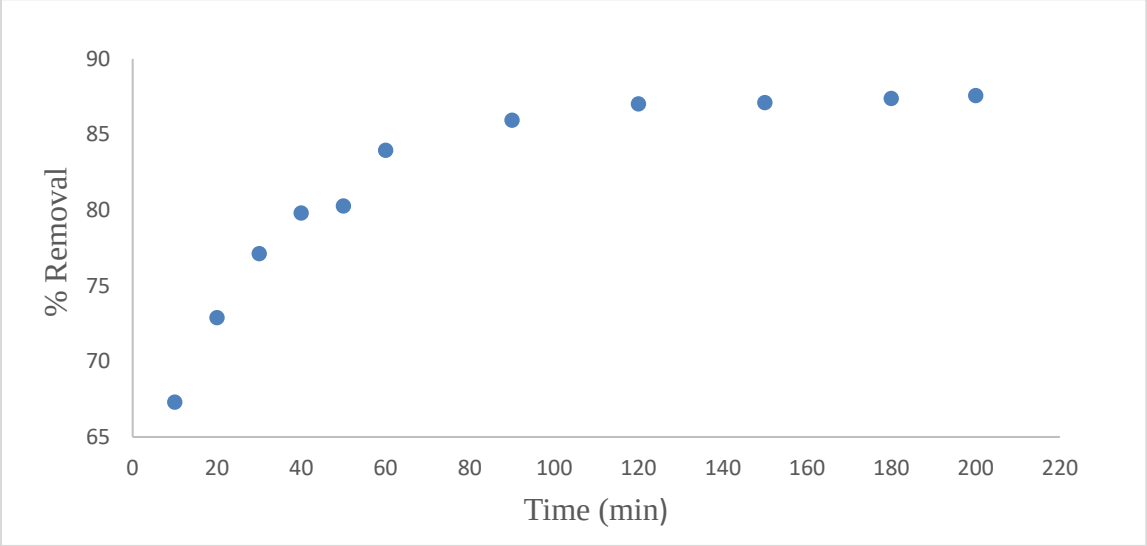

Fig. 5.7. Effect of contact time by Ag-MgOnHap composite (10 mg/L F^- at 250 rpm)

The defluoridation efficiency of the composite increases gradually upon agitation with time. The rise in the percentage removal of fluoride is an indication of an increase in the accessibility of the adsorption sites at the surface through enhanced adsorption capabilities of both MgO and nHaP; as well as the improved surface area created by the exposure to the high intensity of the ultrasound irradiation on the multilayered adsorbent composite phase. The percentage removal by the composite reduces from 60 min with more than 80 % removal, an indication that the number of active adsorption sites has been occupied leading to declining in the driving force for the adsorption process (Srimurali *et al*. 1998). This time with an adsorption capacity of 2.146mg/g was chosen for Ag-MgOnHaP composite and used throughout the studies as the optimum F^- uptake contact time.

The adsorption kinetic experimental data generated at different contact times were evaluated using reaction-based and diffusion-based models to explain the solid-liquid adsorption phenomenon and mechanisms. Figs. 5.8 (a-c) depict the adsorption kinetics curve fittings in predicting the uptake rate and processes of the adsorbate into the adsorbent with pseudo-first-order (Lagergren, 1898), pseudo-second-order (Ho, 2006) and Weber–Morris intra-particle diffusion (Weber and Morris, 1964). These models are generally expressed in equations 3, 4 and 5 respectively.

The pseudo-first-order rate model (Lagergren, 1898) is expressed as in Eq. (3)

$$\log(q_e - q_t) = logq_e - \frac{k_1}{2.303}t \qquad (3)$$

where qe (mg/g) is the maximum defluoridation capacity at pseudo-first-order, qt (mg/g) the fluoride concentration at time t with k_1 (min^{-1}) representing the pseudo-first-order adsorption rate constant. Equation. (4) represent the pseudo-second-order sorption kinetic rate and is used to describe cation exchange and chemisorption reaction mechanisms (Oladoja *et al*. 2016).

$$\frac{t}{q_t} = \frac{1}{k_2\, q_e^2} + \frac{1}{q_e} t \qquad (4)$$

Where K_2 (g/mg min) is the equilibrium rate constant of pseudo-second-order adsorption.
Apart from adsorption occurring at the outer surface of the adsorbent, the adsorbate molecules are often characterized by particle diffusion through the interior of the adsorbent. Hence, the Weber–Morris intra-particle diffusion (Weber and Morris, 1964) equation model typically used in controlling the rate of adsorption of fluoride (Eq. (5)) was also evaluated.

$$q_t = k_i t^{0.5} \qquad (5)$$

Where qt is the amount adsorbed (mg g^{-1}) at a given time, t (min); Ki (mg $g^{-1}min^{-1}$) is the intraparticle diffusion rate constant and is determined from the slope of $t^{0.5}$vs qt.
The different parameters obtained from a linear plot of log (qe– qt) against time, the plot of t/q_t versus time t, and the plot of qt vs. $t^{0.5}$ at various initial fluoride concentrations for the pseudo-first-order, pseudo-second-order, as well as the intra-particle diffusion models respectively are presented Table 5.1. The pseudo-second-order (Fig. 5.8 (b)) with a significantly higher value of 0.999 R^2 when compared to the pseudo-first-order models (Fig. 5.8 (a)), show a better linear fit. This is evidently an indication that the initial fluoride adsorption rate was extremely rapid and defluoridation occurred through chemisorption in contrast to physisorption characterized by weak van der Waal's force (Anthony *et al*. 2015).

The possibility of mass transfer of the adsorbate molecules from the external surface onto the pores of the adsorbent corresponding with the formation of three different phases was observed for the intra-particle diffusion sequences (Fig. 5.8 (c)). The first phase occurred between 10 and 40 min, the second between 50 and 60 min while the third phase is between 90 and 200min. These phases may be governed by the external diffusion, intra-particle diffusion as well as the attachment of adsorbate molecules to the internal surface of sorbent (Ho *et al*. 2000) at equilibrium stage respectively. The rate constant for phase 1, phase 2 and phase 3 (K_1, K_2 and K_3 respectively) (Table 5.1), suggests that the adsorption process was very rapid on the layer and dominates the intra-particle diffusion due to the difference in the rate of mass transfer in the initial and final phase of adsorption based on the higher correlation coefficient value of phase 2 when compared to phases 1 and 3.

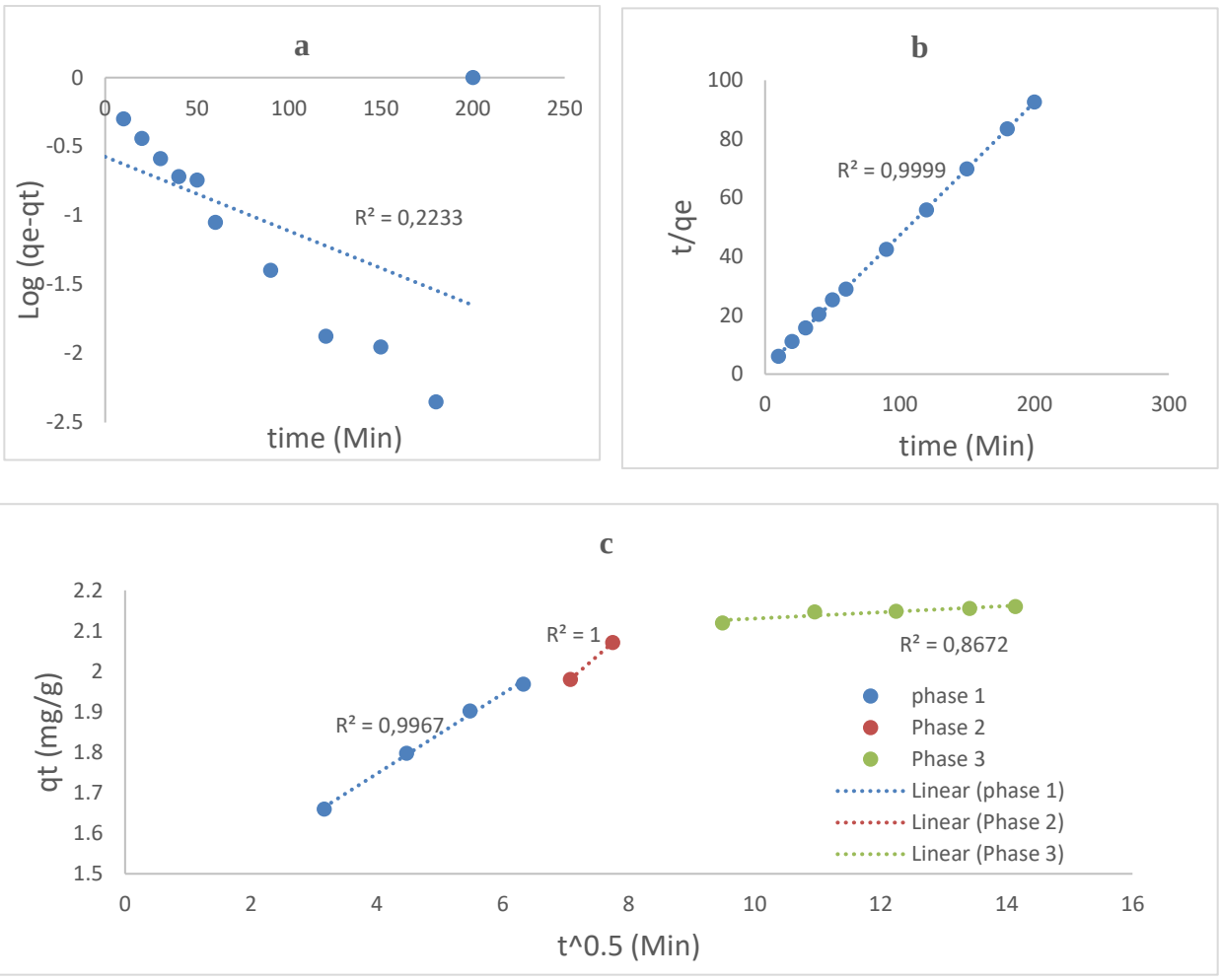

Fig. 5.8. (a) Pseudo-first-order; (b) Pseudo-second order, (c) Intra article plot at various adsorbent dosages (60min, 10 mg/L F^-, pH 6 and 250 rpm shaking)

Table 5.1. Calculated parameters for pseudo-first-order, pseudo-second-order and intra-particle reaction kinetics model of Ag-MgOnHaP composite.

Kinetic models	Parameters	Values
Pseudo-first-order	Qe (mg/g)	0.2667
	k_1 (min^{-1})	0.0124
	R^2	0.2233
Pseudo-second-order	Qe (mg/g)	2.2109
	k_2 (g/min mg)	0.1021
	R^2	0.9999
Intra-particle diffusion	K_1 (mg/g $min^{1/2}$)	0.0988
	K_2 (mg/g $min^{1/2}$)	0.0135
	K_3 (mg/g $min^{1/2}$)	0.0077
	R^2	0.8303

5.3.2.2 Effect of Adsorbent Dosage

Figure 5.9 shows the variation of % F^- removal and adsorption capacity (mg/g) with adsorbent dosage for Ag-MgOnHaP composite. The dosage ranges from 0.1 to 1 g.

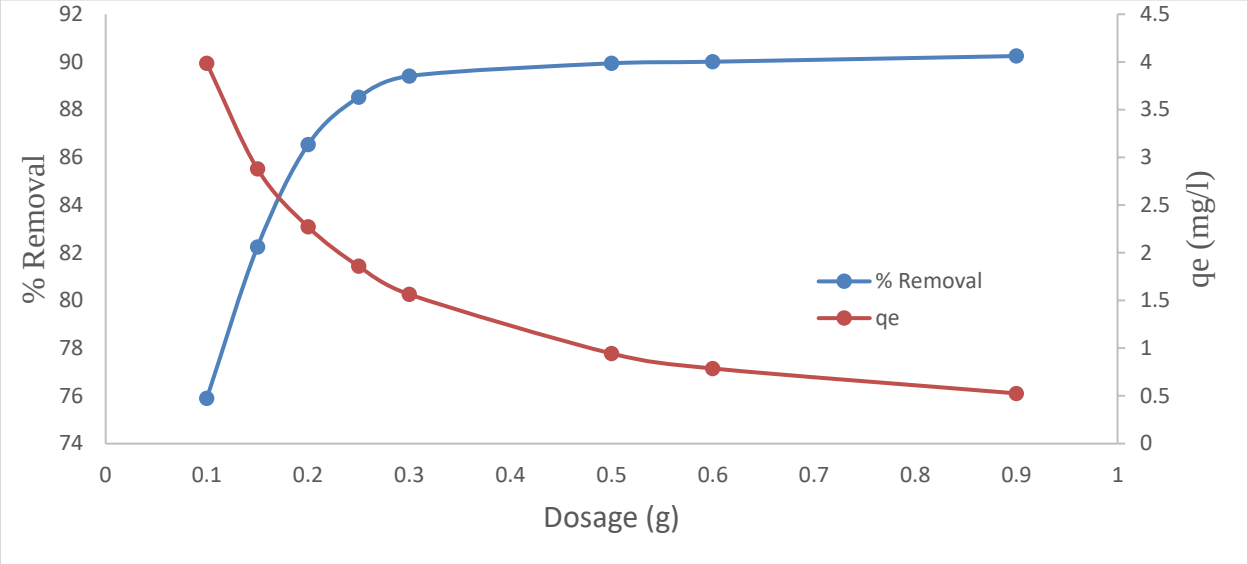

Fig. 5.9. Variation of % F^- removal and defluoridation capacity by Ag-MgOnHap composite as a function of adsorbent dosage (contact time of 60 min, initial F^- concentration of 10 mg/L at 50mL solution volume, pH of 6, shaking speed of 250 rpm at 298K).

It is evident that the percentage defluoridation increase as the adsorbent amount increases up to 0.3g/50 mL with about 90% removal, beyond which the increase in percentage removal was insignificant. This is expected with increasing reactivity at the surface due to the creation of more active contact sites by an overall increase in particle size reduction after ultrasonication agitation. Increasing the adsorbent dosage increase number of adsorption sites, but it is limited due to the density of the particles as the adsorbent dosage increases. In addition to the high density of the adsorbent particles limiting the mobility of the F^-, consequently limiting the access to adsorption sites (Mudzielwana *et al.* 2017); the strong electrostatic attraction between the F^- and OH^- from the bio-reductive and capping agent used in the synthesis of the Ag-MgO nanoparticles embedded on the composite surface may also be a contributing factor to the F^- removal efficiency. In adsorption, increase in adsorbent dosage is inversely proportional to adsorption capacity (Fig. 5.9). Therefore, for the purpose of this study 0.3g/50 mL was chosen as the optimum dosage and subsequently used in further experiments.

5.3.2.3 Effect of pH

Generally, the removal efficiency of a chemical species at water-adsorbent interfaces is dependent on the solution pH. The plot showing the impacts of solution pH on the F^- uptake by Ag-MgOnHap composite at various initial pH ranges between 4 -10 is shown in Fig. 5.10.

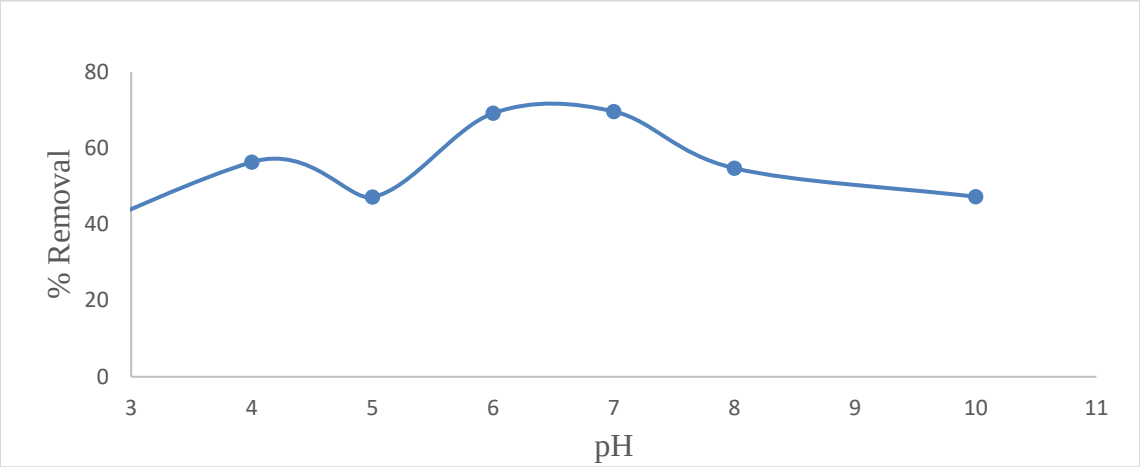

Fig. 5.10. Effect of pH on Defluoridation capacity (contact time of 60 min, initial F- concentration of 10 mg/L, 0.3 g/50 mL and shaking speed of 250 rpm).

Maximum defluoridation was achieved at pH 6 with about 70% removal, and it decreased sharply beyond pH 7 reaching 47.2 % at pH 10. Studies observed such decrease in sorption capacity trends was due to the facts that at alkaline pH, the hydroxyl group is in higher concentration and competes with the F^- anion by occupying some sites on the adsorbent surface, thus, leading to decreased F^- adsorption (Rao *et al*. 2012; Kamble *et al*. 2007). The decrease in F^- adsorption at alkaline pH can be attributed to changes in surface charges of the adsorbent due to the competition from an O-H group which is stronger in this solution medium, resulting in the decrease in the fluoride adsorption capacity. (Subbaiah Muthu Prabhu and Sankaran Meenakshi 2014).

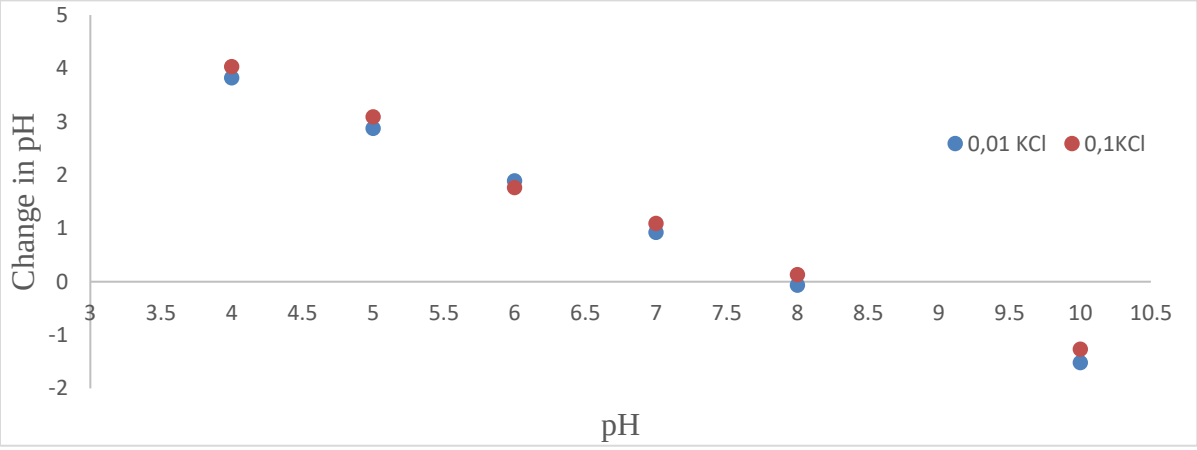

Fig. 5.11. The plot for determination of pHpzc of Ag-MgOnHAp

Furthermore, the surface charge phenomenon occurring within the system was further established by the point of zero charges (pHzpc) value (Fig. 5.11). This is defined as the pH point where the sorbent surface charge takes a zero value, and it identifies the region where the adsorption of F^- will be optimum. In this study, the pHzpc was found to be 8, which is higher than the pH of the solution for Ag-MgOnHAp composite sorption capacity. This is an indication that the surface of the composite possesses an overall positive charge unit, thus demonstrating an anion exchange behavior and could interact with negative F^- species resulting in higher percentage removal (Dhillon and Kumar 2015).

5.3.2.4 Effect of initial concentration and adsorption modeling

Figure 5.12 shows the relationship between deflouridation capacity and removal efficiency of Ag-MgOnHaP composite at various initial fluoride concentrations from 2 to 15mg/L. It can be observed that as the adsorption capacity increased, the removal of fluoride in the solution decreases with the initial concentration at room temperature. This may be due to the unavailability of more unoccupied sorption sites on the adsorbent layered-surface resulting in the overall reduction of fluoride uptake within the solution.

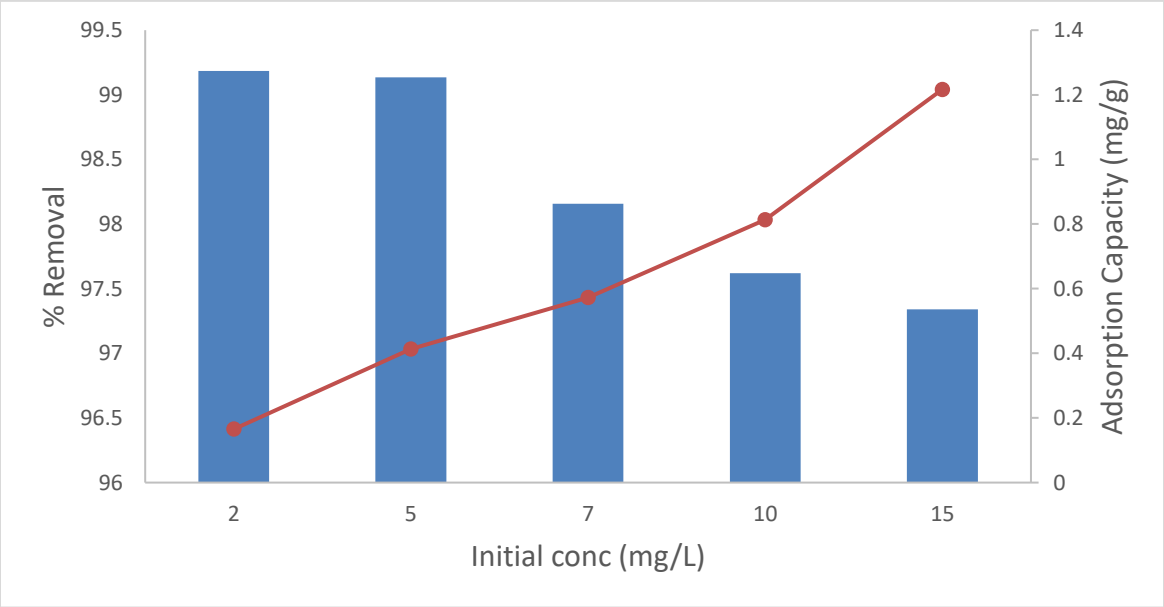

Fig. 5.12. Variation of adsorption capacity with initial F- concentration (optimum time of 60min, adsorbent dosage 0.3 g/50 mL, pH 6 and shaking speed of 250 rpm at 298K).

5.3.2.4.1 Adsorption isotherms

Adsorption isotherms are usually used to express the interaction between the amounts of adsorbate on the adsorbent surfaces in any adsorption-desorption phenomenon. Langmuir (Langmuir, 1916) and Freundlich (Freundlich, 1906) isotherms were modeled and fitted into the sorption experimental data. These models are critical for optimization of the adsorption mechanism pathways, expression of the surface properties and capacities of adsorbents in order to establish the most appropriate adsorption equilibrium correlation (El-Khaiary, 2008; Srivastava 2006).

Langmuir is typically used to quantify and contrast the performance, equilibrium distribution of metal ions between different bio-sorbents in a solid-liquid phase interaction (Foo and Hameed, 2010; Vermeulan *et al*. 1966). The Langmuir adsorption isotherm is valid for monolayer adsorption and is represented by equation (6):

$$q_m = \frac{q_m K_a C_e}{1+K_a C_e} \qquad (6)$$

The linearized Langmuir equation is the most commonly used. It is presented as equation (7):

$$\frac{C_e}{q_e} = \frac{1}{K_a q_m} + \frac{1}{q_m} C_e \qquad (7)$$

where C_e is the equilibrium concentration (mg/L); q_e is the amount of ion adsorbed (mg/g); q_m is q_e for a complete monolayer (mg/g); K_a is adsorption equilibrium constant (L/mg). These parameters can be obtained by the plot of Ce/qe against Ce. A dimensionless parameter, R_L, (equation 8) was also calculated from the Langmuir isotherm adsorption process.

$$R_L = \frac{1}{1+k_a C_i} \qquad (8)$$

where k_a is the Langmuir isotherm constant and C_i is the initial concentration of fluoride (mg/L). R_L value indicates the sorption system to be favorable if $0 < R_L < 1$.
The experimental sorption data were also modeled using the Freundlich isotherm. This model is not restricted to the formation of monolayer and it describes a known relationship between the non-ideal and reversible adsorption processes (Foo and Hameed, 2010). Thus, it can be applied to multilayer adsorption with heterogeneous surfaces. Freundlich isotherm is represented by equation (9):

$$q_e = K_F C_e^{1/n} \qquad (9)$$

The linear form of equation (9) is represented by equation (10):

$$\log q_e = \log K_F + \frac{1}{n} \log C_e \qquad (10)$$

where K_F and 1/n are empirical constants, indicating the adsorption capacity and adsorption intensity, respectively, and can be obtained by plotting $\log q_e$ against $\log C_e$. The values of 1/n are between 0 and 1. The condition for adsorption material is favorable if n value lies within the range of 1 and 10. The different adsorption isotherm model plots and their respective calculated

parameters for Ag-MgOnHaP composite were calculated and presented in Figs. 5.13 (a and b) and Table 5.2.

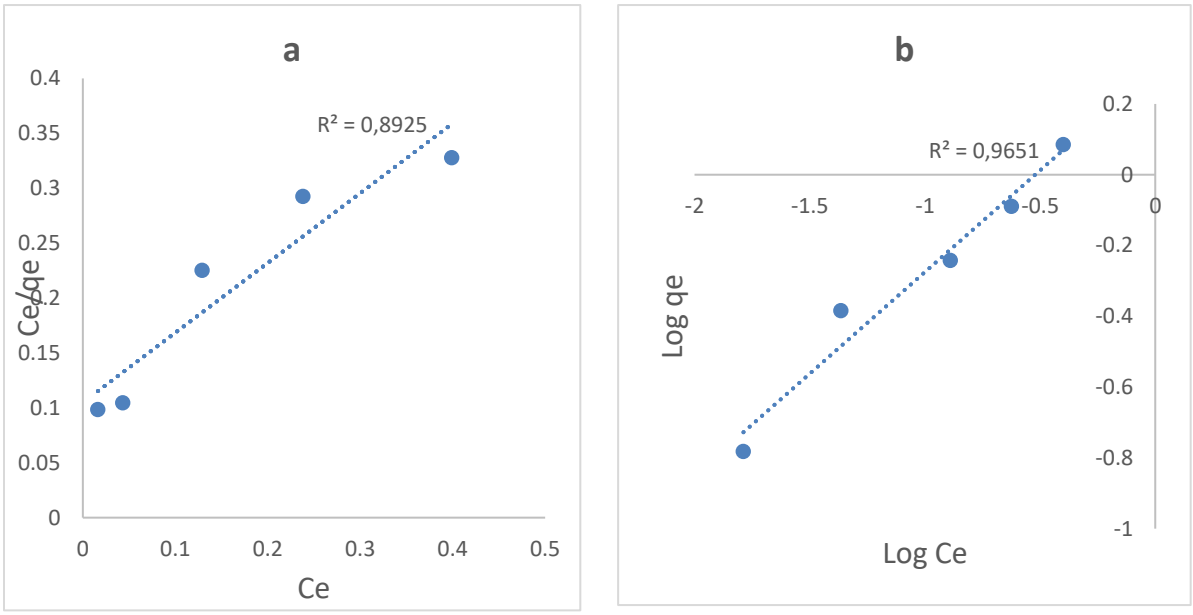

Fig. 5.13. (a) Langmuir sorption isotherm plot; (b) Freundlich sorption isotherm (optimum time of 60min, adsorbent dosage 0.3 g/50 mL, pH 6 and shaking speed of 250 rpm at 298K).

Table 5. 2. Calculated constant values for Langmuir and Freundlich isotherms of Ag-MgOnHaP composite.

Parameters	Langmuir Isotherm	Parameters	Freundlich Isotherm
Qm (mg/g)	1.574	K_F (mg/g) $(mg/L)^{-1/n}$	1.993
K_a (L/mg)	6.057	n	1.741
R^2	0.893	R^2	0.965
R_L	0.0162		

It is evident from the obtained correlation coefficient R^2 and adsorption intensity (n) values that Freundlich model (Fig. 12 (b)) gave a better fit to the experimental data than the Langmuir model (Fig. 12 (a)). An indication that the conditions were favorable for multilayer adsorption process with non-uniform distribution of adsorption heat and affinities on a heterogeneous surface that varies with surface coverage with increasing surface density (Medellin-Castillo *et al*. 2014; Adamson and Gast 1997).

5.3.2.5 Effect of co-ions

Fig. 5.14 (a) show the effects of a multi-component solution of co-existing anions (nitrate, chloride, sulfate, and carbonate) on the defluoridation efficiency of Ag-MgOnHaP composite. The results clearly show that as the concentration of the co-anions increases, adsorption capacity decreases. Figure 5.14 (b) present the effects of individual co-existing anion on the defluoridation efficiency of Ag-MgOnHaP composite. The results show that the presence of Cl^{-}, NO_3^{-}, does not have a significant impact on percentage fluoride uptake efficiency, but SO_4^{2-} and CO_3^{2-} reduce the % F- removal capacity from 90% to 80% and 90% to 83% respectively. This may be attributed with the ability of the CO_3^{2-} competing with the F- for active sites on the adsorbent surface as well as the high coulombic repulsion force, which reduces the fluoride mobility interactions with the active sites (Subbaiah Muthu Prabhu and Sankaran Meenakshi (2014).

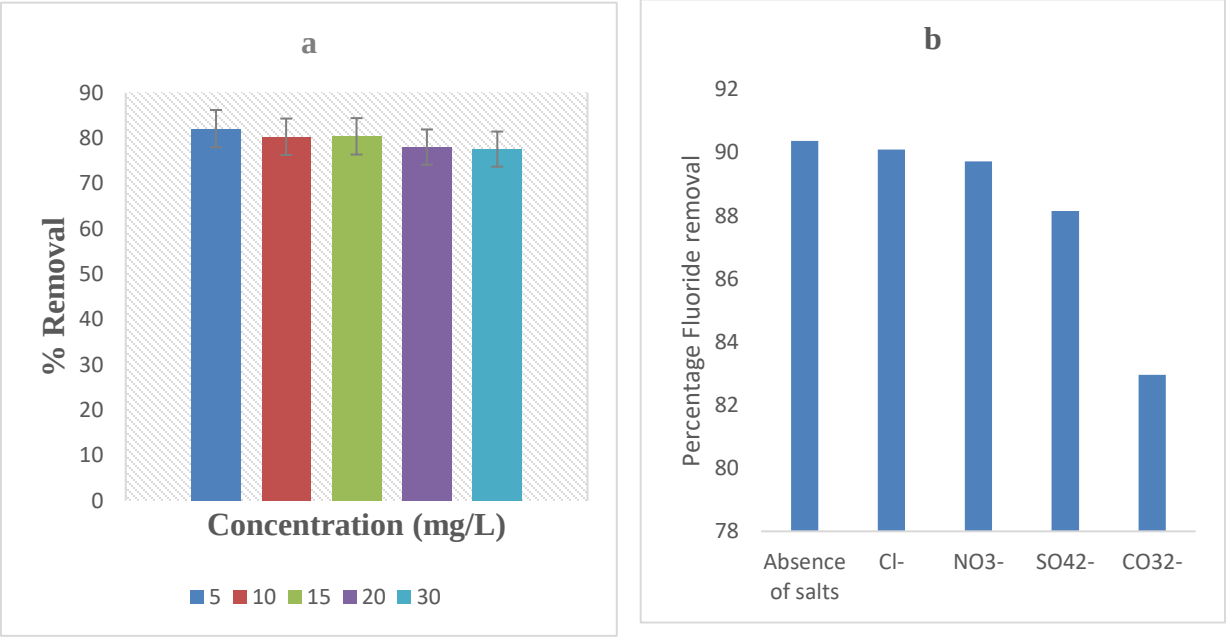

Fig. 5.14. Effects of co-anions on the defluoridation capacity of Ag-MgOnHaP composite.

5.4 Evaluation of antimicrobial activity

The results of the antibacterial activities of Ag-MgOnHaP composite and nHap against isolated gram-negative bacteria (*Escherichia coli and Klebsiella pneumonia*) are presented in Fig. 5.15. *E. coli* with 13mm zone of inhibition was found to be more susceptible than K. *pneumonia* (10 mm). No visible activities were observed on the nHap against any of the strains.

The antibacterial activities of the synthesized Ag-MgOnHaP material may be attributed to many factors. The inactivation mechanism of action of nanoparticles generally against microbes has been a major debate because of the continuous emergence of bacterial resistance (Slavin *et al*. 2017). However, studies have indicated that the antimicrobial susceptibility and mechanisms of nanoparticles do not only rely on the cell wall structures of bacteria type but also on the contact action, cellular enzymes and biochemical events in producing intracellular reactive oxygen species

(ROS) (Ahluwalia *et al*. 2018; Krishnamoorthy *et al*., 2012; Leung *et al*., 2014; Zhu Xiwei *et al*. 2016). In addition, other factors that may be associated with the resulted microbial death could be sizes, structure, and surface properties of the composite since smaller particles with larger surface area possess the affinity for interaction, giving more bactericidal effect than the larger particles (Raghupathi *et al*. 2011; Sharma *et al*. 2009). Therefore, the antimicrobial activity of Ag-MgOnHaP nanocomposites likely occurs due to the penetration of both Ag and Mg ions released from Ag-MgO nanoparticles on the adsorbent surface and their respective interaction with the bacterial genome and other cellular enzymes resulting in cell membrane death of the microbes. Furthermore, it has also been established that the antibacterial activities of nanoparticles depend on the reducing agents and stabilizers used for synthesis (Garmasheva *et al*. 2016; Sharma *et al*. 2009). Thus, the *C. paradisi* peel extracts used in the synthesis of Ag-MgOnHap may have contributed to the antimicrobial activities due to the phytochemical components in the peel segment of citrus, which account for the bioactivity (Aromal and Philip 2012; Gorinstein *et al*. 2001).

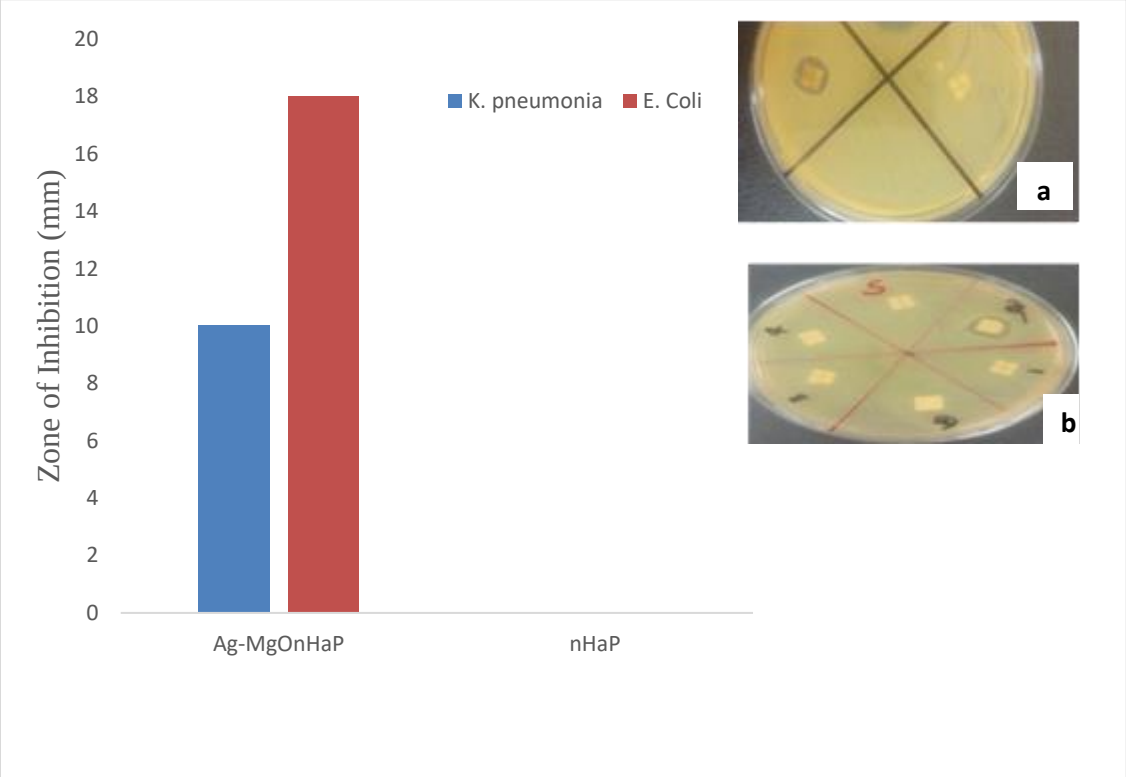

Fig. 5.15. Ag-MgOnHaP antibacterial activity (Inset Diameter of inhibition by the synthesized nanocomposite and the bare nanohydroxyapatite (a) *E. coli* (b) *K. pneumonia*

5.5 Regeneration

The suitability of the fluoride-loaded adsorbent for reuse was evaluated, and the result is presented in Figure 5.16. The percentage fluoride removal of Ag-MgOnHaP composite decreases with increasing regeneration. A fluoride removal of 74.24 % was observed at the 4th cycle of regeneration. This clearly indicates the reuse potential of the adsorbent.

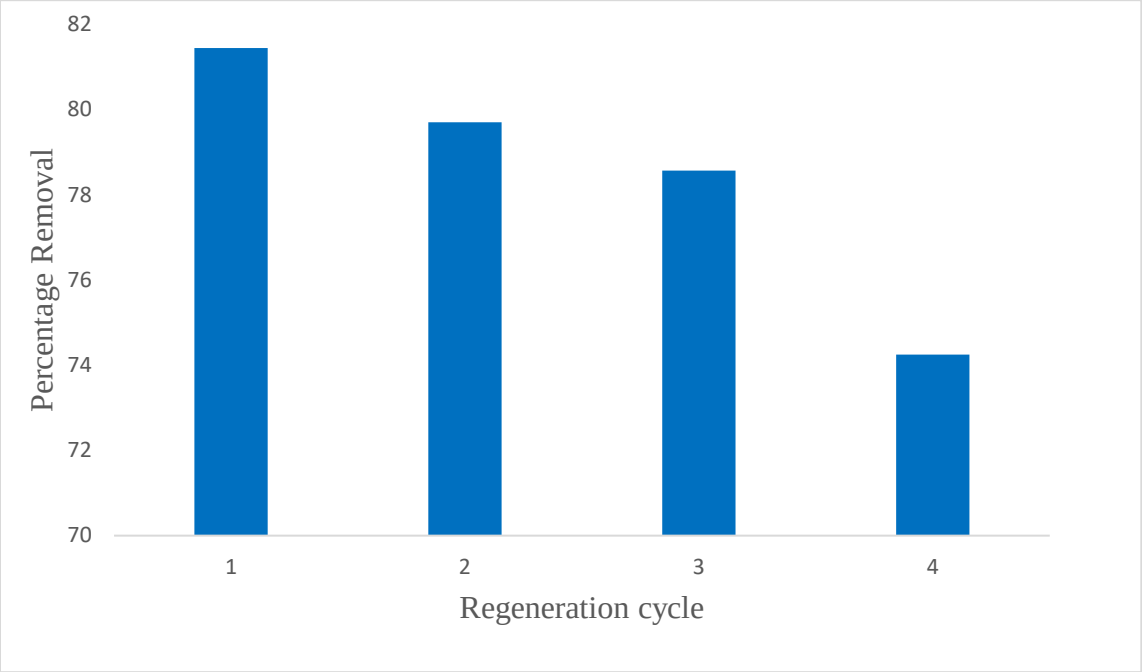

Fig. 5.16. % Fluoride removal onto Ag-MgOnHaP in successive regeneration cycles (5 mg/L initial F-, adsorbent dosage 0.3 g/50 mL, pH 6, shaking speed of 250 rpm at 298K)

5.6 Comparison of Ag-MgOnHaP with other adsorbents

Comparison of defluoridation capacity between the green modified Ag-MgOnHaP adsorbent and other reported sorbents for defluoridation was carried out (Table 5.3). It is important to note that the composition of an adsorbent, different condition of synthesis and other experimental conditions influences the defluoridation capacity of these sorbents. Thus, Ag-MgOnHaP composite shows a better defluoridation capacity than other reported adsorbents consequently confirming its potential for application in household water treatment devices.

Table 5.3. Comparison of maximum adsorption capacities of different adsorbents for defluoriddation.

Adsorbent	Defluoridation Capacity(mg/g)	Experimental conditions	Reference
Nano-hydroxyapatite	1.30	pH 3	(Sundaram et al. 2008)
nHap/chitosan composite	1.56	pH 3, contact time 30min	(Sundaram et al. 2008)
Synthetic HAP	0.49	pH 2, 0.5 g/25 mL	(Gao et al. 2009)
HaP nanorods	1.49	pH 7, contact time 3h, 7 g/L	(Dhiraj et al. 2017)
Ag/MgOnHaP	2.146	pH 6, contact time 60min, 0.3 g/50 mL	This study

5.7 Conclusion

A multi-purpose Ag-MgOnHaP adsorbent was successfully synthesized using aqueous peel extracts of *C. paradisi* as a bio-reductive agent. An observed UV absorption band of 290 nm and 378 nm typical of MgO and Ag nanoparticles respectively anchoring on the nanohydroxyapatite layered surface were observed. Moreover, ultrasound exposure technique produces fine particles with an average particle size of 16.44 nm with an improved contact surface and increased active sites for reaction by the adsorbent. The adsorbent recorded a defluoridation capacity of 2.146 mg/g at 60 min contact time, 0.3g dosage/50 mL, and at circum-neutral pH 6 with pHpzc of 8 at room temperature. The adsorption data fitted well into the Freundlich isotherm model, an indication that adsorption occurred on a multilayered heterogeneous surface. Sorption kinetics fitted better to pseudo-second-order reaction kinetics, indicating the process occurred through chemisorption at 298 K. The synthesized nanocomposite successfully revealed effective antibacterial activity against waterborne bacteria in the order *Escherichia coli* > *Klebsiella pneumonia*. Ag-MgO embedded on the nHaP serves a dual purpose on the surface of the composite both in the defluoridation phenomenon and antimicrobial activity.

Conflicts of interest

The authors declare no conflicts of interest.

Acknowledgment

Authors would like to acknowledge financial support from USAID-PEER Cycle 6-Award No: AID-OAA-A-11-00012; National Research Foundation (South Africa) through the KIC, 2017

grant, University of Venda, South Africa (RPC grant Number: SES/17/ERM/03), Prof Gitari Research Incentive funds and Mintek, South Africa.

References

Adamson, A.W, A.P. Gast, 1997. Physical Chemistry of Surfaces, sixth ed., Wiley- Interscience, New York

Ahluwalia, V., Elumalai, S., Kumar, V., Kumar, S. and Sangwan, R.S., 2018. Nano silver particle synthesis using Swertia paniculata herbal extract and its antimicrobial activity. Microbial pathogenesis, 114, pp.402-408.

Anthony A. Izuagie, Wilson M. Gitari & Jabulani R., Gumbo 2015: Defluoridation of groundwater using diatomaceous earth: optimization of adsorption conditions, kinetics and leached metals risk assessment, Desalination and Water Treatment, DOI: 10.1080/19443994.2015.1083894

Aromal, S.A. and Philip, D., 2012. Green synthesis of gold nanoparticles using Trigonella foenum-graecum and its size-dependent catalytic activity. Spectrochimica Acta Part A: Molecular and Biomolecular Spectroscopy, 97, pp.1-5.

Ayoob, S., Gupta, A.K. and Bhat, V.T., 2008. A conceptual overview on sustainable technologies for the defluoridation of drinking water, Crit. Rev. Environ. Sci. Technol. 38, 401–470.

Bain, R.E., Gundry, S.W., Wright, J.A., Yang, H., Pedley, S. and Bartram, J.K., 2012. Accounting for water quality in monitoring access to safe drinking-water as part of the Millennium Development Goals: lessons from five countries. Bulletin of the World Health Organization, 90(3), pp.228-235.

Balamurugan S., Ashna L., Parthiban P. 2014. Synthesis of nanocrystalline MgO particles by combustion followed by annealing method using hexamine as a fuel. J Nano Tech 6:1–6. doi:10. 1155/2014/841803

Ben Nasr A., Charcosset, C., Ben Amar, R., Walha, K. 2013. Defluoridation of water by nanofiltration, J. Fluor. Chem. 150 92–97. doi:10.1016/j.jfluchem.2013.01.021

Bhatnagar, A., Kumar, E. and Sillanpää, M., 2011. Fluoride removal from water by adsorption—a review. Chemical Engineering Journal, 171(3), pp.811-840.

Cai, H., Xu, L., Chen, G., Peng, C., Ke, F., Liu, Z., et al., 2016. Removal of fluoride from drinking water using modified ultrafine tea powder processed using aball-mill. Applied Surface Science, 375, 74–84.

Chai, L., Wang, Y., Zhao, N., Yang, W. and You, X., 2013. Sulfate-doped Fe_3O_4/Al_2O_3 nanoparticles as a novel adsorbent for fluoride removal from drinking water. Water research, 47(12), pp.4040-4049.

Dankovich, T.A., Levine, J.S., Potgieter, N., Dillingham, R. and Smith, J.A., 2016. Inactivation of bacteria from contaminated streams in Limpopo, South Africa by silver-or copper-nanoparticle paper filters. Environmental science: water research & technology, 2(1), pp.85-96.

Dar Muhammad Sikander, Reena Lawrence and Anam Noor Khan, 2016. Evaluation of the chemical constituents and the antibacterial activity of essential oil of citrus karna fruit peel. IJPSR, Vol. 7(3): 1245-1250. DOI: 10.13040/IJPSR.0975-8232.7 (3).1245-50

Dhillon, A., Nair, M., Bhargava, S. K., & Kumar, D., 2015. Excellent fluoride decontamination and antibacterial efficacy of Fe-Ca-Zr hybrid metal oxide nanomaterial. Journal of Colloid and Interface Science, 457, 289–297.

Dhillon, A. and Kumar, D. 2015. Development of a nanoporous adsorbent for the removal of health-hazardous fluoride ions from aqueous systems, J. Mater. Chem. A 3 (8) 4215–4228.

Dhiraj Mehta, Poonam Mondal, Virendra Kumar Saharan, Suja George. 2017. Synthesis of hydroxyapatite nanorods for application in water defluoridation and optimization of process variables: Advantage of ultrasonication with precipitation method over conventional method. Ultrasonics Sonochemistry 37, 56–70

Dimapilis, E.A.S., Hsu, C.S., Mendoza, R.M.O. and Lu, M.C. 2017. Zinc oxide nanoparticles for water disinfection. Sustainable Environment Research.

El-Khaiary, M.I., 2008. Least-squares regression of adsorption equilibrium data: comparing the options, J. Hazard. Mater. 158 73–87.

Fan, X., Parker, D.J., and Smith M.D., 2003. Adsorption kinetics of fluoride on low cost materials, Water Res. 37; 4929–4937.

Foo K.Y. and Hameed B.H., 2010. Insights into the modeling of adsorption isotherm systems, Review Chemical Engineering Journal 156, 2–10.

Freundlich H.M.F., 1906. Uber die adsorption in l¨osungen, Z. Phys. Chem. 57A 385–470.

Fuller, T., 2006. Rural water supplies and water-quality issues. Healthy Housing Reference Manual, pp.1-12.

Garmasheva, I., Kovalenko, N., Voychuk, S., Ostapchuk, A., Livins'ka, O., & Oleschenko, L. 2016. Lactobacillus species mediated synthesis of silver nanoparticles and their antibacterial activity against opportunistic pathogens in vitro. Bio Impacts: BI, 6(4), 219–223. http://doi.org/10.15171/bi.2016.29

Gao S., R. Sun, Z.G. Wei, H.Y. Zhao, H.X. Li, F. Hu., 2009. Size-dependent defluoridation properties of synthetic hydroxyapatite, J. Fluorine Chem. 130 550–556.

Genevieve A. Kahrilas, Laura M. Wally, Sarah J. Fredrick, Michael Hiskey, Amy L. Prieto, and Janel E. Owens. 2014. Microwave-Assisted Green Synthesis of Silver Nanoparticles Using Orange Peel Extract. ACS Sustainable Chemistry & Engineering 2 (3), 367-376 DOI: 10.1021/sc4003664

Gitari W.M., Ngulube, T., Masindi, V., Gumbo, J.R. 2013. Defluoridation of groundwater using Fe^{3+}-modified bentonite clay: Optimization of adsorption conditions, Desalin. Water Treat. 1–13, doi: 10.1080/ 19443994.2013.855669.

Gitari, W.M., Izuagie, A.A. and Gumbo, J.R. 2017. Synthesis, characterization and batch assessment of groundwater fluoride removal capacity of trimetal Mg/Ce/Mn oxide-modified diatomaceous earth. Arabian Journal of Chemistry.

Gopi, D., Indira, J., Kavitha, L., Sekar, M., Kamachi Mudali, U. 2012. Synthesis of hydroxyapatite nanoparticles by a novel ultrasonic assisted with mixed hollow sphere template method. Spectrochimica Acta Part A 93; 131– 134

Gorinstein, S., Cvikrova, M., Machackova, I., Haruenkit, R., Park, Y.S., Jung, S.T., Yamamoto, K., Ayala, A.L.M., Katrich, E. and Trakhtenberg, S., 2004. Characterization of antioxidant compounds in Jaffa sweeties and white grapefruits. Food Chemistry, 84(4), pp.503-510.

Gosh, A., Mukherjee, K., Gosh, S.K., Saha, B., 2013. Sources and toxicity of fluoride in the environment, Res. Chem. Intermed. 39; 2881–2915.

He, R.X., Liang, R., Peng, P. and Zhou, Y.N., 2017. Effect of the size of silver nanoparticles on SERS signal enhancement. Journal of Nanoparticle Research, 19(8), p.267.

Ho Y.S., 2006. Second-order-kinetic model for the sorption of cadmium onto tree fern: a comparison of linear and non-linear methods, Water Res. 40 119–125.

Ho YS , Ng JCY , McKay G ., 2000. Kinetics of pollutant sorption by biosorbents: review. Sep Purif Methods; 29:189–232 .

Hunter, P. R., MacDonald, A. M., Carter, R. C., 2010. Water Supply and Health. PLoS Med 7(11): e1000361. https://doi.org/10.1371/journal.pmed.1000361

Jevtić, M., Mitrić, M., Škapin, S., Jančar, B., Ignjatović, N., Uskoković, D., 2008. Crystal structure of hydroxyapatite nanorods synthesized by sonochemical homogeneous precipitation. Cryst. Growth Des, 8, 2217–2222.

Jin Ho Bang and Kenneth S. Suslick., 2010. Applications of Ultrasound to the Synthesis of Nanostructured Materials- A review. Adv. Mater. 22, 1039–1059. DOI: 10.1002/adma.200904093

Joseph, S. and Mathew, B., 2013. Synthesis of Silver Nanoparticles by Microwave irradiation and investigation of their Catalytic activity. Research Journal of Recent Sciences, 3, pp.185-191.

Kalsi, P.S., 2007. Spectroscopy of organic compounds. New Age International.

Kamble, S. P., Jagtap, S., Labhsetwar, N. K., Thakare, D., Godfrey, S., Devotta, S., Rayalu S. S., 2007. Defluoridation of drinking water using chitin, chitosan and lanthanum modified chitosan. Chemical Engineering Journal; 129:173-80

Kim, J. and der Bruggen B.V. 2010. The use of nanoparticles in polymeric and ceramic membrane structures: review of manufacturing procedures and performance improvement for water treatment, Environ. Pollut. 158, 2335–2349.

Kousalya G.N., M. Rajiv Gandhi, C. Sairam Sundaram, S. Meenakshi, 2010. Synthesis of nano-hydroxyapatite chitin/chitosan hybrid biocomposites for the removal of Fe(III), Carbohydr. Polym. 82 594–599.

Krishnaraj C., E.G. Jagan, S.Rajasekar, P. Selvakumar, P.T. Kalaichelvan, N. Mohan, 2010. Synthesis of silver nanoparticles using Acalypha indica leaf extracts and its antibacterial activity against water-borne pathogens, Colloids Surf. B 76 50–56.

Kuppusamy, P., Yusoff, M.M., Maniam, G.P. and Govindan, N., 2016. Biosynthesis of metallic nanoparticles using plant derivatives and their new avenues in pharmacological applications–An updated report. Saudi Pharmaceutical Journal, 24(4), pp.473-484.

Lagergren S., 1898. Zur Theorie der sogenannten adsorption geloster stoffe, K. Sven. Vetenskapsakad. Handl. 24 1–39.

Langmuir I., 1916. The constitution and fundamental properties of solids and liquids, J. Am. Chem. Soc. 38 2221–2295.

Leung Y.H., Ng A., Xu X., Shen Z., Gethings L. A., Wong M.T., Chan C., Guo M. Y., Ng Y. H., Djuris˘ic´ A. B. 2014. Mechanisms of antibacterial activity of MgO: non-ROS mediated toxicity of MgO nanoparticles towards Escherichia coli. Small 10(6):1171–1183

Li, Q., Mahendra, S., Lyon, D. Y., Brunet, L., Liga, M. V., Li, D., & Alvarez, P. J., 2008. Antimicrobial nanomaterials for water disinfection and microbial control: potential applications and implications. Water research, 42(18), 4591-4602.

Loganathan, P., Vigneswaran, S., Kandasamy, J., & Naidu, R. 2013., Defluoridation of drinking water using adsorption processes. Journal of Hazardous Materials, 248, 1–19.

Medellin-Castillo N.A., R. Leyva-Ramos, E. Padilla-Ortega, R.O. Perez, J.V. Flores-Cano, M.S. Berber-Mendoza., 2014. Adsorption capacity of bone char for removing fluoride from water solution. Role of hydroxyapatite content, adsorption mechanism and competing anions, J. Ind. Eng. Chem. 20 4014–4021.

Mohapatra, M., Anand S., Mishra, B.K., Dion E. Giles, Singh P., 2009. Review of fluoride removal from drinking water. Journal of Environmental Management 91 (2009) 67–77

Mudzielwana et al., 2017. Synthesis and physicochemical characterization of MnO_2 coated Na-bentonite for groundwater defluoridation: Adsorption modelling and mechanistic aspect. Applied Surface Science 422 (2017) 745–753

Muhammad Rafique, Iqra Sadaf, M. Shahid Rafique & M. Bilal Tahir., 2016. A review on green synthesis of silver nanoparticles and their applications, Artificial Cells, Nanomedicine, and Biotechnology, DOI: 10.1080/21691401.2016.1241792

Mumtaz, N., Pandey, G. and Labhasetwar, P.K., 2015. Global fluoride occurrence, available technologies for fluoride removal and electrolytic defluoridation: a review. Critical Reviews in Environmental Science and Technology, (just-accepted), pp.00-00.

Muthu Prabhu, S., Meenakshi, S., 2014. Enriched fluoride sorption using chitosan supported mixed metal oxides beads: synthesis, characterization and mechanism. J. Water Process Eng. 2, 96e104.

Oladoja N.A., B. Helmreich, H.A. Bello., 2016. Towards the development of a reactive filter from green resource for groundwater defluoridation, Chem. Eng. J. 301166–177.

Onyango, M.S. and Matsuda, H., 2006. Fluoride removal from water using adsorption technique. Advances in fluorine science, 2, pp.1-48.

Pedley Stephen and Guy Howard, 1997. The public health implications of microbiological contamination of groundwater. Quarterly Journal of Engineering Geology, 30, 179-188. 0481-2085/97

Poinern, Gérrard Eddy Jai, Malay K. Ghosh, Yan-Jing Ng, Touma B. Iss,ShashiAnand, and Pritam Singh, 2011. Defluoridation behavior of nanostructured hydroxyapatite synthesized through an ultrasonic and microwave combined technique. Journal of Hazardous Materials 185. 29–37.

Poralan, G. M. Jr., Gambe, J. E., Alcantara, E. M., and Vequizo, R. M., 2015. X-ray diffraction and infrared spectroscopy analyses on the crystallinity of engineered biological hydroxyapatite for medical application. IOP Conf. Series: Mater Sci Eng 79: 012028. doi:10.1088/1757-899X/79/1/012028

Pradeep, T., Anshup, in: Savage, N., Diallo, M., Duncan, J., Street, A. and R. Sustich (Eds.)., 2009. Nanotechnology Applications for Clean Water, William Andrew Publication, USA.

Rajeshkumar, S., and Bharath, L. V., 2017. Mechanism of plant-mediated synthesis of silver nanoparticles–A review on biomolecules involved, characterisation and antibacterial activity. Chemico-Biological Interactions.

Ramesh, M., Malathi, N., Ramesh, K., Aruna, R.M. and Kuruvilla, S., 2017. Comparative evaluation of dental and skeletal fluorosis in an endemic fluorosed district, Salem, Tamil Nadu. Journal of pharmacy & bioallied sciences, 9(Suppl 1), p.S88.

Rashmi R. Devi , Iohborlang M. Umlong , Prasanta K. Raul , Bodhaditya Das , Saumen Banerjee and Lokendra Singh., 2014. Defluoridation of water using nano-magnesium oxide, Journal of Experimental Nanoscience, 9:5, 512-524, DOI: 10.1080/17458080.2012.675522

Rao C.R.N., J. Karthikeyan, 2012. Removal of fluoride from water by adsorption onto lanthanum oxide, Water Air Soil Pollut. 223 1101–1114.

Rayhaneh Amooaghaie, Mohammad Reza Saeri, Morteza Azizi. 2015. Synthesis, characterization and biocompatibility of silver nanoparticles synthesized from Nigella sativa leaf extract in comparison with chemical silver nanoparticles. Ecotoxicology and Environmental Safety, Volume 120, Pages 400-408.

Richardson, S.D., 2003. Disinfection by-products and other emerging contaminants in drinking water. TrAC Trends in Analytical Chemistry, 22(10), pp.666-684.

Santos, H. M., Lodeiro, C. and Capelo-Martínez, J. 2009. The Power of Ultrasound. In Ultrasound in Chemistry, J. Capelo-Martínez (Ed.). doi:10.1002/9783527623501.ch1

Sathiya, C.K. and Akilandeswari, S., 2014. Fabrication and characterization of silver nanoparticles using Delonix elata leaf broth. Spectrochimica Acta Part A: Molecular and Biomolecular Spectroscopy, 128, pp.337-341.

Sawant S.S., A.C. Anil, V. Krishnamurthy, C. Gaonkar, J. Kolwalkar, L. Khandeparker, D. Desai, A.V. Mahulkar, V.V. Ranade, A.B. Pandit, 2008. Effect of hydrodynamic cavitation on zooplankton: a tool for disinfection, Biochem. Eng. J. 42 320–328.

Shahin, H. and Mady, E. 2014. Nanocomposite Electrospun Nanofibers Membrane, Materials 7, 1017-1045; doi: 10.3390/ma7021017

Shannon, M. A., Bohn, P. W., Elimelech, M., Georgiadis, J. G., B. J. Marinas and A. M. Mayes. 2008. Nature, 2008, 452, 301–310.

Sharma, V.K.; Yngard, R.A. and Lin, Y., 2009. Silver nanoparticles: Green synthesis and their antimicrobial activities. Adv. Colloid Interface Sci., 145, 83–96.

Slavin, Y. N., Asnis, J., Häfeli, U. O., & Bach, H. 2017. Metal nanoparticles: understanding the mechanisms behind antibacterial activity. Journal of Nanobiotechnology, 15, 65. http://doi.org/10.1186/s12951-017-0308-z

Snson J.S., Baker, L.A., Fox, P., 1999. Geochemical transformations during artificial groundwater recharge: soil–water interactions of inorganic constituents, Water Res. 33 196–206.

Srimurali, M., Pragathi, A., and Karthikeyan J. 1998. A study on removal of fluorides from drinking water by adsorption onto low-cost materials, Environ. Pollut. 99, 285–289.

Srivastava V.V., M.M. Swamy, I.D. Mall, B. Prasad, I.M. Mishra., 2006. Adsorptive removal of phenol by bagasse fly ash and activated carbon: equilibrium, kinetics and thermodynamics, Colloids Surf. A 272 89–104.

Subbaiah Muthu Prabhu, Sankaran Meenakshi., 2014. Synthesis of surface coated hydroxyapatite powders for fluoride removal from aqueous solution, Powder Technology 268; 306–31. ISSN 0032-5910, https://doi.org/10.1016/j.powtec.2014.08.041.

Sundrarajan, M., Suresh, J. and Gandhi, R. R., 2012. A comparative study on antibacterial properties of MgO nanoparticles prepared under different calcination temperature. Digest Journal of Nanomaterials and Biostructures, 7, 983-989.

Sundaram, C. S., Viswanathan, N., and Meenakshi, S., 2008. Defluoridation chemistry of synthetic hydroxyapatite at nano scale: equilibrium and kinetic studies. Journal of Hazardous Materials, 155(1–2), 206–215.

Sundaram, C. S., Viswanathan, N., and Meenakshi, S., 2009. Defluoridation of water using magnesia/chitosan composite. Journal of Hazardous Materials, 163(2–3), 618–624.

Sundaram C. S., Viswanathan, N., Meenakshi, S., 2008. Uptake of fluoride by nanohydroxyapatite/ chitosan, a bioinorganic composite, Bioresour. Technol. 99 8226–8230.

Sushma, N.J., Prathyusha, D., Swathi, G., Madhavi, T., Raju, B.D.P., Mallikarjuna, K. and Kim, H.S., 2016. Facile approach to synthesize magnesium oxide nanoparticles by using Clitoria ternatea—characterization and in vitro antioxidant studies. Applied Nanoscience, 6(3), pp.437-444.

Tang, Zhen-Xing, & Lv, Bin-Feng., 2014. MgO nanoparticles as antibacterial agent: preparation and activity. Brazilian Journal of Chemical Engineering, 31(3), 591-601. https://dx.doi.org/10.1590/0104-6632.20140313s00002813

Tufenkji, N. and Emelko, M.B., 2011. Groundwater Pollution: Impacts on Human Health: Fate and Transport of Microbial Contaminants. Encyclopedia of Environmental Health, J. Nriagu, Ed., Elsevier Publishing Inc.

UK Groundwater Forum., 2011. Groundwater and Pathogens. Available online: http://www.groundwateruk.org/Groundwater-issues-pathogens.aspx (accessed on April 2017).

USGC., 2016. Contaminants Found in Groundwater Available online: http://water.usgs.gov/edu/groundwater-contaminants.html (accessed on July 2017)

Veerasamy, R., Xin, T.Z., Gunasagaran, S., Xiang, T.F.W., Yang, E.F.C., Jeyakumar, N. and Dhanaraj, S.A., 2011. Biosynthesis of silver nanoparticles using mangosteen leaf extract and evaluation of their antimicrobial activities. Journal of Saudi Chemical Society, 15(2), pp.113-120.

Vermeulan T.H., Vermeulan K.R. and Hall L.C., 1966. Fundamental‘‘ Ind. Eng. Chem. 5, p212–22

Veselinović, L., Karanović, L., Stojanović, Z., Bračko, I., Marković, S., Ignjatović, N. and Uskoković, D., 2010. Crystal structure of cobalt-substituted calcium hydroxyapatite nanopowders prepared by hydrothermal processing. Jnl Applied Crystallography, 43: 320–327. doi: 10.1107/S0021889809051395

Weber, W. J., Morris, J. C., 1964. Equilibria and capacities for adsorption on carbon, J. Sanitary Eng. Div. 90 79–91.

WHO, 2000. Global Water Supply and Sanitation Assessment 2000 Report, World Health Organization, 92 4 156202 1, Geneva, Switzerland

WHO, Guidelines for drinking water quality, forth ed., World Health Organization, Geneva, 2011.

World Health Organization and UNICEF, 2017. Progress on drinking water, sanitation and hygiene: 2017 update and SDG baselines. World Health Organization.

WHO/UNICEF JMP (Joint Monitoring Programme for Water Supply and Sanitation)., 2010. JMP Rapid Assessment on Drinking-water Quality pilot report 2010. 8-10.

Wilson, R.M., Elliott, J.C., Dowker, S.E.P., 1999. Am. Mineral, 84, 1406.

Zhu Xiwei, Dan Wu, Wei Wang, Fatang Tan, Po Keung Wong, Xinyun Wang, Xiaolin Qiu, Xueliang Qiao., 2016. Highly effective antibacterial activity and synergistic effect of Ag-MgO nanocomposite against Escherichia coli, In Journal of Alloys and Compounds, Volume 684 , Pages 282-290, ISSN 0925-8388.

CHAPTER SIX

GREEN SYNTHESIS OF AgMgOnHAP NANOPARTICLES SUPPORTED ON CHITOSAN MATRIX: DEFLUORIDATION AND ANTIBACTERIAL EFFECTS IN GROUNDWATER

Introduction

This main part of this chapter focuses on the Green Synthesis of AgMgOnHaP nanoparticles supported on Chitosan matrix. The defluoridation and antibacterial application in groundwater were explored and reported. This output of this chapter was prepared as an article under review for publication in Springer Environmental Science and Pollution Research Journal.

W. B. Ayinde; W. M. Gitari; Samie Amidou; M. Munkombwe and James Smith (2019**). Green Synthesis of AgMgOnHaP nanoparticles supported on Chitosan matrix: defluoridation and antibacterial effects in groundwater** (Submitted to *Springer Environmental Science and Pollution Research*), (Manuscript ID: ESPR-D-19-02543) (Under Review).

,

Green Synthesis of AgMgOnHaP nanoparticles supported on Chitosan matrix: defluoridation and antibacterial effects in groundwater

Wasiu Babatunde Ayinde[a*], Wilson Mugera Gitari[a], Munkombwe Muchindu[b], Amidou Samie[c], James Smith[d]

[a]Environmental Remediation and Nanoscience (EnviReN), Department of Ecology and Resource Management, School of Environmental Sciences. University of Venda, Private Bag X5050, Thohoyandou, 0950, Limpopo Province, South Africa.; mugera.gitari@univen.ac.za

[b]Mintek, South Africa, Advanced Materials Division (Nanotechnology Innovation Centre). MunkombweM@mintek.co.za

[c]Molecular Parasitology and Opportunistic Infections Program, Department of Microbiology, School of Mathematical and Natural Sciences. University of Venda. samie.amidou@univen.ac.za

[d] Engineering Systems and Environment., School of Engineering and Applied Science, University of Virginia, Charlottesville, Virginia. jsmith@virginia.edu

*Correspondence: email: twasiu33@gmail.com; Tel. +27 838734688

Abstract

This study demonstrates the development of new metal-metal oxide nanoparticles impregnated on a chitosan polymer backbone (AgMgOnHaP@CSn) using sol-gel biosynthesis approach and its potential application in removing fluoride and pathogens from groundwater. The identification and properties of the nanocomposite have been carried out using different surface morphology and mineralogical techniques such as UV–vis spectroscopy, SEM-EDS, XRD, FTIR, and TEM. The formation of the nano-adsorbent from the different surface functionalization precursors and phases were supported by the various characterization methods. A mesoporous adsorbent with a BET surface area of 55.27 m^2/g at an average size of about 35.36 nm and a pore diameter of 33.67 nm was synthesized. Batch fluoride sorption experiments were conducted based on the optimization of several operational parameters. The adsorption kinetic mechanisms followed the pseudo-second-order with the rate demining step controlled by diffusion model phenomenon. The sorption of fluoride by AgMgOnHaP@CSn on the surface and interfacial chemistry was best described by the Langmuir isotherm model with the sorption capacity of 6.86 mg/g at 303 K and pH 7. In addition, the antibacterial activity of AgMgOnHaP@CSn was shown against both gram-positive and gram-negative bacteria.

Keywords: Biosynthesis; AgMgOnHaP@CSn nanocomposite; simultaneous fluoride and pathogen removal

6.1 Introduction

The consumption of adequate potable water is an important part affecting the overall well-being of every human life at every social level. In conventional water treatment, the removal of waterborne pathogens in addition to other toxic inorganic chemical pollutants is one of the major concern in relation to the provision of potable drinking water in developing areas of the world. The World Health Organisation in its annual progress reports estimated around 1.8 billion people use heavily polluted contaminated source of drinking water resulting in more than 200 million death every year (WHO and UNICEF 2014; 2017). Water from the public water-treatment systems aimed at preventing and protecting people found in those areas from such contaminants are often less reliable in terms of supplying the required water quality. Groundwater is used as an alternative water supply for potable and domestic purposes by over 50% of the global population, especially in developing countries (Gitari *et al*. 2013; Jadhav 2015). However, due to natural and anthropogenic processes, the quality of this water source may be jeopardized by toxic inorganic and pathogenic pollutants leading to health problems and in some cases death over a long period of consumption.

One of such contaminants associated with many aquifers is fluoride. The rapid increase in fluoride contamination of groundwater has become a recurring global problem to human health. Fluoride is one of the common anions found naturally in different water resources and generally leached into groundwater by slow dissolution of fluorine-based mineral rocks and through anthropogenic activities (García and Borgnino 2015). Several studies on the health benefit associated with the acceptable amount (< 1.5 mg/L) of fluoride for human growth and development has been reported (Jones et al. 2005; Armfield 2010; Peckham and Awofeso 2014). However, excess intake of fluoride (> 1.5 mg/L) can cause various non-skeletal detrimental health diseases and in severe cases leading to dental or crippling skeletal fluorosis; depending upon the dosage and period of ingestion (Ayoob *et al*. 2008; Edition 2011). Moreover, the majority of global water-related outbreaks are often associated with the consumption of microbiologically-contaminated water sources; which are responsible for an estimated 2.2 million deaths worldwide (Ashbolt 2004; Bitton 2014). The purification of water disinfection by use of traditional methods such as chlorination, boiling and ultraviolet (UV) irradiation is rapidly becoming a major challenge due to the formation and release of harmful carcinogenic disinfection by-products (DBPs) and utilization of high amounts of energy (Hijnen 2006; Chlorine Chemistry Council and American Chemistry Council 2006).

The focal points by various researchers towards the reduction of fluoride concentration and pathogens in groundwater have been on the use of a sustainable, eco-friendly type of materials and technologies in order to increase the selectivity and disruption of such pollutants for effective water treatment. Such established material and technologies together with their mode of operation and mechanisms have been critically reviewed and reported (Mohapatra *et al*. 2009; Jadhav 2015; Yadav *et al*. 2018). However, these methods often create some drawbacks, which further

compromise the quality of the water and adversely affects human health. These include the introduction of toxic by-products, low adsorption rate, the high cost of energy and operational cost, etc. Although adsorption through the use of different sorbent materials is termed as the effective technique for water purification, research is tasked to find a sustainable, multifunctional, and integrated materials with the potential for ion-exchange and microbial disinfection in water.
Nowadays, the development and functionalization of polymer-based composites as potential water treatment material is increasing. Biopolymeric sorbents have been documented to be well suited for the removal of different water-related contaminants such as fluoride and microorganism, even at low concentration (Kamble et al. 2007; Viswanathan and Meenakshi 2010; Lai *et al*. 2019). With more emphasis on surface functionality and improved specific surface area in composite materials, the introduction of nanophase metal/metal oxide decorated on a natural polymer in the development of an efficient synergistic hybrid material in a multitude of water treatment applications is on the rise.

Sustainable natural biopolymers such as cellulose, chitosan, and starch, which are in abundance have been exploited and regarded as a significant template in the polymeric-based adsorbent. This is simply due to the ease of functionalization, non-toxic, biodegradable, structural diversity and the tendency to increase adsorptive capacities of metal ions as well as antimicrobial properties in water purification (Guibal 2004; Li *et al*. 2010; Wang 2018; Sekar, and Manickam 2019).
In order to improve the water-related burden, we have recently reported the successful development of a multi-functional metal/metal oxides composite using green methods for fluoride and pathogen removal from water (Ayinde *et al*. 2018a; 2018b). However, in this study, a comprehensive approach to the improvements of this composite material was investigated through the development of a novel metal-metal oxide impregnated chitosan (AgMgOnHaP@CSn). Its potential for fluoride removal in an aqueous system using various adsorption parameters was evaluated and the experimental data were fitted to the different sorption kinetics and isotherm models. In addition, microbial studies were carried out to evaluate the possible antimicrobial property of the adsorbent simultaneously with the fluoride removal process with a focus on improving water quality at the household level for safe human consumption.

6.2 Materials and methods

6.2.1 Materials

All chemicals were of analytical reagent grade. Highly viscous Chitosan (CS) from crab shell (Degree of N-deacetylation of 95%) was purchased from Sigma-Aldrich. $Ca(NO_3)_2.4H_2O$, KH_2PO_4, $Mg(NO_3)_2.6H_2O$, $AgNO_3$, $NaClO_2$, H_2SO_4, NaF, NaOH, acetic acid (glacial, 99-100%), and other chemicals used were purchased from Rochelle chemicals, South Africa and used directly without further purification. Ultrapure Milli-Q water (18.2 MΩ/cm) was used in the preparation and dilution of standards throughout the experiment.

6.2.2 Preparation of nanohydroxyapatite (nHaP)

Synthetic nanohydroxyapatite (nHaP) was prepared as described by Poinern *et al*. (2011) by reacting 40 mL of 0.32 M $Ca(NO_3)_2 \cdot 4H_2O$ with 60 mL of 0.19 M KH_2PO_4 solution under continuous stirring with the Ca/P ratio maintained at 1.67. Subsequently, aqueous NH_4OH (25%) was added dropwise to adjust the pH value to 9, and the solution was stirred for 6h and thereafter left to age for 24 h at room temperature. During the mixing process, the pH value was continually checked and maintained at 9 (using NH_4OH). The composite solution was thereafter subjected to ultrasound agitation at 100% amplitude (0.5 cycles) for 1 h. The product obtained after the sonication was filtered and dried at 40 ◦C in an oven for 24 h before being ground into a fine powder.

6.2.3 Preparation of AgMgOnHaP@chitosan nanocomposite

The AgMgOnHaP@CSn nanocomposite was prepared by sol-gel method. An aqueous homogeneous solution of bio-reduced seed growth Ag-MgO mixture was prepared as described in our earlier work published elsewhere (Ayinde *et al*. 2018a). The bio-reduced Ag-MgO solution mixture was slowly added to 1 % wt./v chitosan solution (highly viscous >400 mPa.s, 1% (v/v) acetic acid (40 °C)) under continuous stirring for 2h. The bio-process growth kinetics of the Ag-MgO on a chitosan network was monitored using UV–Vis spectroscopy. To this continuously stirred bio-reduced reaction mixture (AgMgO@CSn), 5 g of nHaP was dispersed into the mixture and was vigorously stirred for 6 h at room temperature and thereafter, the solution mixture was neutralized with 1 M NaOH solution to induce precipitation. The obtained precipitate was rinsed severally with ultrapure Milli-Q water (18.2 MΩ/cm), filtered and oven-dried at 50 °C for 24 h to obtain the AgMgOnHaP@CSn composite powder, which was subsequently used for the tests.

6.2.4 AgMgOnHaP@CSn Composite characterization and analysis

The bioprocess kinetics seed growth was monitored using SPECTROstar Nano/ BMG LABTECH UV-Visible Spectrophotometers in the wavelength range 220–600 nm. The main functional reactive groups of the synthesized AgMgOnHaP@CSn composite were recorded by using Bruker: ALPHA FT-IR Spectrophotometer (4000-400 cm^{-1}) with 24 scans. Surface morphology and elemental analysis of the composite were characterized using SEM and SEM-EDX with an FEI Nova NanoSEM 230 with the field emission gun equipped with an Oxford Xmax SDD detector operating at an accelerating voltage of 20Kv for the EDS detector (Oxford X-Max with INCA software). Transmission electron microscopy (TEM) images were taken using an FEI Tecnai20 equipped with a LaB6 emitter, operating at 200 kV and fitted with a Gatan Tridiem GIF with a 2kX2k CCD camera. Images were collected using the Digital Micrograph suite of programs in relation to size and shape. The surface area, pore area and pore volume of the synthesized nanocomposite were measured using nitrogen adsorption Brunauer–Emmett–Teller (BET) surface area and porosity analyzer (Micromeritics ASAP2020). The adsorption-desorption plots were used to calculate the specific surface area. The surface interaction and composition of the fluoride loaded sorbent was studied by the X-Ray Photoelectron Spectrometer Microprobe (XPS) (Thermo Scientific ESCAlab 250Xi,), with a monochromatic Al Kα X-ray source (1486.7 eV). The high-

resolution scans were conducted according to the peak being examined with a pass energy of 20 eV (Pressure <10-8 mBar) and spot size of 900 µm with a wide survey scan between 0-1300 eV. Fluoride ion and pH measurements were determined using a fluoride ion-selective electrode (9609 BNWP Orion, USA) coupled to an ISE/pH/EC electrode (Thermo SCIENTIFIC-ORION VERSA STAR Advanced Electrochemistry meter fluoride ion-selective electrode) calibrated with four fluoride standards containing TISAB III.

6.2.5 pH at point-of-zero-charge (pHpzc)

The pH at a point-of-zero charge of AgMgOnHaP@CSn was determined in 1 M, 0.1 M and 0.01M KCl solutions for consistency of results. The pH of solutions was adjusted to desired values by adding 0.1 M HCl or 0.1 M NaOH. The new pH, therefore, constituted the initial pH (pHi) of solutions. Aliquots of 25 mL of solutions were pipetted into 50 mL plastic bottles. A mass of 0.25 g of adsorbent was then weighed into each of the bottles. The bottles were corked and shaken inside a thermostated water bath shaker at 150 rpm for 24 h. After equilibration, the equilibrium pH (pHe) of each mixture was quickly measured and recorded.

6.2.6 Batch Fluoride adsorption experiments

Batch fluoride sorption studies were performed and evaluated on the synthesized AgMgOnHaP@CSn towards the removal of fluoride in simulated fluoride-rich water. The effects of contact time, pH, adsorbent dose, and co-existing ions on the equilibrium adsorption capacity were optimized. Standard stock fluoride ion solution (1000 mg/L) was prepared by dissolving 2.210 g NaF into 1000 mL of ultrapure water at ambient condition. The desired fluoride solution was prepared by appropriate dilution of the standard stock solution. Batch adsorption experiments were carried out by mixing 225 mg of AgMgOnHaP@CSn with 50mL of 10 mg/L F^- solution. The mixture was shaken thoroughly using a reciprocating shaker (STUART SSL2) at 250 rpm. The solution was then filtered, and the residual fluoride ion concentration was determined. The pH values of the solution were adjusted by 0.1 mol/L HCl or NaOH. The effect of co-existing anions on the defluoridation efficiency of the adsorbent was evaluated at anion concentration of 100 mg/L in a 10 mg/L fluoride solution. The adsorption isotherm experiments were conducted by varying fluoride concentrations within the range of 5–100 mg/L in a constant-temperature water-bath shaker in the temperature range of 303; 313 and 323 K. Adsorption isotherms and kinetic models were adopted and used to model adsorption data. All the experiments were conducted in triplicate, and the mean of the results computed. Equations 1 and 2 were used to determine the percentage fluoride removal and adsorption capacity, q_e (mg/g) of the adsorbent.

$$\%\ \text{Adsorption} = \frac{(C_o - C_e)}{C_o} \times 100 \qquad (1)$$

$$q_e = (C_O - C_e) \times \frac{V}{m} \qquad (2)$$

Where: C_o is the initial F^- concentration (mg/L); C_e is the F^- concentration at equilibrium (mg/L); V is the volume of solution (L) and m is the dried mass of the adsorbent (g).

6.2.7 Statistical tools

The computations were done using OriginPro 8.SR0 and Excel software. The best-fit sorption models were analyzed using the linear and non-linear analysis, Adjusted correlation coefficient (Adj. R^2) and chi-square analysis ($\chi 2$) were computed.

6.2.8 Evaluation of antimicrobial activity

Antimicrobial susceptibility test was analyzed from the observed zone of inhibition (mm) using the standard Agar-Well disc diffusion methods (Kirby Bauer disk diffusion test). The indicator strains used were Escherichia *coli* (ATCC 35218) and *Staphylococcus aureus* (ATCC 33591). 1 mg/mL of the synthesized AgMgOnHaP@CSn nanocomposites were prepared and dispersed in ultrapure Milli-Q water (18.2 MΩ/cm) using an ultrasonicator bath (SCIENCETEC, Model 705). Mueller Hinton agar (MHA) was used for the cultivation of freshly grown bacteria at turbidity of 0.5 McFarland suspension. 50 µL of each strain was spread on 20 mL of solidified and dried agar plates. Wells were punctured at equidistance using sterile pipette tips. 50 µL (1 mg/mL) of AgMgOnHaP@CSn was dispensed into the wells already inoculated with the bacterial cell suspension. The plates were incubated at 37◦C for 24 h and the observed zone of inhibition was measured and recorded. The processes were performed in duplicates.

6.3 Results and Discussion

6.3.1 FT-IR study

Fig. 6.1 shows the characteristic peaks associated with the surface functional reactive groups between the pure chitosan and the synthesized nanoparticle-chitosan matrix nanocomposites. The FTIR spectra display the main functional groups on both materials surfaces, which include broad bands variation ranging between 3038-3349, 2882-2927, and 2037-2080 cm^{-1} corresponding to the stretching vibration of -OH groups in form of phenols, alcohols, absorbed water or carboxylic acids; asymmetric and symmetric C-H bond (CH_3 and CH_2) groups of chitosan, and other various metabolites within the extracts used for the bioreduction (Kalsi 2007). The well-distinct peaks at 1640 and 1546 cm^{-1} corresponds to C=O of an amide group (C=ONHR) and the vibrations of amine group NH_2. These peaks were observed to have shifted to 1667 cm^{-1} and disappeared respectively in the nanocomposite. Thus, the shifting and complete disappearance of these peaks (-OH, C=O and NH_2) is an indication of their respective possible surface interaction in the overall reduction of the Ag and MgO ions into nanoparticles dispersed in the polymer matrix (Frindy *et al*. 2015; Singh et al. 2018; Ayinde *et al*. 2018a). The presence of bending vibration of methylene groups in the region of 1354-1357 cm^{-1} and asymmetric vibration of C-O groups at 1150 cm^{-1} is evident from the spectra. Furthermore, characteristic peaks associated with the hydroxyapatite and Mg-O absorption within the composite appear at 1425, 1022 and 552 cm^{-1} which are attributed to the vibrational mode of CO_3^{2-}, the asymmetric phosphate group, PO_4^{3-} stretching and bending modes, Mg–O-Mg deformation (Koutsopoulos 2002; Balamurugan *et al*. 2014). Similar vibrational bands of these groups have been reported in our previous studies (Ayinde *et al*. 2018b).

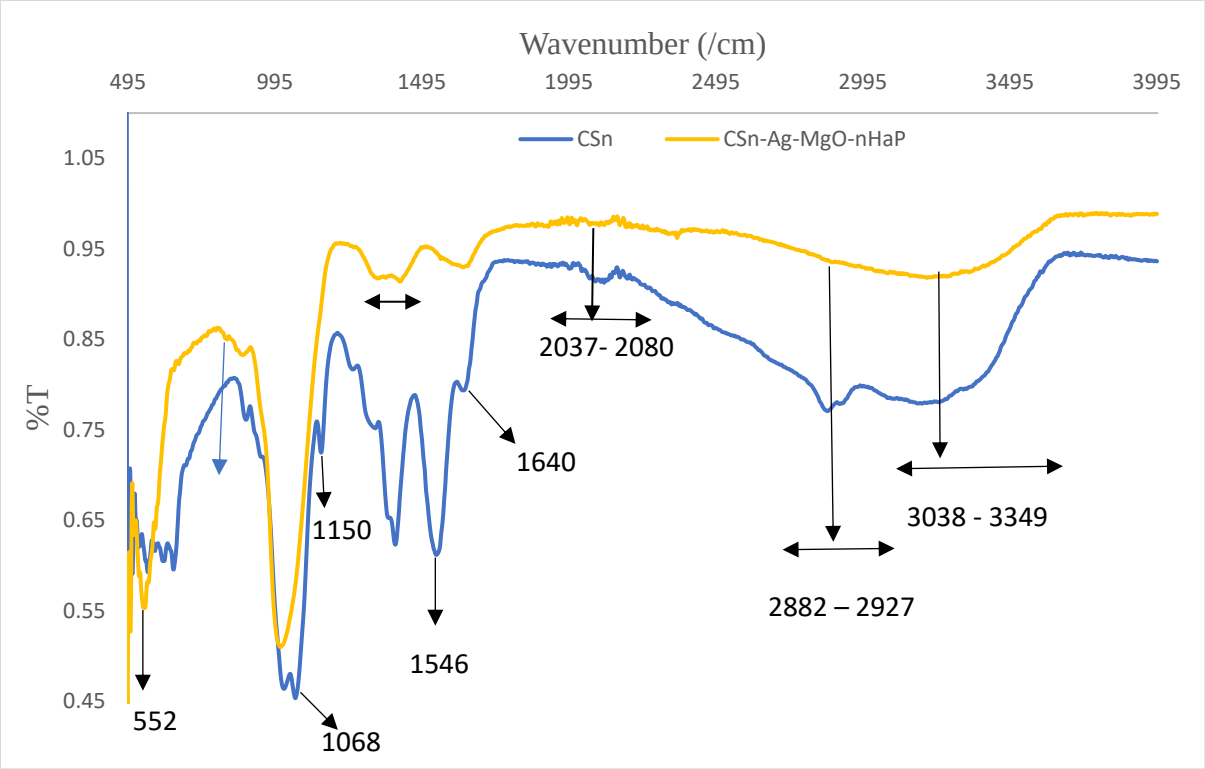

Fig. 6.1. FTIR spectra of CSn and AgMgOnHaP@CSn nanocomposite**.**

6.3.2 UV–Vis absorption analysis

The UV–vis absorption spectra of the pure chitosan and the respective hybrids of biosynthesized Ag-MgO reinforced chitosan nanocomposite is displayed in Fig. 6.2. The presence of the metal ion nanoparticles within the chitosan layer is depicted by the different absorption bands, with an increase in the absorption wavelength upon the nanoparticle impregnation. As shown in the spectrum, the absence of Ag and MgO nanoparticles in the polymer matrix was confirmed by the absence of an absorption band in the pure chitosan. However, the sum of each component of the mixture was affirmed by the emergence of a sharp peak appearing at around 290 nm to a broad plateau plasmon absorbance above 440 nm on the Ag-MgO reinforced chitosan composite clearly indicates the bio-reduction processes of both Ag and MgO ions due to the interaction and coordination of bonds within the bioactive functional species within the peel extracts as well as the –OH and $–NH_2$ groups of the chitosan polymer matrix (Higazy et al. 2010; Kuppusamy et al. 2016), thus, resulting in the formation of biomolecular capped Ag-MgO nanocomposite dispersed in the polymer matrix. The color variation of the nanoparticle-chitosan (from light yellow to dark brown), the intensity of the band in the low-UV region at 290 nm typical of MgO together with broadband ranging between 410 and 440 nm associated with AgNps are similar to our earlier report (Ayinde et al. 2018a). Chitosan polymer matrix served as anchoring sites, allowing stabilization of the nanoparticles throughout the polymeric surfaces. The nucleation, growth and optical properties of these nanoparticles across the chitosan are attributed to the mutual vibration of

electrons of metal nanoparticles in resonance with lightwave serving and UV-shielding ability of MgO nanoparticles as the basis for measuring adsorption of the material onto the surface of metal nanoparticles (Anandalakshmi *et al*. 2016; De Silva *et al*. 2017).

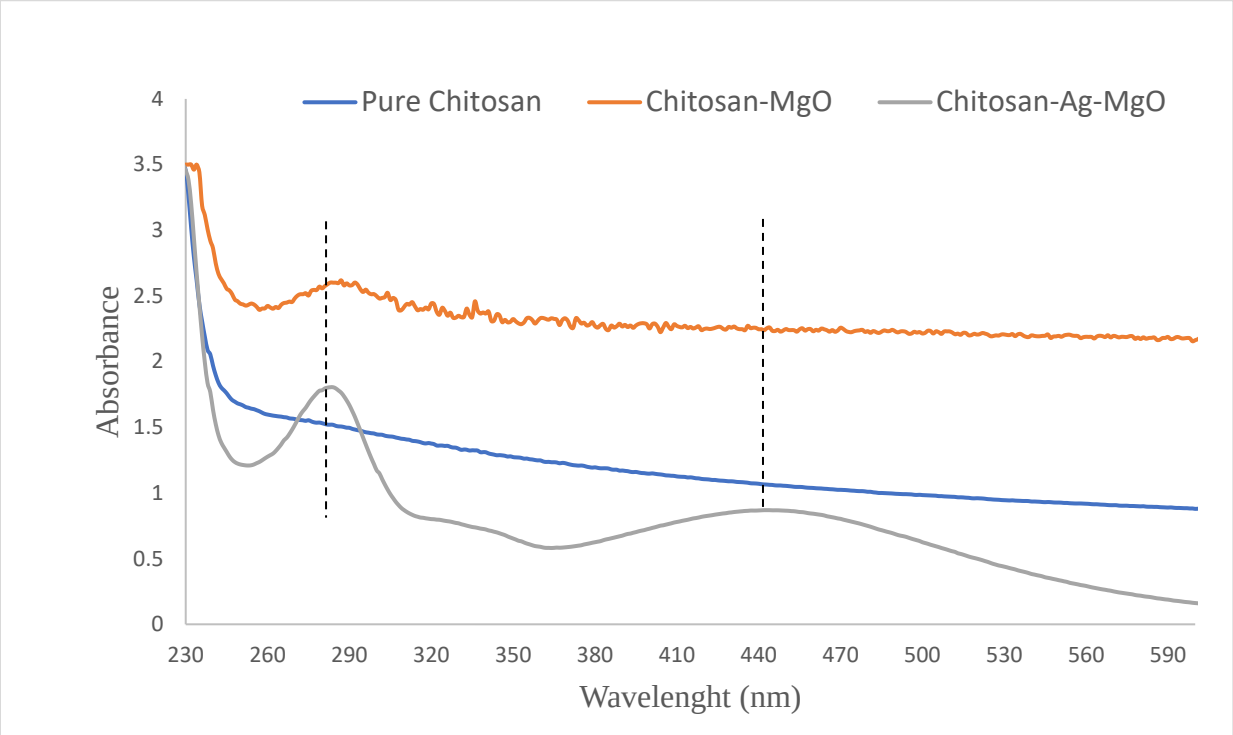

Fig. 6. 2. UV-visible spectra of CSn and CSn-Ag-MgO nanocomposite.

6.3.3 Surface electron micrograph analysis

The different structural and morphological transformations induced during the synthesis and application of AgMgOnHaP reinforced chitosan network in fluoride removal is shown in Figs. 6.3 (a-e). Figs. 6.3 (a-c) represent the photographic images of the dried bio-reduced surface-modified chitosan nanofibers upon dispersion of AgMgO and hydroxyapatite nanoparticles respectively. As explained in the optical study (UV-vis), the color transformation is an indication of the impregnation of the AgMgO nanoparticles across the biopolymeric composite. Furthermore, the introduction of hydroxyapatite changes the structural surface of the composite from fibrous-like (6.3 (a) and (b)) to irregular granules (6.3 (c)). This was further illustrated and supported by the SEM and TEM images with their respective elemental compositions (EDS) as displayed in Fig. 6.3 (d-e). The AgMgOnHaP nanoparticles appeared to be homogeneously dispersed within the aggregated biopolymeric composite with a diameter ranging between 5-30 µm. The EDS mappings show the formation of AgMgOnHaP@CSn based on the different elemental peaks as well as its ability to successfully adsorb fluoride on its surface through the inherent chemical compositions and presence of fluoride peak (Fig. 6.3(e)).

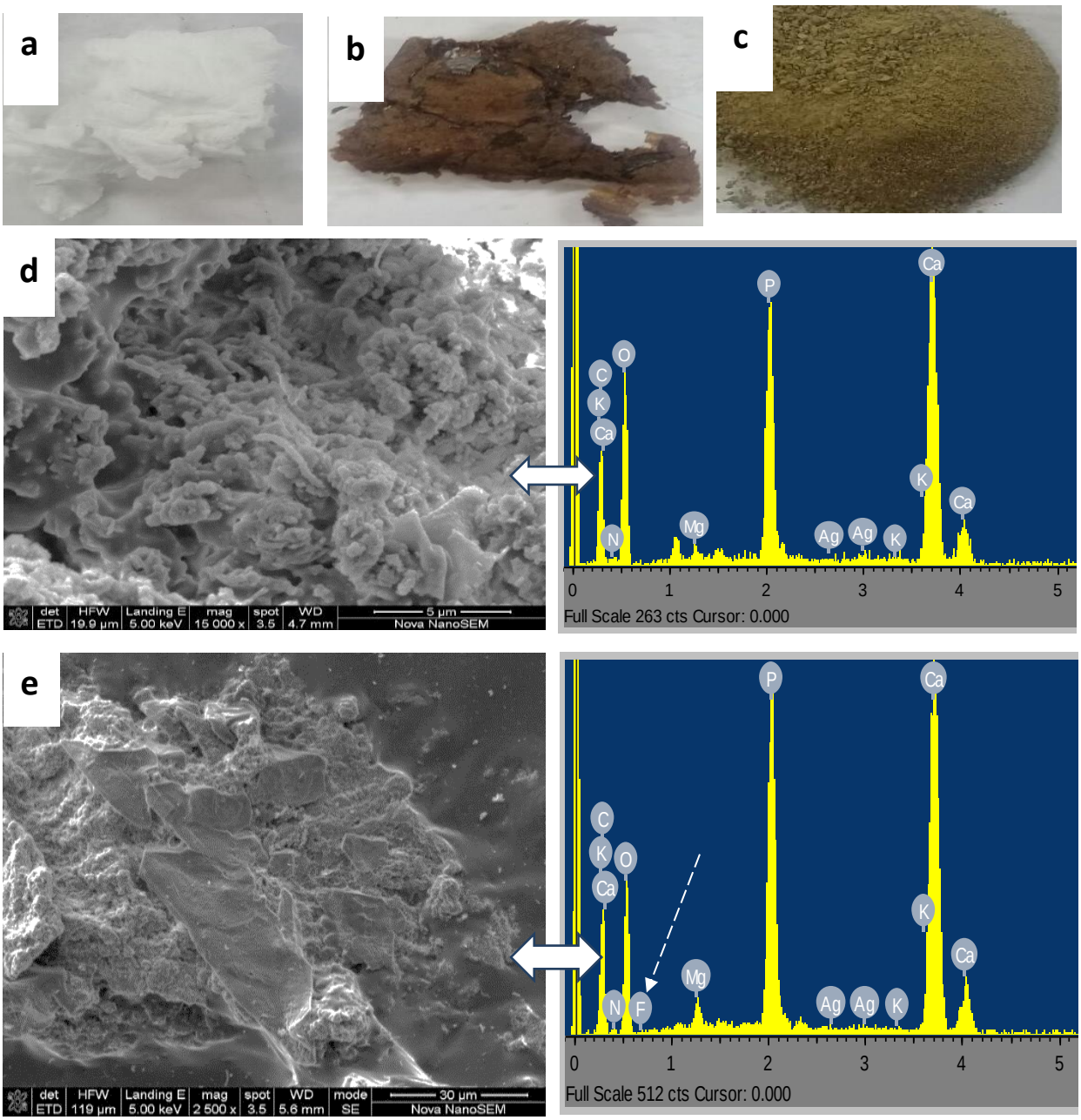

Fig. 6.3. Photographic images of pure chitosan (a); AgMgO@CSn (b); AgMgOnHaP@CSn (c); SEM-EDS images of AgMgOnHaP@CSn (x15,000) (d) and fluoride-sorbed AgMgOnHaP reinforced chitosan nanocomposite (x 2500) (e).

Fig. 6.4 shows the TEM micrograph of AgMgO/nHaP reinforced chitosan nanocomposite at different magnifications. The images reveal an aggregation of uniformly mixed biopolymeric nanocomposite and mostly spherically-stretched in shape, which appeared elongated in the assemblies of polymer with an average particle size distribution ranging from 10 to 200 nm.

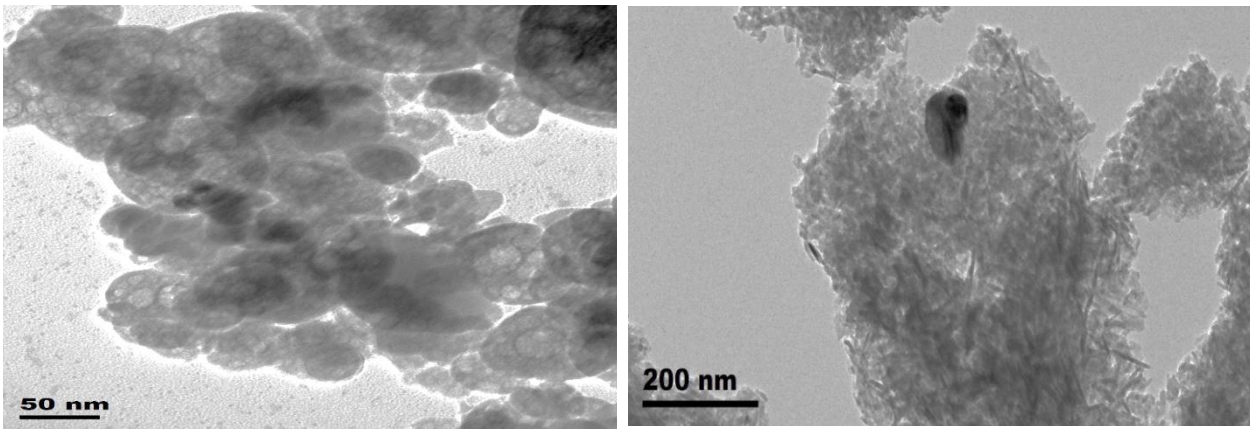

Fig. 6.4. TEM images of AgMgO/nHaP reinforced chitosan nanocomposite at different magnification.

The Brunauer–Emmett–Teller (BET) surface areas of AgMgOnHaP@CSn bio-sorbents determined from the N_2 adsorption isotherm by surface area and porosity analyzer (Micromeritics ASAP2020) was estimated to be 55.27 m²/g with a pore volume of ~ 0.48 cm^3/g. The composite micropore and mesopore area is 2.37 m²/g and 57.08 m²/g respectively, with an average size of about 35.36 nm and a pore diameter of 33.67 nm. The obtained values confirm that the surface structure of AgMgOnHaP@CSn sorbent has a distribution of mesopores (Sing 1985).

6.4 Batch adsorption studies

6.4.1 Kinetics analysis on fluoride sorption by AgMgOnHaP@CSn nanocomposite

The adsorption kinetics of any sorbent-sorbate solution process depends on the time of interaction of the solution mixture. Fig. 6.5(a) shows the sorption of fluoride ions onto AgMgOnHaP@CSn nanocomposite at different contact time ranging from 2 to 60 min. This was conducted with an initial fluoride concentration of 10 mg/L with an adsorbent load of 225 mg per 50 mL at a rotation speed of 250 rpm. As shown in the sorption plot, the percentage uptake of fluoride increased swiftly as the time of exposure increases between 2 and 25 mins with more than 75 % uptake, followed by a slow sorption process, which became constant from 30 mins up until 60 min. The rapid rate of fluoride being adsorbed on the composite is simply due to the synergistic effects by the assembly, leading to creation and availability of more active functional groups (binding sites) with improved surface area to attach F^- ions on the AgMgOnHaP@CSn. However, the relatively slow sorption phenomenon between 30 and 60 min may be attributed to the saturation of the fluoride active binding sites on the composite surface, thus, reaching attainment to the equilibrium of the sorption process. Consequently, the contact time of 30 min was chosen as the optimum time for the adsorption of F^- onto the AgMgOnHaP@CSn nanocomposite and was used in subsequent experiments.

Furthermore, in order to investigate the factors controlling rate-limiting step of the fluoride sorption process, the linear fittings of the Lagergren pseudo-first and the pseudo-second-order kinetic models together with the intra-particle diffusion model (Lagergren 1898; Weber and Morris

1964; Ho *et al*. 2000) were used to fit the experimental data. The mathematical expressions of these three models are given in Eqs. (2), (3) and (4), respectively.

$$\log(q_e - q_t) = \log q_e - \frac{K_1}{2.303} t \quad (2)$$

$$\frac{t}{q_t} = \frac{1}{K_2 q_e^2} + \frac{t}{q_e} \quad (3)$$

$$q_t = k_i t^{0.5} + C \quad (4)$$

where q_e and q_t are the amounts of fluoride adsorbed by the adsorbent ($mg.g^{-1}$) at equilibrium and at time t (min), respectively; with K_1, K_2, and K_i (min^{-1}) representing the rate constant of the pseudo-first-order, pseudo-second-order, intraparticle diffusion respectively. C is a constant related to the thickness of the boundary layer ($mg\ g^{-1}$).

The kinetic fitting plots, as well as their respective modelling parameters values obtained, are shown in Figs. 6.5 (b–d) and Table 6.1. The obtained correlation coefficients fittings for the kinetic model linear plots suggests that fluoride sorption favorably suited the pseudo-second-order rate law (0.999); an assumption that the process involves an exchange or sharing of electrons leading to the formation of a bond between the active binding sites on the AgMgOnHaP@CSn surface and the fluoride ions (Ruthven 1984). This surface interaction was supported by the XPS and EDS spectra. In addition, the fluoride sorption system is also governed by the intra-particle diffusion mechanism through the pores of the nanocomposite (Fig. 6.5(d)); which is sectionalized into three different linear phases. The sorption steps were more rapid in the first and second stages; which is an attribution of intraparticle-diffusional process (Machado *et al*. 2012), while phase 2 provided the best correlation coefficient data than other phases (phase 2 > phase 1> phase 3) followed by the attainment of equilibrium at phase 3 where the rate of the fluoride sorption is insignificant (as indicated by the contact time plot). These phase dynamics is dependent on the mesoporous nature of the material, which enables easy accessibility to the active sites by the fluoride ions through the pore width (Dąbrowski, 2001).

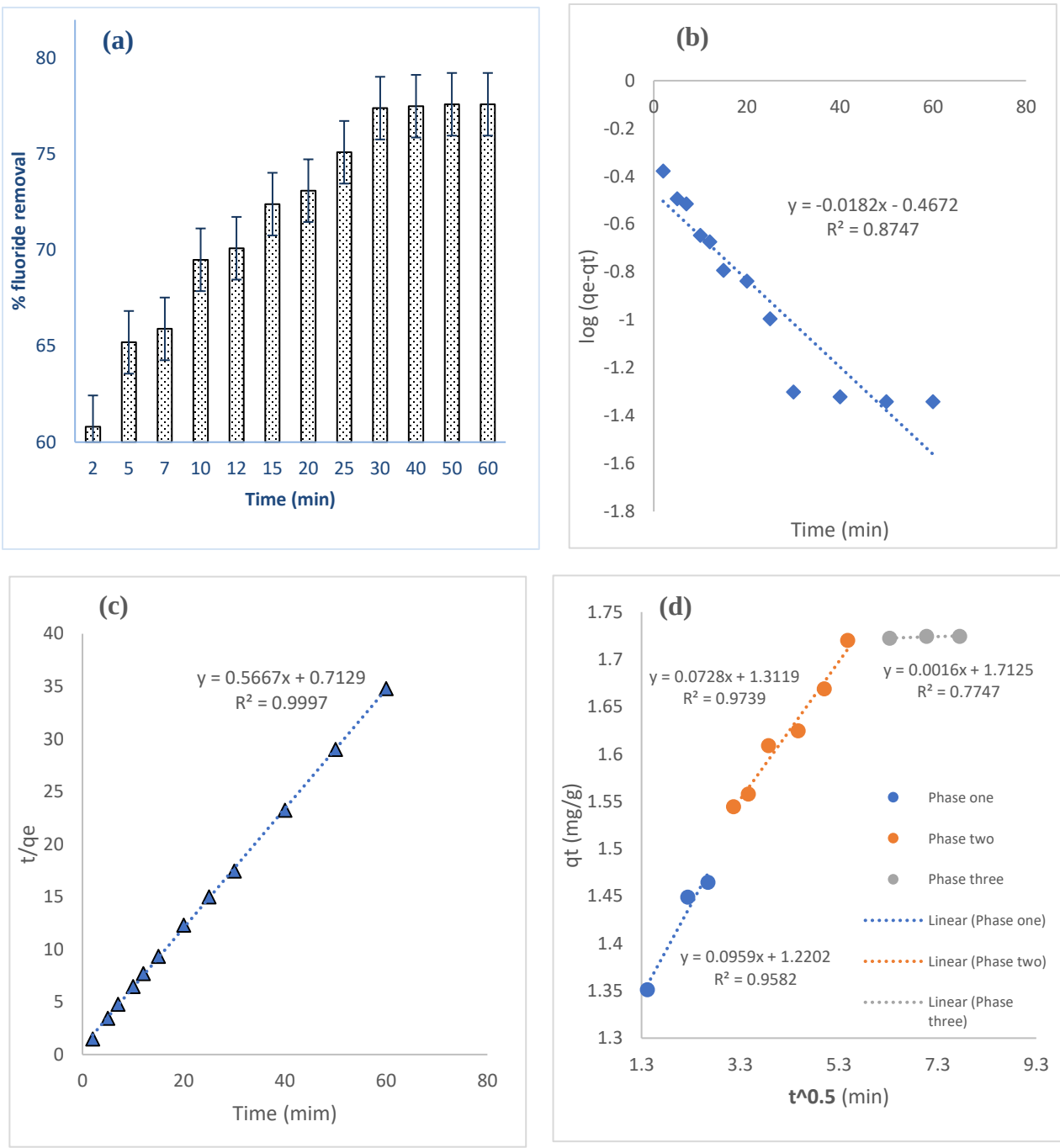

Fig. 6.5. (a) Effect of contact time; (b) Lagergren pseudo-first-order kinetics; (c) Pseudo-second-order kinetics; and(d) intraparticle diffusion model on fluoride removal by AgMgOnHaP@CSn nanocomposite (initial F^- concentration 10 mg/L, dose 225 mg per 50 mL at room temp with an agitation speed of 250 rpm).

Table 6.1. Kinetic model parameters of F^- uptake by AgMgOnHaP@CSn nanocomposite

Pseudo-first-order kinetic model			**Pseudo-second-order kinetic model**		
q_{cal} (mg/g)	k_1 (min^{-1})	R^2	q_{cal} (mg/g)	k_2 (g/min mg)	R^2
0.341	0.0419	0.8747	1.765	0.45	0.9997

Intra-particle diffusion equation								
C_1 (mg/g)	K_{i1} (mg/g.$min^{0.5}$)	R^2_1	C_2 (mg/g)	K_{i2} (mg/g.$min^{0.5}$)	R^2_2	C_3(mg/g)	K_{i3} (mg/g.$min^{0.5}$)	R^2_3
1.22	0.096	0.9582	1.3119	0.0728	0.9739	1.7125	0.0016	0.7747

6.4.2 Effect of solution pH and point of zero charge (pH_{pzc}) on fluoride sorption

The state of the ionic strength phenomenon on the sorbent-solution interface was determined by pH and point of zero charge analysis. In the adsorption process, the solution pH is an important parameter due to its role in the ionization/dissociation degree between the sorbent-sorbate interfaces (Wu *et al*. 1999). Fig. 6.6 (a) shows the effect of solution pH from 3 to 12 on the adsorption of fluoride by AgMgOnHaP@CSn nanocomposite. As shown in the graph, the percentage uptake of F^- increased as the solution pH increases from 3 to 7 with maximum fluoride uptake at pH 7. Thereafter, the rate of fluoride removal by the sorbent decreases gradually as the pH increases from 7 to 9 and drops sharply at a pH of 12. The fluoride sorption efficiency by this composite in the solution pH is a function of the functional groups (-OH and $-NH_2$) acting as the binding site, which chemically affects fluoride uptake during the sorbent-sorbate interaction. Firstly, the dissociation equilibrium of chitosan group in aqueous solution is pH-dependent, this is because many primary amine groups possesses a pKa ranging between 6.1 and 6.3, which makes chitosan a weak base (Craver and Carraher 2000). Therefore, in acidic solution, most of the amino groups of chitosan in the composite will be protonated and presented in the form of NH_3^+, thus, making the sorbent-sorbate interaction to be more of electrostatic attraction. Subsequently, at higher pH the amino groups with the polymer matrix are deprotonated resulting in electrostatic repulsion between F- and NH_3^+ ions hence decreasing the adsorption process. Secondly, the sorbate-sorbent surface adsorption mechanism is also dependent on chemisorption based on the -OH group. This is made possible by the small ionic size of the fluorine atom and its ability to possibly act as a hydrogen bond acceptor thus enabling fluorine to be substituted for the hydroxyl group thereby increasing the binding affinity at the weak acidic region (Abeles and Alston 1990). Also, at higher pH competition from O-H group is much stronger in this solution medium with the F^- anion, resulting in a decrease in the fluoride adsorption capacity (Rao and Karthikeyan 2012).

Similar reports on the mechanisms of adsorption by chitosan groups occurring simultaneously have been reported by different kinds of literature, where it was concluded that physical and chemical surface interaction occurring with multilayer adsorption played an important role in the adsorption processes (Uzun and Güzel 2005; Sakkayawong *et al*. 2005).

Fig. 6.6(b) shows the effect of the pH point of zero charge (pH_{pzc}) of AgMgOnHaP@CSn nanocomposite on fluoride removal as a function of initial solution pH. The pH_{pzc} is the pH value at which the surface of an adsorbent is required to have a net neutral charge. The pH_{pzc} value was obtained to be ~ 10.6 for AgMgOnHaP@CSn composite. Consequently, comparing Figs. 6.6 (a) and (b), the obtained values indicated that pH < pH_{pzc} leading to the conclusion that the increase in fluoride sorption was due to the predominating positive charges at the surface of the AgMgOnHaP@CSn adsorbent, which favors the anion exchange phenomenon between the sorbent-sorbate system.

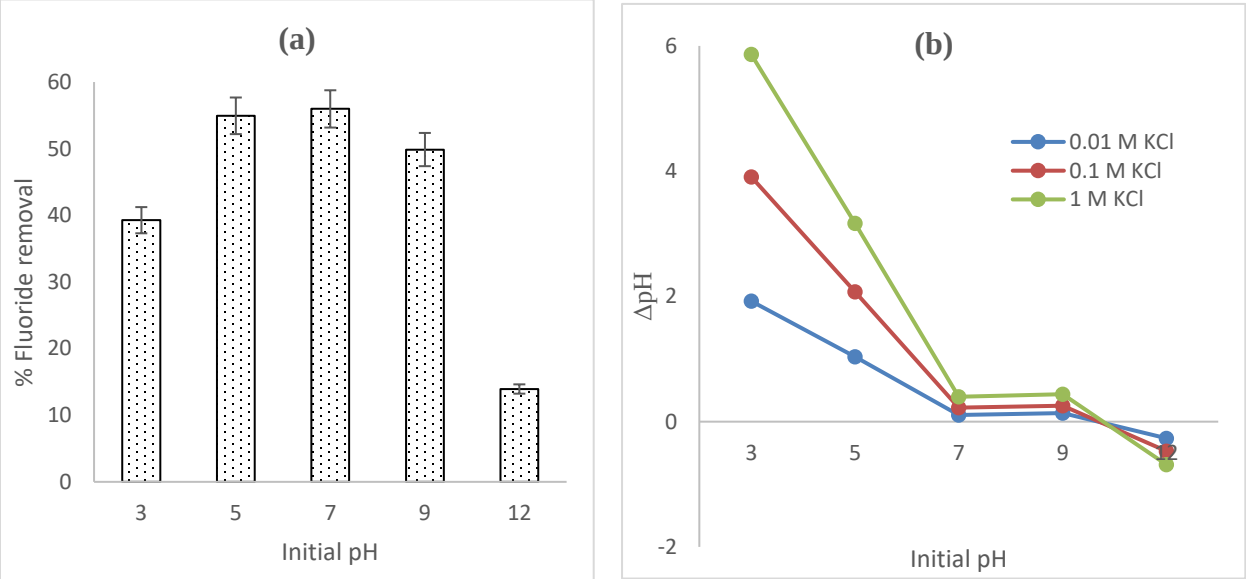

Fig. 6.6. (a) Percentage fluoride uptake by AgMgOnHaP@CSn nanocomposite; (b) pHpzc of AgMgOnHaP@CSn as a function of pH (initial F^- concentration 10 mg/L, dose 225 mg per 50 mL at room temp with an agitation speed of 250 rpm)

6.4.3 Effect of AgMgOnHaP@CSn dosage

Fig. 6.7 shows the effect of AgMgOnHaP@CSn dose ranging from 0.1 to 0.35 g as a function of fluoride sorption at an initial adsorbate concentration of 10 mg/L. As observed in the adsorption plot, the percentage removal of fluoride increased with increase in sorbent dosage, while the adsorption capacity of the adsorbent decreases. This phenomenon is associated with the creation of a greater number of active functional sites across the adsorbent surface, which enables more chemical interaction between the movement of fluoride ions to the sorbent interface and ultimately leading to more uptake of fluoride ions. This trend suggests that the BET specific surface area,

total porosity (pore volume and average pore width) of the AgMgOnHaP@CSn composites play an important role in the overall fluoride sorption process.

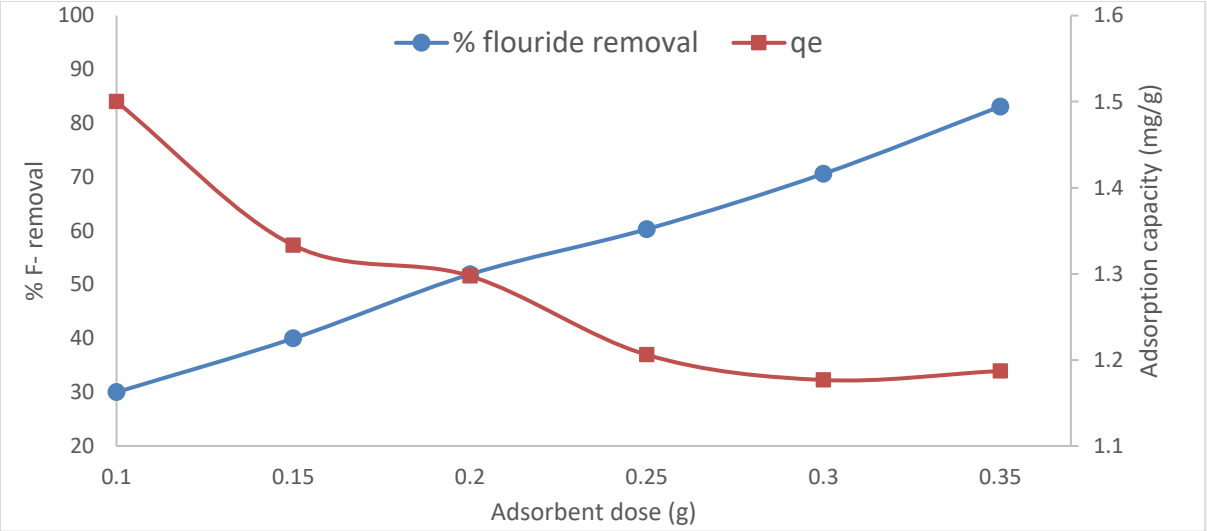

Fig. 6.7. Effect of AgMgOnHaP@CSn sorbent dosage on fluoride sorption (initial F^- concentration 10 mg/L, contact time of 40 min at room temp at an agitation speed of 250 rpm).

6.4.4 Fluoride sorption isotherms study

The fundamental relationship of fluoride sorption on the AgMgOnHaP@CSn sorbent underlying the mechanisms and dynamics of the adsorption systems process relative to the equilibrium concentration is described by adsorption isotherms models. In this study, the non-linear forms of Langmuir and Freundlich isotherm models (Freundlich 1906; Langmuir 1916) were used to fit and evaluate the fluoride sorption isotherm experimental data. The sorption isotherms parameters were obtained by using 250 mg of AgMgOnHaP@CSn per 50 mL of fluoride solution (5-100 mg/L) for a period of 40 min at different temperature and at an agitation speed of 150 rpm.

Equation (5) gives the non-linear Langmuir model, which is applicable to homogeneous adsorption systems describing monolayer adsorption systems in a sorbent-sorbate interface, and is written as follows:

$$q_e = \frac{Q_m K_L C_e}{1 + K_L C_e} \qquad (5)$$

where Q_m (mg/g) is the maximum adsorption capacity assuming a complete monolayer of an adsorbent, C_e (mg/L) is the equilibrium F^- ion concentration in the solution, q_e (mg/g) is the amount of F^- ion adsorbed per unit mass AgMgOnHaP@CSn sorbent at equilibrium, K_L (L/mg) is the Langmuir sorption equilibrium constant.

In addition, the fundamental characteristics of Langmuir isotherm can further be determined in terms of a dimensionless constant separation factor for the fluoride equilibrium parameter, R_L (Weber and Chakravorti 1974), which is expressed as:

$$R_L = \frac{1}{1 + k_L C_i} \qquad (6)$$

where Ci (mg/L) is the initial fluoride concentration and K_L is the Langmuir equilibrium constant The R_L value is useful in determining if an sorption process is irreversible (R_L= 0), linear (R_L= l), favorable (0 < R_L< 1) or unfavorable (R_L> l).

On the other hand, the Freundlich model (Freundlich, 1906) is used to describe the adsorption characteristics for a multilayer surface system, and the nonlinear empirical equation (7) is shown below as:

$$q_e = K_F C_e^{1/n} \qquad (7)$$

where q_e (mg/g) is the equilibrium sorption capacity of the adsorbent, C_e (mg/L) is the equilibrium concentration of the fluoride, K_F [(mg/g)/(mg/L)^n] and 1/n are empirical Freundlich constant and intensity parameter respectively; describing the strength and magnitude of the multilayer adsorption system. The adsorption isotherm is favorable when 0 < 1/n < 1, unfavorable when 1/n > 1 and irreversible when 1/n = 1.

Figures 6.8 (a-b) and Table 6.2 show the non-linear Langmuir and Freundlich isotherm plots as well as the respective obtained parameters for fluoride sorption by AgMgOnHaP@CSn sorbent at different experimental temperature. The experimental data described by the adsorption isotherm region (Fig. 6.8 a-b) show an increase in adsorption capacities as the fluoride concentration increases, which were later characterized by saturation at high concentration.
The respective adsorption isotherm model parameters (Table 6.2) reveal the effect of varying temperature on fluoride sorption capacity by AgMgOnHaP@CSn composite. The results demonstrate that the values of the Qm and K_L are not all consistent and decreases as the temperature increases, which is an indication that the adsorption phenomenon is governed by an exothermic process (Tran *et al*. 2016). Thus, a comparison of the obtained results by virtue of the non-linear regression coefficient (R^2) and lower chi-square ($\chi 2$) values respectively show that the sorption process is well-described according to the Langmuir monolayer isotherm model, with maximum sorption capacity of 6.88 mg/g at 313 K. The trend in the feasibility of the Langmuir model as observed by the values of the dimensionless constant, R_L which ranges 0 and 1, affirms the favorable uptake of the fluoride.

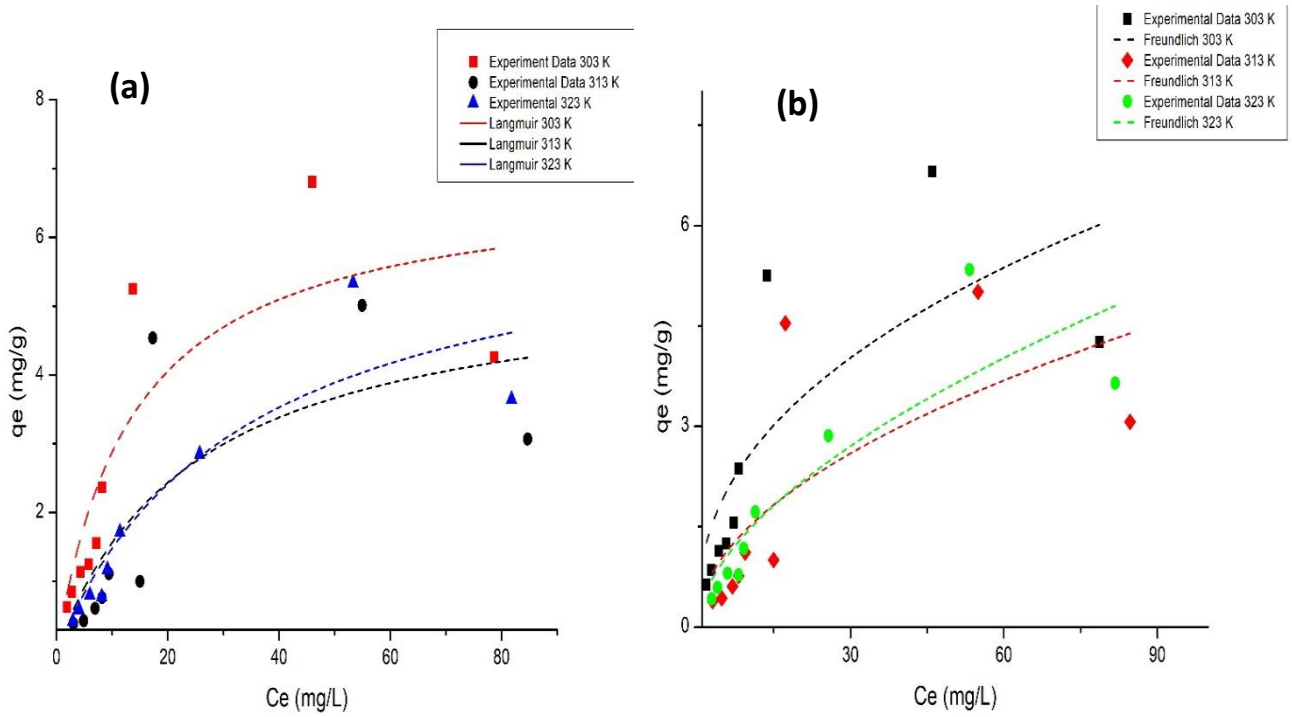

Fig. 6.8. (a) Langmuir; (b) Freundlich adsorption isotherms of fluoride onto AgMgOnHaP@CSn adsorbent at various temperatures.

Table 6.2. Adsorption parameters of fluoride removal by AgMgOnHaP@CSn adsorbent

T (K)	Non-Linear Langmuir isotherm					Non-Linear Freundlich isotherm			
	Qm (mg/g)	K_L (L/mg)	R_L	Adj. R^2	$\chi 2$	K_F [(mg/g)/(mg/L)n]	n	Adj .R^2	$\chi 2$
303	6.86	0.1	0.5	0.716	1.4	0.97	2.4	0.57	2.12
313	5.53	0.04	0.71	0.56	1.48	0.46	2	0.46	1.81
323	6.55	0.03	0.77	0.84	0.44	0.38	1.7	0.77	0.65

6.4.5 Influence of interfering co-ions

The effect of other typical co-existing anions present in the water on fluoride sorption using AgMgOnHaP@CSn sorbent is shown in Fig. 6.9. This was experimentally carried out by mixing 10 mg/L of fluoride ion with 100 mg/L of the respective co-existing anion. The result indicates a noticeable reduction in fluoride removal rate, especially with the carbonate anion. This can be explained by the fact that CO_3^{2-} in solution hydrolyzes to produce more hydroxyl ions, which compete with fluoride for sorption sites resulting in decreasing fluoride sorption efficiency by the adsorbent of fluoride.

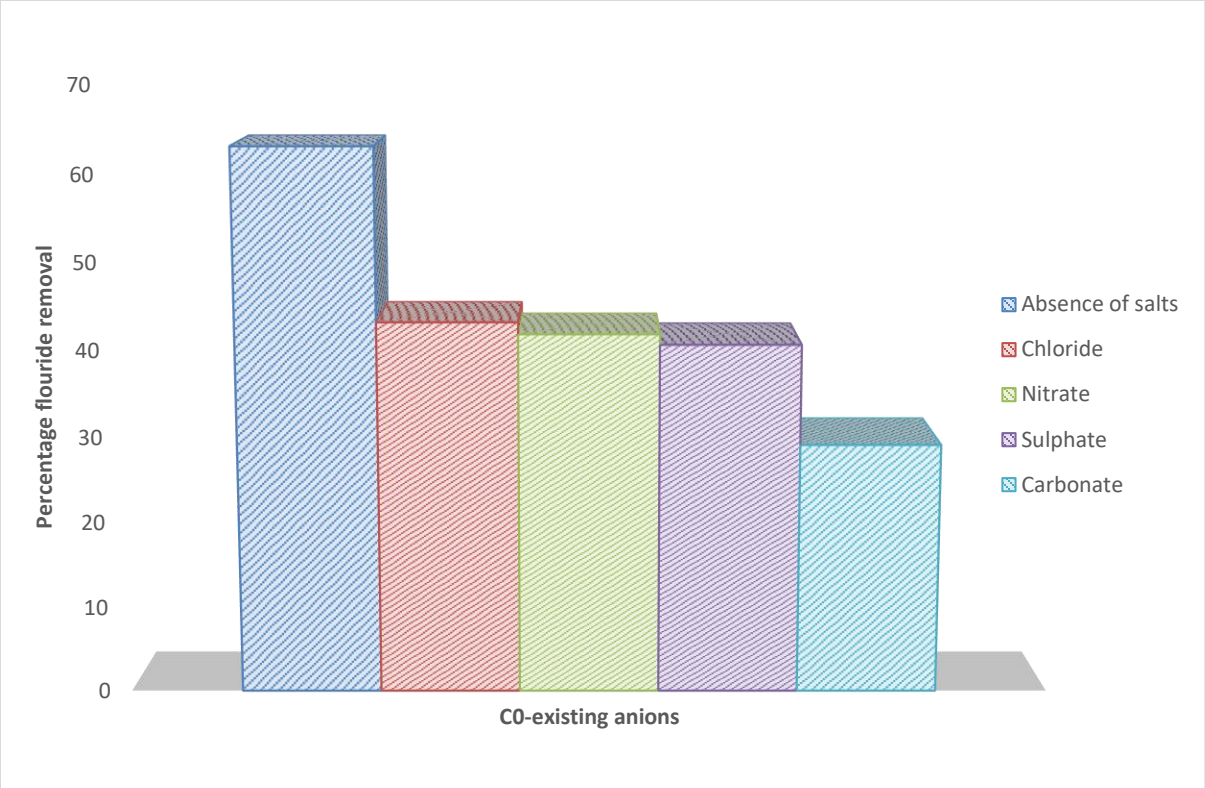

Fig. 6.9. Effect of different ions on fluoride removal by AgMgOnHaP@CSn (initial F^- concentration 10 mg/L, adsorbent dose: 0.25 g contact time of 40 min at room temp at an agitation speed of 250 rpm.

6.4.6 X-ray photoelectron spectroscopy and possible surface reactions

The mechanisms and possible interaction at the solution interface across the fluoride loaded AgMgOnHaP@CSn nanocomposite are presented by the XPS spectra in Fig. 6.10. The survey spectra show the presence of Mg, Ca, P, O, Ag and F together with C elemental signals, thus corroborating the interaction of F^- ions with the nanocomposite. The binding energy lines at around 533, 286.7, 349.1, 367.8, 134.6, 1307.8 and 686.9 eV are attributed to O 1s, C 1s, Ca 2p, Ag 3d, P 2p, Mg 1s and F 1s, respectively, thus, confirming the formation of AgMgOnHaP@CSn and its interaction with F^- without any other impurity. The C 1s peak showed four components: at 285, 286.2, 287.4 and 289.2 eV characteristics of C-C, C-O or C-N, C=O and O-C=O respectively (Moulder *et al*. 1995; Rouxhet and Genet 2011). The peak around 399.5 eV could be attributed to the N atom in the NH_2 and CN groups on the surfaces of the chitosan matrix. The O 1s peak was resolved into three components which were found near 531.6, 532.9 and 534.5 supporting the lattice O atoms with carbonyl and Mg atoms (Moulder *et al*. 1995; McIntyre and Chen 1998) The presence of the F 1s (686.9 eV) and Ca 2p (347.7 eV) is attributed to the product exchange of reaction between -OH and the F ion which could lead to the changes in surface and formation of Ca---F bonds.

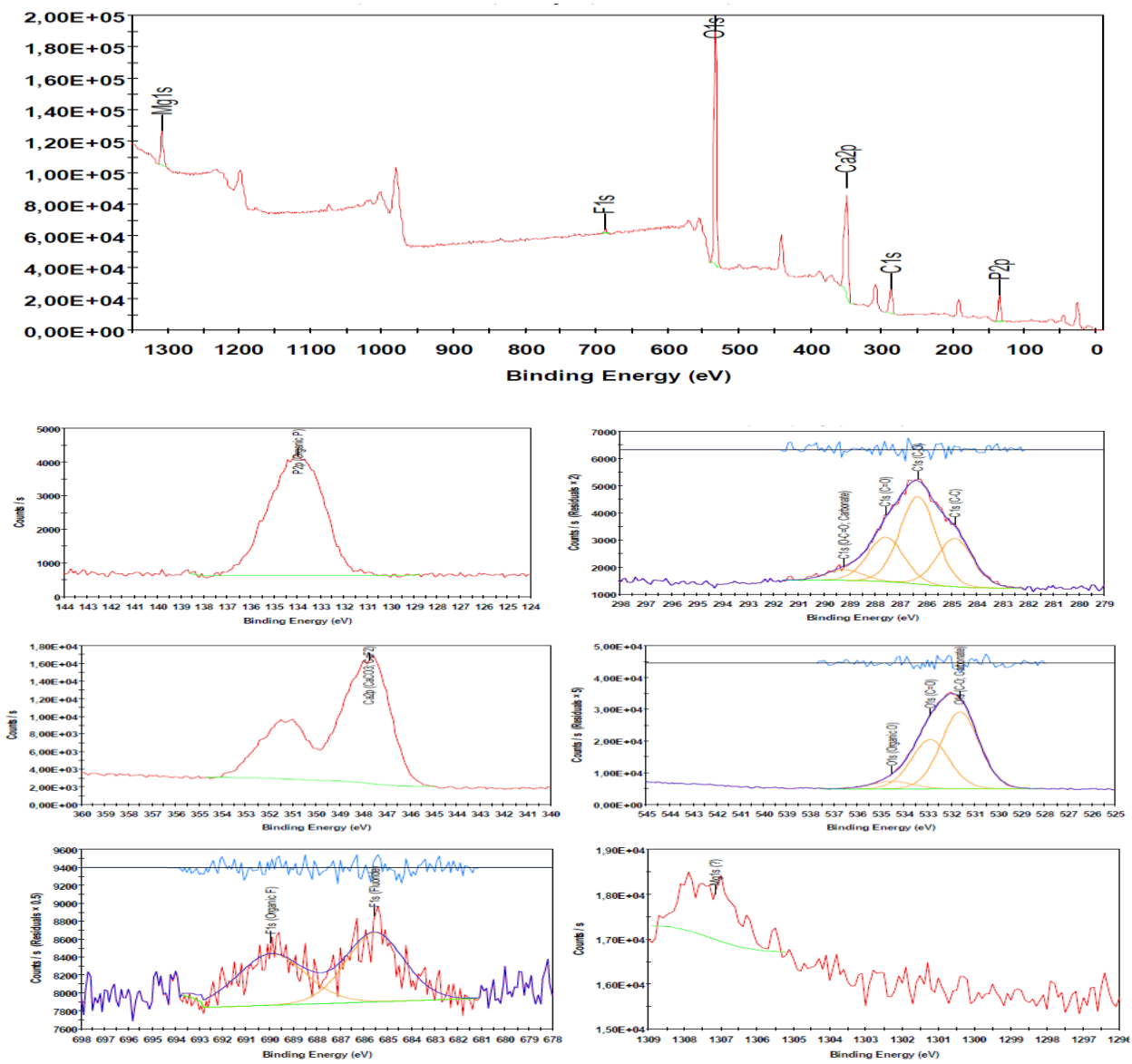

Fig. 6.10. XPS survey spectrum for fluoride loaded AgMgOnHaP@CSn with peak component positions

Based on the above findings, the possible surface mechanisms for fluoride removal by AgMgOnHaP@CSn indicate the presence of an assemblage of reactive binding active sites on the adsorbent surface. The XPS study further demonstrates the presence of fluoride as confirmed by the EDS, FTIR and pH analysis. These exchange binding sites include -OH, -MgO, -NH_2, and possible formation of NH_3^+ in solution, thus enhancing the fluoride sorption capacity. Therefore, the possible multiple mechanisms for the fluoride sorption by the sorbent was suggested in Fig. 6. 11. As explained earlier (pH and pHpzc), the predominating positive charges at the surface of the AgMgOnHaP@CSn adsorbent attracts the fluoride ion by electrostatic attraction. Furthermore, due to the -OH group and F− ion having similar ionic dimensions (Ayoob *et al*. 2008) upon hydroxylation, fluoride ions complete their coordination with the -OH group in the composite

through ion-exchange mechanisms. Also, the observed fluoride removal capacity by the AgMgOnHaP@CSn adsorbents may be attributed to several factors across the developed nanostructured phase such as the improved surface area and adsorptive pore-filling, as well as the relative hydrophilic character of the polymer matrix.

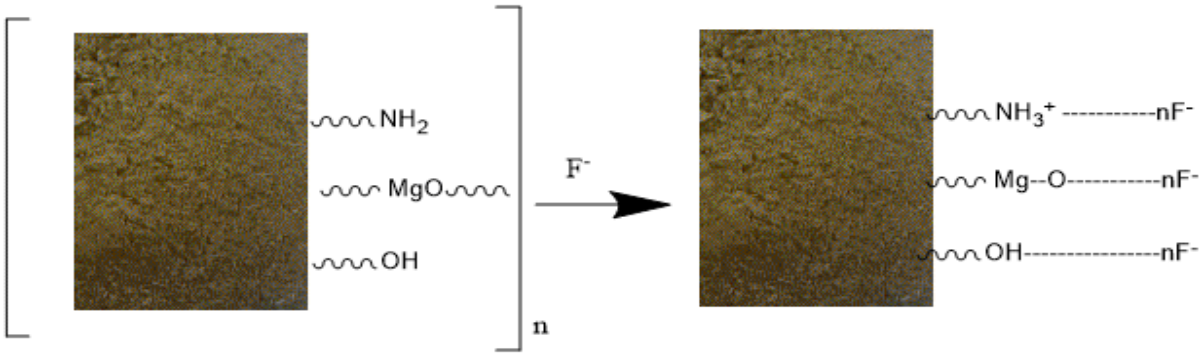

Fig. 6. 11. A possible mechanism of fluoride sorption by AgMgOnHaP@CSn composite.

6.5 Antimicrobial activity and probable mechanisms of action

The antimicrobial activity of the synthesized AgMgOnHaP@CSn nanocomposites against different bacterial strains is shown in Fig. 6.11 and Table 6.3 respectively. The zone of inhibition (mean and standard deviation) was measured to be higher for gram-positive *Staphylococcus aureus* (ATCC 33591) when compared to gram-negative *Escherichia coli* (ATCC 35218) (Table 6.3). The P-value is 0.2578, which is considered not significant while the t-test value is 2.333 with 1 degree of freedom. Studies and reviews have shown the potential of Ag, MgO and chitosan nanomaterials antibacterial properties against both gram-positive and gram-negative bacteria (Li *et al*. 2008; Raghunath and Perumal 2017; Ayinde *et al*. 2018a; Siddiqi *et al*. 2018). Therefore, the probable mechanism of AgMgOnHaP@CSn nanocomposites is attributed to the inherent synergistic antibacterial activity of these nanomaterials. Such synergistic properties include wide contact interaction due to larger surface area and surface charges between the bacterial cells' walls and AgMgOnHaP@CSn nanocomposite (Raafat *et al*. 2008; Lu *et al*. 2013).

Table 6.3. Antibacterial activity of the AgMgOnHaP@CSn nanocomposite.

	Zone of inhibition (mm)		
Microorganisms	**Mean**	**Std. Deviation**	**Std error of mean**
Staphylococcus aureus (ATCC 33591)	12	1.414	1
Escherichia coli (ATCC 35218)	8.9	0.7071	0.5

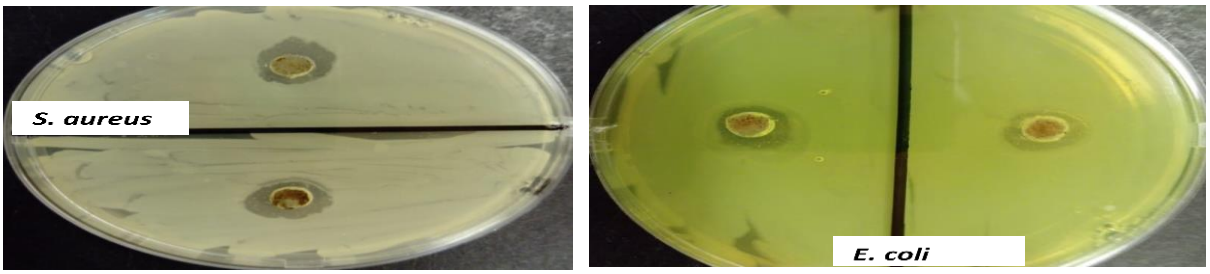

Fig. 6.11. Antimicrobial activity of AgMgOnHaP@CSn nanocomposites against Gram-positive *Staphylococcus aureus* (ATCC 33591) and Gram-negative *Escherichia coli* (ATCC 35218).

6.6 Comparison with other studies

The comparison of the fluoride sorption capacity of AgMgOnHaP@CSn with different composite sorbents; clearly show that the adsorption capacity of AgMgOnHaP@CSn is higher than most reported fluoride sorbents (Sundaram *et al*. 2008; Poinern et al. 2011; Devi 2012; Ayinde *et al*. 2018b). This could be attributed to the surface functionality and improved specific surface area in composite materials, as well as the tendency to increase adsorptive capacities of metal ions by the polymeric material. Furthermore, considering the use of sustainable, eco-friendly and non-toxic precursors as well as the possibility of simultaneously removing fluoride and pathogens from water shows the significance of the study towards its applicability in household water treatment.

6.7 Conclusion

AgMgO/nHaP reinforced chitosan nanocomposite (AgMgOnHaP@CSn) was synthesized for fluoride sorption and pathogen removal capability through various synthesis parameters. Structural and morphological evidence was supported by the different characterization technique results showing the interaction of the nanoparticles across the chitosan biopolymer template. The structural surface area of AgMgOnHaP@CSn was estimated to be 55.27 m^2/g with an average size of about 35.36 nm. It has a distribution of mesopores with a pore volume of ~ 0.48 cm3/g at and a pore diameter of 33.67 nm. Excellent fluoride removal efficiency with an adsorption capacity of 6.87 mg/g by modified polymer component of AgMgOnHaP@CSn was recorded when compared to previously reported studies; with improved overall morphological properties suitable for water treatment. The fluoride sorption experimental data are well described by Langmuir adsorption isotherm model and the process is exothermically governed. The sorption reaction mechanisms are diffusion-controlled and follow the pseudo-second-order sorption rate. The plausible fluoride sorption mechanism by the composite is attributed to a combination of binding activity, which is more of ligand exchange, electrostatic attraction, and improved structural surface modification. In addition to this, the AgMgOnHaP@CSn composite further provides the potential antimicrobial application to eliminate pathogens from contaminated groundwater. Overall, the developed AgMgOnHaP@CSn possesses the potential application towards the reduction of fluoride and pathogens from contaminated water at the household level.

Conflicts of interest

The authors declare no conflicts of interest.

Acknowledgment

Authors would like to acknowledge financial support from USAID-PEER Cycle 6-Award No: AID-OAA-A-11-00012; National Research Foundation Grant No: 114726; University of Venda, South Africa (RPC grant Number: SES/17/ERM/03) and Prof Gitari DHET Research incentive funds.

References

Abeles RH, Alston TA (1990) Enzyme inhibition by fluoro compounds. J Biol Chem

265(28). pp.16705-16708.

Anandalakshmi K, Venugobal J, Ramasamy V (2016) Characterization of silver nanoparticles by

green synthesis method using Pedalium murex leaf extract and their antibacterial activity. Appl Nanosci 6(3), pp.399-408.

Armfield JM (2010) Community effectiveness of public water fluoridation in reducing

children's dental disease. Public Health Rep 125(5), pp.655-664.

Ayinde WB, Gitari WM, Munkombwe M, Amidou S (2018a) Biosynthesis of Ultrasonically

Modified Ag-MgO Nanocomposite and Its Potential for Antimicrobial Activity. J Nanotechnol 2018. https://doi.org/10.1155/2018/9537454

Ayinde WB, Gitari WM, Munkombwe M, Amidou S (2018b) Green synthesis of Ag/MgO

nanoparticle modified nanohydroxyapatite and its potential for defluoridation and pathogen removal in groundwater. Physics and Chemistry of the Earth Parts A/B/C, 107, pp.25-37. https://doi.org/10.1016/j.pce.2018.08.007

Ayoob S, Gupta AK, Venugopal TB (2008) A conceptual overview on sustainable technologies

for defluoridation of drinking water. Crit. Rev. Environ. Sci. Technol. 38:6, 401-470. https://doi.org/10.1080/10643380701413310

Balamurugan S, Ashna L, Parthiban P (2014)Synthesis of nanocrystalline MgO particles by

combustion followed by annealing method using hexamine as a fuel. J Nano Tech 6:1–6. doi:10. 1155/2014/841803

Bitton G (2014) Microbiology of Drinking Water: Production and Distribution. John Wiley & Sons. doi:10.1002/9781118743942

Chlorine Chemistry Council and American Chemistry Council (2006) Drinking Water Chlorination: A Review of Disinfection Practices and Issues. Water conditioning and purification international p.68.

Craver C, Carraher C (2000) Applied polymer science: 21st century. 1st edn. Elsevier Science.

Dąbrowski A (2001) Adsorption—from theory to practice. Adv Colloid Interface Sci 93(1-3), pp.135-224.

De Silva RT, Mantilaka MMMGPG, Ratnayake SP, Amaratunga, GAJ, de Silva KN (2017) Nano-MgO reinforced chitosan nanocomposites for high-performance packaging applications with improved mechanical, thermal and barrier properties. Carbohydr Polym 157, pp.739-747.

Devi RR, Umlong IM, Raul PK, Das B, Banerjee S, Singh L (2012) Defluoridation of water using nano-magnesium oxide. J. Exp. Nanosci., 9, pp. 512-523

Edition F (2011) Guidelines for drinking-water quality. WHO Chron 38(4), pp.104-108

Freundlich HMF (1906) Uber die adsorption in l¨osungen, Z. Phys. Chem. 57A 385–471.

Frindy S, el Kadib A, Lahcini M, Primo A, García H (2015) Copper Nanoparticles Stabilized in a Porous Chitosan Aerogel as a Heterogeneous Catalyst for C−S Cross-coupling. ChemCatChem 7(20), pp.3307-3315.

García MG, Borgnino L (2015) Fluoride in the Context of the Environment. Fluorine: Chemistry, analysis, function, and effects. Pages 3-21 http://dx.doi.org/10.1039/9781782628507-00003

Gitari WM, Ngulube T, Masindi V, Gumbo JR (2013) Defluoridation of groundwater using Fe^{3+}-modified bentonite clay: Optimization of adsorption conditions, Desalin. Water Treat 1–13. doi: 10.1080/ 19443994.2013.855669

Guibal E (2004) Interactions of metal ions with chitosan-based sorbents: a review. Sep Purif Technol 38(1), pp.43-74.

Higazy A, Hashem M, ElShafei A, Shaker N, Hady MA (2010) Development of antimicrobial jute packaging using chitosan and chitosan–metal complex. Carbohydr Polym 79(4), pp.867-874.

Hijnen, W., Beerendonk, E. & Medema, G. J. 2006. Inactivation credit of UV radiation for viruses, bacteria and protozoan (oo)cysts in water: a review. Water Res 40, 3–22

Ho YS, Ng JCY, McKay G (2000) Kinetics of pollutant sorption by biosorbents: review. Sep Purif Methods 29:189–232.

Jadhav SV, Bringas E, Yadav GD, Rathod VK, Ortiz I, Marathe KV (2015) Arsenic and fluoride contaminated groundwaters: a review of current technologies for contaminants removal. J Environ Manage 162, pp.306-325.

Jones S, Burt BA, Petersen PE, Lennon MA (2005) The effective use of fluorides in public health. Bull. W. H. O. 83, pp.670-676.

Kalsi, PS (2007) Spectroscopy of organic compounds. New Age International.

Kamble SP, Jagtap S, Labhsetwar NK, Thakare D, Godfrey S, Devotta S, Rayalu SS (2007) Defluoridation of drinking water using chitin, chitosan and lanthanum-modified chitosan. Chem Eng J 129(1-3), pp.173-180. https://doi.org/10.1016/j.cej.2006.10.032

Koutsopoulos S (2002) Synthesis and characterization of hydroxyapatite crystals: a review study on the analytical methods. J Biomed Mater Res 62(4), pp.600-612. doi: 10.1002/jbm.10280

Kuppusamy P, Yusoff MM, Maniam GP, Govindan N (2016) Biosynthesis of metallic nanoparticles using plant derivatives and their new avenues in pharmacological applications–An updated report. Saudi Pharm. J 24(4), pp.473-484.

Lagergren S., 1898. Zur Theorie der sogenannten adsorption geloster stoffe, K. Sven. Vetenskapsakad. Handl. 24 1–39.

Lai CW, Lee KM, Leo BF, Wong CPP, Chong SW (2019) Polymers as Water Disinfectants. In: Das R. (eds) Polymeric Materials for Clean Water pp. 149-165. Springer Series on Polymer and Composite Materials. Springer, Cham. https://doi.org/10.1007/978-3-030-00743-0_7

Langmuir I (1916) The constitution and fundamental properties of solids and liquids. Part I. solids. J Am Chem Soc 38:2221–2295

Li LH, Deng JC, Deng HR., Liu ZL, Li XL (2010) Preparation, Characterization and antimicrobial activities of chitosan/Ag/ZnO blend films. Chem Eng J 160(1), pp.378-382. https://doi.org/10.1016/j.cej.2010.03.051

Li Q, Mahendra S, Lyon DY, Brunet L, Liga MV, Li D, Alvarez PJ (2008) Antimicrobial nanomaterials for water disinfection and microbial control: potential applications and implications. Water Res 42(18), pp.4591-4602.

Lu Z, Rong K, Li J, Yang H, Chen R (2013) Size-dependent antibacterial activities of silver nanoparticles against oral anaerobic pathogenic bacteria. J Mater Sci Mater Med 24(6), pp.1465-1471. doi: 10.1007/s10856-013-4894-5.

Machado FM, Bergmann CP et al (2012) Adsorption of Reactive Blue 4 dye from water solutions by carbon nanotubes: experiment and theory. Phys Chem Chem Phys 14(31), pp.11139-11153.

Mohapatra M, Anand S, Mishra BK, Giles D, Singh P (2009) Review of fluoride removal from drinking water. J Environ Manage 91(1), pp.67-77.

Moulder JF, Stickle WF, Sobol PE, Bomben KD (1995) Handbook of X-ray photoelectron spectroscopy: a reference book of standard spectra for identification and interpretation of XPS data. Physical Electronics, Eden Prairie, MN.

Peckham S, Awofeso N (2014) Water fluoridation: a critical review of the physiological effects of ingested fluoride as a public health intervention. The Scientific World Journal vol. 2014. https://doi.org/10.1155/2014/293019.

Poinern GEJ, Ghosh MK, Ng YJ, Issa TB, Anand S, Singh P (2011) Defluoridation behavior of nanostructured hydroxyapatite synthesized through an ultrasonic and microwave combined technique. J Hazard. Mater 185(1), pp.29-37.

Raafat D, Von Bargen K., Haas A, Sahl HG (2008) Insights into the mode of action of chitosan as an antibacterial compound. Appl Environ Microbiol 74(12), pp.3764-3773.

Raghunath A, Perumal E (2017) Metal oxide nanoparticles as antimicrobial agents: a promise for the future. Int J Antimicrob Agents, 49(2), pp.137-152.

Rao CRN, Karthikeyan J (2012) Removal of fluoride from water by adsorption onto lanthanum oxide. Water Air Soil Pollut 223, 1101–1114.

Rouxhet PG, Genet MJ (2011) XPS analysis of bio-organic systems. Surface and Interface Analysis 43(12), pp.1453-1470. https://doi.org/10.1002/sia.3831

Ruthven DM (1984) Principles of adsorption and adsorption processes. John Wiley & Sons.

Sakkayawong N, Thiravetyan P, Nakbanpote W (2005) Adsorption mechanism of synthetic reactive dye wastewater by chitosan. J Colloid Interface Sci 286(1), pp.36-42

Sekar AD, Manickam M (2019) Current Trends of Electrospun Nanofibers in Water and Wastewater Treatment. In Water and Wastewater Treatment Technologies pp. 469-485. Springer, Singapore. https://doi.org/10.1007/978-981-13-3259-3_21

Siddiqi KS, Husen A, Rao RA (2018) A review on biosynthesis of silver nanoparticles and their biocidal properties. J Nanobiotechnol 16(1), p.14.

Sing KS (1985) Reporting physisorption data for gas/solid systems with special reference to the determination of surface area and porosity (Recommendations 1984). Pure Appl Chem 57(4), pp.603-619.

Singh J, Dutta T, Kim KH, Rawat M, Samddar P, Kumar P (2018) Green' synthesis of metals and their oxide nanoparticles: applications for environmental remediation J Nanobiotechnol 16(1), p.84.

Sundaram CS, Viswanathan N, Meenakshi S (2008) Defluoridation chemistry of synthetic hydroxyapatite at nano scale: equilibrium and kinetic studies. J. Hazard Mater. 155 (1–2), 206–215.

Tran HN, You SJ, Chao HP (2016) Thermodynamic parameters of cadmium adsorption onto orange peel calculated from various methods: a comparison study. J. Environ. Chem. Eng. 4 (3), 2671e2682.

Uzun I, Güzel F (2005) Rate studies on the adsorption of some dyestuffs and p-nitrophenol by chitosan and monocarboxymethylated (mcm)-chitosan from aqueous solution. J Hazard. Mater 118(1-3), pp.141-154.

Viswanathan N, Meenakshi S (2010) Enriched fluoride sorption using alumina/chitosan composite. J Hazard. Mater 178(1-3), pp.226-232.

Wang D (2018) A critical review of cellulose-based nanomaterials for water purification in industrial processes. Cellulose pp.1-15. https://doi.org/10.1007/s10570-018-2143-2

Weber TW, Chakravorti RK (1974) Pore and solid diffusion models for fixed-bed adsorbers. AIChE J 20(2), pp.228-238.

Weber WJ, Morris JC (1964) Equilibria and capacities for adsorption on carbon. J Sanitary Eng Div 90(3), pp.79-108.

World Health Organization and UNICEF (2017) Progress on drinking water, sanitation and hygiene: 2017 update and SDG baselines. World Health Organization.

WHO/UNICEF Joint Water Supply and Sanitation Monitoring Programme (2014) Progress on drinking water and sanitation: 2014 Update. World Health Organization.

Wu FC, Tseng RL, Juang RS (1999) Role of pH in metal adsorption from aqueous solutions containing chelating agents on chitosan. Ind Eng Chem Res 1999, 38 (1), pp 270–275. doi: 10.1021/ie980242w

Yadav KK, Gupta, N, Kumar V, Khan SA, Kumar A (2018) A review of emerging adsorbents and current demand for defluoridation of water: bright future in water sustainability. Environ Int 111, pp.80-108.4(a). doi: 10.1016/j.envint.2017.11.014

CHAPTER SEVEN

BIOSYNTHESIS OF NANOFIBROUS CELLULOSE DECORATED Ag-MgO-NANOHYDOXYAPATITE COMPOSITE FOR FLUORIDE AND BACTERIAL REMOVAL IN GROUNDWATER

Introduction

This chapter addresses the biosynthesis of nanofibrous cellulose decorated Ag-MgO-nanohydroxyapatite composite for fluoride and bacterial removal in groundwater This work is presented as a prepared article journal for publication to Journal of Biological Macromolecule by Elsevier.

Ayinde W. B, Gitari W. M, James A. Smith and Samie Amidou (2019**). Biosynthesis of nanofibrous cellulose decorated Ag-MgO-nanohydroxyapatite composite for fluoride and bacterial removal in groundwater.** (Ready for submission to *Journal of Biological Macromolecule*

Biosynthesis of nanofibrous cellulose decorated Ag-MgO-nanohydoxyapatite composite for fluoride and bacterial removal in groundwater

Ayinde W. B[a], Gitari W. M[a], James A. Smith[b] and Samie Amidou[c]

[a]Environmental Remediation and Nanoscience (EnviReN), Department of Ecology and Resource Management, School of Environmental Sciences. University of Venda, Private Bag X5050, Thohoyandou, 0950, Limpopo Province, South Africa.; mugera.gitari@univen.ac.za

[b] Engineering Systems and Environmet., School of Engineering and Applied Scienc, University of Virginia, Charlottesville, Virginia. jsmith@virginia.edu

[c]Molecular Parasitology and Opportunistic Infections Program, Department of Microbiology, School of Mathematical and Natural Sciences. University of Venda. samie.amidou@univen.ac.za

Correspondence: email: twasiu33@gmail.com; Tel. +27 838734688

Abstract

The study centered on a sustainable and innovative approach in the assembly of modified Ag-MgO-nanohydroxyapatite on a nanofibrous cellulose template as a multifunctional adsorbent. A homogeneous composite mixture of Ag-MgO-nanohydroxyapatite was dispersed onto the cellulose nanofiber obtained from sawdust (CNF-AgMgOnHaP) via hydrothermal bio-reduction route using *Citrus paradisi* peel extract and the cellulose as reducing, stabilizing and capping agents. Surface morphology and mineralogical properties of the nanocomposite were examined by UV–vis spectroscopy, SEM-EDS, XRD, FTIR, TEM and BET tests. Batch fluoride sorption studies with equilibrium isotherms, kinetics, and thermodynamic parameters have been studied on the adsorbent to validate the experimental data. Antibacterial activity of the adsorbent against typical waterborne pathogen was also evaluated. The results showed successful synthesis of modified multi-structural CNF-AgMgOnHaP composite with an improved surface area of 160.17 m^2/g. The sorption of fluoride by the adsorbent was found to be strongly dependent on the different sorption conditions with maximum defluoridation capacity of 8.71 mg/g at 303 K, pH of 5 with 0.25g dosage at 10 min contact time (25 ± 3 °C). Equilibrium fluoride sorption onto the CNF-AgMgOnHaP was best described by Freundlich isotherm model across all the operating temperatures. The overall kinetic results indicated that the mechanisms not only depend on using the pseudo-second-order process but were also governed by mass transfer of the adsorbate molecules from the external surface onto the pores of the adsorbent. The thermodynamic parameters revealed that the adsorption process of F^- onto CNF-AgMgOnHaP was endothermic and spontaneous at the sorbent/solution interface. The synthesized composite also provides some antibacterial activity against both gram-negative and gram-positive water bacteria strains.The overall results suggested that CNF-AgMgOnHaP nanocomposite had the potential for simultaneous defluoridation and antibacterial application in groundwater.

Keywords: Bio-reduction, core-shell nanocomposite, cellulose nanofiber, *Citrus paradise peel*, simultaneous microbial-fluoride removal

7.1 Introduction

Water, according to the United Nations World Water Development Reports [1], is at the core of sustainable development. It is a recognized fact that the most important aspect of improving the health of people is to provide safe and clean water to communities. Lack of centralized treated water supply systems means most rural communities of most developing and sub-Saharan African countries rely on unsafe surface water and groundwater sources for their domestic water supply [2-3]. Most of the untreated waters in these rural communities are susceptible to toxic inorganic and pathogenic pollutants introduced by natural and anthropogenic activities thereby resulting in death from water-related diseases [4]. Among the different toxic inorganic contaminants in the groundwater resources, fluoride concentration is of substantial significance from the perspectives of public health worldwide. It is estimated that over 27 nations and 200 million people across the globe face issues of excess fluoride in drinking water, with high health effects and morbidity in a number of regions depending on the geographical and economic status [5-7].

Fluoride, below the recommended limit of 1.5 mg/L is an important component in preventing tooth cavities, and facilitating the mineralization of bone, dental enamel and arduous tissues in human [8-10]. However, in excess, it can be detrimental to human health, leading to dental or crippling skeletal fluorosis [10-12]. In addition to fluoride epidemics, most acute water-related diseases are often associated with consumption of microbiologically contaminated water, which are responsible for an estimated 2.2 million deaths yearly worldwide [10; 13-14]. Water disinfection using conventional methods such as chlorination and ultraviolet (UV) irradiation is rapidly becoming a major challenge due to the formation of harmful carcinogenic disinfection by-products (DBPs) [15-16]. The importance of removing this toxic substance and water disinfection through innovative and sustainable technology in controlling human loss cannot be overstated. The techniques towards such pollutants removal are based on the principle of sorption as well as chemically-cell death by disrupting the cell walls of the microbes, especially at the point of use [17-18]. Generally, many of the materials developed so far based on such technologies and their mode of operation as well as mechanisms have been reviewed and reported [7; 19-21]. However, challenges like high costs of operation, low adsorption capacity, incomplete pollutant removal and release of toxic sludge [8; 22-23]; arising from these technologies has been a major source of concern in reducing this environmental menace.

In order to overcome these drawbacks, intense efforts are now being channeled towards fabricating a high capacity, eco-friendly and sustainable multifunctional biopolymeric-reinforced composites to solve these recurring water-borne epidemics. Biopolymeric-reinforced composite provides the solution for a sustainable economic and ecologically viable multifunctional water purification techniques to simultaneously remove fluoride and pathogens in groundwater for application in household water treatment devices.

Nanocellulose has been receiving considerable interest in the preparation of new composite material in targeting some selective toxic metal ions in water purification techniques due to its

surface functionalizable hydroxyl, inherent hydrogen bonds and van der Waal forces, which may enhance the adsorption capacity of the targeted chemical species [24-25]. In addition, its numerous remarkable properties, such as mechanical strength, biodegradability, non-toxicity properties, and renewability, etc. serves as an edge for its application in water treatment compared to other equivalent sorbent materials [26]. This study proposes to fabricate a novel multifunctional biopolymer-metal oxide nanoparticle reinforced composites that are envisaged towards efficient pathogenic microorganisms and fluoride removal from aqueous solution. Therefore, the main foci of this study were to isolate cellulose nanofiber from sawdust; biosynthesize a modified Ag-MgO nanoparticles using *Citrus paradisi* (Grapefruit red) peel extracts as a bio-reducing, stabilization and capping agent on nanohydroxyapatite nanocomposite. Furthermore, the development of an enhanced multifunctional adsorbent through impregnation of the Ag-MgOnHaP onto the cellulose nanofiber matrix for simultaneous fluoride and pathogen removal in aqueous media was carried out and reported.

7.2 Materials and methods

7.2.1 Chemicals

All chemicals were of analytical reagent grade. $Ca(NO_3)_2.4H_2O$, KH_2PO_4, $Mg(NO_3)_2.6H_2O$, $AgNO_3$, $NaClO_2$, H_2SO_4, NaF, NaOH and other chemicals used were purchased from Rochelle chemicals, South Africa and used directly without further purification. The raw material used in the preparation of cellulose nanofiber in this work is sawdust/wood chips and the peel of *Citrus paradisi* (Grapefruit red). Raw sawdust was collected from School of Agriculture, University of Venda, South Africa. Deionized water from a Millipore water (18.2 MΩ/cm) was used in the preparation and dilution of standards throughout the experiment.

7.2.2 Preparation of Citrus paradisi peel extract

The fruit peels of *Citrus paradisi* (Grapefruit red) were removed, cleaned thoroughly using ultrapure (18.2 MΩ/cm) water to remove any dust particles adhering to the surface and cut to small pieces. 30g of the peel was added to 100 mL of Ultrapure water and boiled for 20 minutes at 70 °C. The extract was cooled and filtered through Whatmann No.1 filter paper and stored at 4 °C for further use.

7.2.3 Preparation of cellulose nanofibers from Sawdust biomass (CNF)

Extraction of cellulose nanofiber was carried out by a modified purification of sawdust through chemical (alkaline-acid) and mechanical (ultrasound) mode of treatments as described by Kamphunthong *et al*. [27], and Mandal and Chakrabarty [28]. The sawdust was first dried in sunlight and then cut to small sizes using a domestic blending machine (PHILIP, 400W, HR 2103) and passed through a 100-mesh sieve. The ground pieces were further dried in a hot air oven overnight at 65 °C before the alkaline pretreatment. The pre-treatment soaking was carried out in an alkali solution (4 Wt. % NaOH solution) at room temperature for 3h followed by continuous washing with Millipore water (18.2 MΩ/cm). The obtained pre-treated fibers were delignified by bleaching with a buffer solution (pH 4.5) of acetic acid 5% (w/v), sodium chlorite ($NaClO_2$) and

Millipore water boiled for 3h at 70 °C with a pulp-to-liquor ratio of 1: 1. The mixture was allowed to cool and filtered using excess ultra-pure water (18.2 MΩ/cm). The bleaching process was repeated three times. The obtained delignified and hemicellulose free cellulose fibers were further subjected to acid hydrolysis using 8.5M of sulphuric acid (fiber to liquor ratio of 1:10) for 1 h at 50 °C. The reaction mixture was stopped by washing severally (10-fold excess Millipore water), followed by centrifugation at 4,500 rpm at room temperature for 30 min until the resultant supernatant liquor becomes turbid (pH in the range of 5–6). The resulting suspension (colloidal cellulose particles) was then subjected to sonication for 45 min in an ice bath throughout the entire ultrasonication to obtain the nanofibers. The obtained suspension was stored in the refrigerator at 4 ◦C until use.

7.2.4 Preparation of nanohydroxyapatite (nHaP)

Synthetic nanohydroxyapatite (nHaP) was prepared as described by Poinern *et al*. 2011 [29] by reacting 40 mL of 0.32 M $Ca(NO_3)_2{\cdot}4H_2O$ with 60 mL of 0.19 M KH_2PO_4 solution under continuous stirring with the Ca/P ratio maintained at 1.67. Subsequently, aqueous NH_4OH (25%) was added dropwise to adjust the pH value to 9, and the solution was stirred for 6hr and thereafter left to age for 24 h at room temperature. During the mixing process, the pH value was continually checked and maintained at 9 (using NH_4OH). The composite solution was thereafter subjected to ultrasound agitation at 100 % amplitude (0.5 cycles) for 1 h. The product obtained after the sonication was filtered and dried at 40 ◦C in an oven for 24 h before being ground into a fine powder.

7.2.5 Synthesis conditions of Cellulose-nanofiber-AgMgOnanohydoxyapatite

The Cellulose-nanofiber-AgMgOnanohydoxyapatite composite was synthesized by incorporating nanohydroxyapatite bound to Ag-MgO nanoparticle into a cellulose nanofiber matrix via bio-reduction and *in situ* precipitation method at room temperature.

For this, 10 g (w/w%) of the obtained colloidal cellulose suspension from sawdust (CNF) was added to a mixture of solutions containing 40 mL of aqueous *Citrus paradisi* peel extracts, 60 mL 1 mM $AgNO_3$ and 20 mL 0.1 M $Mg(NO_3)_2.6H_2O$. The solution was mixed under continuous stirring for 12 h at 40 °C. The bio-process seed growth kinetics of the nanocomposite through color variation was monitored using UV–Vis spectroscopy. To this continuously stirred bio-reduced reaction mixture (CNF-AgMgO), 5 g of nHaP was dispersed into the mixture and was agitated on a magnetic stirrer for 8 h to achieve homogenous mixing. The mixture was filtered and oven-dried at 60 °C for 24 h and then ground to obtain Cellulose-nanofiber AgMgOnHaP (CNF-AgMgOnHaP) composite powder. The synthesis routes were repeated by varying the colloidal cellulose suspension loading within the CNF-AgMgOnHaP composite from 10 to 100 (w/w %) in order to evaluate the optimum loading weight percentage required for optimum defluoridation.

7.2.6 Material characterization

The CNF-AgMgOnHaP composite kinetic growth rate was characterized using UV-Visible Spectrophotometers (220–600 nm), (SPECTROstar Nano/ BMG LABTECH). Surface

morphology and elemental analysis of the nano-adsorbent composite were characterized using SEM with an FEI Nova NanoSEM 230 with the field emission gun equipped with an Oxford Xmax SDD detector operating at an accelerating voltage of 20Kv for the EDS detector (Oxford X-Max with INCA software). Bruker: ALPHA FT-IR Spectrophotometer was used to obtain the FTIR spectra (4000 - 400 cm^{-1}). The determination of the crystalline phases present in materials was identified by X-ray diffraction machine (Bruker D8 Advance, Cu-K radiation, wavelength 1.54443Å Lynx-eye XE detector). Transmission electron microscopy (TEM) images were taken using an FEI Tecnai20 equipped with a LaB6 emitter, operating at 200 kV and fitted with a Gatan Tridiem GIF with a 2kX2k CCD camera. Images were collected using the Digital Micrograph suite of programs in relation to size and shape. The surface area, pore area and pore volume of the synthesized nanocomposite were measured using nitrogen adsorption Brunauer–Emmett–Teller (BET) surface area and porosity analyzer (Micromeritics ASAP2020). The adsorption-desorption plots were used to calculate the specific surface area. F^- and pH were determined using a fluoride ion-selective electrode (9609 BNWP Orion, USA) coupled to an ISE/pH/EC electrode (Thermo SCIENTIFIC-ORION VERSA STAR Advanced Electrochemistry meter fluoride ion-selective electrode) calibrated with four fluoride standards containing TISAB III at the volume ratio of 1:10 as in the case of the samples. UP400S (400W at 24 kHz power control amplitude 20-100% ultrasonic device with ultrasonic horn H14) from Hielscher Ultrasonic was used for sonicating purposes. The surface interaction and composition of the fluoride loaded sorbent was studied by the X-Ray Photoelectron Spectrometer Microprobe (XPS) (Thermo Scientific ESCAlab 250Xi,), with a monochromatic Al Kα X-ray source (1486.7 eV). The high-resolution scans were conducted according to the peak being examined with a pass energy of 20 eV (Pressure <10-8 mBar) and spot size of 900 μm with a wide survey scan between 0-1300 eV.

7.2.7 Batch Fluoride adsorption experiments

Batch fluoride sorption studies were performed and evaluated with the synthesized CNF-AgMgOnHaP for the removal of fluoride in simulated and field groundwater. The effects of contact time, pH, adsorbent dose, initial adsorbate concentration and coexisting ions on the equilibrium adsorption capacity were optimized. Standard stock fluoride ion solution (1000 mg/L) was prepared by dissolving 2.210 g NaF into 1000 mL of ultrapure water at ambient condition. The desired fluoride solution was prepared by appropriate dilution of the standard stock solution. Batch adsorption experiments were carried out by mixing 0.225 g of CNF-AgMgOnHaP with 50mL of 10 mg/L F^- solution. The mixture was shaken thoroughly using a reciprocating shaker (STUART SSL2) at 250 rpm. The solution was then filtered, and the residual fluoride ion concentration was determined. The pH values to the solution were adjusted by 0.1 mol/L HCl or NaOH. The effect of co-existing anions on the defluoridation efficiency of the adsorbent was evaluated at anion concentration of 10 - 30 mg/L in a 10 mg/L fluoride solution. The adsorption isotherm experiments were conducted by varying fluoride concentrations within the range of 5–100 mg/L in a constant-temperature water-bath shaker in the temperature range of 303; 313 and 323 K. Adsorption isotherms and kinetic models were adopted and used to model adsorption data. All the experiments were conducted in triplicate, and the mean of the results computed. Equations

1 and 2 were used to determine the percentage fluoride removal and adsorption capacity, q_e (mg/g) of the adsorbent.

$$\% \text{ Adsorption } = \frac{(C_o - C_e)}{C_o} \times 100 \quad (1)$$

$$q_e = (C_O - C_e) \times \frac{V}{m} \quad (2)$$

Where: C_o is the initial F^- concentration (mg/L); C_e is the F^- concentration at equilibrium (mg/L); V is the volume of solution (L) and m is the dried mass of the adsorbent (g).

7.2.8 pH at point-of-zero-charge (pHpzc)

The pH at the point-of-zero charge of CNF-AgMgOnHaP was determined in 1 M, 0.1 M and 0.01M KCl solutions for consistency of results. The pH of solutions was adjusted to desired values by adding 0.1 M HCl or 0.1 M NaOH. The new pH, therefore, constituted the initial pH (pH_i) of solutions. Aliquots of 25 mL of solutions were pipetted into 50 mL plastic bottles. A mass of 0.25g of adsorbent was then weighed into each of the bottles. The bottles were corked and shaken inside a constant-temperature water bath shaker at 150 rpm for 24 h. After equilibration, the equilibrium pH (pHe) of each mixture was quickly measured and recorded.

7.2.9 Statistical tools

The computations were done using OriginPro 8.SR0 and Excel software. The best-fit sorption models were analyzed using the linear and non-linear analysis, Adjusted correlation coefficient (Adj. R^2) and chi-square analysis ($\chi 2$) were computed.

7.2.10 Regeneration of CNF-AgMgOnHaP composite

The regeneration experiments were conducted to evaluate the reusability of the spent sorbent using 0.01 M NaOH and 0.1 M Na_2CO_3 solutions. In each case of the desorption process, 0.25 g of CNF-AgMgOnHaP composite was added to 50 mL of 10 mg/L fluoride solution. The fluoride loaded adsorbent was agitated separately with 50 mL of 0.01 M NaOH and 0.1 M Na_2CO_3 for 30 mins, thereafter the adsorbent was filtered and subsequently analyzed for residual fluoride. The collected adsorbent on filter membrane was washed with Milli-Q water and then dried at 80 ˚C for 3 h. The regenerated adsorbent was then re-used for further fluoride removal up to four regeneration cycles.

7.2.11 Antibacterial Evaluation of the composite

The bacterial resistance of the biosynthesized CNF-AgMgOnHaP nanocomposite was determined qualitatively from the observed zone of inhibition (mm) using the standard Agar-Well disc diffusion methods (Kirby Bauer disk diffusion test). The indicator strains used are Escherichia *coli (ATCC 35218), Staphylococcus aureus (ATCC 33591) and Klebsiella pneumoniae (ATCC 700603).* Bacterial suspensions were prepared with the turbidity of 0.5 McFarland. 50 µL of each strain was spread plated evenly on 20 mL of solidified and dried freshly prepared MHA agar plates. Wells were punctured at equidistance using sterile pipette tips. 50 µL each of CNF-AgMgOnHaP

was dispensed into the wells already inoculated with the bacterial cell suspension. The plates were incubated at 37°C for 24 h and the diameter of the zone of growth inhibition around the different sample concentration (1-10 mg/mL) was measured in millimeter (mm). The measured zones of inhibition were used to determine the antibacterial activities of the nanocomposite.

7.3. Results and Discussion

7.3.1 Effects of Cellulose nanofiber loading (wt. %) in CNF-AgMgOnHaP adsorbent on adsorption

The percentage weight effects of cellulose nanofiber in the CNF-AgMgOnHaP composite was evaluated for fluoride sorption capacity. This was carried out by contacting 0.225 g of the composite with 50 mL of 10 mg/L initial fluoride solution at 250 rpm for 30 min. Table 7.1 shows the percentage of fluoride removal results. The result suggests that the more the CNF weight content, the higher the content of hydroxyl groups within the composite and thus, creating more binding site for fluoride sorption capacity of the composites.

Table 7.1. Optimization of CNF % weight in the CNF-AgMgOnHaP adsorbent for F^- removal.

CNF (w/w %)	Average equilibrium fluoride concentration (Ce) (mg/L)	% fluoride removal
10	3.307	66.93
30	1.364	86.36
50	0.476	95.24
70	0.343	96.57
100	0.096	99.04

7.3.2 Structural Morphological analysis

7.3.2.1 UV-Visible study

The successful impregnation of the Ag-MgO nanoparticles on the cellulose nanofiber matrix is shown in the UV–visible absorbance spectra (Fig. 7.1). The bio-reduction formation of the nanoparticles by aqueous peel extracts of *C. paradisi* is indicated by a change in the color of the reaction solution from colorless to light yellow. As shown in the spectra, no visible absorption peak was observed in the bare cellulose nanofiber (CNF), however, two different distinct peaks were observed in the CNF-AgMgO composite. An absorption band is observed in the low UV region range from 270-290 nm typical of MgO together with a broad band around 420 nm associated with the characteristic absorption of silver nanoparticles [30-31]. The change in the reaction mixture color variation is attributed to surface plasmon resonance of excited electrons and O^{2-} surface anions at the surface of Ag and MgO nanoparticles respectively in resonance to lightwave [32-34]. The availability and interaction of the bioactive functional species in *C. paradisi peel* extracts and that of the cellulose hydroxyl groups with the silver ions may be responsible for the rate of bio-reduction as shown in the optical property of biomolecular-capped Ag-MgO nanocomposite into the nanofiber [35-36]. Furthermore, the cellulose fiber matrix used during the synthesis in addition to contributing as reducing agents also provided good stability to the CNF-AgMgO composite thereby preventing agglomeration resulting in uniform nucleation and growth conditions for impregnated nanoparticles [37-38].

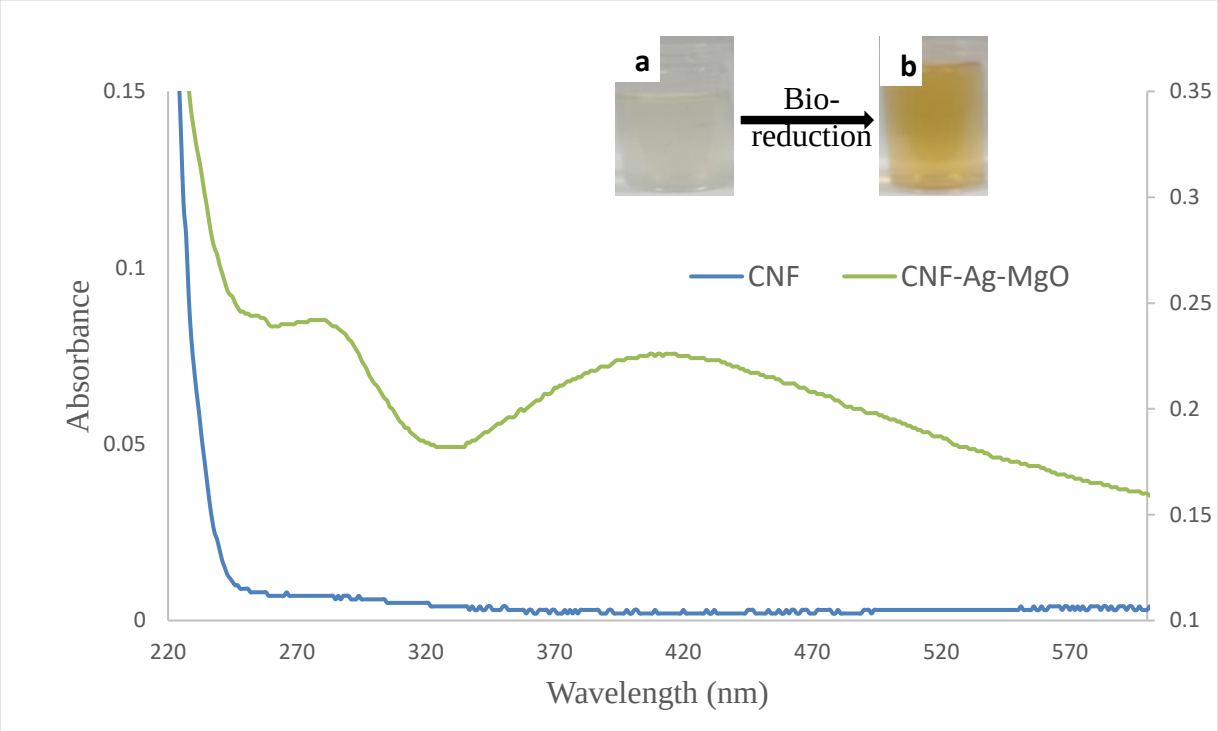

Fig. 7.1. UV–Vis spectrum of CNF-AgMgO synthesized using *C. paradisi* peel extracts at 40 ± 2 °C for 12 h.

7.3.2.2 Electron microscopic analysis

Figure 7. 2 (a)-(n) shows the SEM images, different size distributions with associated EDS patterns as well as the TEM micrographs of CNF, CNF-AgMgO, together with the optimized CNF-AgMgOnHaP composite before and after fluoride sorption respectively. The images of successfully extracted fine and uniform cellulose fibril structure from sawdust and its corresponding compositions are shown in Fig. 7.2 (a-d). The typical elemental composition of the CNF derived from a saw-dust waste constituent is shown on the EDS spectrum (Fig. 7.2(b). The obtained fiber is elongated (Fig. 7.2 (d) with a wide width diameter of about 0.5 μm. Fig. 7.2 (e) showed the SEM image of the synthesized bio-reduced CNF-AgMgO nanocomposite from the *C. paradisi* peel extracts with the EDS (Fig. 7.2 (f) revealing the presence of the Ag-MgO nanoparticles on the cellulose fiber network. The TEM micrograph (Figs. 7.2 g, h) displayed a web-like layout surface structure with a thin-long threadlike individual size of about 30-50 nm in width. It is important to note that the morphologies of CNF and the bio-reduced CNF-AgMgO nanocomposite still remain the same elongated rod-like structure, confirming that the nanofibrous morphology and the impregnation of the nanoparticles on the surface of CNF. Figs. 7.2 (i-n) shows the different structural modifications of the nHaP impregnated CNF-AgMgO (CNF-AgMgOnHaP) and its corresponding defluoridated CNF-AgMgOnHaP composites. Figs. 7. 2 (i) and 7.2 (l) represent the SEM images CNF-AgMgOnHaP and fluoride sorbed CNF-AgMgOnHaP, and it can be observed there is a granulated aggregation of nanoparticles on the cellulose fiber of both composites. This could be attributed to the very irregular surface of the incorporated nanohydroxyapatite powder after drying the composite [39]. The presence of the inherent elemental distribution around the cellulose matrix of the synthesized CNF-AgMgOnHaP adsorbent is shown in Fig. 7.2 (j), and the aggregation of the adsorbent at a size distribution range of 50 nm is presented Fig. 7.2 (k). The corresponding morphological structure of the sorbed fluoride-CNF-AgMgOnHaP composites is presented in Fig. 7.2 (l-n). The presence of elemental fluorine in the EDX spectrum (Fig. 2(m)) suggested the potential of the material towards deflouridation.

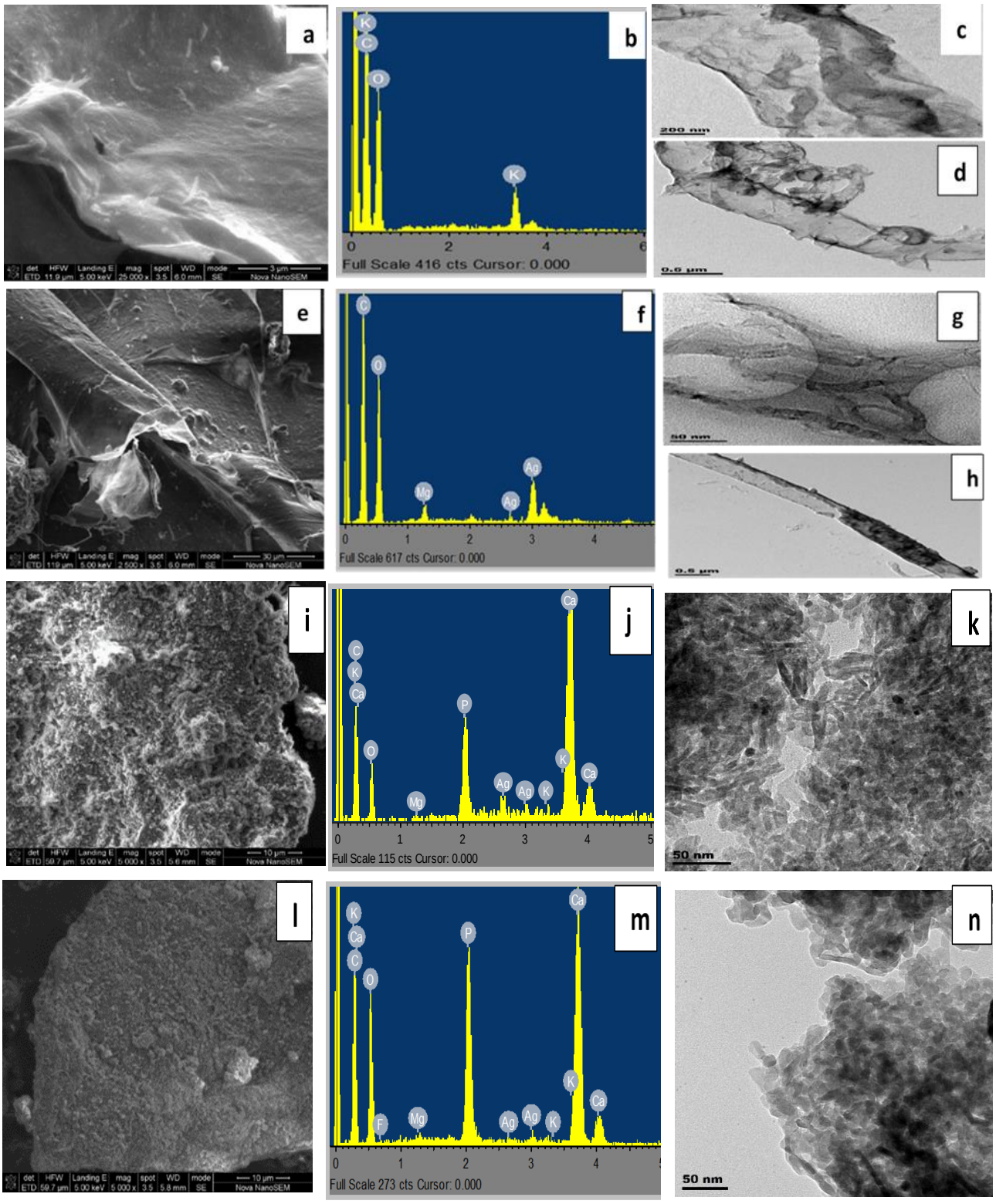

Fig. 7.2. SEM; EDS and TEM of (a-d) CNF derived from saw-dust waste, (e-h) CNF-AgMgO composite, (i-k) CNF-AgMgOnHaP adsorbent before fluoride sorption, (l-n) CNF-AgMgOnHaP adsorbent after fluoride sorption.

7.3.2.3 FTIR spectroscopy

Fig. 7.3 shows the changes in the FTIR spectra of the cellulose nanofiber from saw-dust and the CNF-AgMgOnHaP adsorbent matrix. The major functional groups characteristic peaks observed in the CNF are found at 3343, 2904, 1640, 1425-1433, 1320-1335, 1162, 1054-1052, 895-585 cm^{-1} while the spectrum of CNF-AgMgOnHaP composite showed adsorption bands at 3229, 1634, 1432-1353, 1017, 893, 595, 558 cm^{-1}. In both spectrums, the presence of a strong stretching vibration derived from OH− group is seen at 3343 cm^{-1} featuring in the CNF which became broader and shifted to a lower range of 3230–3229 cm^{-1} in the CNF-AgMgOnHaP composite. The broadness of the band in the composite may be attributed to the contribution of OH− groups in the matrix through oxidation of the cellulose in the bio-reduction of the impregnated nanoparticles across the composite [40]. The bands at 2904, 1320 -1335, 1140 -1117 cm^{-1} represent C–H symmetrical stretching, CH_2 wagging vibration, in-the-plane -CH bending mode, stretching vibration from C-O and C-O-C groups respectively characteristics of a natural fiber [41]. Furthermore, characteristic peaks at around 1436- 1450, 1032 -1020, 912 - 656, 598 - 474 cm^{-1} assigned to vibrational mode of CO_3^{2-}, the asymmetric phosphate group, PO_4^{3-} stretching and bending modes, Mg–O-Mg deformation of the Mg-O absorption respectively featured in the CNF-AgMgOnHaP composite spectra [42-44]. Therefore, the result obtained from the FTIR spectrometry suggests the presence of nanohydroxyapatite (nHaP) and MgO species impregnation within the CNF matrix.

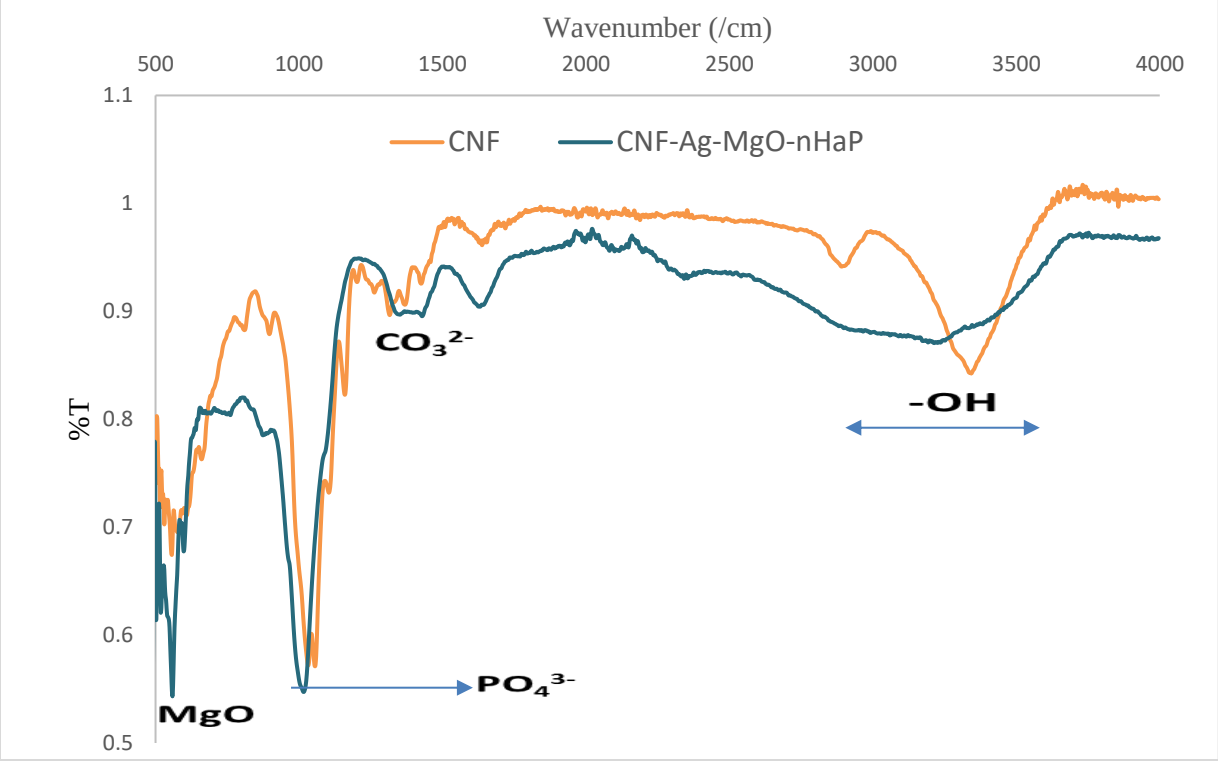

Fig. 7.3. The FTIR spectra of (a) CNF; (b) CNF-AgMgOnHaP adsorbent.

7.3.2.4 Specific surface area by Brunauer–Emmett–Teller (BET)

Table 7. 2 shows the specific surface area of CNF-AgMgOnHaP adsorbent as examined through BET at an ambient temperature of 22 ^{o}C. The CNF-AgMgOnHaP composite has BET surface area of 160.17 m²/g with a micropore and mesopore area of 5.46 m²/g and 196.12 m²/g. The composite average pore width was found to be 9.5541 nm and thus, categorized to be micro-mesoporous in nature [45]. The increase in the surface area of CNF-AgMgOnHaP composite is attributed to increasing in the availability of numerous binding functional groups within the matrix as compared to specific surface area of soft cellulose pulp (1 and 4 m^2/g) [46-47]; apatite materials (36.00 m^2/g; 69.68 m^2/g) [48-49]; as well as silver and MgO nanoparticles respectively (56.9 m^2/g and 114.03 m^2/g) [50-51].

Table 7. 2. BET Surface analysis parameters of CNF-AgMgOnHaP adsorbent.

BET Parameter	Methods	Values
Surface area	BET Surface Area	160.17 m^2/g
	Langmuir Surface Area	220.45 m^2/g
	t-Plot External Surface Area	154.71 m^2/g
Pore Area		
Micropore area	t-Plot Micropore Area	5.46 m^2/g
Mesopore area	BJH Adsorption	196.12 m^2/g
	BJH Desorption	223.89 m^2/g
Pore volume		
Micropore volume	Single point adsorption	0.38 cm^3/g
	Single point desorption	0.38 cm^3/g
	t-Plot micropore volume	0.0008 cm^3/g
Mesopore volume	BJH Adsorption	0.39 cm^3/g
	BJH Desorption	0.397 cm^3/g
Pore size		
Adsorption average pore width	4V/A by BET	9.55 nm
Desorption average pore width	4V/A by BET	9.53 nm
Mesopore size	BJH Adsorption	7.91 nm
	BJH Desorption	6.91 nm

7.3.2.5 XRD analysis

Fig. 7.4 shows the XRD patterns between the extracted CNF from sawdust and the CNF-AgMgOnHaP composite. The XRD of the extracted CNF (Fig. 4(a)) shows a broad intensive peak at 22.9◦ (2 0 0 planes), which is a characteristic peak pattern structure of the cellulose [52-53]. However, a change in the structural orientation was observed in the CNF-AgMgOnHaP composite diffractogram. The crystalline phases and intensities observed in the adsorbent XRD spectrum (b) illustrates the presence of different components in the composite in comparison to that of the CNF (spectrum a). The diffraction peaks at 16.89, 26.33, 31.81, 32.15, 39.7, 46.65, and 49.89◦ in 2θ revealed the presence of hexagonal carbonate-hydroxyapatite (Entry no: 96-9003-551)[54]; triclinic crystal system of silver attached to the phosphate groups (Entry no: 96-100-8002)[55]. Furthermore, characteristic crystal structure peaks for monoclinic Mg within the apatite phase at the 2θ value of 6.91, 31.52, 19.36 and 53.49° (Entry no: 96-231-0425) [56] were also identified (Fig. 4(b)). The typical defined cellulose peaks were also visible in the patterns of the composites. These results suggest that the difference observed on the surface crystallinity between these materials arises as a result of the impregnated nanoparticles on the CNF polymer matrix morphology.

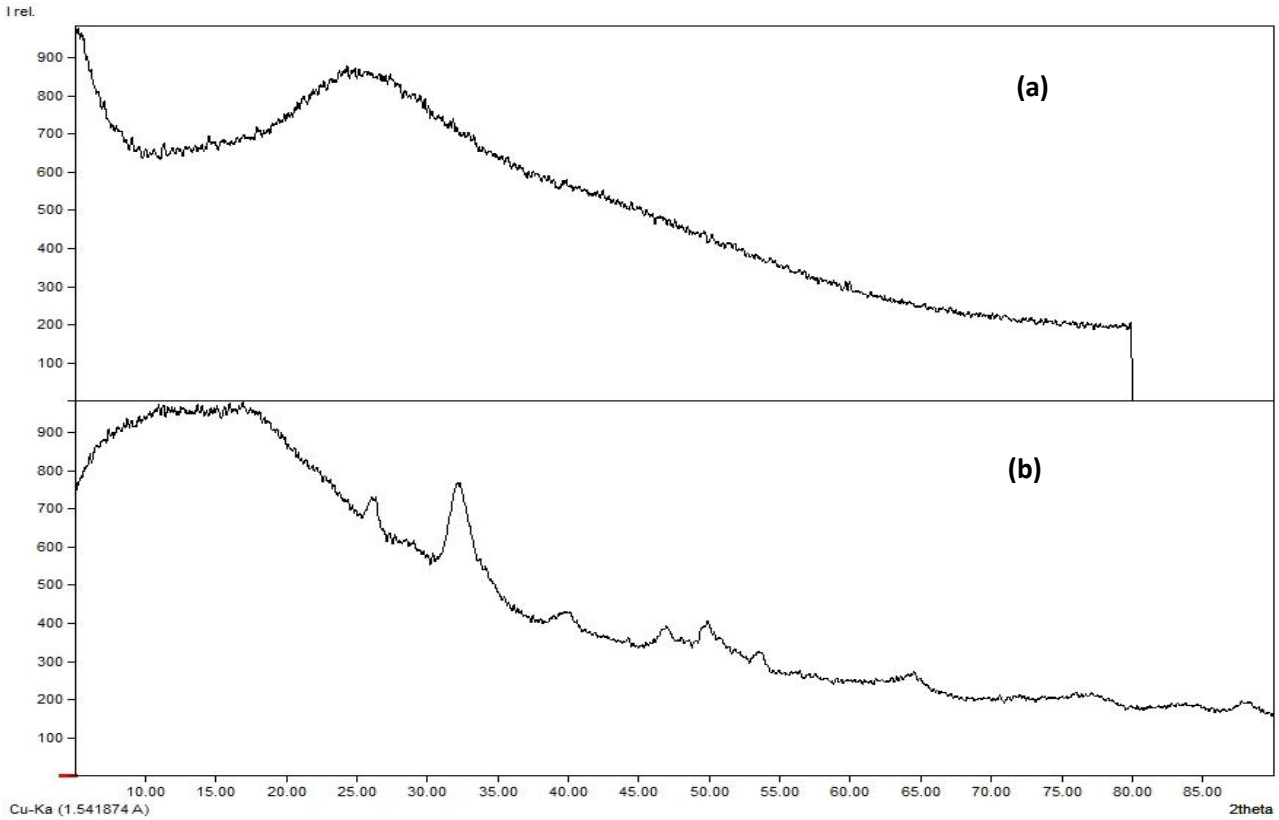

Fig. 7.4. XRD patterns of (a) CNF from saw-dust (b) CNF-AgMgOnHaP composite.

7.3.3 Fluoride adsorption experiments

7.3.3.1 Effect of contact time

The removal of fluoride using CNF-AgMgOnHaP adsorbent was investigated as a function of contact time within the range of 0-30 mins using 0.225 g sorbent dose per 50 mL of 10 mg/L initial fluoride concentration (Fig. 7.5). The fluoride sorption process evidently increased sharply as the time increases within the first 10 min of contact time with about 93 % of F^- removal. Subsequently, the adsorption rate became slower with increasing contact time (10-20 min) with no appreciable difference in the percent fluoride removal until complete saturation was achieved. Therefore, a contact time of 10 min was chosen as the optimum time for fluoride sorption by CNF-AgMgOnHaP. The rate of fluoride removal within the rapid equilibration time was due to the presence of free and abundant binding sites across the adsorbent surface. This rapid interaction at the earlier stage suggests the presence and availability of the high amount of hydroxyl groups (supported by FTIR (Fig. 7.3)) within the composite, which lead to high F^- sorption due to the easy exchange of the fluoride ions with the CNF-AgMgOnHaP surface hydroxyl groups. Furthermore, the improved surface area and wider pores dimensions may also facilitate the high fluoride sorption accessibility to the binding sites of the adsorbent.

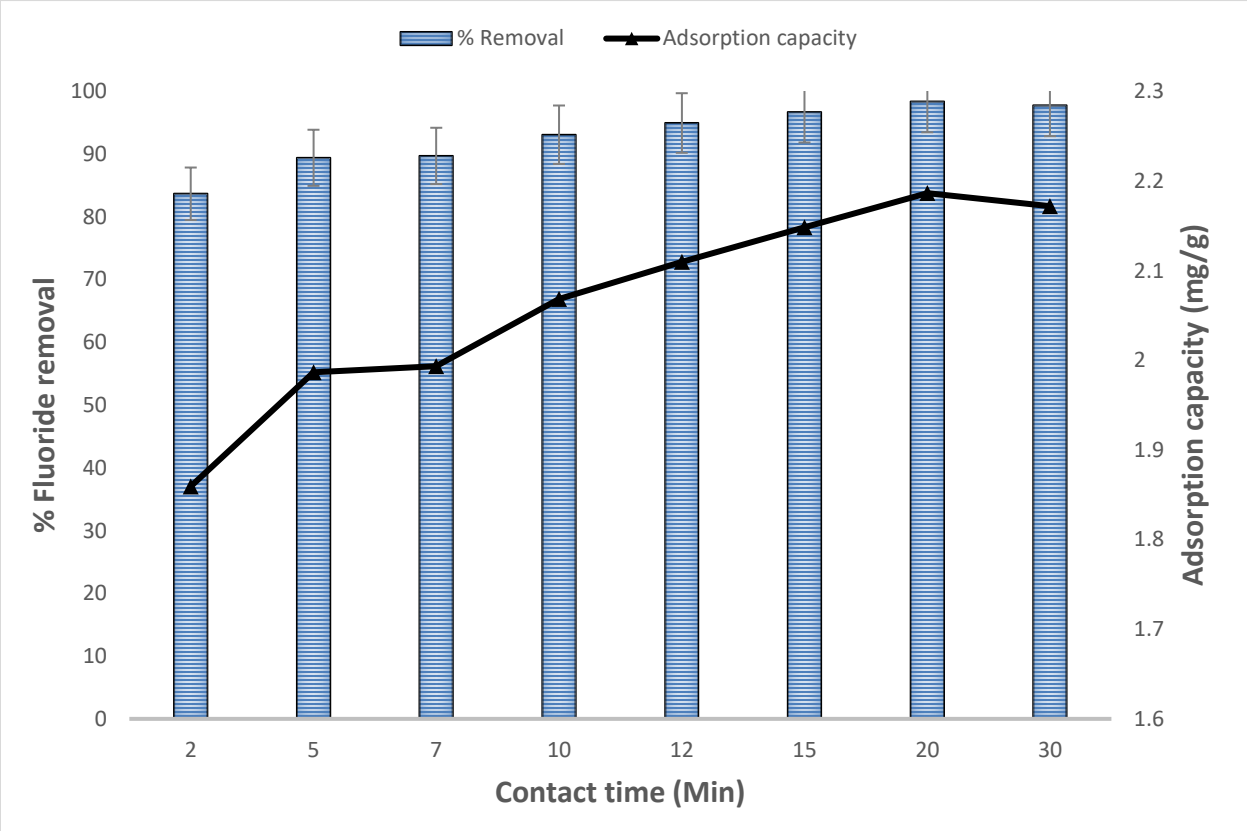

Fig. 7.5. Effect of contact time on CNF-AgMgOnHaP adsorbent**.**

7.3.3.2 Effect of sorbent dosage

The adsorption efficiency for F^- ion as a function of CNF-AgMgOnHaP dosage was investigated and the result is depicted in Fig. 7.6. The F- removal efficiency increases with increase in adsorbent dosage (0.1-0.35 g) attaining a constant optimum removal at 0.35 g. This may be attributed to the fact that increasing the dose of CNF-AgMgOnHaP creates more vacant available surface binding sites favoring the fluoride sorption. In addition, the increased structural surface area and porosity of the synthesized adsorbent as confirmed by the BET analysis may have contributed to the high fluoride sorption capacity.

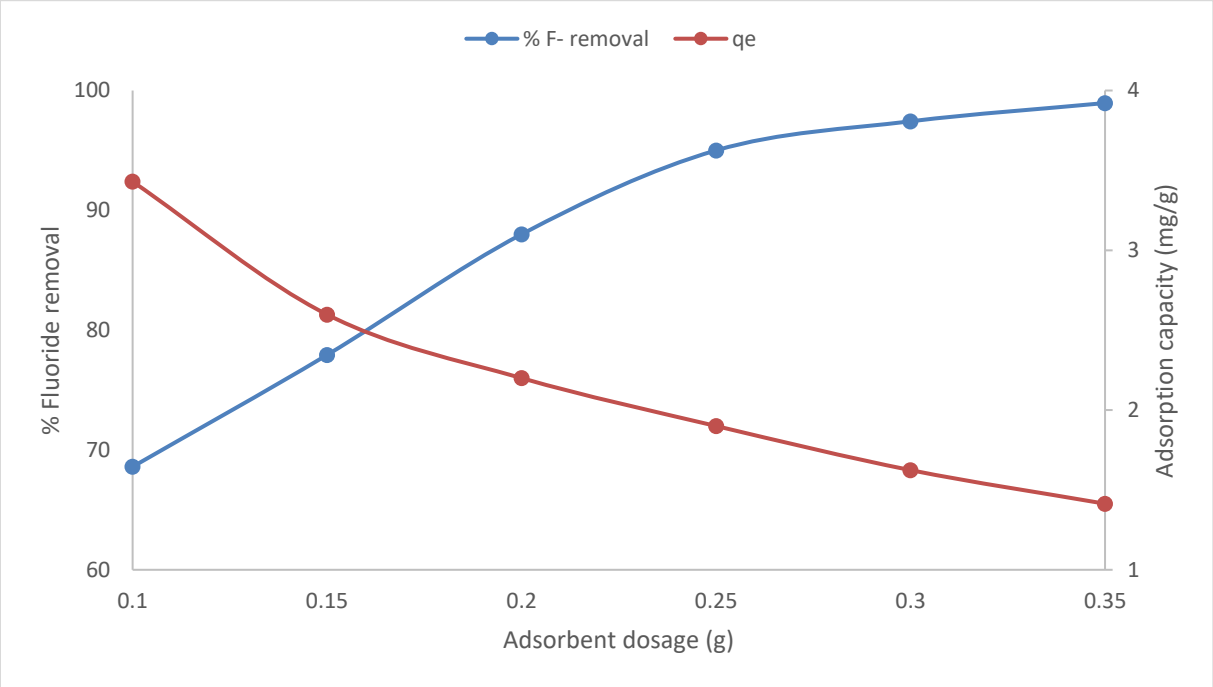

Fig. 7.6. Effect of sorbent dose on the removal of F^- ions by CNF-AgMgOnHap composite (contact time of 10 min, initial F^- concentration of 10 mg/L at 50mL solution volume, pH of 5, shaking speed of 250 rpm).

7.3.3.3 Effect of pH and surface charges on fluoride sorption.

The effect of initial solution pH (3-12) as it affects the surface charges of the CNF-AgMgOnHaP adsorbent in the removal of fluoride is shown in Figs. 7.7 (a-b). It is evident from the plot (Fig. 7.7 (a)) that fluoride sorption capacity by the adsorbent was pH-dependent and the maximum sorption percentage was observed at pH 5. Thereafter, the rate of removal dropped from 87% at pH 7 to 82% at pH 9 with significant adsorption reduction after pH 9 to pH 12 to 54%. This variation might be attributed to the changes within the solution pH environment which ultimately changes the surface charge and the protonation/deprotonation of the binding functional groups across the CNF-AgMgOnHaP adsorbent, as well as the solubility of fluoride ion species during the process [57-58]. Furthermore, the surface charges distribution of the CNF-AgMgOnHaP adsorbent in fluoride sorption at different initial solution pH (3-12) were also evaluated by its point of zero charge

(pHpzc). The pHpzc is defined as that pH value at which the net surface charge density of an adsorbent is zero [59]. As shown in Fig. 7.7 (b), the pHpzc value of the CNF-AgMgOnHaP was at ~ 4.7 which is lower than the optimum pH value of 5. Consequently, the surface of the sorbent becomes negatively charged in the solutions at which the equilibrium pH was greater than pHpzc.

This means that there are abundant negatively charges on the surface of CNF-AgMgOnHaP at pH > 4.7 which interacts and replaced the fluoride ions in solution, thus leading to an increase in F^- sorption capacity. One of the main contributing surface groups for high adsorption of F- by the adsorbent is the availability -OH groups in the cellulose and hydroxyapatite (recognized by FTIR in Section 3.1.4). It is known that both F and -OH are structurally isoelectronic, having comparable ionic radius and can easily replace one another through ligand-exchange progress, which ultimately favors large F^- anions removal with high sorption capacity and selectivity [60; 10]. In addition, the hydrolyzing agent in the isolation of the stabilized cellulose nanofiber, sulfuric acid reacts with the cellulose surface hydroxyl groups to form sulfate half-esters, which also contributed to the negatively charged surface of the adsorbent, thus high adsorption of fluoride by CNF-AgMgOnHaP [61]. Therefore, the interaction between these surface groups and fluoride ions easily facilitates the high fluoride sorption capacity through ion-exchange mechanism, formation of an ion pair, or through H-bonding with the negatively charged surface. A similar pattern of surface exchange mechanisms of fluoride removal was reported elsewhere [22; 62].

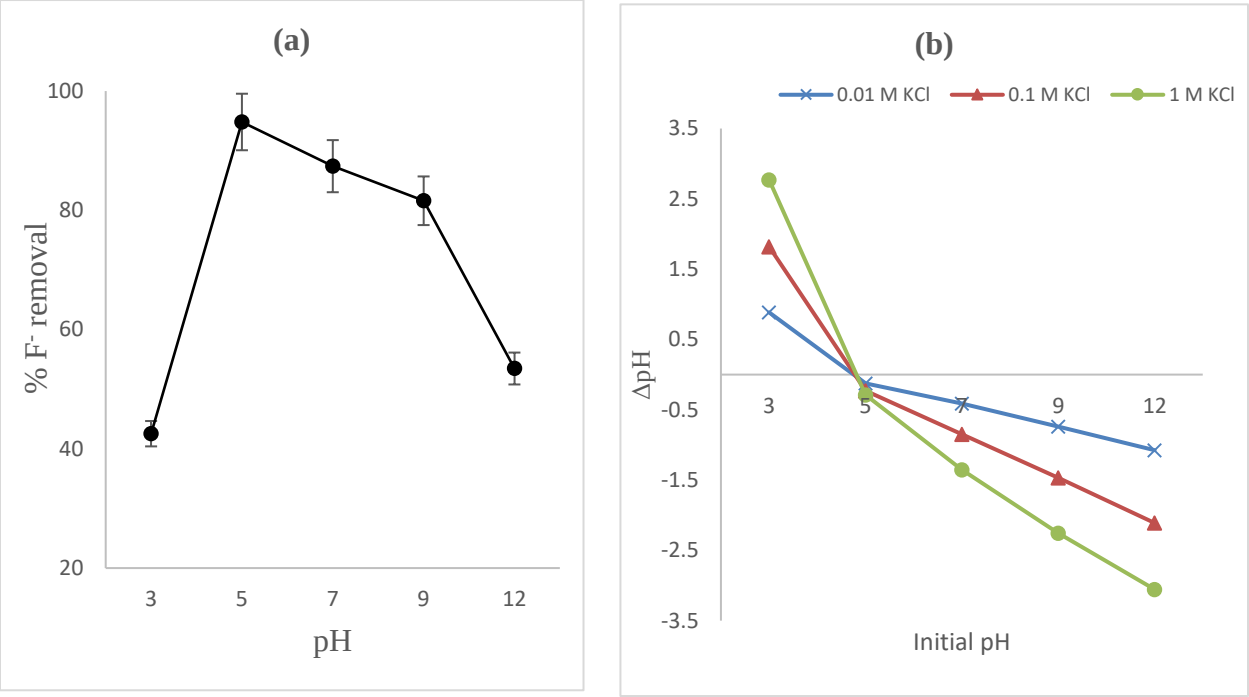

Fig. 7.7. (a) Effect of initial solution pH; (b) pH_{pzc} of CNF-AgMgOnHaP (adsorbent dose: 0.25 g volume of solution: 25 mL, contact time: 24 h at 150 rpm).

7.3.3.4 Effect of co-existing ions

The possible interference of coexisting ions (such as Cl^-, NO_3^-, CO_3^{2-}, and SO_4^{2-}) along with fluoride for the active sorption sites in the sorbent material was examined, and the results are presented in Figs. 7.8 (a-b). Fig. 7.8 (a) illustrates the variation of F^- removal efficiency by the adsorbent with the existence of co-anion in water. The result showed that the presence of anions like Cl^-, NO_3^-, and SO_4^{2-} had a slight effect on fluoride sorption by CNF-AgMgOnHaP with NO_3^- interfering in the least when compared with the anion-free water. However, the competitiveness of CO_3^{2-} appeared to have much effect with the F^- for surface binding sites leading to reduction in % fluoride removal from ~93 % to ~80 %. In addition, the effect of co-anion composite concentrations (10-50 mg/L) as a function of percentage fluoride removal by the CNF-AgMgOnHaP composite is depicted in Fig. 8(b). Evidently from the plot (7.8 (b)), at higher composite anion concentration, the surface potential affinity for fluoride by the sorbent reduces. This may be due to strong hydrolysis contribution by stable CO_3^{2-} ions surface complex formation, which hinders fluoride ions being sorbed by the CNF-AgMgOnHaP composite.

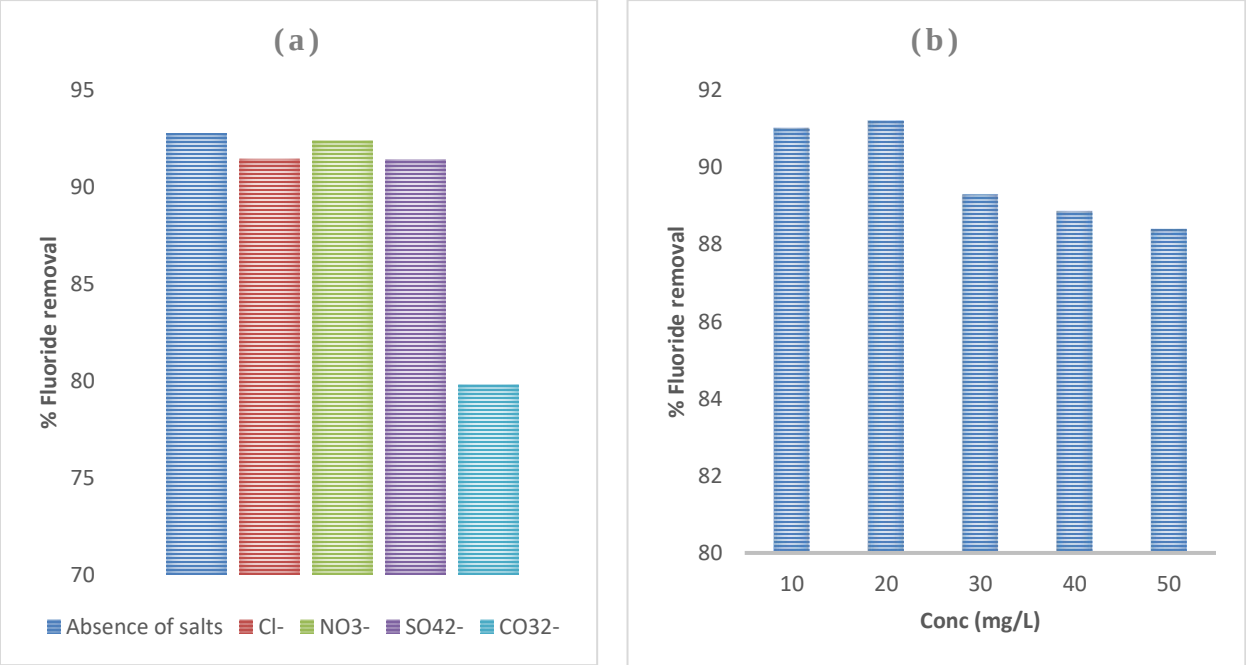

Fig. 7. 8. Effect of (a) co-anions (0.25 g at 10 mg/L of fluoride ion with 100 mg/L of the respective co-existing anion); (b) co-anion composite concentration on fluoride sorption by CNF-AgMgOnHaP composite (adsorbent dose: 0.25 g, 10 mg/L, contact time 10 min at 250 rpm).

7.3.3.5 Effect of initial concentration and adsorption isotherm

The rate of fluoride uptake by CNF-AgMgOnHaP composite as a function of initial fluoride concentrations (5–100 mg/L) at the different temperature (303, 313 and 323 K) are shown in Fig. 7.9 (a) and (b). As observed in Fig. 7.9 (a), the % F^- removal is found to decrease with increasing initial adsorbate concentration. This may be due to the reduction of active binding sites on the CNF-AgMgOnHaP adsorbent surface leading to its saturation by the sorbed fluoride ion.

Furthermore, in contrast to Fig. 7.9 (a), the F^- sorption capacity increased gradually as the fluoride concentration increases from 5 to 100 mg/L (Fig. 7. 9(b)). This suggests that as the concentration increases the driving force for overcoming the mass transfer resistance between the adsorbate in solution and adsorbent phases increases in the liquid-solid adsorption system [62].

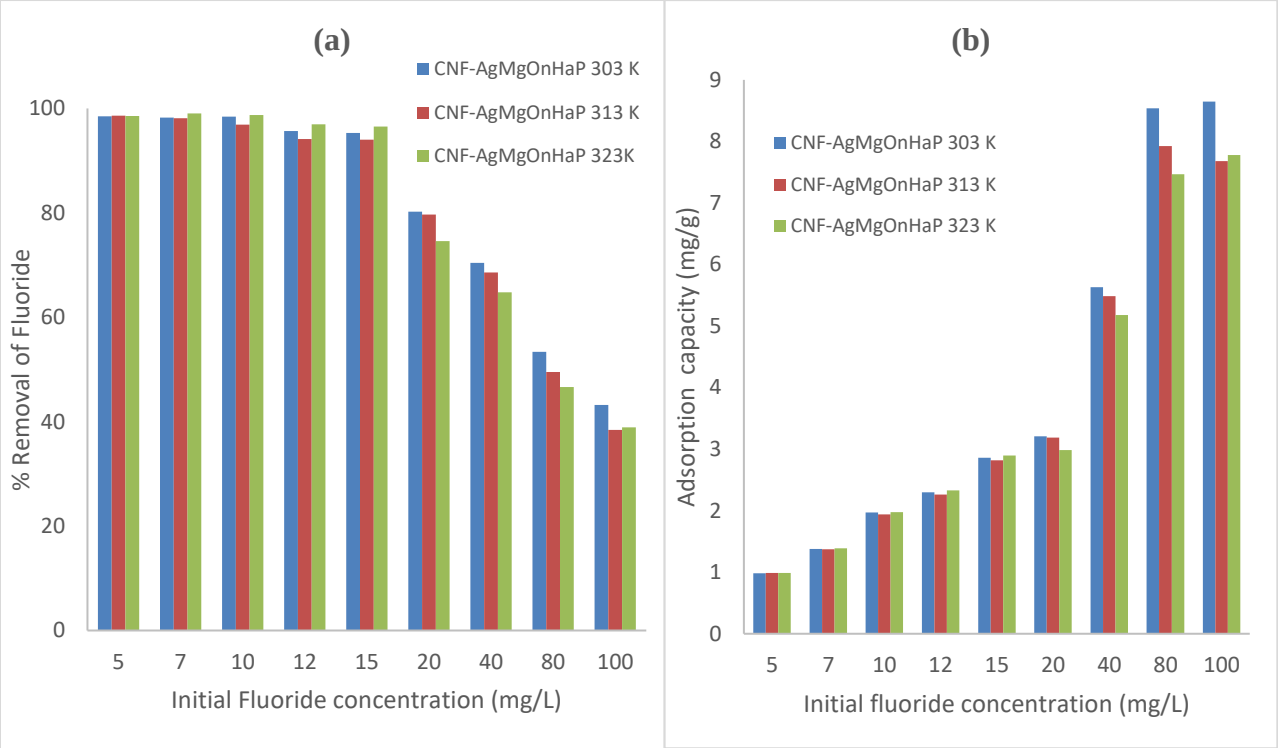

Fig. 7.9. Effect of initial fluoride concentration on CNF-AgMgOnHaP adsorbent at different temperatures.

To determine the adsorption interaction and mechanism of the F^- ions on the CNF-AgMgOnHaP composite surface, the non-linear forms of Langmuir [64] ((Eq. (3) and Freundlich [65] (Eq. (5), as well as the linear form of Dubinin–Radushkevich [66] (Eqs. (6) – (9)) isotherm models were used to evaluate the adsorption process.

These equations were simply used to calculate the adsorption parameters because of the usefulness of their model parameters, their clarity, and easy interpretability as well as to reduce their respective error functions [59; 66].

The non-linear forms of the Langmuir adsorption isotherm model [64] assume possible monolayer of F^- sorption onto the surface of CNF-AgMgOnHaP containing a finite number of uniform adsorption binding sites without migration of adsorbed molecules on the surface at a fixed temperature and is given as:

$$q_e = \frac{Q_m K_L C_e}{1+K_L C_e} \qquad (3)$$

where Q_m (mg/g) is the maximum adsorption capacity which assumes the complete monolayer of an adsorbent, C_e (mg/L) is the adsorbate equilibrium concentration, q_e (mg/g) is the amount of F^- ion adsorbed at equilibrium, K_L (L/mg) is the Langmuir adsorption equilibrium constant.

The fundamental characteristics of the Langmuir isotherm model can also be calculated in terms of a dimensionless parameter called the separation factor, R_L [67] (Eq. (4)), denoted as:

$$R_L = \frac{1}{1+k_L C_i} \quad (4)$$

where Ci (mg/L) is the initial fluoride concentration and K_L is the Langmuir equilibrium constant The R_L value is useful in determining if an sorption process is irreversible (R_L= 0), linear (R_L= l), favorable (0 < R_L< 1) or unfavorable (R_L> l).

The Freundlich adsorption isotherm [65], which is an empirical model describing the surface heterogeneity of the CNF-AgMgOnHaP sorbent through a multilayer adsorption system was also applied. It is expressed below as:

$$q_e = K_F C_e^{1/n} \quad (5)$$

where q_e (mg/g) is the equilibrium adsorption capacity of the CNF-AgMgOnHaP adsorbent, C_e (mg/L) is the equilibrium concentration, K_F [(mg/g)/(mg/L)^n] and 1/n are empirical Freundlich constant describing sorption capacity and intensity parameter respectively. K_F characterizes the strength of adsorption; while n indicates the magnitude of the adsorption driving force or the surface heterogeneity [59]. The adsorption isotherm is favorable when 0 < 1/n < 1, unfavorable when 1/n > 1 and irreversible when 1/n = 1.

The equilibrium adsorption results were also fitted into the linearized form of Dubinin Radushkevich isotherm model [66], which accounts for the effects of the porous nature of the CNF-AgMgOnHaP adsorbent as well as the mean free energy (E) of the sorption process. The D-R equations are shown below;

$$q_e = q_{max} \exp(-\beta_D \varepsilon^2) \quad (6)$$

$$\varepsilon = RT \ln\left[1 + \frac{1}{C_e}\right] \quad (7)$$

The energy E ((kJ/mol)) of F^- sorption from Dubinin-Radushkevich is

$$E = \frac{1}{\sqrt{2\beta_D}} \quad (8)$$

The general linearized form of the D-R is in equation (9):

$$\ln q_e = \ln q_{max} - \beta_D \varepsilon^2 \quad (9)$$

where q_{max} (mg/g) is the CNF-AgMgOnHaP adsorption capacity; β_D (mol^2/kJ^2) is the activity coefficient constant related to mean sorption energy; ε is the Polanyi potential, and E (kJ/mol) is the mean adsorption energy. The slope of the plot of ln q_e against ε^2 gives β_D and the intercept gives the adsorption capacity q_{max} of CNF-AgMgOnHaP. If the magnitude of E is between 8 and 16 kJ/mol, the adsorption process occurred via chemisorption, while for values where E < 8 kJ/mol, the adsorption process is of a physical nature.

Fig. 7.10 and Table 7.3 show the adsorption isotherms plots together with the corresponding calculated parameters of the sorbed F^- on CNF-AgMgOnHaP composite at the different temperatures.

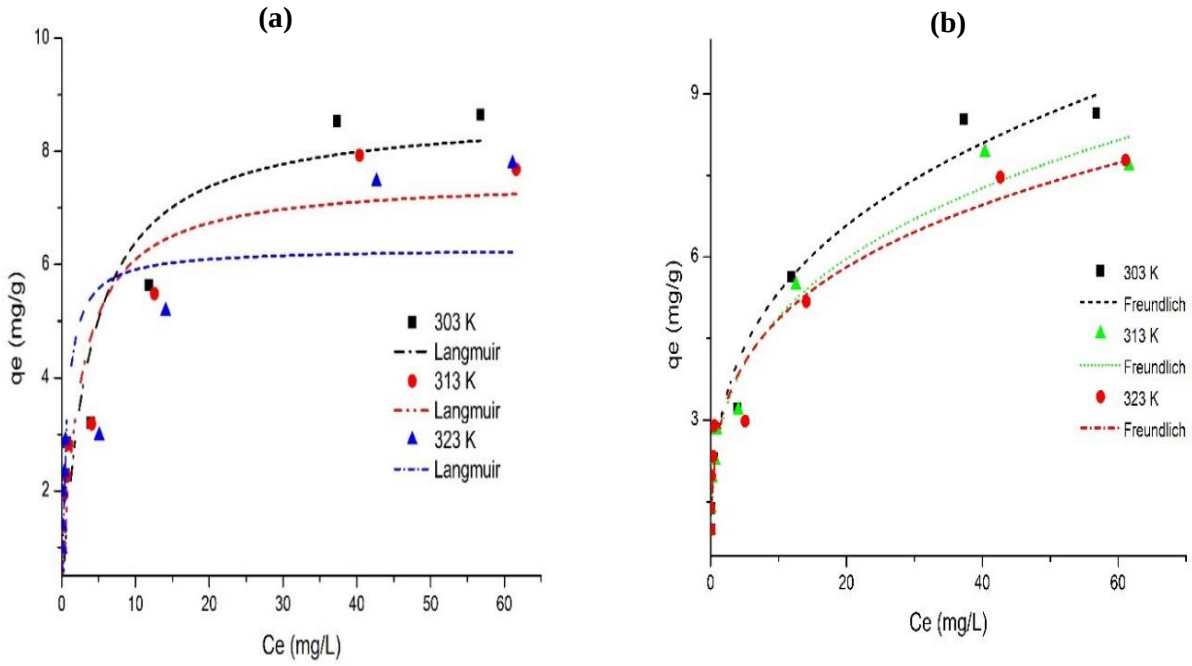

Fig. 7. 10. Non-linear isotherms by (a) Langmuir; (b) Freundlich methods, for the sorption of fluoride by CNF-AgMgOnHaP composite at 303 K, 313 K, and 323K.

Table 7.3. Isotherm parameters for the sorption of fluoride by CNF-AgMgOnHaP composite

	Temperature (K)	303	313	323
Non-Linear	**Langmuir isotherm**			
	Q_m (mg/g)	8.715	7.52	6.286
	K_L (L/mg)	0.275	0.426	1.566
	R_L	0.27	0.19	0.06
	Adj. R^2	0.813	0.845	0.709
	Red. $\chi 2$	1.632	1.085	1.879
	RSS	11.42	7.59	13.16
	Freundlich isotherm			
	K_F [(mg/g)/(mg/L)^n]	2.686	2.547	2.671
	n	3.345	3.519	3.853
	Adj. R^2	0.973	0.973	0.952
	Red. $\chi 2$	0.308	0.188	0.308
	RSS	2.158	1.318	2.158
Linear	**Dubinin-Radushkevvich**			
	β_{DR} (mol^2/kJ^2)	4.00E-08	3.00E-08	3.00E-08
	q_{max}(mg/g)	5.046	4.448	4.804
	E (kJ/mol)	3.535	4.083	4.083
	R^2	0.749	0.698	0.759

As shown in Table 7.3, the respective values of Q_m and K_F from the nonlinear plots decrease as the temperature increases, an indication that the adsorption of F^- by the CNF AgMgOnHaP

composite is unfavorable at higher temperatures. The Langmuir constant (K_L) values increases with respect to temperature changes indicating the existence of electrostatic attraction between the F^- and CNF AgMgOnHaP surface [67]. The obtained R_L values lying between 0 and 1 also confirm the favorability of the adsorption activity across all the operating temperature. Furthermore, since n lies between 1 and 10 as shown in Table 7.3, it demonstrates the physical adsorption of F- onto the adsorbent. It is important to note that the experimental maximum adsorption capacities were observed to be similar to the calculated Langmuir maximum adsorption capacities (Q_m) for all the temperature. In addition, the adsorption energies E (kJ/mol) values obtained by the linear D-R model generally increased as the temperature increases (Table 7.3). These values suggested that physical adsorption mechanism was involved in the F- sorption process. Consequently, based on the higher correlation coefficients (Adj. R^2) and lower Chi-square ($\chi 2$) values comparison (Table 7.3), it was found that the fluoride sorption onto the CNF-AgMgOnHaP was best described by Freundlich isotherm model across all the operating temperature than other models. This suggested that the dominated adsorption mechanisms on the adsorbent surface occurred through multilayer binding sites.

7.3.3.6 Adsorption kinetic

In order to evaluate the mechanism and time dependence kinetic parameters of F- sorption by CNF-AgMgOnHaP surface, the contact time experimental data (Fig. 7.5) were fitted to both reaction and diffusion-based kinetic models.

The Lagergren [70] pseudo-first-order model can be used for simple sorption process and its linear equation is stated in Eq. (10):

$$\log(q_e - q_t) = \log q_e - \frac{K_1}{2.303}\, t \qquad (10)$$

The linearized pseudo-second-order (Eq. (11)) model, which is normally used to describe cation exchange and chemisorption reaction mechanisms [71] was also employed and is represented by Eq (11) :

$$\frac{t}{q_t} = \frac{1}{K_2 q_e^2} + \frac{t}{q_e} \qquad (11)$$

The linear form of the intra-particle diffusion model [72] given in Eq. (12) was also used to describe the transfer of the solute in the solid-liquid system.

$$q_t = k_i t^{0.5} + C \qquad (12)$$

where q_e and q_t are the amounts of adsorbate uptake per mass of CNF-AgMgOnHaP adsorbent ($mg.g^{-1}$) at equilibrium and at time t (min), respectively; with K_1, K_2 and K_i (min^{-1}) representing the rate constant of the pseudo-first-order, pseudo-second-order and intraparticle diffusion rate constant respectively.

The normalized standard deviation (S.D. (%)) usually use to describe the applicability of the kinetic model in the fluoride sorption process on the adsorbent was determined using Eq. (13).

$$S.D.(\%) = 100\sqrt{\frac{\sum\left[\frac{q_e\,exp - q_e cal}{q_e exp}\right]2}{N-1}} \qquad (13)$$

where N is the number of data points, $q_{e,\,exp}$ and $q_{e,\,cal}$ (mg/g) are the experimental and the calculated equilibrium sorption capacity, respectively.

The calculated corresponding adsorption kinetic parameters from the three different model plots for fluoride sorption are summarized in Table 7.4. On the basis of higher correlation coefficient (R^2) and the lowest S.D. and Root Mean Square Error (RMSE) values obtained with regards to reaction-based pathways, the pseudo-second-order model was the most suitable model that best describes the fluoride sorption behavior on the adsorbent surface. This confirmed that the reaction rate was rapid as observed in Fig. 7.5. This is an indication that the reaction mechanism may have been controlled by chemisorption which involved sharing or exchange of ion between the CNF-AgMgOnHaP adsorbent and the sorbed F^-. This was supported by the XPS and pH at various reaction solution pH. In addition, the intraparticle diffusion models parameters (Table 7.4) further demonstrated that the overall kinetic models might not only depend upon the chemical adsorption process but were also governed by equilibrium diffusion mechanism through mass transfer of the adsorbate molecules from the external surface through the pores of the adsorbent [73].

Table 7.4. Kinetic model parameters for adsorption of F^- by CNF-AgMgOnHaP

Model	Values
Pseudo-First order	
q_{cal} (mg/g)	0.843
k_1 (min-1)	0.233
R^2	0.89
RMSE	0.240
S. D. (%)	63.53
Pseudo-second order	
q_{cal} (mg/g)	2.241
k_2 (g/min mg)	0.67
R^2	0.999
RMSE	0.082
S. D. (%)	18.21
Intra-particle diffusion	
C_1 (mg/g)	1.64
C_2 (mg/g)	1.62
C_3(mg/g)	1.9
K_{i1} (mg/g.min$^{0.5}$)	0.155
K_{i2} (mg/g.min$^{0.5}$)	0.143
K_{i3} (mg/g.min$^{0.5}$)	0.064
R^2_1	1
R^2_2	0.99
R^2_3	1

7.3.3.7 Thermodynamic parameters

The thermodynamic parameters (Table 7.5); such as standard enthalpy change (ΔH°), standard free energy (ΔG°), and standard entropy change (ΔS°) were evaluated from the experimental sorption data (303–323 K) using the following equations (Eqs. (14)–(17));

$$\Delta G^\circ = -RT \ln Kc \quad (14)$$

$$Kc = qe/Ce \quad (15)$$

$$\ln K_c = -\frac{\Delta H^\circ}{RT} + \frac{\Delta S^\circ}{R} \quad (16)$$

$$\Delta G^\circ = \Delta H^\circ - T\Delta S^\circ \quad (17)$$

where R (8.314 J mol^{-1} K^{-1}) is the gas constant, T is the absolute temperature (K). The equilibrium constant values K_c were obtained by plotting qe/Ce against Ce and extrapolating to zero [74-75].

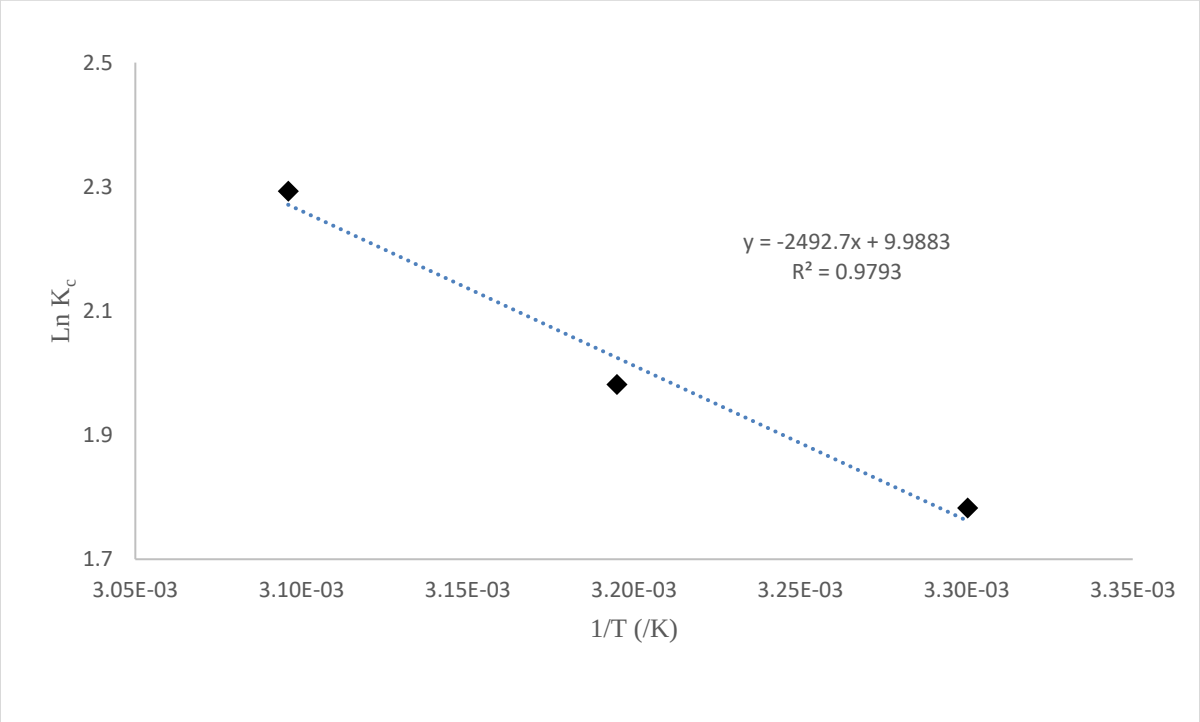

Fig. 7.11. ln K_c as a function of reciprocal of adsorption temperatures.

Table 7.5: Fluoride adsorption thermodynamic parameters.

Temperature (K)	ΔH◦ (KJ/mol)	ΔS◦ (J/mol K)	ΔG◦ (kJ/mol)
	20.73	83.05	
303			-4.44
313			-5.27
323			-6.10

The calculated thermodynamic parameters are listed in Table 7.5. The positive value of ΔH° is an indication that the fluoride sorption process is endothermic. This was further displayed by the decrease in the values of Qm and K_F respectively as well as the increased Ka values from the nonlinear isotherm parameters (Table 7. 3) as the temperature increases. The values of ΔG° obtained are all negative across the temperature range, which imply that the fluoride adsorption process occurred favorably and spontaneously with minimal requirements of the adsorption and activation energies [76]. The positive ΔS° values suggest that the F^- sorption phenomenon was governed by the increasing randomness of the F^- ions at the CNF-AgMgOnHaP adsorbent-solution interface.

7.3.4 Surface chemistry

Fig. 7. 12 shows the wide XPS spectra elemental analysis whose peaks are fitted according to the surface composition and chemistry of the fluoride sorbed CNF-AgMgOnHaP adsorbent. The main elements of the adsorbent as displayed by the XPS spectrum include carbon, oxygen, calcium, phosphorus, magnesium, fluorine and traces of silver content. As shown in Fig. 7.12, the C1s (287.1 eV) spectra is resolved into four gaussian peaks assigned to C-C (284.9 eV), C-O contribution of -OH groups (286.3 eV), C=O (287.6 eV) and O-C=O (289.2 eV) bonding states [77-78], associated with the cellulose nanofiber layer within the composite formation. The peaks of O 1 s and Mg 1s, which appeared in the range of 531–535 eV (deconvoluted into three major peaks) and 1307.2 eV (single peak) respectively, are a representation of lattice O atoms bonded with carbonyl, Mg atoms, hydroxyl groups and adsorbed water [77-78]. The presence of 2p (134.0 eV) and Ca 2p (347.7 eV) has been attributed to organic P and Ca—C=O interaction for calcium phosphates in the hydroxyapatite. The fewer related peak at ~367.8 eV (two lines) corresponded to the characteristic peak of Ag NPs confirming its existence within the composite. The appearance of F 1s peak at 685 eV which was resolved into two peaks located at 685.5 and 689.9 eV attributed to inorganic and organic fluoride respectively, is an indication of F- ions being bounded to the CNF-AgMgOnHaP adsorbent. This was further supported by the possible Ca---F bond as shown by the Ca 2p (347.7 eV). Thus, the XPS, EDS, FTIR, and solution pH results clearly show that the possible surface mechanisms of fluoride removal by CNF-AgMgOnHaP composite could have

occurred via ligand exchange and electrostatic attraction between F^- and the OH^-, Mg^{2+} or Mg--OH^+ and Ca---OH^+ species at the sorbent-sorbate solution interface.

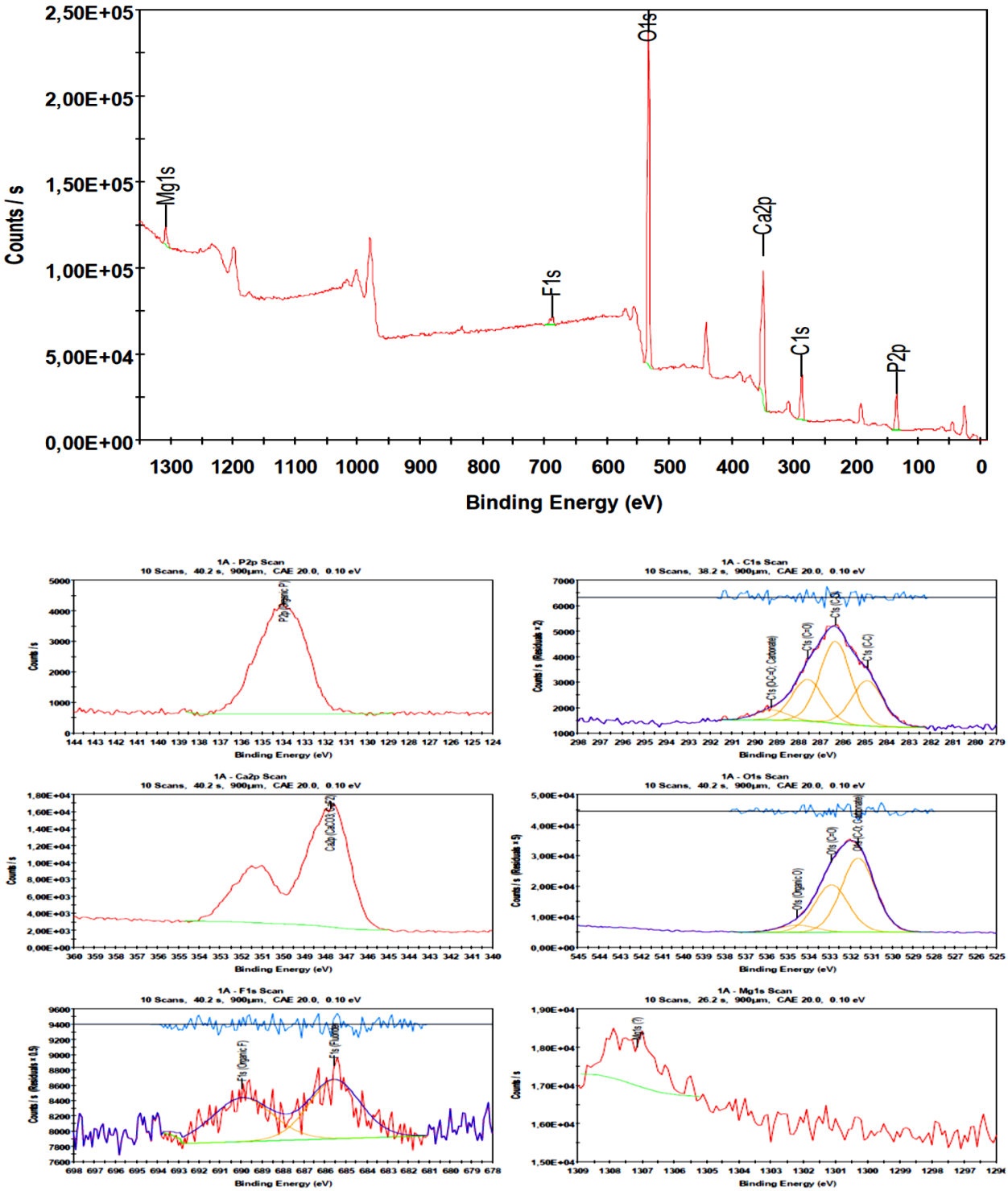

Fig. 7.12. Wide-scan XPS spectra of CNF-AgMgOnHaP adsorbent after fluoride adsorption

7.3.5 Regeneration and reusability of CNF-AgMgOnHaP adsorbent

Fig. 7.13 depicts the reusability trend against the percent fluoride removal from aqueous solution at various cycles of defluoridation (1−5) with an adsorbent dose of 0.25 g/ 50mL at 25 ± 3 °C. This was done based on the analysis from the effects of co-existing anions, which suggested that the capacity of CNF-AgMgOnHaP adsorbent to remove fluoride in solution was low in alkaline solution. Therefore, different concentrations of NaOH and Na_2CO_3 was used in this study.

As shown in Fig 7.13, fluoride removal by sorbent regenerated with NaOH was observed to be very low when compared to that regenerated with Na_2CO_3. On both regenerants, the percentage fluoride removal by the composite decreases (~48 % for NaOH and 46 % Na_2CO_3) with increasing regeneration cycle. It is important to note that the type of surface interaction between the regenerants and the adsorbent determines the reusability property; hence, the provision of better regeneration capability by the adsorbent may have been through electrostatic and chemisorption interactions between the adsorbent and F^-, which occurs naturally in the groundwater [79-80]. Consequently, the regenerated CNF-AgMgOnHaP adsorbent possess a greater economic potential in the removal and recovery of fluoride ions even in the presence of limiting solution parameter.

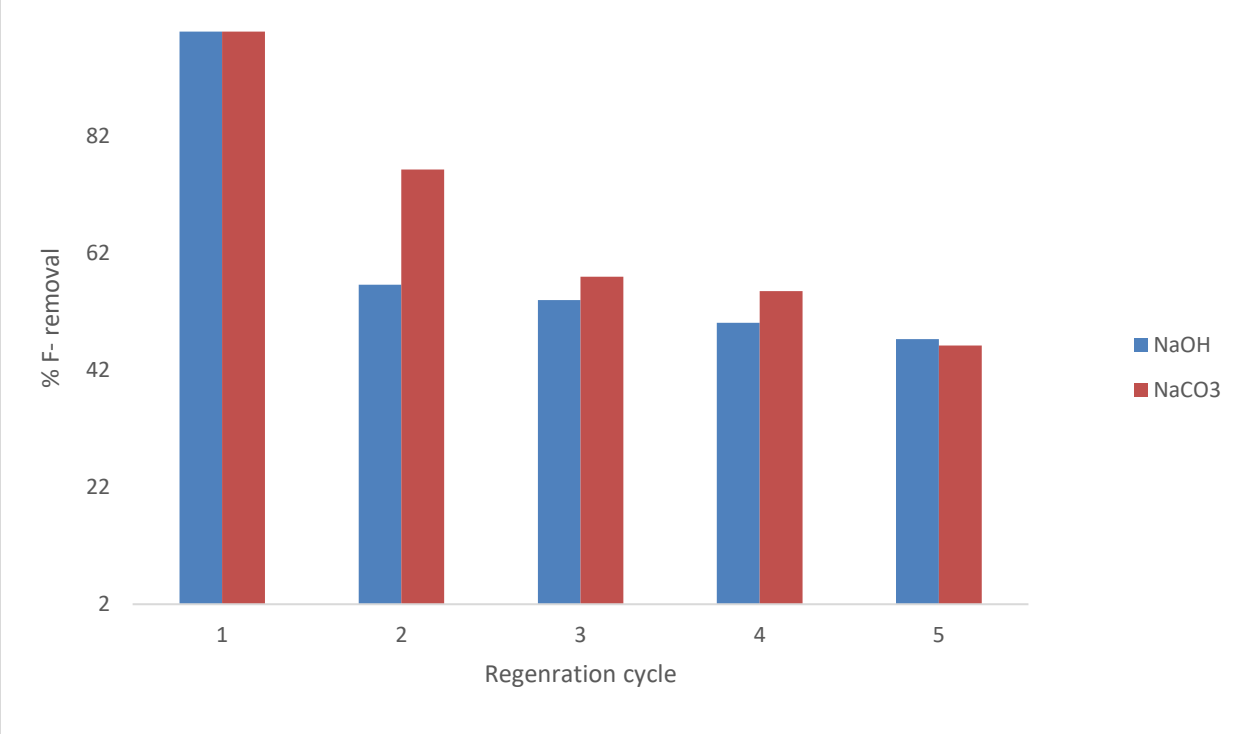

Fig. 7.13. Percent fluoride removal as a function of defluoridation cycle using 0.01 M NaOH and 0.1 M Na_2CO_3 as regenerates (initial fluoride concentration: 10 mg/L, volume of solution: 50 mL, adsorbent dosage: 0.25 g contact time: 30 min at 250 rpm).

7.4 Antibacterial activity of CNF-AgMgOnHaP adsorbent

Figs. 7.14 (a and b) displayed the observed antibacterial property of CNF-AgMgOnHaP adsorbent through the values exhibited by the zone of inhibition against gram-negative and gram-positive bacterial strains. The diameter of the zone of inhibition was found to increase with an increase in the concentration of the adsorbent (Fig. 7.14 (b)). The observed zone of inhibition demonstrated that CNF-AgMgOnHaP adsorbent possesses antibacterial activity against all the bacterial strains. However, this antibacterial property varies, with higher antimicrobial potency observed towards *E. Coli* compared to S. aureus and K. pneumonia.

The antibacterial potency observed by this material depends upon several factors, including the synergistic effects of Ag-MgO within the synthesized CNF-AgMgOnHaP composite. It has been established that MgO and Ag-based materials have excellently broad-spectrum, potent antimicrobial properties and are easily impregnated into cellulosic materials as a stabilizing agent [81-83]. The antibacterial property of the CNF-AgMgOnHaP adsorbent may be due to the diffusion of Ag-MgO nanoparticles within the adsorbent through the release of metal ions disrupting the cell wall structure of the bacteria genome in producing intracellular reactive oxygen species (ROS) resulting in the microbial cell death [18; 84-85], the Ag-MgO nanocomposite antibacterial activity may also depend on the reducing and capping agents used in the synthesis route, as well as the size and surface properties of the composite [36; 86-87]. Therefore, the adsorbent presents specific antibacterial activity against all the bacteria strains.

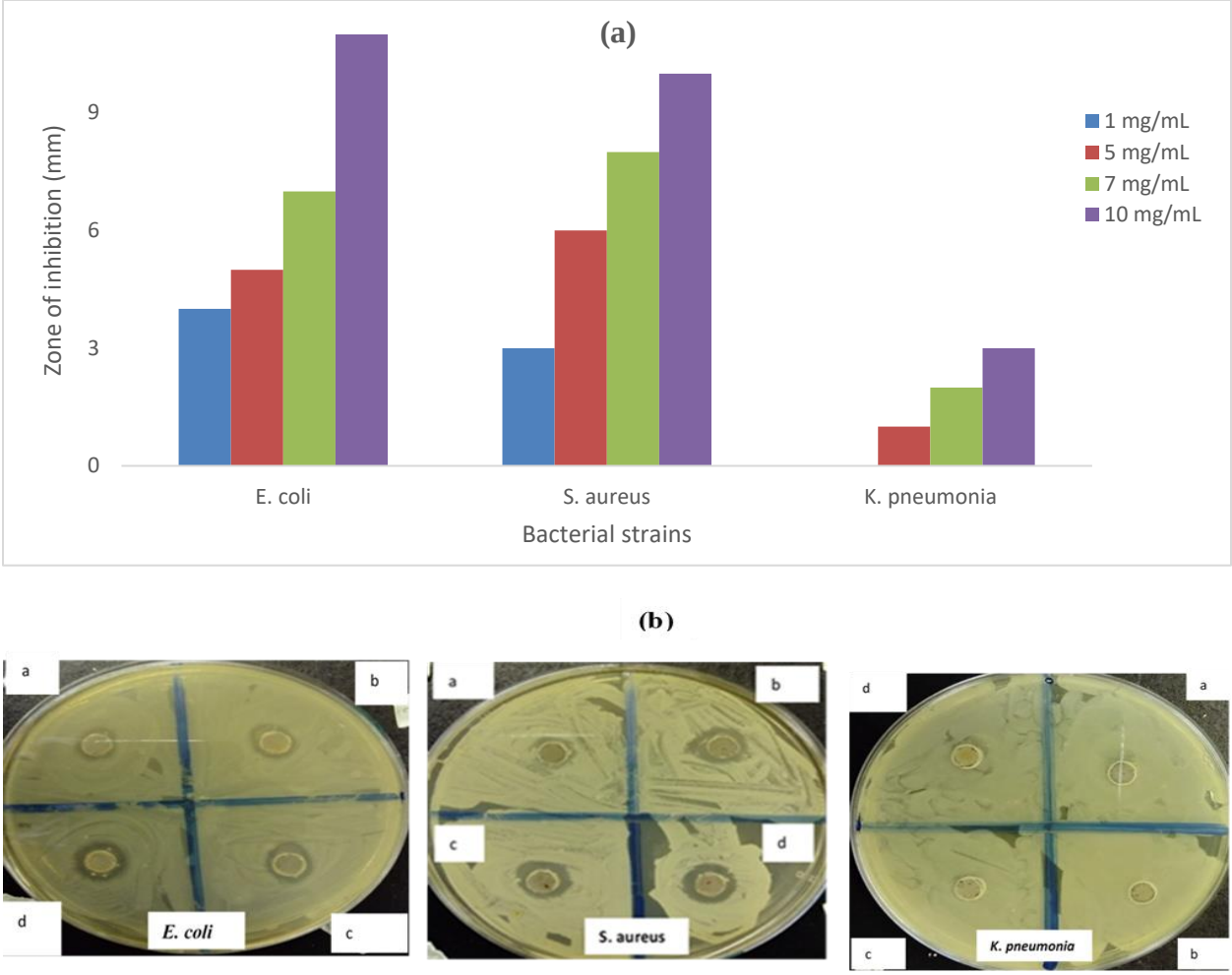

Fig. 7.14. (a) Graphical representation (b) Photographic plate of antibacterial activity by the CNF-AgMgOnHaP composite against *E. coli*, *S. aureus* and *K. pneumonia* at varying concentration range.

7.5 Conclusions

CNF-AgMgOnHaP composite was successfully biosynthesized through the impregnation and dispersion of Ag-MgO and nHap nanoparticles by a simple hydrothermal method. The structural morphology and optical properties provided evidence showing the aggregation of nanoparticles on the biopolymeric cellulose fiber matrix after modification. The increased surface area of CNF-AgMgOnHaP composite by BET analysis showed the availability of numerous binding functional groups within the matrix, which was in agreement with other Spectro-analytical results. The sorption of fluoride by the adsorbent was found to be strongly dependent on the different sorption conditions with the optimum adsorption conditions determined at 10 min (25 ± 3 °C), 0.25g adsorbent dose, pH 5, with maximum defluoridation capacity of 8.712 mg/g at 303K. The sorbate-sorbent interaction was well documented by adsorption isotherms and kinetic models and based on the higher correlation coefficients (R^2) and lower Chi-square ($\chi 2$) values comparison, it was found that the fluoride sorption onto the CNF AgMgOnHaP was best described by Freundlich

isotherm model across all the operating temperatures. Based on higher correlation coefficient (R^2) and the lowest S.D. and RMSE values obtained with regards to reaction-based pathways, the pseudo-second-order model was the most suitable model that best describes the fluoride sorption behavior on the adsorbent surface. However, the overall kinetic results indicated that the mechanisms not only depend on the chemical adsorption process but were also governed by mass transfer of the adsorbate molecules from the external surface through the pores of the adsorbent. The thermodynamic parameters revealed that the adsorption process of F- onto CNF AgMgOnHaP was endothermic and spontaneous in nature. The synthesized composite also provides some antibacterial activity against both gram-negative and gram-positive water bacteria strains. Consequently, the synthesized CNF AgMgOnHaP composite can be used as a suitable and viable adsorbent in the simultaneous removal of fluoride and pathogen in drinking water.

Conflicts of interest

The authors declare no conflicts of interest.

Acknowledgment

Authors would like to acknowledge financial support from USAID-PEER Cycle 6-Award No: AID-OAA-A-11-00012; National Research Foundation Grant No: 114726; University of Venda, South Africa (RPC grant Number: SES/17/ERM/03), Prof Gitari DHET Research incentive funds and Mintek, South Africa.

References

1. WWAP (United Nations World Water Assessment Programme)., 2015. The United Nations World Water Development Report 2015: Water for a Sustainable World. Paris, UNESCO.
2. Gitari W.M., Ngulube, T., Masindi, V., Gumbo, J.R. 2013. Defluoridation of groundwater using Fe3+-modified bentonite clay: Optimization of adsorption conditions, Desalin. Water Treat. 1–13, doi: 10.1080/ 19443994.2013.855669.
3. Ncube, E.J., Schutte, C.F., 2005. The occurrence of fluoride in South African groundwater: a water quality and health problem. Water SA 31 (1), 35–40.
4. World Health Organization and UNICEF, 2017. Progress on drinking water, sanitation and hygiene: 2017 update and SDG baselines. World Health Organization.
5. Mumtaz, N., Pandey, G. and Labhasetwar, P.K., 2015. Global fluoride occurrence, available technologies for fluoride removal and electrolytic defluoridation: a review. Critical Reviews in Environmental Science and Technology, DOI: 10.1080/10643389.2015.1046768
6. Zhang, T., Li, Q., Xiao, H., Mei, Z., Lu, H., & Zhou, Y., 2013. Enhanced fluoride removal from water by non-thermal plasma modified CeO2/Mg-Fe layered double hydroxides. Applied Clay Science, 72, 117–123.

7. Ayoob, S. and Gupta, A.K., 2006. Fluoride in drinking water: a review on the status and stress effects. Critical Reviews in Environmental Science and Technology, 36(6), pp.433-487.
8. Singh, J., Singh, P. and Singh, A., 2016. Fluoride ions vs removal technologies: a study. Arabian Journal of Chemistry, 9(6), pp.815-824.
9. Loganathan, P., Vigneswaran, S., Kandasamy, J., & Naidu, R. 2013., Defluoridation of drinking water using adsorption processes. Journal of Hazardous Materials, 248, 1–19.
10. WHO, Guidelines for drinking water quality, forth ed., World Health Organization, Geneva, 2011.
11. Miretzky, P., Cirelli, A.F., 2011. Fluoride removal from water by chitosan derivatives and composites: a review. J. Fluor. Chem. 132, 231e240.
12. Ramesh, M., Malathi, N., Ramesh, K., Aruna, R.M. and Kuruvilla, S., 2017. Comparative evaluation of dental and skeletal fluorosis in an endemic fluorosed district, Salem, Tamil Nadu. Journal of pharmacy & bioallied sciences, 9(Suppl 1), p.S88.
13. Ashbolt, N.J., 2004. Microbial contamination of drinking water and disease outcomes in developing regions. Toxicology, 198(1-3), pp.229-238.
14. Bitton, G., 2014. Microbiology of Drinking Water: Production and Distribution. John Wiley & Sons.
15. Hijnen, W., Beerendonk, E. & Medema, G. J. 2006. Inactivation credit of UV radiation for viruses, bacteria and protozoan (oo)cysts in water: a review. Water Res. 40, 3–22.
16. Chlorine Chemistry Council and American Chemistry Council, 2006. Drinking Water Chlorination: A Review of Disinfection Practices and Issues. WATER CONDITIONING AND PURIFICATION INTERNATIONAL, p.68.
17. Momba, M.N.B., 2013. Selection and Use of Home Water-treatment Systems and Devices: Report to the Water Research Commission. Water Research Commission.
18. Dankovich, T.A., Levine, J.S., Potgieter, N., Dillingham, R. and Smith, J.A., 2016. Inactivation of bacteria from contaminated streams in Limpopo, South Africa by silver-or copper-nanoparticle paper filters. Environmental science: water research & technology, 2(1), pp.85-96.
19. Bhatnagar, A., Kumar, E. and Sillanpää, M., 2011. Fluoride removal from water by adsorption—a review. Chemical Engineering Journal, 171(3), pp.811-840.
20. Yadav, K.K., Gupta, N., Kumar, V., Khan, S.A. and Kumar, A., 2018. A review of emerging adsorbents and current demand for defluoridation of water: Bright future in water sustainability. Environment international, 111, pp.80-108.
21. Tian, Y., Wu, M., Liu, R., Wang, D., Lin, X., Liu, W., Ma, L., Li, Y. and Huang, Y., 2011. Modified native cellulose fibers—A novel efficient adsorbent for both fluoride and arsenic. Journal of hazardous materials, 185(1), pp.93-100.
22. Gitari, W.M., Izuagie, A.A. and Gumbo, J.R., 2017. Synthesis, characterization and batch assessment of groundwater fluoride removal capacity of trimetal Mg/Ce/Mn oxide-modified diatomaceous earth. Arabian Journal of Chemistry.
23. Ferroudj, N., Nzimoto, J., Davidson, A., Talbot, D., Briot, E., Dupuis, V., Bée, A., Medjram, M.S. and Abramson, S., 2013. Maghemite nanoparticles and maghemite/silica

nanocomposite microspheres as magnetic Fenton catalysts for the removal of water pollutants. Applied Catalysis B: Environmental, 136, pp.9-18.

24. Gopakumar, D.A., Manna, S., Pasquini, D., Thomas, S. and Grohens, Y., 2018. Nanocellulose: Extraction and application as a sustainable material for wastewater purification. In New Polymer Nanocomposites for Environmental Remediation (pp. 469-486).
25. Kalia, S., Dufresne, A., Cherian, B.M., Kaith, B.S., Avérous, L., Njuguna, J. and Nassiopoulos, E., 2011. Cellulose-based bio-and nanocomposites: a review. International Journal of Polymer Science, 2011.
26. Fu, L.H., Xie, Y.M., Bian, J., Ma, M.G., Tian, C.H. and Jin, X.J., 2015. Microwave-assisted rapid synthesis of lignocellulose/hydroxyapatite nanocomposites. Materials Letters, 159, pp.51-53.
27. Kamphunthong, W., Hornsby, P. and Sirisinha, K., 2012. Isolation of cellulose nanofibers from para rubberwood and their reinforcing effect in poly (vinyl alcohol) composites. Journal of Applied Polymer Science, 125(2), pp.1642-1651.
28. Mandal, A. and Chakrabarty, D., 2011. Isolation of nanocellulose from waste sugarcane bagasse (SCB) and its characterization. Carbohydrate Polymers, 86(3), pp.1291-1299.
29. Poinern, Gérrard Eddy Jai, Malay K. Ghosh, Yan-Jing Ng, Touma B. Iss, ShashiAnand, and Pritam Singh, 2011. Defluoridation behavior of nanostructured hydroxyapatite synthesized through an ultrasonic and microwave combined technique. Journal of Hazardous Materials 185. 29–37.
30. Athar, T., 2013. Synthesis of MgO Nanoparticles via Sol–Gel Method. Materials Focus, 2(6), pp.493-496.
31. Karthiga, P., 2017. Preparation of silver nanoparticles by Garcinia mangostana stem extract and investigation of the antimicrobial properties. Biotechnology Research and Innovation.
32. Mulvaney, P., 1996. Surface plasmon spectroscopy of nanosized metal particles. Langmuir, 12(3), pp.788-800.
33. Stankic, S., Sterrer, M., Hofmann, P., Bernardi, J., Diwald, O. and Knözinger, E., 2005. Novel optical surface properties of Ca2+-doped MgO nanocrystals. Nano letters, 5(10), pp.1889-1893.
34. Sterrer, M., Berger, T., Diwald, O. and Knözinger, E., 2003. Energy Transfer on the MgO Surface, Monitored by UV− Induced H2 Chemisorption. Journal of the American Chemical Society, 125(1), pp.195-199.
35. Barud, H.S., Regiani, T., Marques, R.F., Lustri, W.R., Messaddeq, Y. and Ribeiro, S.J., 2011. Antimicrobial bacterial cellulose-silver nanoparticles composite membranes. Journal of Nanomaterials, 2011, p.10.
36. Kuppusamy, P., Yusoff, M.M., Maniam, G.P. and Govindan, N., 2016. Biosynthesis of metallic nanoparticles using plant derivatives and their new avenues in pharmacological applications–An updated report. Saudi Pharmaceutical Journal, 24(4), pp.473-484.
37. Kolarova, M., Samec, D., Kvitek, O., Reznickova, A., Rimpelova, S., and Svorcik, V. (2017). “Preparation and characterization of silver nanoparticles in methyl cellulose matrix and their antibacterial activity,” Japanese Journal of Applied Physics 56(6S1), 06GG09. DOI: 10.7567/JJAP.56.06GG09

38. Xiong, R., Lu, C., Zhang, W., Zhou, Z. and Zhang, X., 2013. Facile synthesis of tunable silver nanostructures for antibacterial application using cellulose nanocrystals. Carbohydrate polymers, 95(1), pp.214-219.
39. Mujahid, M., Sarfraz, S. and Amin, S., 2015. On the Formation of Hydroxyapatite Nano Crystals Prepared Using Cationic Surfactant. Materials Research, 18(3), pp.468-472.
40. Maryan, A.S., Montazer, M. and Harifi, T., 2015. Synthesis of nano silver on cellulosic denim fabric producing yellow colored garment with antibacterial properties. Carbohydrate polymers, 115, pp.568-574
41. Fan, M., Dai, D. and Huang, B., 2012. Fourier transform infrared spectroscopy for natural fibres. In Fourier transform-materials analysis. InTech.
42. Koutsopoulos, S., 2002. Synthesis and characterization of hydroxyapatite crystals: a review study on the analytical methods. Journal of Biomedical Materials Research Part A, 62(4), pp.600-612.
43. Balamurugan S, Ashna L, Parthiban P (2014) Synthesis of nanocrystalline MgO particles by combustion followed by annealing method using hexamine as a fuel. J Nano Tech 6:1–6. doi:10. 1155/2014/841803
44. Prabhu, S.M., Elanchezhiyan, S.S., Lee, G., Khan, A. and Meenakshi, S., 2016. Assembly of nano-sized hydroxyapatite onto graphene oxide sheets via in-situ fabrication method and its prospective application for defluoridation studies. Chemical Engineering Journal, 300, pp.334-342.
45. Hwang, N. and Barron, A.R., 2011. BET surface area analysis of nanoparticles. The Connexions project, pp.1-11.
46. Banavath, H.N., Bhardwaj, N.K. and Ray, A.K., 2011. A comparative study of the effect of refining on charge of various pulps. Bioresource technology, 102(6), pp.4544-4551.
47. Lü, L., Lu, D., Chen, L., Luo, F. 2010. Removal of Cd(II) by modified lawny grass cellulose adsorbent. Desalination, 259(1-3), 120-130.
48. Mohammad, N.F., Othman, R. and Yeoh, F.Y., 2015. Controlling the pore characteristics of mesoporous apatite materials: hydroxyapatite and carbonate apatite. Ceramics International, 41(9), pp.10624-10633.
49. Akram, M., Alshemary, A.Z., Goh, Y.F., Ibrahim, W.A.W., Lintang, H.O. and Hussain, R., 2015. Continuous microwave flow synthesis of mesoporous hydroxyapatite. Materials Science and Engineering: C, 56, pp.356-362.
50. Hou, S., Li, J., Huang, X., Wang, X., Ma, L., Shen, W., Kang, F. and Huang, Z.H., 2017. Silver Nanoparticles-Loaded Exfoliated Graphite and Its Anti-Bacterial Performance. Applied Sciences, 7(8), p.852.
51. Maliyekkal, S.M., Antony, K.R. and Pradeep, T., 2010. High yield combustion synthesis of nanomagnesia and its application for fluoride removal. Science of the total environment, 408(10), pp.2273-2282.
52. Klemm, D., Heublein, B., Fink, H. P., & Bohn, A. (2005). Cellulose: Fascinating biopolymer and sustainable raw material. Angewand te Chemie-International Edition, 44, 3358–3393.
53. Wada M, Heux L, Sugiyama J (2004) Polymorphism of cellulose I family: reinvestigation of cellulose IV. Biomacromolecules 5:1385–1391

54. Fleet, M.E., Liu, X. and King, P.L., 2004. Accommodation of the carbonate ion in apatite: An FTIR and X-ray structure study of crystals synthesized at 2–4 GPa. American Mineralogist, 89(10), pp.1422-1432.
55. Averbuch-Pouchot, M.T. and Guitel, J.C., 1976. Structure cristalline d'un tripolyphosphate acide mixte zinc–argent nonahydraté: Zn_2Ag_0, 62H0, 38P3O10. 9H2O. Acta Crystallographica Section B, 32(8), pp.2270-2274.
56. Calvo, C.R.I.S.P.I.N., 1967. The crystal structure of α-Mg2P2O7. Acta Crystallographica, 23(2), pp.289-295.
57. Chen, H., Zhang, Z., Wang, X., Chen, J., Xu, C., Liu, Y., Yu, Z. and Wang, X., 2018. Fabrication of Magnetic Fe/Zn Layered Double Oxide@ Carbon Nanotube Composites and Their Application for U (VI) and 241Am (III) Removal. ACS Applied Nano Materials, 1(5), pp.2386-2396.
58. Samadi, N., Hasanzadeh, R. and Rasad, M., 2015. Adsorption isotherms, kinetic, and desorption studies on removal of toxic metal ions from aqueous solutions by polymeric adsorbent. Journal of Applied Polymer Science, 132(11).
59. Tran, H.N., You, S.J., Hosseini-Bandegharaei, A. and Chao, H.P., 2017. Mistakes and inconsistencies regarding adsorption of contaminants from aqueous solutions: a critical review. Water research, 120, pp.88-116.
60. Swain, S.K., Mishra, S., Patnaik, T., Patel, R.K., Jha, U. and Dey, R.K., 2012. Fluoride removal performance of a new hybrid sorbent of Zr (IV)–ethylenediamine. Chemical Engineering Journal, 184, pp.72-81.
61. Voisin, H., Bergström, L., Liu, P. and Mathew, A., 2017. Nanocellulose-based materials for water purification. Nanomaterials, 7(3), p.57
62. Nayak, B., Samant, A., Patel, R. and Misra, P.K., 2017. Comprehensive understanding of the kinetics and mechanism of fluoride removal over a potent nanocrystalline hydroxyapatite surface. ACS Omega, 2(11), pp.8118-8128.
63. Tanhaei, B., Ayati, A., Lahtinen, M. and Sillanpää, M., 2015. Preparation and characterization of a novel chitosan/Al2O3/magnetite nanoparticles composite adsorbent for kinetic, thermodynamic and isotherm studies of Methyl Orange adsorption. Chemical engineering journal, 259, pp.1-10.
64. Langmuir I., 1916. The constitution and fundamental properties of solids and liquids, J. Am. Chem. Soc. 38 2221–2295.
65. Freundlich H.M.F., 1906. Uber die adsorption in l¨osungen, Z. Phys. Chem. 57A 385–470.
66. Dubinin, M., Radushkevich, L., 1947. Equation of the characteristic curve of activated charcoal. Chem. Zentr. 1 (1), 875.
67. Tran, H.N., Wang, Y.F., You, S.J. and Chao, H.P., 2017. Insights into the mechanism of cationic dye adsorption on activated charcoal: the importance of π–π interactions. Process Safety and Environmental Protection, 107, pp.168-180.
68. Hall, K.R., Eagleton, L.C., Acrivos, A., Vermeulen, T., 1966. Pore-and solid-diffusion kinetics in fixed-bed adsorption underconstant-pattern conditions. Ind. Eng. Chem. Fundam. 5 (2),212–223.
69. Helfferich, F.G. and Dranoff, J.S., 1963. Ion Exchange. McGraw-Hill, New York (1962), 624 pp

70. Lagergren S., 1898. Zur Theorie der sogenannten adsorption geloster stoffe, K. Sven. Vetenskapsakad. Handl. 24 1–39.
71. Ho YS , Ng JCY , McKay G ., 2000. Kinetics of pollutant sorption by biosorbents: review. Sep Purif Methods; 29:189–232 .
72. Weber, W.J. and Morris, J.C., 1964. Equilibria and capacities for adsorption on carbon. Journal of the Sanitary Engineering Division, 90(3), pp.79-108.
73. Machado, F.M., Bergmann, C.P., Lima, E.C., Royer, B., de Souza, F.E., Jauris, I.M., Calvete, T. and Fagan, S.B., 2012. Adsorption of Reactive Blue 4 dye from water solutions by carbon nanotubes: experiment and theory. Physical Chemistry Chemical Physics, 14(31), pp.11139-11153.
74. Viswanathan, N., Pandi, K. and Meenakshi, S., 2014. Synthesis of metal ion entrapped silica gel/chitosan biocomposite for defluoridation studies. International journal of biological macromolecules, 70, pp.347-353.
75. Biggar, J.W. and Cheung, M.W., 1973. Adsorption of Picloram (4-Amino-3, 5, 6 Trichloropicolinic Acid) on Panoche, Ephrata, and Palouse Soils: A Thermodynamic Approach to the Adsorption Mechanism 1. Soil Science Society of America Journal, 37(6), pp.863-868.
76. Tran, H.N., You, S.J. and Chao, H.P., 2017. Fast and efficient adsorption of methylene green 5 on activated carbon prepared from new chemical activation method. Journal of environmental management, 188, pp.322-336.
77. Rouxhet, P.G. and Genet, M.J., 2011. XPS analysis of bio-organic systems. Surface and Interface Analysis, 43(12), pp.1453-1470.
78. Bomben, K.D., Moulder, J.F., Sobol, P.E. and Stickle, W.F., 1995. Handbook of X-ray photoelectron spectroscopy: a reference book of standard spectra for identification and interpretation of XPS data. Physical Electronics, Eden Prairie, MN.
79. Newberg, J.T., Starr, D.E., Yamamoto, S., Kaya, S., Kendelewicz, T., Mysak, E.R., Porsgaard, S., Salmeron, M.B., Brown Jr, G.E., Nilsson, A. and Bluhm, H., 2011. Formation of hydroxyl and water layers on MgO films studied with ambient pressure XPS. Surface Science, 605(1-2), pp.89-94.
80. Akharame, M.O., Fatoki, O.S. and Opeolu, B.O., 2018. Regeneration and reuse of polymeric nanocomposites in wastewater remediation: the future of economic water management. Polymer Bulletin, pp.1-35.
81. Kim, M.K., Sundaram, K.S., Iyengar, G.A. and Lee, K.P., 2015. A novel chitosan functional gel included with multiwall carbon nanotube and substituted polyaniline as adsorbent for efficient removal of chromium ion. Chemical Engineering Journal, 267, pp.51-64.
82. Vivekanandhan, S., Christensen, L., Misra, M. and Mohanty, A.K., 2012. Green process for impregnation of silver nanoparticles into microcrystalline cellulose and their antimicrobial bionanocomposite films. Journal of Biomaterials and Nanobiotechnology, 3(03), p.371.
83. Rafique, M., Sadaf, I., Rafique, M.S. and Tahir, M.B., 2017. A review on green synthesis of silver nanoparticles and their applications. Artificial cells, nanomedicine, and biotechnology, 45(7), pp.1272-1291.

84. Tang, Z.X. and Lv, B.F., 2014. MgO nanoparticles as antibacterial agent: preparation and activity. Brazilian Journal of Chemical Engineering, 31(3), pp.591-601.
85. Cai, Y., Wu, D., Zhu, X., Wang, W., Tan, F., Chen, J., Qiao, X. and Qiu, X., 2017. Sol-gel preparation of Ag-doped MgO nanoparticles with high efficiency for bacterial inactivation. Ceramics International, 43(1), pp.1066-1072.
86. Horie, M., Fujita, K., Kato, H., Endoh, S., Nishio, K., Komaba, L.K., Nakamura, A., Miyauchi, A., Kinugasa, S., Hagihara, Y. and Niki, E., 2012. Association of the physical and chemical properties and the cytotoxicity of metal oxide nanoparticles: metal ion release, adsorption ability and specific surface area. Metallomics, 4(4), pp.350-360.
87. Lu, Z., Rong, K., Li, J., Yang, H. and Chen, R., 2013. Size-dependent antibacterial activities of silver nanoparticles against oral anaerobic pathogenic bacteria. Journal of Materials Science: Materials in Medicine, 24(6), pp.1465-1471.

CHAPTER EIGHT

DEFLUORIDATION AND REMOVAL OF PATHOGENS FROM GROUNDWATER BY HYBRID CROSS-LINKED BIOPOLYMERIC MATRIX IMPREGNATED Ag-MgOnHAP NANOCOMPOSITE

Introduction

This chapter focuses on the synthesis of hybrid cross-linked biopolymeric matrix impregnated Ag-MgOnHaP nanocomposite and its application towards the removal of fluoride and bacterial in groundwater. The outputs established from this work is presented as a prepared article journal for publication to Journal of Applied Materials and Interface by ACS.

Ayinde W. B, Gitari W. M, Muchindu M, Samie Amidou, and James A. Smith (2019.) **Defluoridation and removal of pathogens from groundwater by hybrid cross-linked biopolymeric matrix impregnated Ag-MgOnHaP nanocomposite**. (Ready for submission to *Journal of Applied Materials and Interface*).

Defluoridation and removal of pathogens from groundwater by hybrid cross-linked biopolymeric matrix impregnated Ag-MgOnHaP nanocomposite

Ayinde W. B[a*], Gitari W. M[a], Muchindu M[b], Samie Amidou[c], and James A. Smith[d]

[a]Environmental Remediation and Nanoscience (EnviReN), Department of Ecology and Resource Management, School of Environmental Sciences. University of Venda, Private Bag X5050, Thohoyandou, 0950, Limpopo Province, South Africa.; mugera.gitari@univen.ac.za

[b]Mintek, South Africa, Advanced Materials Division (Nanotechnology Innovation Centre). MunkombweM@mintek.co.za

[c]Molecular Parasitology and Opportunistic Infections Program, Department of Microbiology, School of Mathematical and Natural Sciences. University of Venda. samie.amidou@univen.ac.za

[d] Engineering Systems and Environmet., School of Engineering and Applied Science, University of Virginia, Charlottesville, Virginia. jsmith@virginia.edu

*Correspondence: email: twasiu33@gmail.com; Tel. +27 838734688

Abstract

This study investigates the removal of fluoride ions and pathogens from contaminated aqueous solution using synthesized glutaraldehyde crosslinked cellulose-chitosan supported by a hybrid 3 layered metal-metal oxide nanocomposite material (CECS@nHapAgMgO). Various techniques like Fourier Transform Infrared (FTIR), Brunauer-Emmet-Teller (BET), X-ray diffraction (XRD), scanning electron microscopy and elemental composition determination (SEM-EDS), transmission electron microscopy (TEM), XPS were used to analyze their morphology, structure and surface and physicochemical properties. Batch sorption experiments were conducted to evaluate the adsorption kinetics, isotherm, effect of pH and the effect of co-existing anions on fluoride uptake. The synthesized CECS@nHapAgMgO nanocomposite showed crystalline irregular multiple layered structural arrangements with a thickness of 23.74 m^2/g m, pore and particle sizes of 0.062 cm^3/g 9.89 nm respectively. It possessed a fluoride sorption capacity of 26.11 mg/g with an optimum pH 5.0 (±0.5) and inclined to higher temperature and pHpzc of 7.27. Freundlich isotherm was more applicable for describing the fluoride sorption equilibrium compared to other adsorption isotherm models. Although, results of sorption kinetics study indicate that the pseudo-second-order model best fitted to the experimental data, intraparticle diffusion and boundary layer mechanisms were also involved in the fluoride sorption rate. The thermodynamic analysis demonstrates that the fluoride uptake process was feasible and exothermic in nature with non-spontaneity mechanisms. CECS@nHapAgMgO showed an effective antibacterial property to gram-positive and gram-negative strains. This material has shown excellent potential applications for household water treatment technology.

Keywords: Biosynthesis; CECS@nHapAgMgO nanosorbent; simultaneous fluoride and pathogen removal

8.1 Introduction

According to the World Health Organization, (2016), water is essential to sustain life, and a satisfactory (adequate, safe and accessible) supply must be available to all. The frequency and intensity of local water crises have been increasing, with serious implications for public health, environmental sustainability, food, energy security, and socio-economic growth of many countries (WWDR, 2015). Out of the abundance of global water resources, less than 1% of freshwater sources can be used for drinking purposes. The existence of hazardous and toxic pollutants in the available freshwater resources due to human and natural activities has become one of the most serious environmental problems leading to serious health implications. Water from most public water-treatment systems aimed at preventing and protecting people from such contaminants are often less reliable in terms of supplying the required water quality. Globally, groundwater is an important natural source of water supplies and accounts for approximately one-third of all available freshwater resources (UNESCO, 2009). Among the naturally and anthropogenic deposited inorganic chemical species include fluoride, arsenic, iron, lead, nitrate, sulfate, trace and heavy metals, while bacterial, virus and protozoans are the major causes of microbiological origin. Fluoride is the most significant naturally occurring inorganic pollutants found in groundwater. Its concentrations in groundwater in the ranges from 0.01 to 48 mg/L globally (Mumtaz *et al*., 2015). The impacts of fluoride on human health can be beneficial (0.5-1.5 mg/L) or detrimental (> 1.5 mg/L), which depends on the concentration and constant consumption (WHO, 2011; 2016; Dhillon and Kumar, 2015). However, more than 200 million people globally consume far more than the permissible limit 1.5 mg/L from drinking water resources, thus creating serious health diseases (WHO, 2011; Miretzky and Cirelli, 2011; Mumtaz *et al*., 2015). Fluorosis is a chronic health hazard affecting a large population as a result of excess fluoride consumption. Other health effects include discolored teeth, deformed bones and dental fluorosis, crippling skeletal fluorosis, skeletal cancer, and neurotoxicological effects, etc. (Mjengera and Mkongo, 2003; Harrison, 2004; Ayoob and Gupta, 2006; Choi *et al*., 2012). Moreover, microbes are responsible for several waterborne diseases and contamination of drinking-water by microbial pathogens can cause disease outbreaks and contribute to background rates of disease affecting human health at the global scale (LeChevallier and Au, 2004).Therefore, removing the contaminants from drinking water using different technologies is essential to reducing this global menace.

Various methods have been developed and used for fluoride and pathogen removals (Ayoob *et al*, 2008; Mohapatra *et al*. 2009; Miretzky and Cirelli, 2011; Loganathan, 2013; Pelgrift and Friedman, 2013). However, different surveys have shown that no single method is enough to remove all pollutants from water. High costs of handling, low fluoride uptake capacities, complexity, use of chemicals, the introduction of secondary pollutants are some of the challenges facing these methods. Thus, the existing technologies are not “100%” effective to supply potable water and focus should be the point of use as an alternative to the sophisticated techniques (Ayoob *et al*, 2008; Upadhyayula *et al*., 2009, WHO, 2011). Available technologies for water treatment

are reaching their limits in providing sufficient quality to meet human and environmental needs (Qu *et al*., 2013). There is, therefore, need to develop sustainable, eco-friendly, efficient and low-cost advanced materials adsorbents.to treat and provide fluoride and microbiologically safe drinking water. Nanotechnological influences on the use of materials loaded with nanoparticles are on the rise towards overcoming these water-related problems. Recently, the diversity of applications through surface functionalization and polymeric blending with metal and metal oxide nanoparticles has become a method for providing polymeric materials with combined advantages, fascinating and desirable properties. The use of adsorbents containing natural polymers has received great attention, in particular, polysaccharides such as chitosan and cellulose, are among the most abundant biomaterials on earth, having low cost, environmentally friendly, renewable and biodegradable properties (Marchessault *et al*., 2006; Muzzarelli, 2012; Fan *et al*., 2012; Rojas, 2016). These polymeric materials have been regarded as a useful material for various purposes including water purification (Sundaram *et al*, 2009; Pandi and Viswanathan, 2015; Kunduru *et al*., 2017).

Cellulose is the most abundant and renewable natural polymers worldwide. It is a linear polysaccharide of β-D, 1,4, glucose unit linked by a glycosidic bond. Nano-cellulose is a term referring to either cellulose nanowhiskers (CNW) or cellulose nanofibers (CNF) and because of its remarkable physical properties and unique surface chemistry, cellulose and its derivatives have gained significant attention in many applications (Li et al., 2015; Grishkewich *et al*., 2017). Chemical modifications of cellulose increase its adsorption capacity, hydrophobicity or hydrophilicity, elasticity, microbial resistance, heat and mechanical resistance for chemical and biological decontaminants in aqueous solutions (Sundarama *et al*, 2009; Abdul Khalil *et al*., 2016; Thakur and Voicu, 2016). Chitosan on the hand, is a naturally occurring biodegradable and biocompatible polycationic polymer with a chemical structure of 1-4-linked-2-amino-2-deoxy-b-D-glucopyranose acquired from the N-deacetylation chitin, the second most abundant polysaccharide after cellulose (Gandhi *et al*, 2010; Thakur and Voicu, 2016). It is known to be a very reactive sorbent material compared to cellulose because of the large number of amine groups, thus ease of chemical modification, complexation, and adsorption of metal anions by ion exchange (Allan 1984; Kurita 2006; Bhatnagar and Sillanpää, 2009; Miretzky and Cirelli, 2011). Several methods have been adopted to modify chitosan and cellulose either physically or chemically in order to improve the adsorption capacity and separation performances in water purification. Crosslinking with glutaraldehyde (GLA) is among the methods employed in chemical modifications of chitosan and cellulose. Although, this method can reduce the adsorption capacity as it diminishes the quantities of free amino groups, disruption of the hydrogen bonding and collapse of the pore structure of chitosan (Miretzky and Cirelli, 2011; Mohamed *et al*., 2015); the superior mechanical strength of cellulose limits the network porosity of its native and crosslinked forms enhance the sorption selectivity as well as ensure the overall stability of the polymeric composite materials (Miretzky and Cirelli, 2011; Abdul Khalil *et al*., 2016; Udoetok *et al*., 2016).

In the present study, an in-situ sol-gel green synthesis methods was used in the preparation of glutaraldehyde cross-linked cellulose-chitosan impregnated with 3-layered nanoparticle material (CECS@nHapAgMgO) for selective application in fluoride and pathogen removal in aqueous solution. The polymer framework was used here for stabilization of the nanoparticles, for increased adsorption capacity and as a disinfectant. The impregnation of the nanoparticles within the crosslinked polymer matrix, before and after fluoride sorption was investigated using several physical and chemical techniques which include BET, SEM-EDS, TEM, XPS, XRD, and FTIR spectroscopy. The applicability of the prepared composites for the removal of fluoride from aqueous solutions was evaluated under different experimental sorption conditions. The possible sorption isotherms and kinetic mechanisms, as well as antibacterial potency of multifunctional biopolymer complex (CECS@nHapAgMgO), were studied and reported.

8.2 Materials and methods

8.2.1 Materials

All chemicals were of analytical reagent grade. Highly viscous Chitosan (CS) from crab shell (Degree of N-deacetylation of 95%) was purchased from Sigma-Aldrich. $Ca(NO_3)_2.4H_2O$, KH_2PO_4, $Mg(NO_3)_2.6H_2O$, $AgNO_3$, NaF, NaOH, acetic acid (glacial, 99-100%), and other chemicals used were purchased from Rochelle chemicals, South Africa and used directly without further purification. Ultrapure Milli-Q water (18.2 MΩ/cm) was used in the preparation and dilution of standards throughout the experiment.

8.2.2 Preparation of nanohydroxyapatite (nHaP)

Synthetic nanohydroxyapatite (nHaP) was prepared as described by Poinern et al. (2011) by reacting 40 mL of 0.32 M $Ca(NO_3)_2{\cdot}4H_2O$ with 60 mL of 0.19 M KH_2PO_4 solution under continuous stirring with the Ca/P ratio maintained at 1.67. Subsequently, aqueous NH_4OH (25%) was added dropwise to adjust the pH value to 9, and the solution was stirred for 6h and thereafter left to age for 24 h at room temperature. During the mixing process, the pH value was continually checked and maintained at 9 (using NH_4OH). The composite solution was thereafter subjected to ultrasound agitation at 100% amplitude (0.5 cycles) for 1 h. The product obtained after the sonication was filtered and dried at 40 ◦C in an oven for 24 h before being ground into a fine powder.

8.2.3 Preparation of MCC to nanocrystalline cellulose

This was achieved by dispersing 1 % (w/v) of microcrystalline cellulose (2 g) into 200 mL ultrapure Milli-Q water (18.2 MΩ/cm) for 1h under continuous at room temperature. The resulting suspension was then sonicated at 100% amplitude (0.5 cycles) using Hielscher Ultrasonics UP400S (400W at 24 kHz, amplitude 20–100% with ultrasonic horn H14) for 30 min and subsequently kept in a refrigerated at 4 ◦C for further use.

8.2.4 Preparation of Cellulose supported chitosan@nHapAgMgO composite

Synthesis of CECS@nHapAgMgO nanocomposite was carried out by adding the prepared resulting nanocrystalline cellulose suspension (1 % (w/v)) to 1 % wt./v chitosan solution (highly viscous >400 mPa.s, 1% (v/v) acetic acid) under continuous stirring for 2h. (40 °C). To this solution, an aqueous solution containing 60 mL $AgNO_3$ (3 mM), 20 mL (0.1M) ($Mg(NO_3)_2.6H_2O$), and *Citrus paradisi* peel extract (40 mL) were added and stirred for another 2 h at 40 °C. The mixture was thereafter cross-linked with the dropwise addition of 4 mL 1 wt% glutaraldehyde under continuous. The color of the solution progressed from colorless to yellow and finally to dark yellow (bio-process growth kinetics) during this reaction period was monitored using UV–Vis spectroscopy. To this continuously stirred bio-reduced reaction mixture, 5 g of nHaP was dispersed into the mixture and the final solution was vigorously stirred for 12 h at room temperature. Thereafter, the solution mixture was neutralized until pH 7 with 1 M NaOH solution to induce precipitation. The obtained precipitate (brown) was rinsed severally with ultrapure Milli-Q water (18.2 MΩ/cm), filtered and oven-dried at 50 °C for 24 h to obtain the CECS@nHapAgMgO composite powder, which was subsequently used for the tests. The sequence of the experimental protocol was carried out by varying the % wt. ratio (1:1; 1:2 and 2:1) of nanocellulose and chitosan (CE/CS) solution in the reaction mixture.

8.2.5 Characterization of CECS@nHapAgMgO nanocomposite

The bioprocess kinetics seed growth was monitored using SPECTROstar Nano/ BMG LABTECH UV-Visible Spectrophotometers in the wavelength range 220–600 nm. The main functional reactive groups of the synthesized CECS@nHapAgMgO composite were recorded by using Bruker: ALPHA FT-IR Spectrophotometer (4000-400 cm^{-1}) with 24 scans. Surface morphology and elemental analysis of the composite were characterized using SEM and SEM-EDX with an FEI Nova NanoSEM 230 with the field emission gun equipped with an Oxford Xmax SDD detector operating at an accelerating voltage of 20Kv for the EDS detector (Oxford X-Max with INCA software). The surface area, pore area and pore volume of the synthesized nanocomposite were measured using nitrogen adsorption Brunauer–Emmett–Teller (BET) surface area and porosity analyzer (Micromeritics TRISTA 3020 analyzer (USA). XRD measurements were performed using a multipurpose X-ray diffractometer D8-Advance from Bruker operated in a continuous J-J scan in locked coupled mode with Cu-K_a radiation (lKa_1=1.5406Å) with a LynxEye (Position sensitive detector). The adsorption-desorption plots were used to calculate the specific surface area. The surface interaction and composition of the fluoride loaded sorbent was studied by the X-Ray Photoelectron Spectrometer Microprobe (XPS) (Thermo Scientific ESCAlab 250Xi,), with a monochromatic Al Kα X-ray source (1486.7 eV). The high-resolution scans were conducted according to the peak being examined with a pass energy of 20 eV (Pressure <10-8 mBar) and spot size of 900 μm with a wide survey scan between 0-1300 eV. Fluoride ion and pH measurements were determined using a fluoride ion-selective electrode (9609 BNWP Orion, USA) coupled to an ISE/pH/EC electrode (Thermo SCIENTIFIC-ORION VERSA STAR Advanced Electrochemistry meter fluoride ion-selective electrode) calibrated with four fluoride standards containing TISAB III.

8.2.6 pH at point-of-zero-charge (pHpzc)

The pH at a point-of-zero charge of CECS@nHapAgMgO was determined in 1 M, 0.1 M and 0.01M KCl solutions for consistency of results. The pH of solutions was adjusted to desired values by adding 0.1 M HCl or 0.1 M NaOH. The new pH, therefore, constituted the initial pH (pHi) of solutions. Aliquots of 25 mL of solutions were pipetted into 50 mL plastic bottles. A mass of 0.25 g of adsorbent was then weighed into each of the bottles. The bottles were corked and shaken inside a thermostated water bath shaker at 150 rpm for 24 h. After equilibration, the equilibrium pH (pHe) of each mixture was quickly measured and recorded.

8.2.7 Adsorption studies

The fluoride sorption by the synthesized CECS@nHapAgMgO was performed and evaluated using batch analysis in simulated fluoride-rich water. Standard stock fluoride ion solution (1000 mg/L) was prepared by dissolving 2.210 g NaF into 1000 mL of ultrapure Milli-Q water at ambient condition. The desired fluoride solution was prepared by appropriate dilution of the standard stock solution. Batch adsorption experiments were carried out by mixing 0.225 g of CECS@nHapAgMgO with 50mL of 10 mg/L initial F^- solution. The mixture was shaken thoroughly using a reciprocating shaker (STUART SSL2) at 250 rpm. The solution was then filtered, and the residual fluoride ion concentration was determined. The pH values of the solution were adjusted by 0.1 mol/L HCl or NaOH. The effects of contact time, pH, and co-existing ions on the equilibrium adsorption capacity were optimized. The effect of co-existing anions ((CO_3^{2-}, NO_3^-, SO_4^{2-} and Cl^-)) on the defluoridation efficiency of the adsorbent was evaluated at anion concentration of 100 mg/L in a 10 mg/L fluoride solution. The adsorption isotherm experiments were conducted by varying fluoride concentrations within the range of 5–150 mg/L in a thermostated water-bath shaker in the temperature range of 298, 303; 313 and 323 K. The CECS@nHapAgMgO dose was kept at 0.3 g. Adsorption isotherms and kinetic models were adopted and used to model adsorption data. All the experiments were conducted in triplicate, and the mean of the results computed. Equations 1 and 2 were used to determine the percentage fluoride removal and adsorption capacity, q_e (mg/g) of the adsorbent.

$$\%\,\text{Adsorption} = \frac{(C_o - C_e)}{C_o} \times 100 \qquad (1)$$

$$q_e = (C_O - C_e) \times \frac{V}{m} \qquad (2)$$

Where: C_o is the initial F^- concentration (mg/L); C_e is the F^- concentration at equilibrium (mg/L); V is the volume of solution (L) and m is the dried mass of the adsorbent (g).

8.2.8 Regeneration of CECS@nHapAgMgO

Regeneration of the adsorbent was carried out as follows: 0.3 g of fluoride loaded CECS@nHapAgMgO was agitated with 100 mL of 0.01 M Na_2CO_3 and water for 30 mins on a Table Shaker. After agitation, the adsorbent was filtered, and the filtrate was diluted to 100 mL and subsequently analyzed for desorbed fluoride. The collected adsorbent on filter membrane was washed with Milli-Q water and then dried at 50◦C for 1 h. Regenerated adsorbent was then re-used for defluoridation for up to three regeneration-reuse cycles.

8.2.9 Statistical tools

The statistical tools used in the present study to evaluate the best-fit sorption models and the prediction quality, through the linear and non-linear analysis were adjusted correlation coefficient (Adj. R^2), chi-square analysis ($\chi 2$) (Eq. 3), Root Mean Squared Errors (RMSE) (Eq.4) and Sum of Squared Errors (SSE) (Eq.5). Adjusted R-square, which measures the proportion of variation by only those independent variables that really help in explaining the dependent variable by the model. Generally, the larger the value, the better the model fits the data. Furthermore, The chi-square analysis ($\chi 2$), RMSE, SSE are the most commonly used statistical tool and error functions in predicting sorption modeling. The smaller the values of these error functions, the better the prediction quality. The computations were done using OriginPro 8.SR0 and XLSTAT data analysis (Addinsoft) for Microsoft Excel software.

$$\chi^2 = \sum \frac{(q_{exp} - q_{Cal})^2}{q_{Cal}} \quad (3) \quad ,$$

$$RMSE = \sqrt{\frac{1}{n-2}\sum_{i=1}^{n}\left(q_{e,exp} - q_{e,calc}\right)^2}_{i} \quad (4)$$

$$SSE = \sum_{i=1}^{n}\left(q_{e,calc} - q_{e,exp}\right)^2 \quad (5)$$

where q_{exp} and q_{Cal} represent the experimental and calculated values of the amount adsorbed (mg/g) respectively.

8.2.10 Evaluation of antimicrobial activity

Antimicrobial susceptibility test was analyzed from the observed zone of inhibition (mm) test using the standard Agar-Well disc diffusion methods (Kirby Bauer disk diffusion test). The bacterial indicator strains used were *Escherichia coli* (ATCC 35218), *Klebsiella pneumonia* (derived from ATCC-BAA-1705) and *Staphylococcus aureus* (ATCC 43300). 1000 µg/mL of the synthesized CECS@nHapAgMgO nanocomposites were prepared and dispersed in ultrapure Milli-Q water (18.2 MΩ/cm) using an ultrasonicator bath (SCIENCETEC, Model 705). Mueller Hinton agar (MHA) was used for the cultivation of freshly grown bacteria at turbidity of 0.5 McFarland suspension. 50 µL of each strain was spread on 20 mL of solidified and dried agar plates. Wells were punctured at equidistance using sterile pipette tips. 50 µL (1000 µg/mL) of CECS@nHapAgMgO was dispensed into the wells already inoculated with the bacterial cell suspension. The plates were incubated at 37 ˚C for 24 h and 48 h and the observed zone of inhibition was measured and recorded. The processes were performed in duplicates. Minimum inhibitory concentration (MIC) of CECS@nHapAgMgO was also determined using the microtiter broth-dilution method as described by Samie *et al*. (2005).

8.3 Results and Discussion

8.3.1 UV-Visible analysis

The optical properties of the bio-reduction of the nanoparticles on the crosslinked polymer composite (CECS@nHapAgMgO) are shown in Fig. 8.1. The color transition in the bioprocess of CECS@nHapAgMgO indicates changes in electronic transition and the formation of the nanoparticles on the polymer complex was similar to our previous study (Ayinde et al., 2018). No characteristic plasmon band resonance peak was observed in both the CE and CS material. However, two complimenting peaks were seen in the CECS@nHapAgMgO nanocomposite. A strong surface plasmon absorption plateau couples with a broad band were observed at 287 and 444 nm of the spectrum. These are characteristics of the formation of MgO and Ag nanoparticles respectively. Hence showing the successful impregnation of the AgMgO layer on the CECS@nHapAgMgO nanocomposite. Similar results were reported in our previous work (Ayinde et al., 2018).

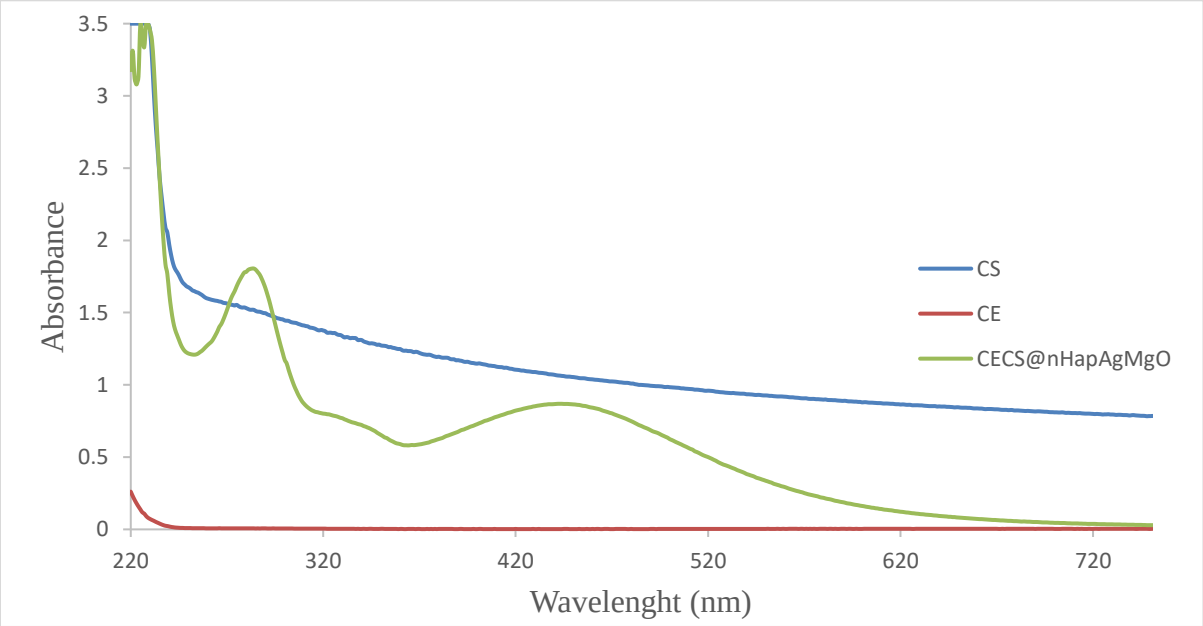

Fig. 8.1. UV–Vis monitoring of CECS@nHapAgMgO nanocomposite

8.3.2 Effect of CE/CS content (wt. %) on fluoride adsorption

Table 8. 1 shows the effect of fluoride ion percentage removal efficiency of CECS@nHapAgMgO nanocomposites with different cellulose/chitosan (CE/CS) content (initial fluoride concentration 10 mg/L; composite dose: 0.3 g/50 mL; 250 rpm; pH: 7 at room temperature). The impact of the wt. % variation was observed to be an important factor affecting the sorption of fluoride by the composites. Although the fluoride removal capacity increases with increased polymer contents, the highest fluoride uptake tendency was observed with the composite containing the CE/CS (2:1) wt. % ratio. This highest-value fluoride uptake associated with the 2:1 wt. % may be attributed to the availability of more free hydroxyl groups in the cellulose framework whereas the functionality of the amine group in the chitosan (CS) may have been hindered by the crosslinking density of the

crosslinking agent (glutaraldehyde) in the polymer network. Therefore, CE/CS (2:1) wt. % ratio was used for subsequent sorption studies.

Table 8.1. Effect of CE/CS content (wt.%) on fluoride adsorption

CE/CS (w%)	Percentage Fluoride removal
1:1	40
1:2	57
2:1	76

8.3.3. Structural analysis

Fig. 8.2 (a-c) and 8.3 (a-c) show the SEM micrographs of the cross-linked CECS@nHapAgMgO nanocomposite material before and after fluoride treatment respectively. The surface morphology micrographs of synthesized CECS@nHapAgMgO nanocomposites (Fig. 8.2 (a)) displayed a dense irregular multiple-layered structure, which changes hierarchically in the SEM micrographs of fluoride-treated CECS@nHapAgMgO composite (Fig. 8.2 (a)). The EDS patterns (Fig 8.2(c) and 8.3(c)) show various elemental analysis within the synthesized CECS@nHapAgMgO nanocomposite. The presence of Ag and MgO on the spectra confirmed the successful metal and metal oxide species reduction onto the polymer matrix. Ca and P peaks are introduced by the nanohydroxyapatite templates. Characteristics of the crosslinked cellulose-chitosan matrices existed on the composite by the presence of C, N and O elements. Furthermore, the existence of F peak in the fluoride treated CECS@nHapAgMgO (Fig. 8.2(c) when compared to CECS@nHapAgMgO (Fig. 8.3(c)) confirms the uptake capability of the sorbent material.

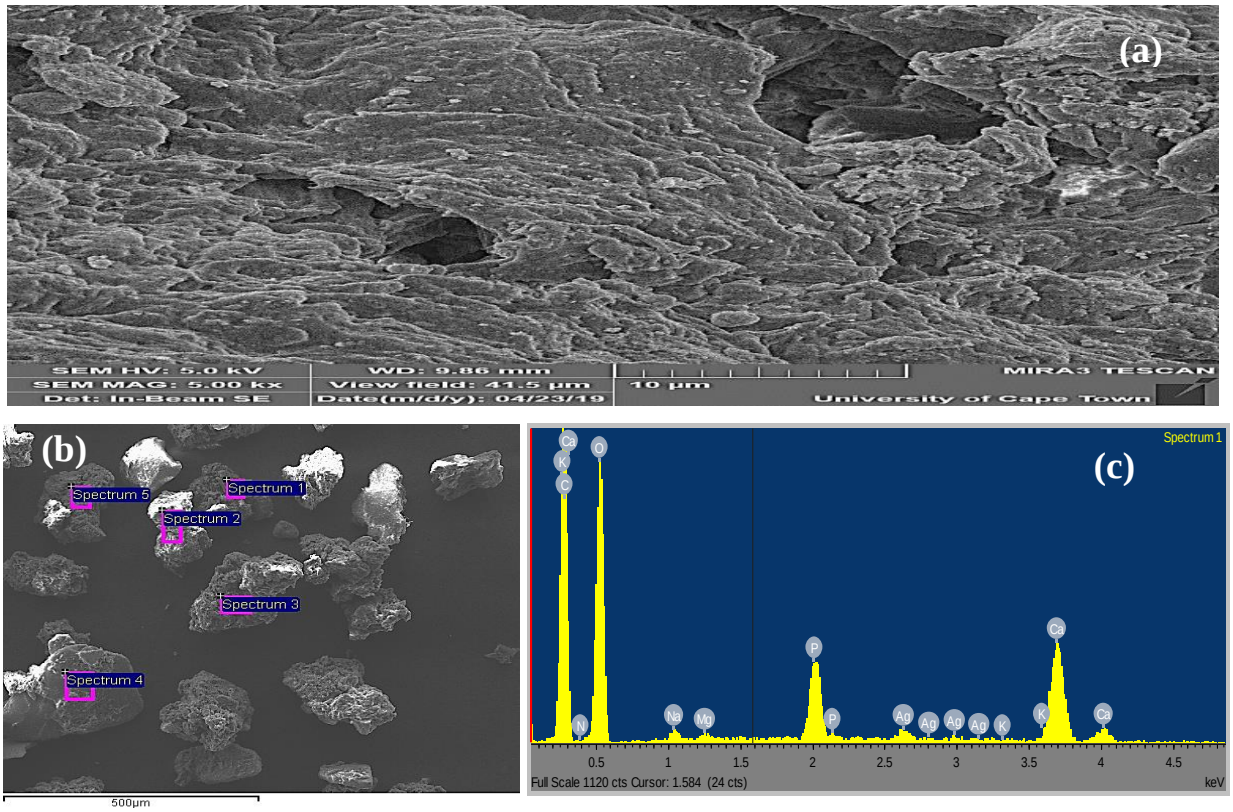

Fig. 8.2. (a) SEM image; and ((b)-(c)) EDS mapping and spectrum of CECS@nHapAgMgO

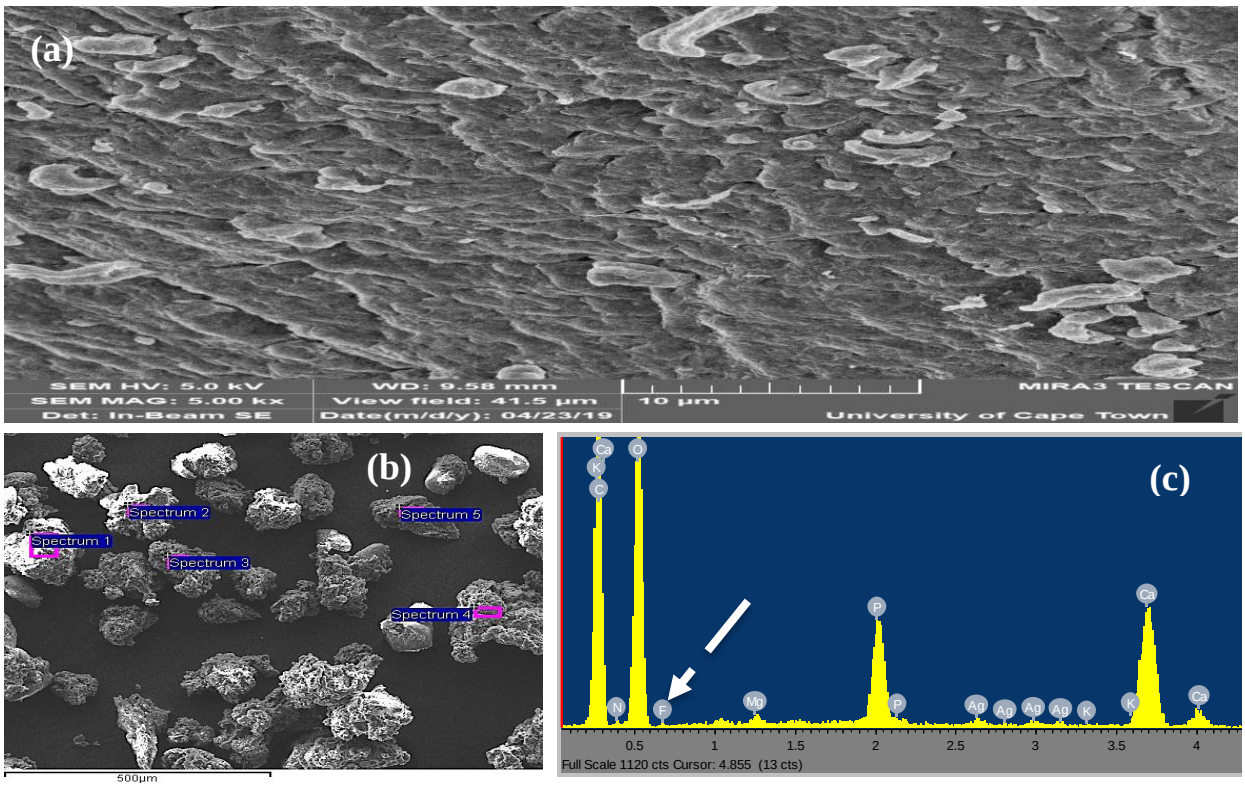

Fig. 8.3. (a) SEM image; and (b-c) EDS mapping and spectrum of f-CECS@nHapAgMgO

8.3.4 XRD analysis

The phase distributions of the nanocrystalline cellulose (CE), chitosan (CS) and the before and after fluoride uptake by the synthesized crosslinked CECS@nHapAgMgO nanocomposite is shown in Fig. 8.4. As shown from the XRD diffractograms, 2θ peaks at ~16, ~23.9, and ~ 38° are related to a typical peak pattern structure of native cellulose I structure silver (ICDD: PDF database 1999 no: 00-003-0289) (Wada *et al*., 2004; Klemm *et al*., 2004) while broad band at 20° with no crystalline phase is an indication of the presence of chitosan material (Wang *et al*., 2004). Moreover, well defined sharp peaks complimenting the CE and CS peaks emerged from the synthesized CECS@nHapAgMgO nanocomposite diffractogram, thus, indicating the presence of higher crystalline regions. This may be as a results of the disruption and transformation of the amorphous regions in the polymeric blend to the crystalline phase during sol-gel preparation by the presence of 2θ diffraction peaks at 16.89, 26.33, 31.81, 32.15, 39.7, 46.65, and 49.89∘ characteristic of hexagonal carbonate-hydroxyapatite (ICDD: PDF database 1999 no: 00-009-0432); and triclinic crystal system of silver (ICDD: PDF database 1999 no: 00-004-0783). The percentage crystallinity as obtained is 75 and 14.58 %, for hydroxyapatite and Silver-3C respectively. These structural transformations may give reason to the more uniform hierarchical structures as earlier shown in SEM images. Although a decrease in intensity was observed in the f- CECS@nHapAgMgO, the crystal arrangement remained the same after the fluoride treatment.

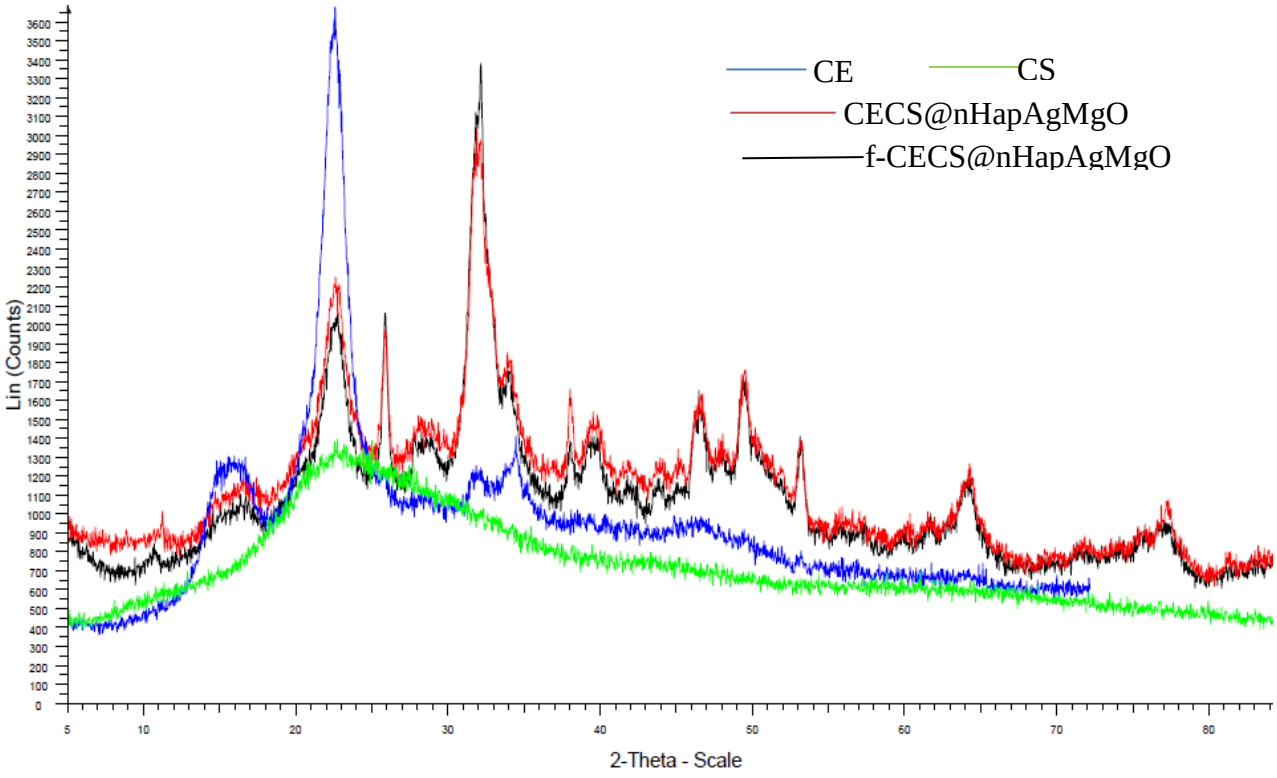

Fig. 8.4. XRD diffractogram of CECS@nHapAgMgO nanocomposite

8.3.5 Adsorption studies

8.3.5.1 Adsorption Kinetic model analysis

In adsorption system design, the efficiency of CECS@nHapAgMgO composite to remove fluoride ions can be assessed by the rate of sorption from aqueous solution through mass transport and chemical reaction processes. Generally, sorption kinetics determines the rate of fluoride sorption by the sorbent and it is dependent on equilibrium contact time of reaction during the adsorbate-adsorbent interface. Thus, adsorption kinetics provides vital insights into the reaction pathways, mechanism as well as the rate-determining the phase of sorption processes.

Fig. 8.5 displays the residence time of fluoride uptake between 0-150 min of reaction at the adsorbate-adsorbent interface. The trend followed rapid sorption of fluoride at the initial stage up until 40 min and, subsequent gradual decreased in sorption reaction occurred with time until equilibrium is reached. The initial rapid rate fluoride sorption is due to the immediate uptake of more unoccupied active surface binding sites of the CECS@nHapAgMgO composites by the fluoride ions in solution. However, the slower rate as the contact time increases is undoubtedly due to the active surface binding sites getting occupied by the F^- ions, thereby impeding the exchange of aggregated fluoride molecules on the CECS@nHapAgMgO composite surface.

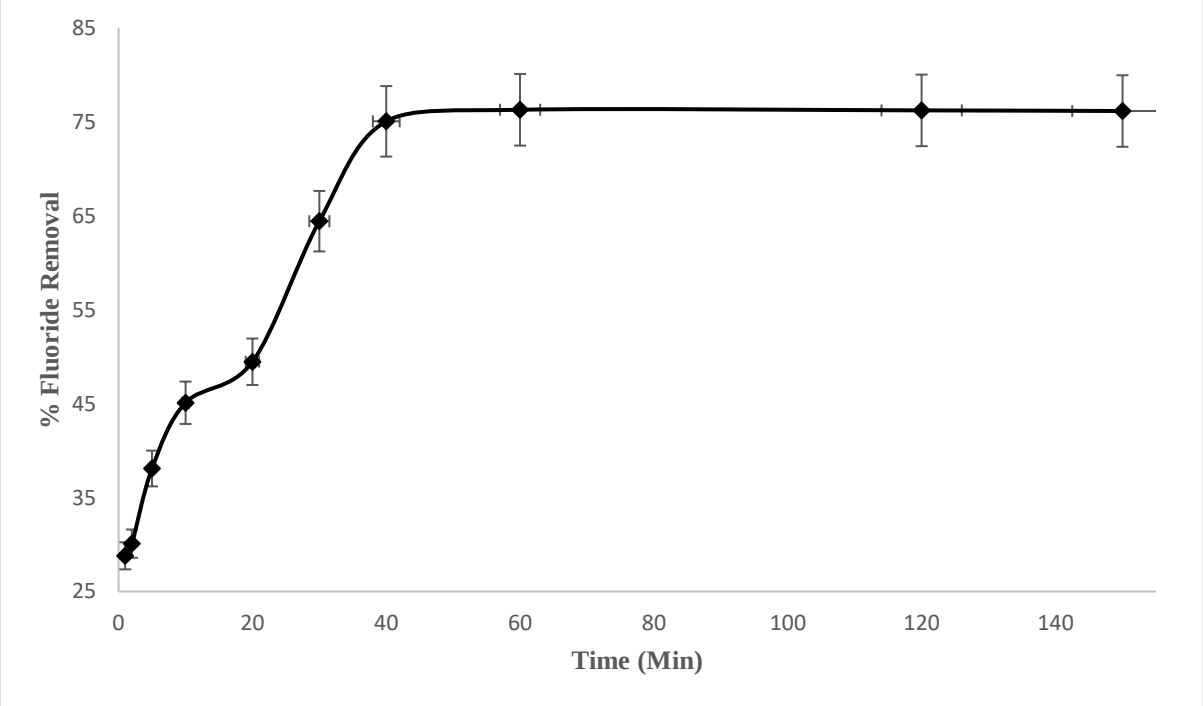

Fig. 8.5. Effect of contact time on fluoride uptake by CECS@nHapAgMgO (sorbent dose 0.3g; initial F^- concentration 10 mg/L; 298 K at 250 rpm)

The adsorption mechanisms of the fluoride from the solution to the active binding sites on the CECS@nHapAgMgO surface is best to describe by the different fittings on adsorption kinetics models. The experimental data were analyzed using four kinetic models to describe the sorption reaction pathways of fluoride on the CECS@nHapAgMgO nanocomposite. These include the pseudo-first-order, the pseudo-second-order, Elovich, and Intraparticle diffusion models.

8.3.5.1.1 Reaction-based and intraparticle diffusion kinetic models

On the basis of reaction pathway on the fluoride adsorption system onto the synthesized CECS@nHapAgMgO sorbent, the pseudo-first-order (Lagergren, 1898) and pseudo-second-order (Ho et al., 2000) were used to describe the sorbate/sorbent adsorption system. Pseudo-first-order explains the sorption rate based on physisorption phenomenon, while the pseudo-second-order is normally used to describe cation exchange and chemisorption reaction mechanisms. The linear equations of Lagergren pseudo-first and pseudo-second-order kinetic model for fluoride sorption process are expressed in Eq. (6) and (7) respectively:

$$\log(q_e - q_t) = \log q_e - \frac{K_1}{2.303} t \qquad (6)$$

$$\frac{t}{q_t} = \frac{1}{K_2 q_e^2} + \frac{t}{q_e} \qquad (7)$$

where q_e and q_t are the amounts of fluoride uptake per mass of the CECS@nHapAgMgO sorbent (mg/g) at equilibrium and at time t (min) respectively; with K_1, K_2 (min^{-1}) representing the rate constant of the pseudo-first-order and pseudo-second-order respectively.

In addition, another chemical adsorption model suitable for a multilayer adsorbing surfaces is Elovich equation. It is used to explain the mechanisms of chemisorption of fluoride onto CECS@nHapAgMgO sorbent, but the equation does not propose any definite mechanism for adsorbate–adsorbent (Ho, 2006). The mathematical linear form of the Elovich equation (Eq. 8) is given below:

$$q_t = \frac{1}{b}\ln(ab) + \frac{1}{b}\ln(t) \qquad (8)$$

Where q_t is the amount of fluoride sorbed on CECS@nHapAgMgO at a time t, a is the initial fluoride adsorption rate (mg/g min) and b is the desorption constant related to the surface coverage and the activation energy for chemisorption (g/mg). The constants a and b were obtained from the slope and intercept of the linear plot of q_t versus ln t.

The intra-particle diffusion order by the sorbent affecting fluoride adsorption in the solid-liquid system was also explained by using the intra-particle diffusion model (Weber and Morris, 1964) This model normally describe the movement of adsorbate from the exterior surface to the interior surface of adsorbent through surface and pore diffusion mechanisms. The linear form of the intra-particle diffusion model is given in Eq. (9).

$$q_t = k_i t^{0.5} + C \quad (9)$$

where q_t is the amount of fluoride sorbed on CECS@nHapAgMgO at a time t, K_i (mg/g/min$^{0.5}$) is the rate constant of the intra-particle diffusion model, while C (mg/g) is a constant often related proportionally to the boundary layer thickness.

The fluoride sorption kinetics model profile and parameters used in predicting the sorption mechanisms from aqueous solution are shown in Fig. 8.6 (a–d) and Table 8.2 respectively. The adsorption kinetics experimental data for fluoride uptake was best described and fit better with the pseudo-second-order kinetic model as compared to the other models based on higher Adj. R^2 and lower RMSE, SSE values (Adj. R^2 = 1, RMSE = 0.00 and SSE = 0.00) (Table 8.2). The reaction pathway model sequence of fitness follows the order Pseudo first order < Elovich < Pseudo-second order kinetic model. Therefore, this suggests that the fluoride ions interact with the heterogeneous surface sites on CECS@nHapAgMgO through chemical bond exchange mechanisms in the sorbate-sorbent interface. The low value of the Weber Morris intraparticle diffusion rate constant k_{id} (0.08 mg/g/min$^{0.5}$) exhibited by the movement of the fluoride across the heterogeneous surface binding sites on CECS@nHapAgMgO is an indication of slow diffusion of the bulky fluoride molecule during the sorption process. Although the profile plot is linear (Fig. 8.6 (d)), the inability of the straight line to pass through the origin plot showed that other mechanisms may also be involved in the rate-controlling step with the intra-particle diffusion model (Yousef *et al*., 2011).

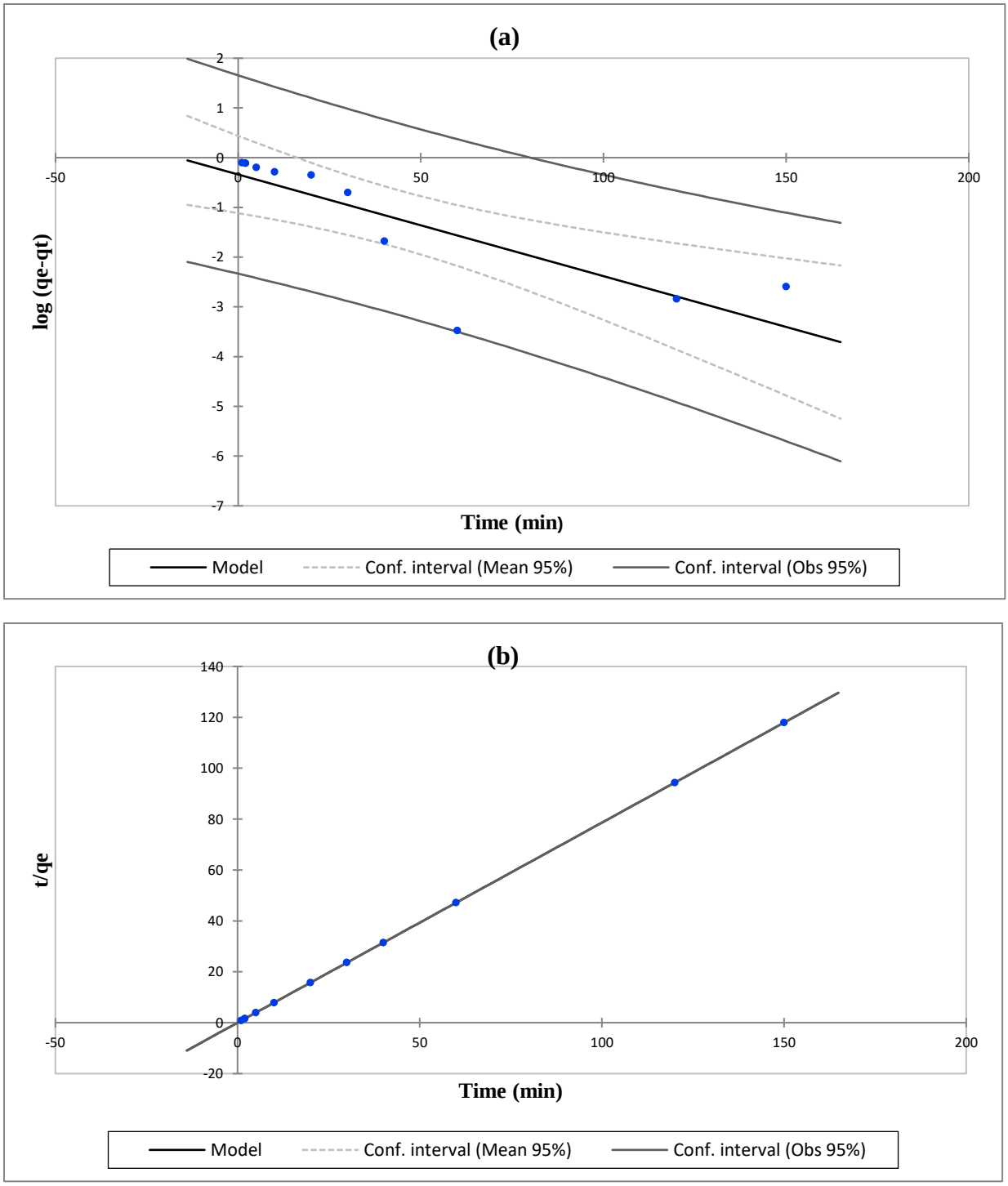

Fig. 8.6. (a) Pseudo-first order and (b) Pseudo-second order plot for fluoride sorption of onto CECS@nHapAgMgO.

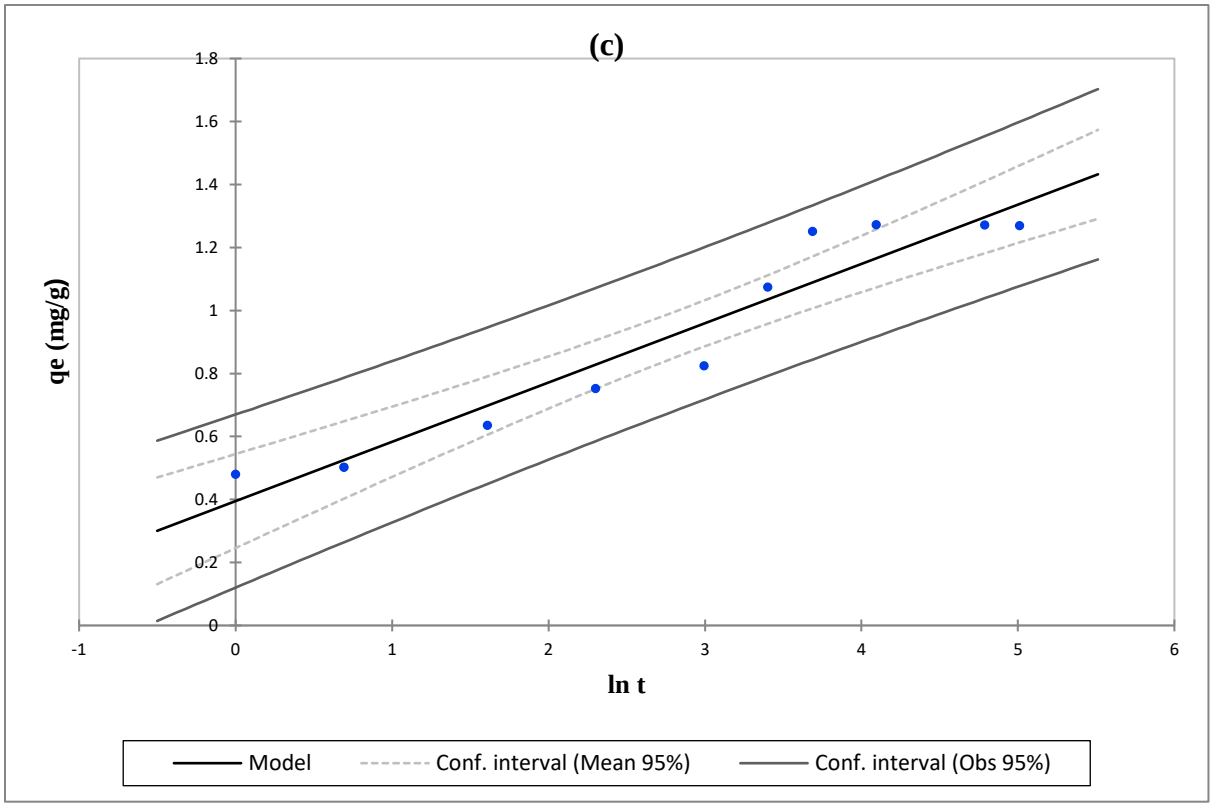

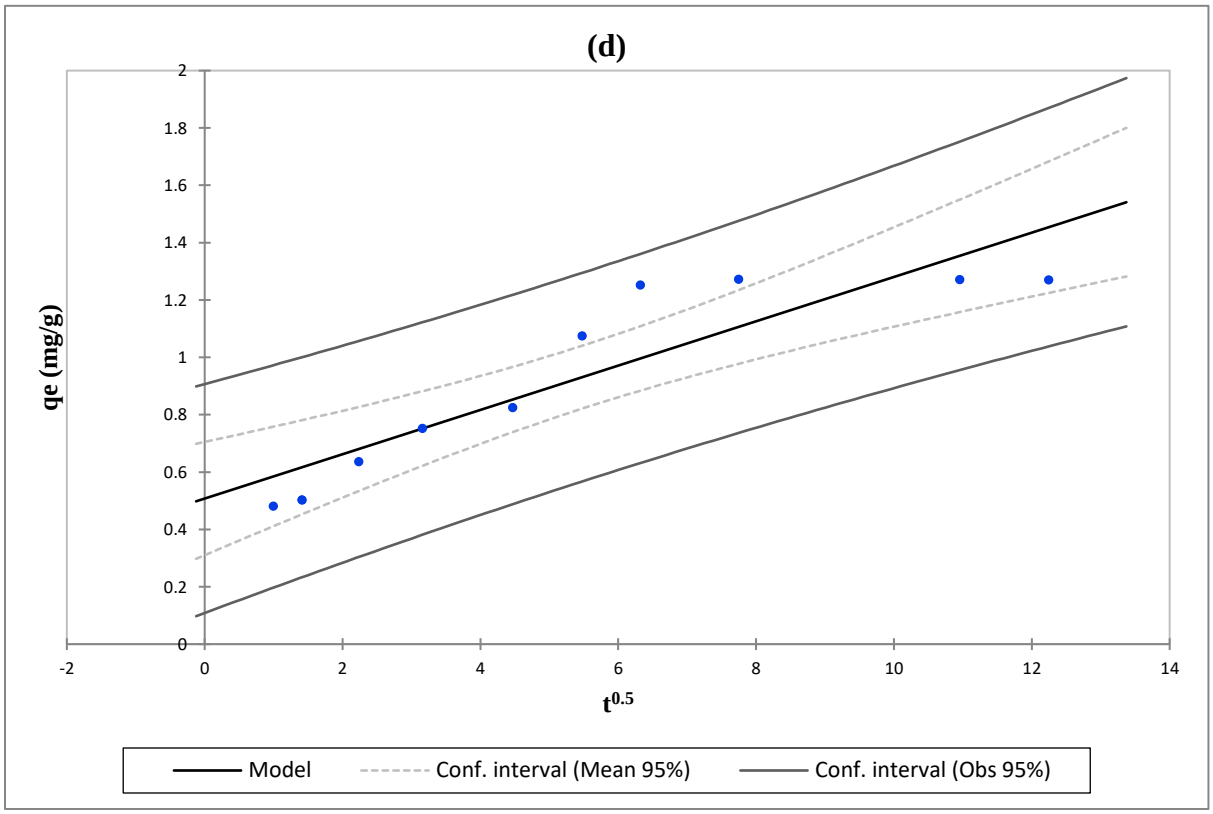

Fig. 8.6. (c) Elovich kinetic plots and (d) Intra-particle diffusion plots for fluoride sorption of onto CECS@nHapAgMgO composite.

Table 8. 2. Parameters, correlation coefficients and error functions obtained from the fluoride sorption kinetic analysis by CECS@nHapAgMgO composite.

	Kinetic models	Parameters	Values
Linear	**Pseudo first order**	K_1 (min^{-1})	0.05
		q_{calc} (mg/g)	0.46
		Adj. R^2	0.63
		RMSE	0.79
		SSE	5.08
	Pseudo second order	K_2 (g/min mg) x 10^{13}	7.73
		q_{calc} (mg/g)	1.27
		Adj. R^2	1.00
		RMSE	0.00
		SSE	0.00
	Elovich kinetic model	a (mg/g/min)	1.53
		b (g/mg)	5.31
		Adj. R^2	0.91
		RMSE	0.10
		SSE	0.08
	Intra particle diffusion	Ki_d	0.08
		C	0.51
		Adj. R^2	0.79
		RMSE	0.15
		SSE	0.18

8.3.5.2 Fluoride sorption isotherms studies

The probable equilibrium of the adsorption in an adsorbent-adsorbate interaction was studied through modeling the experimental data with different adsorption isotherms at different temperature conditions. These include Langmuir, Freundlich, Temkin, and Dubinin-Radushkevich, isotherm models. The fluoride experimental sorption data obtained from the CECS@nHapAgMgO nanocomposite were fitted to both non-linear mathematical forms (Eqs. 10 and 11) of Langmuir and Freundlich models respectively (Langmuir, 1916; Freundlich, 1906). Langmuir assumes that the adsorption occurs on a monolayer where all adsorption active sites are identical and equivalent with no lateral interaction and steric hindrance between the adsorbed molecules, even on adjacent sites (Vijayaraghavan *et al*., 2006). Freundlich, on the other hand, assumes heterogeneous surfaces with a non-uniform distribution of heat of adsorption over the adsorbent (Adamson, 1997).

$$q_e = \frac{Q_m K_L C_e}{1 + K_L C_e} \qquad (10)$$

$$q_e = K_F C_e^{1/n} \quad (11)$$

where Q_m (mg/g) is the maximum adsorption capacity assuming a complete monolayer of an adsorbent, C_e (mg/L) is the equilibrium F- ion concentration in the solution, q_e (mg/g) is the amount of F- ion adsorbed per unit mass of CECS@nHapAgMgO sorbent at equilibrium, K_L (L/mg) is the Langmuir sorption equilibrium constant. K_F [(mg/g)/(mg/L) ^{n}] and 1/n show the empirical Freundlich constant and intensity parameter respectively; describing the strength and magnitude of the multilayer adsorption system. The adsorption isotherm is favorable when $0 < 1/n < 1$, unfavorable when $1/n > 1$ and irreversible when $1/n = 1$.

The favorability of Langmuir model process was also examined by the essential characteristics (Eq. 12) in terms of a dimensionless constant separation factor for the fluoride equilibrium parameter, R_L (Weber and Chakravorti, 1974).

$$R_L = \frac{1}{1 + k_L C_i} \quad (12)$$

where Ci (mg/L) is the initial fluoride concentration and K_L is the Langmuir equilibrium constant The R_L value is useful in determining if an sorption process is irreversible ($R_L = 0$), linear ($R_L = 1$), favorable ($0 < R_L < 1$) or unfavorable ($R_L > 1$).

Temkin model considers that the heat of adsorption would decrease linearly rather than logarithmically with an increase of adsorbent coverage, due to some indirect adsorbate-adsorbate interactions and further suggests that the adsorption process is governed by a uniform distribution of binding energies, up to maximum binding energy (Tempkin and Pyzhev, 1940). The linear form of Temkin is shown in Eq. 13.

$$q_e = B \ln K_T + B \ln C_e \quad (13)$$

[where $B = RT/b_T$]

B_T, and K_T relates to the heat of sorption constant (J/mol), the Temkin isotherm equilibrium binding constant (L/g) of the adsorbent- adsorbate interactions and Temkin isotherm constant respectively. R is universal gas constant (8.314J/mol/K) and T is the operating sorption Temperature in Kelvin.

The Dubinin-Radushkevich isotherm model (Dubinin and Radushkevich, 1947) accounts for the pore filling interaction of the adsorbent as well as the mean free energy (E) of the sorption process and mechanism involved was also modeled for the fluoride uptake by the CECS@nHapAgMgO sorbent. Dubinin-Radushkevich isotherm model is illustrated in Eqs 14 and 15;

$$q_e = q_{max}\ \exp(-\beta_D \varepsilon^2) \quad (14)$$

$$\varepsilon = \mathrm{RT} \ln\left[1 + \frac{1}{C_e}\right] \quad (15)$$

The value of mean adsorption energy E (kJ/mol) of F^- sorption from Dubinin-Radushkevich is given in Eq 16;

$$E = \frac{1}{\sqrt{2\beta_D}} \quad (16)$$

The general linearized form of the D-R (Eq 17) is expressed as

$$\ln q_e = \ln q_{max} - \beta_D \varepsilon^2 \quad (17)$$

where q_{max} (mg/g) is the adsorption capacity; β_D (mol^2/kJ^2) is the activity coefficient constant related to mean sorption energy; ε is the Polanyi potential, and E (kJ/mol) is the mean adsorption energy. R is the universal gas constant (8.314 kJ/mol), T (K) is the absolute temperature. If the magnitude of E is between 8 and 16 kJ/mol, the adsorption process occurred via chemisorption, while for values where E < 8 kJ/mol, the adsorption process is of a physical nature.

The non-linear adsorption isotherms plots and their respective parameters of fluoride uptake by CECS@nHapAgMgO nanocomposite at the studied solution temperatures are shown in Fig. 8.7(a–b) and Table 8.3.

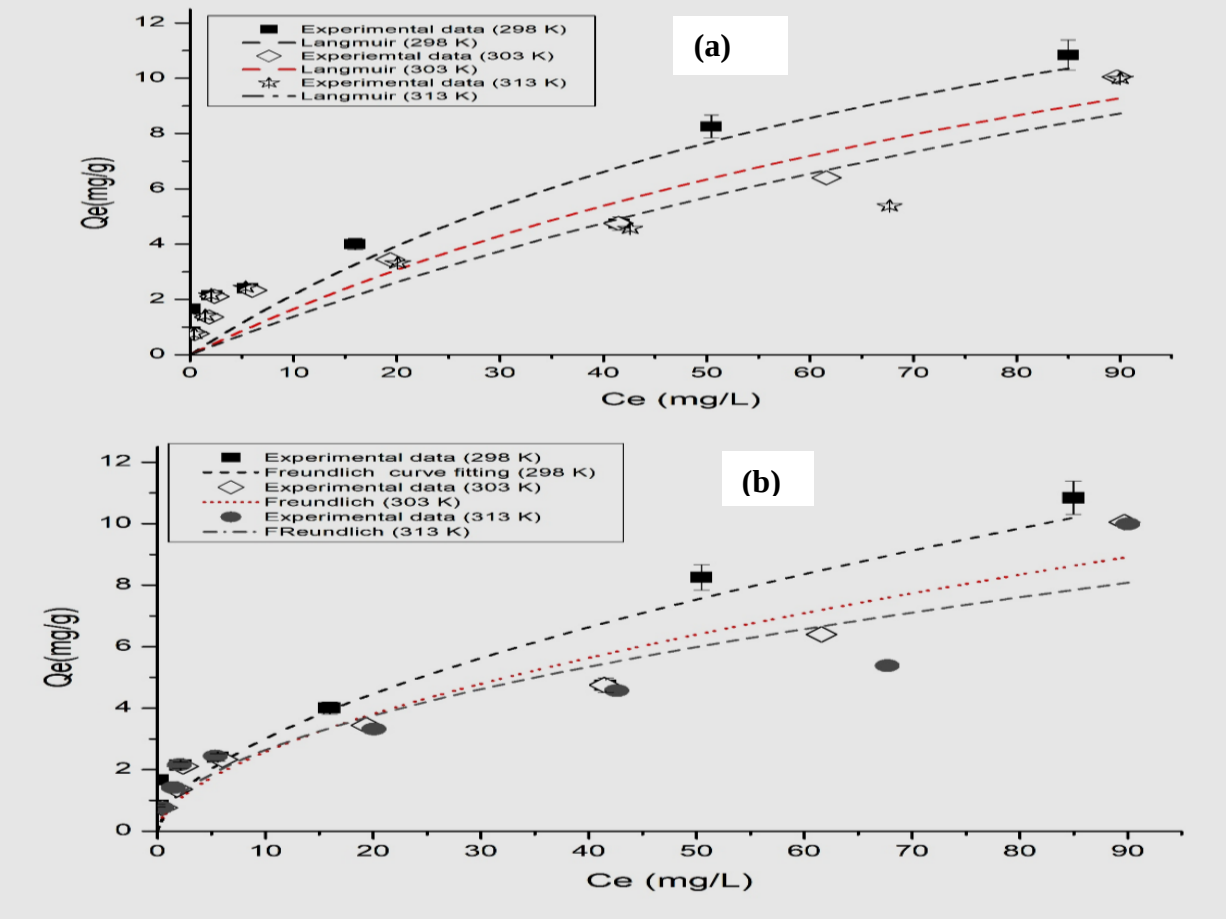

Fig. 8.7. (a) Langmuir; (b) Freundlich adsorption isotherms of fluoride onto CECS@nHapAgMgO sorbent at various temperatures.

From the results, the theoretical monolayer adsorption capacity (Qmax) of fluoride increases as the sorption temperatures increased with maximum fluoride uptake capacity on CECS@nHapAgMgO sorbent found to be 20.83, 21.99, and 26.11 mg/g, respectively (Table 8.3). This implied that the fluoride sorption efficiency in aqueous solution system is dependent on the sorption temperature. This result has practical significance in the sense that this composite could be used as best sorbents for fluoride removal at varying temperature conditions. In contrast, the Freundlich constants K_F for fluoride removal was found to be independent of sorption temperature (298, 303 and 313 K) with values ranging from 0.81, 0.70 and 0.82 respectively. The favorability of fluoride sorption by the sorbent was also confirmed by the values of both R_L (0.9-0.95) and n (1.75-196) as the temperature increased respectively. The applicability and best-fit isotherm model parameters obtained by the non-linear Langmuir and Freundlich models (Table 8.3) were determined by the adjusted coefficients of determination (R^2), reduced Chi-squared and Residual sum of square (RSS) values. Therefore, based on higher Adj. R^2, lower Red. $\chi 2$, and RSS values; the Freundlich model compared to those of the Langmuir model clearly support the fluoride equilibrium sorption process on the CECS@nHapAgMgO sorbent (Table 8.3). Freundlich applicability suggests that the fluoride adsorption takes place firstly within the stronger

heterogeneous adsorption active binding sites and that subsequently the binding strength decreases with the increasing degree of site occupation.

Table 8.3. Fluoride sorption non-linear isotherms parameters by CECS@nHapAgMgO sorbent

	Temperature (K)	298	303	313
Non-Linear	**Langmuir isotherm**			
	Q_m (mg/g)	20.83	21.99	26.11
	K_L (L/mg)	0.012	0.008	0.006
	Adj. R^2	0.83	0.85	0.74
	Red. $\chi 2$	2.12	1.40	2.28
	RSS	12.71	8.42	13.69
	R_L	0.90	0.93	0.95
	Freundlich isotherm			
	K_F [(mg/g)/(mg/L) ^{n}]	0.81	0.70	0.82
	n	1.75	1.77	1.96
	Adj. R^2	0.88	0.92	0.83
	Red. $\chi 2$	1.52	0.73	1.47
	RSS	9.14	4.39	8.84

Furthermore, Table 8.4 shows the relative isotherm parameters values obtained from the slope and intercept of a plot of q_e versus In C_e, and In q_e versus ε^2 based on the linear Temkin and D-R equations for fluoride removal by CECS@nHapAgMgO respectively. Although, Temkin equation is assumed to be excellent for predicting the gas-phase equilibrium, the obtained Adj. R^2 values show it is appropriate for F^- ions uptake by the synthesized composite at elevated temperature (Table 8.4). Also, the Temkin heat of sorption B_T for the fluoride ions in the composite layer increases with the surface coverage of the adsorbate-sorbate interaction as the fluoride sorption temperatures increases. Lower values obtained from the D-R models (0.45-0.50) suggest it is not perfectly suitable for the equilibrium fluoride sorption process across the operating temperatures. However, the fluoride sorption values for the mean free adsorption energy (E) of the D-R isotherm model decreased from 7.45 to 1.58 kJ/mol as the temperature increases from 298 to 313 K. Thus, indicating, the possibility that the fluoride ions are attached to the surface of the adsorbent with weak van der Waal's forces of attraction.

Table 8.4. Curve fittings parameters for linear regression method of Temkin and D-R models

	Temperature (K)	298	303	313
Linear	**Temkin**			
	B_T (J/mol)	0.68	1.43	3.39
	K_T (L/g)	243.33	1.67	1.05
	Adj. R^2	0.49	0.74	0.83
	RMSE	2.51	1.58	1.22
	Dubinin-Radushkevvich			
	β_D (mol^2/kJ^2)	9×10^{-09}	2×10^{-07}	2×10^{-07}
	q_{max}(mg/g)	4.58	3.86	3.83
	E (kJ/mol)	7.45	1.58	1.58
	Adj. R^2	0.49	0.45	0.50
	RMSE	0.61	0.62	0.57

Consequently, the applicability of the equilibrium fluoride sorption uptake by the CECS@nHapAgMgO sorbent based on best correlation coefficients and lower error values are in the order, Freundlich > Langmuir > Temkin > D-R isotherm models.

8.3.5.3 Thermodynamics of fluoride sorption by CECS@nHapAgMgO composite

As stated earlier, Table 8.3 clearly shows that the maximum sorption capacity of fluoride increases from 20.83 to 26.11 mg/g with increasing temperature (298 to 313 K), thus, showing the favorability of the adsorption process towards high temperature. The thermodynamic parameters (Table 8.5); such as standard enthalpy change (ΔH°), standard free energy (ΔG°), and standard entropy change (ΔS°) were evaluated from different operating temperature of experimental sorption data (298–313 K) using the equations (18)–(20). The respective values of ΔH° and ΔS° were calculated from the slope and intercept on the plot of ln K_C against 1/T (Eq. (20)).

$$\Delta G° = -RT \ln Kc \quad (18)$$

$$\Delta G° = \Delta H° - T\Delta S° \quad (19)$$

$$\ln K_c = -\frac{\Delta H°}{RT} + \frac{\Delta S°}{R} \quad (20)$$

where R (8.314 J mol^{-1} K^{-1}) is the gas constant, T is the absolute temperature (K). The equilibrium constant values K_c must be dimensionless and were obtained derived by multiplying the Langmuir constant (K_L) by the molecule weight of adsorbate (F^-; 18.99 g/mol), 1,000, and then 55.5 (the number of moles of pure water per liter) (Zhou and Zhou, 2014; Tran *et al*., 2016).

Fig. 8.8 shows the linear profile of temperature dependence of the equilibrium constant (K_c) from the equilibrium sorption data. The different thermodynamic parameters at varying temperature are

shown in Table 8.5. The negative values of ΔH° and ΔG° across all the operating temperatures indicated that the fluoride sorption process was exothermically and spontaneously inclined. The negative ΔG° also implied the feasibility of the sorption process. In addition, the negative value of ΔS° showed the decrease in the randomness at the sorbate-sorbent interface towards equilibrium may be due to the unavailability of active surface binding sites by the fluoride ions as well as the gradual diffusion of fluoride ions across the heterogeneous surface of the porous CECS@nHapAgMgO composite. Thus, restricting the exchange of aggregated fluoride molecules on the sorbent surface, which amounts to decrease in the entropy as supported by the kinetic analysis.

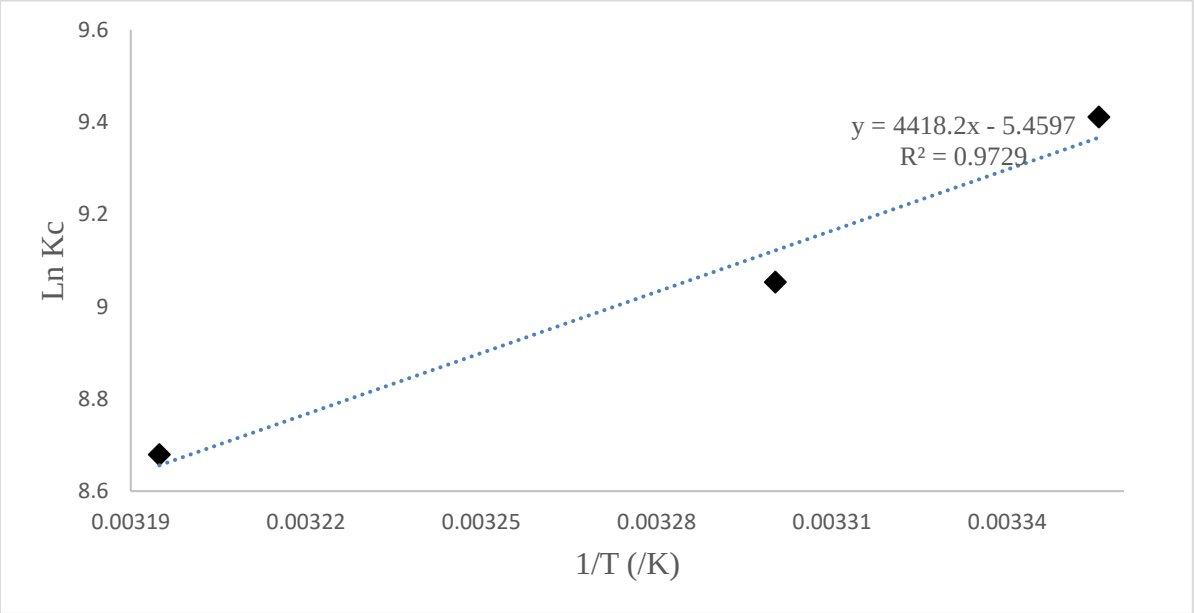

Fig. 8.8. Plots of ln Kc against 1/T for adsorption of fluoride onto CECS@nHapAgMgO composite at 0.3 g, 24 h at160 rpm.

Table 8.5. Thermodynamic parameters of fluoride uptake by CECS@nHapAgMgO composite

Thermodynamic parameters			
Temperature (K)	ΔH◦ (KJ/mol)	ΔG◦ (kJ/mol)	ΔS◦ (J/mol K)
	-36.74		-45.39
298		-23.21	
303		-22.98	
313		-22.53	

8.3.6 Effect of competing anions

Fig. 8.9 shows the influences of other competing anions characteristics of natural aqueous solution on fluoride sorption by the CECS@nHapAgMgO composite at all optimal parameters. This was carried out reacting 10 mg/L of fluoride ion with 100 mg/L of the respective co-existing anion (Cl^-, NO_3^-, SO_4^{2-}, CO_3^- and HCO_3^-). Apart from Cl^-, NO_3^-, SO_4^{2-}, the affinity for fluoride uptake by the sorbent was hindered by the presence of slightly alkaline anions (CO_3^- and HCO_3^-) leading to the development of more competing for the negative charge at the surface for adsorption sites.

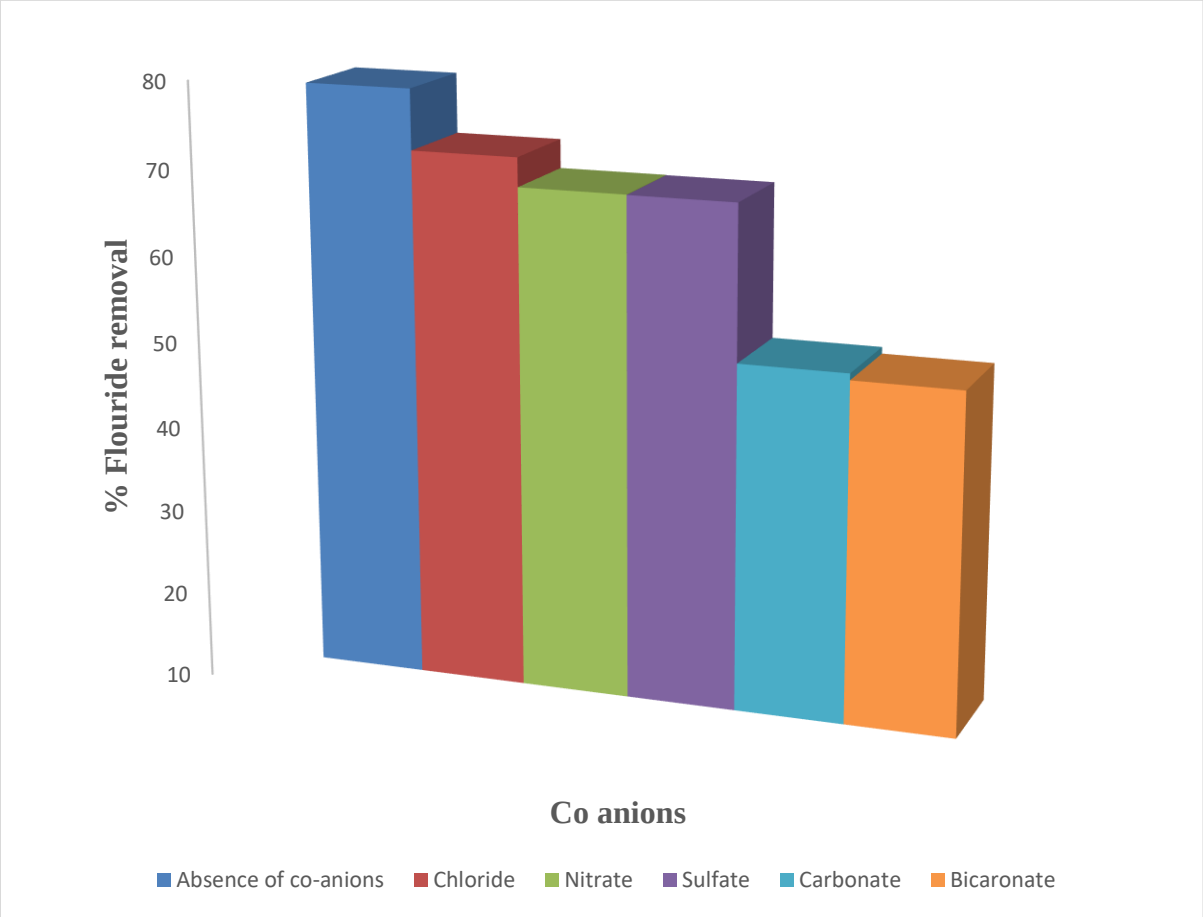

Fig. 8.9. Effect of competing anions on fluoride sorption efficiency (initial F^- concentration 10 mg/L, sorbent dose: 0.3 g contact time of 40 min at room temp at an agitation speed of 250 rpm.)

8.4 Mechanisms of fluoride Sorption

Analytical techniques like Fourier transform infrared spectroscopy and X-ray photoelectron spectroscopy were employed to compliments solution pH analysis and sorption models and thermodynamic analysis essential to confirm the surface chemistry in the fluoride uptake process by the composite.

8.4.1 BET Specific surface area

Generally, adsorption capacity depends upon porosity as well as chemical functional groups at the adsorbent surface. The BET specific surface areas and pore volumes of CECS@nHapAgMgO composite were found to be 23.74 m^2/g and 0.062 cm^3/g with an average particle size of 9.89 nm. This suggests that the CECS@nHapAgMgO nanocomposite is mesoporous in nature.

8.4.2 FTIR analysis

The possible active binding functional groups at the surface of the CECS@nHapAgMgO composite before and after fluoride sorption process were identified by ATR-FTIR analysis. Fig. 8.10 show the phases of vibrational frequencies during the sorption mechanism. A strong and sharp band at 3324.24 cm^{-1} which became broader and shifted to 3360.12 cm^{-1} showed the presence of -OH and -NH stretching vibrations of hydroxyl and amine groups on the surface of the CECS@nHapAgMgO composite. The broadness of the peak after fluoride sorption may be associated with the ligand-exchange mechanism between F and -OH having a comparable ionic radius as well as the electrostatic attraction with the -NH group (Sundaram *et al*., 2009; Loganathan *et al*., 2013). The bands at 2886.57, between 1640 and 1560 cm^{-1} are ascribed to the stretching and asymmetric vibrational bonds of -CH ($–CH_3$), -C=O and -CN of an amide group respectively (Kalsi, 2007). In addition, typical characteristic bands of a C-O vibrational stretching of CO_3^{2-}groups (1421.13 cm^{-1}), which almost disappeared in the fluoride sorbed CECS@nHapAgMgO spectrum also indicated the role of the carbonate group in the fluoride uptake. Other similar prominent groups in the spectra include bending vibration of methylene groups (1314 cm^{-1}), stretching vibration from C-O and C-O-C groups respectively characteristics of a natural fibre (1140 cm^{-1}) asymmetric stretching phosphate group, PO_4^{3-} (1022 cm^{-1}) and 552 cm^{-1} which are attributed to the vibrational and bending modes of Mg-O-Mg deformation (Koutsopoulos, 2002; Balamurugan *et al*., 2014; Fan *et al*., 2012). Therefore, the provided FTIR results assume that fluoride uptake reaction occurred as a result of chemical bond exchange between the surface-active groups and fluoride ions.

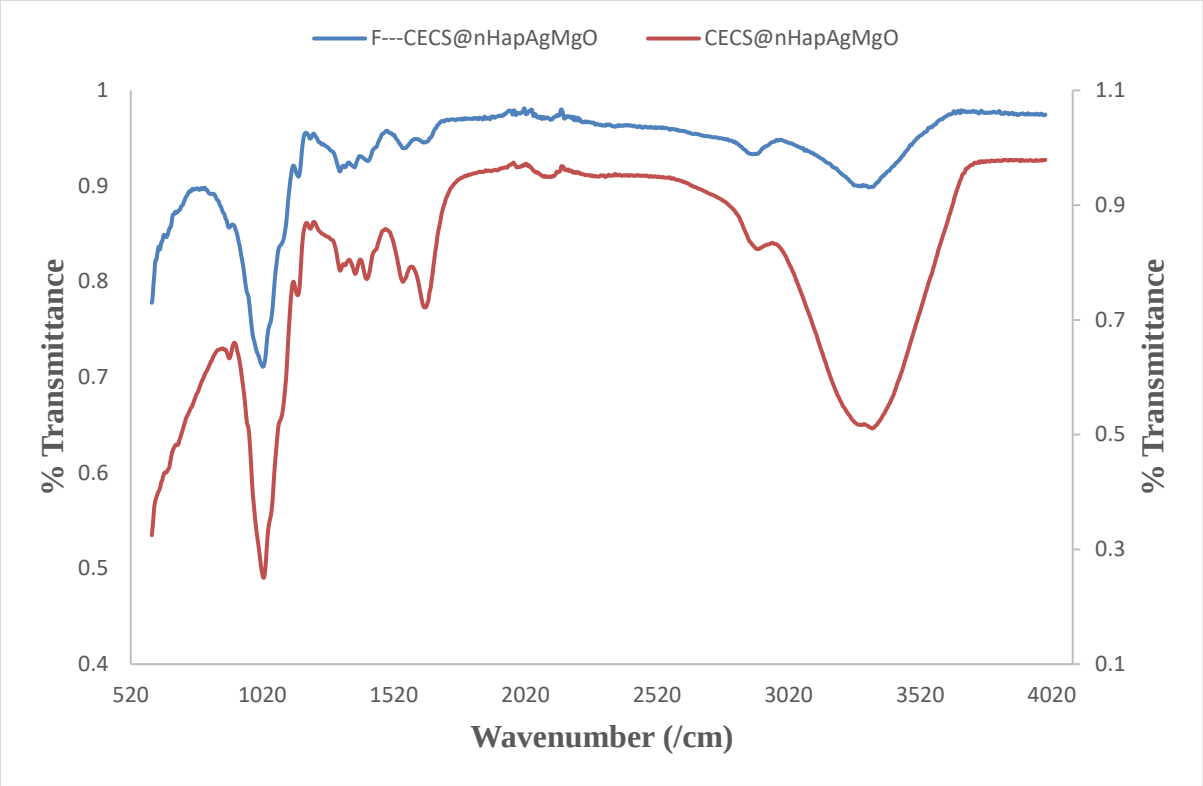

Fig. 8.10. FTIR spectra of before and after fluoride uptake by CECS@nHapAgMgO nanocomposite

8.4.3 Effect of solution pH on fluoride sorption

In sorption process, one of the vital factors that determine the charge interaction between an adsorbent and the speciation of sorbate in solution is the pH of the medium. Fig. 8.11 (a) shows the influence of solution pH (3.0 -12.0) on fluoride sorption onto CECS@nHapAgMgO composite at room temperature. As indicated on the pH profile, fluoride sorption capacity apparently increased as the pH increases from 3.0 to 5.0 reaching maximum percentage removal value of ≈ 97 % at pH 5.0. However, at pH > 5 (7 to 12), a significant decrease in fluoride uptake percentages occurred with the lowest value of 59 % at a pH of 12. The optimal pH value for the fluoride sorption was assigned 5.0 and this was used for the subsequent sorption experimental processes. The effects of pH on fluoride being sorbed by the composite can best be explained on the structural composition of the synthesized CECS@nHapAgMgO material. It is important to note that fluoride sorption mechanisms are directly dependent to the type, amounts as well as positioning of the surface chemical groups inherent in the developed polymeric-metal metal oxides hybrid sorbent as well as how these chemical structures relate to F^- in solution condition of pH region. As revealed by the FTIR spectrum, the main functional groups in the synthesized CECS@nHapAgMgO sorbent are the hydroxyl and the amino groups. However, to best explain the effects of pH on fluoride sorption, the point of zero charge must be evaluated. The pH point of zero charge (PZC) is that point where the sorbent surface charge density takes a zero value (possess an equal number

of positive and negative charges). The pH PZC value obtained from the plot (Fig. 8. 11(b)) is ≈ 7.27. Therefore, with the pH PZC (7.27) greater than the optimum pH value (5), it can be concluded that the overall surface charge on the active binding sites of the CECS@nHapAgMgO sorbent responsible for the improved fluoride uptake between the sorbent-sorbate system is predominantly positive charges.

This phenomenon in solution pH media is related to the inherent chemical functional groups on the sorbent having their own pKa in solution as well as through ligand-exchange capability. The predominating positively charged on the sorbent surface is due to the presence of a large number of primary amine groups each possessing a pKa ranging between 6.1 and 6.3, which makes chitosan a weak base (Craver and Carraher, 2000). Therefore, in acidic solution (H^+), most of the amino groups in the composite will be protonated (--NH_3^+) so the negatively charged fluoride ions can electrostatically adsorb onto the CECS@nHapAgMgO sorbent. As the solution pH increases (pH > 7), a significant reduction in fluoride uptake occurred because of the presence of more dissociated equilibrium anionic groups (from deprotonation chemical functional groups) at the surface of the CECS@nHapAgMgO sorbent, thereby, creating stronger electrostatic repulsion phenomena.

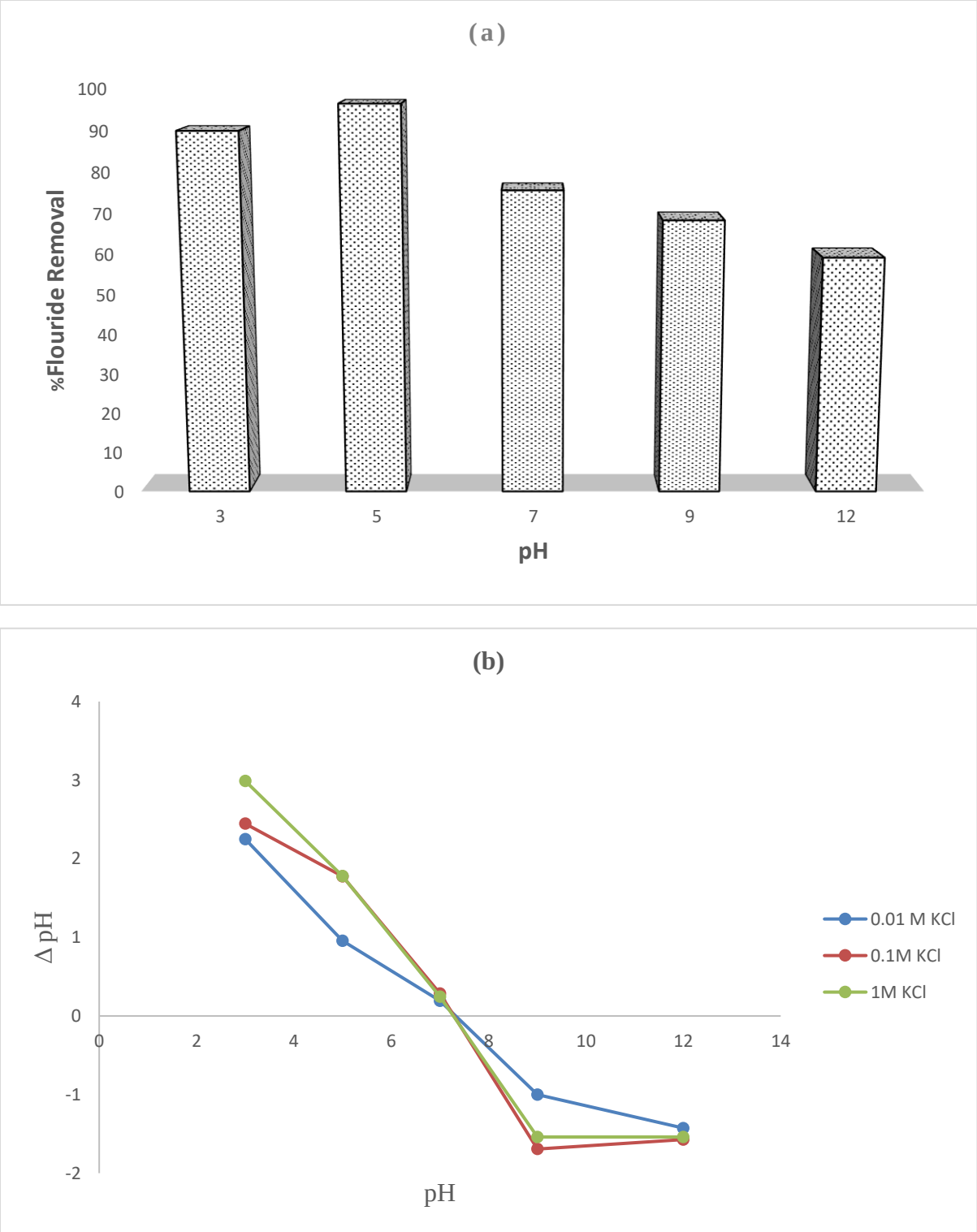

Fig. 8. 11. (a) Effects of pH; (b) pH Point of Zero Charge (PZC) (Initial fluoride concentration = 10 mg/L, sorbent dosage = 0.3 g/L, temperature = 25 ± 2 °C at 250 rpm).

8.4.4 XPS analysis

In order to explain the possible fluoride sorption mechanism between the sorbent-surface interface, the sorbent was examined by XPS. Fig. 8.12 shows the surface elemental composition and bonding possibilities of the CECS@nHapAgMgO sorbent before and after fluoride uptake in aqueous solution. The successful ability of the synthesized sorbent to bind with the fluoride ions was confirmed by the presence of the F1s spectrum at 689 eV (Fig. 8.13). Other peaks values detected supporting the synthesised CECS@nHapAgMgO and their corresponding electronic configuration which were consistent in Fig (a and b) are 2p (134.0 eV); (C1s (C-C (284.9 eV), C-O contribution of -OH groups (286.3 eV), C=O (287.6 eV) and O-C=O (289.2 eV); O 1 s (C-O (531.1 eV), C=O (532.9 eV), and Organic O (534.7 eV)); Ca 2p (347.7 eV), Mg 1s (1306 eV) and single Ag peak 367. These elemental compositional variations confirmed the presence of hybrid inorganic and organic molecular layers associated with the developed CECS@nHapAgMgO composite (Bomben *et al*., 1995; Rouxhet and Genet, 2011; Newberg *et al*., 2011). The peak reduction in the associated C 1s contents (C-O from the hydroxyl and carbonate groups) showed the possible ligand exchange with the fluoride ions, thus leading to the enhanced binding affinity to the CECS@nHapAgMgO composite. Hence, complementing the FTIR, solution pH analysis and EDS, the probable multiple mechanisms for the fluoride sorption by the CECS@nHapAgMgO sorbent is shown in Fig 8.14.

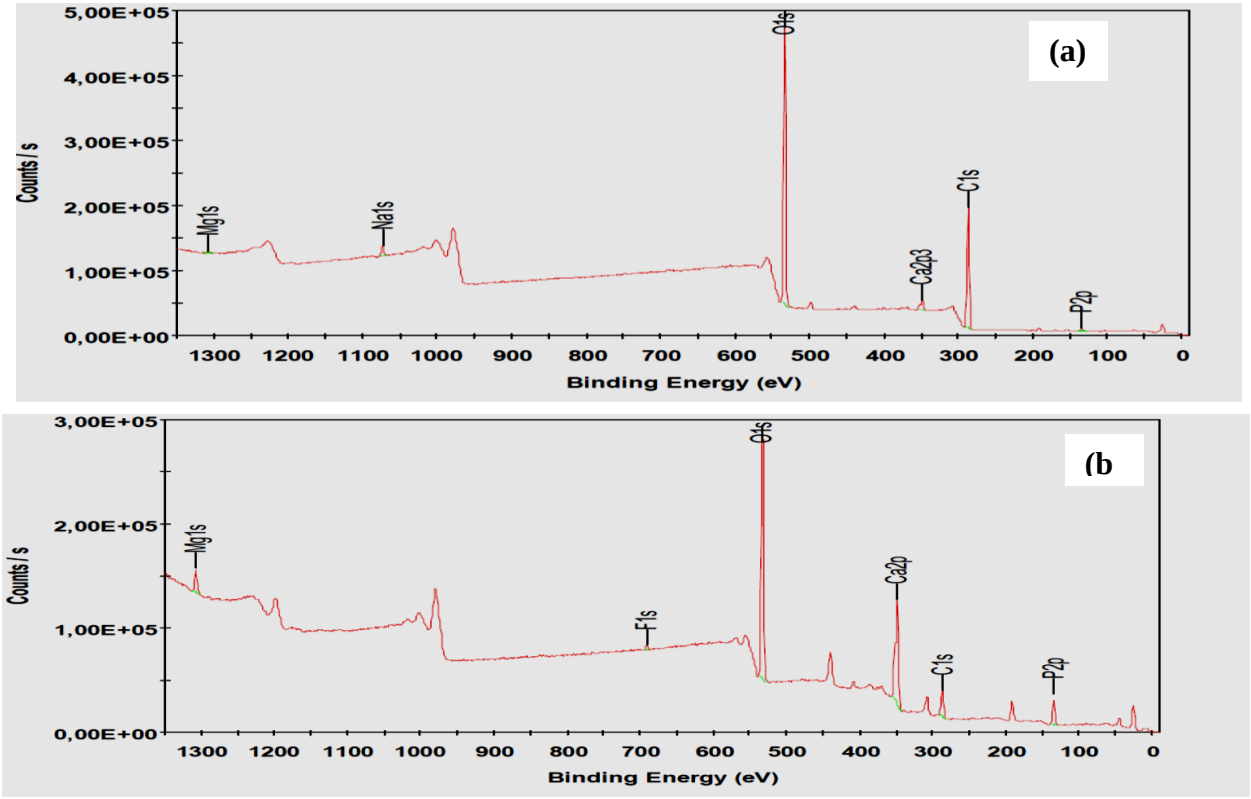

Fig. 8.12. XPS survey spectra of CECS@nHapAgMgO nanocomposite (a) before; (b) after fluoride removal.

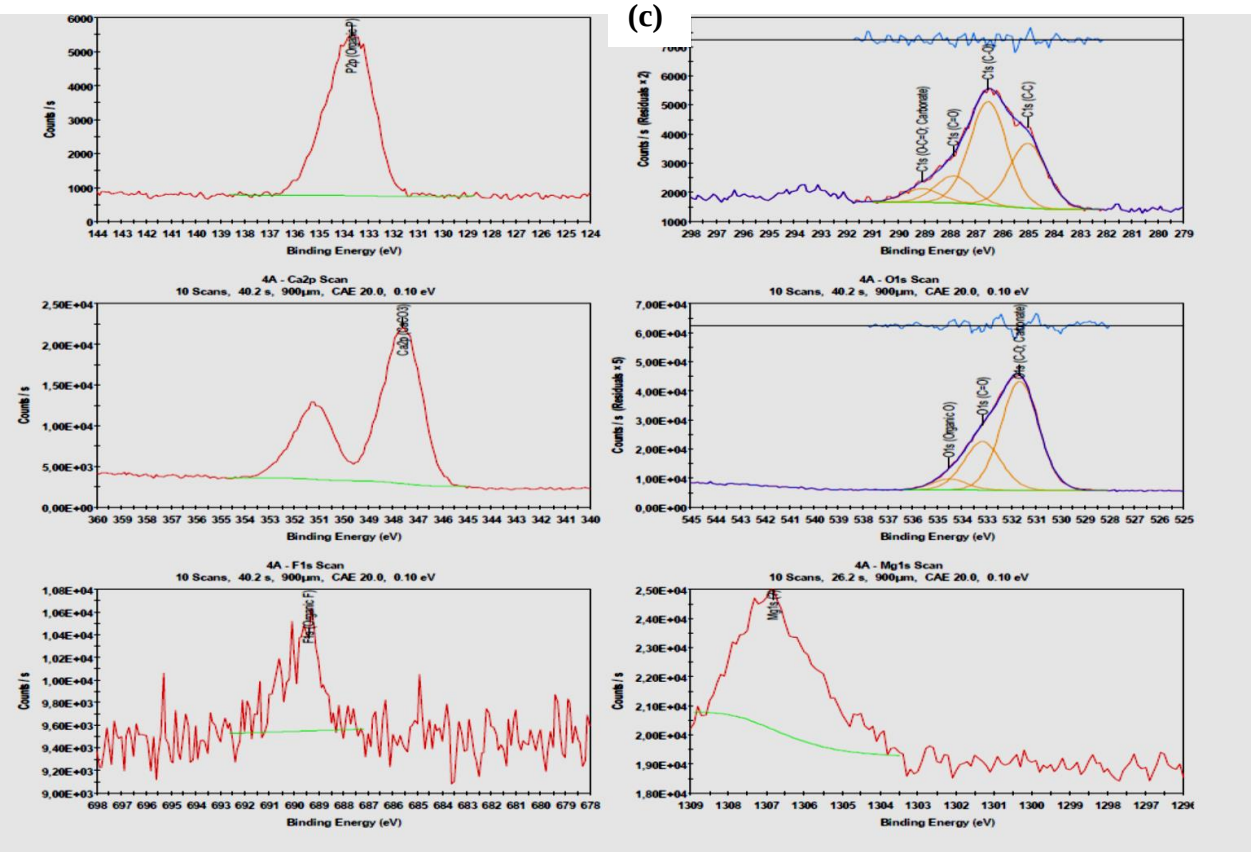

Fig. 8.13. CECS@nHapAgMgO nanocomposite of P2p, C1s, Ca2p, O1s F1s, Mg1s, spectra after fluoride sorption.

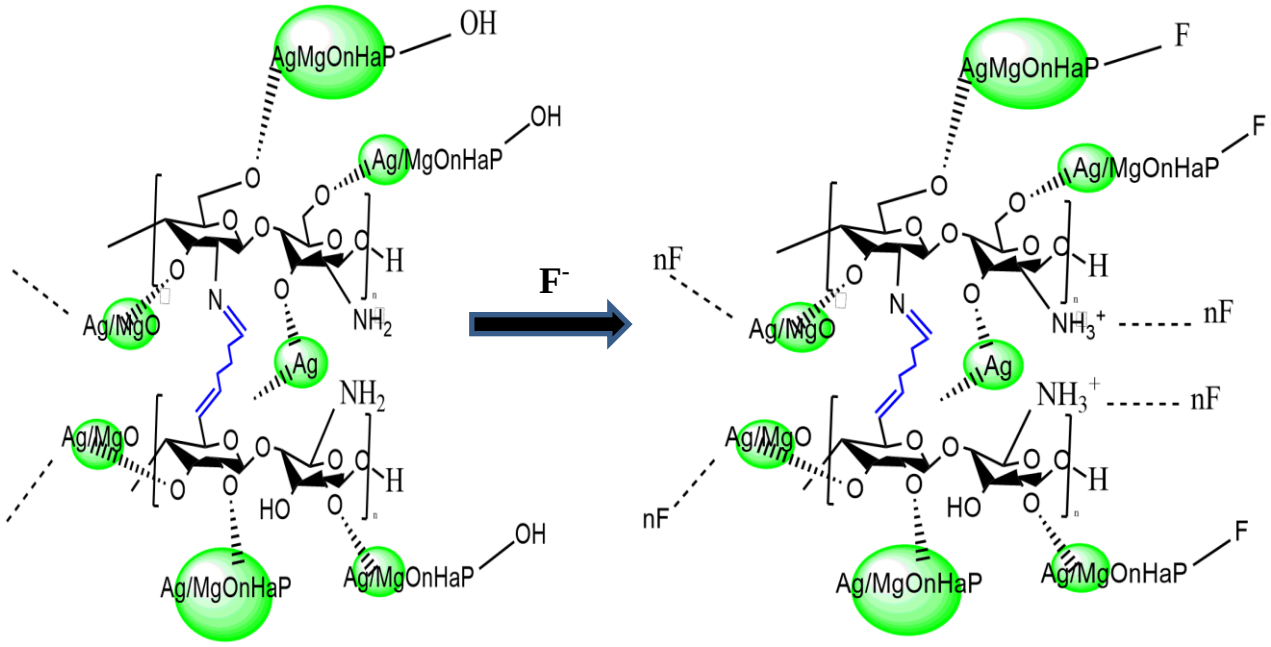

Fig. 8.14. Probable surface mechanism of fluoride ions by CECS@nHapAgMgO nanocomposite

8.5 Regeneration study

The feasibility of reuse for the active binding sites of CECS@nHapAgMgO after fluoride sorption in treatment processes was carried out for its potential economic viability. This was done using a slightly alkaline solution and water-based on the desorption capability earlier reported in coexisting anion interference. 0.01M Na_2CO_3 and water was used with 0.3g/50 mL fluoride sorbed CECS@nHapAgMgO at 250 rpm at three (3) different cycles of regenerations. As shown in Fig 8.15 the reusability of the sorbent decreases as the number of cycles increases. The use of water as a regenerant is more favorable to fluoride uptake by the sorbent compared to 0.01M Na_2CO_3 after, three cycles. Although, the use of water as a regenerant provides a better, easy and of no cost for the reuse as well as in the removal of dead microbial cells on the sorbent surface, the introduction of contaminants depending on the sources of water may hinder its usage for this process.

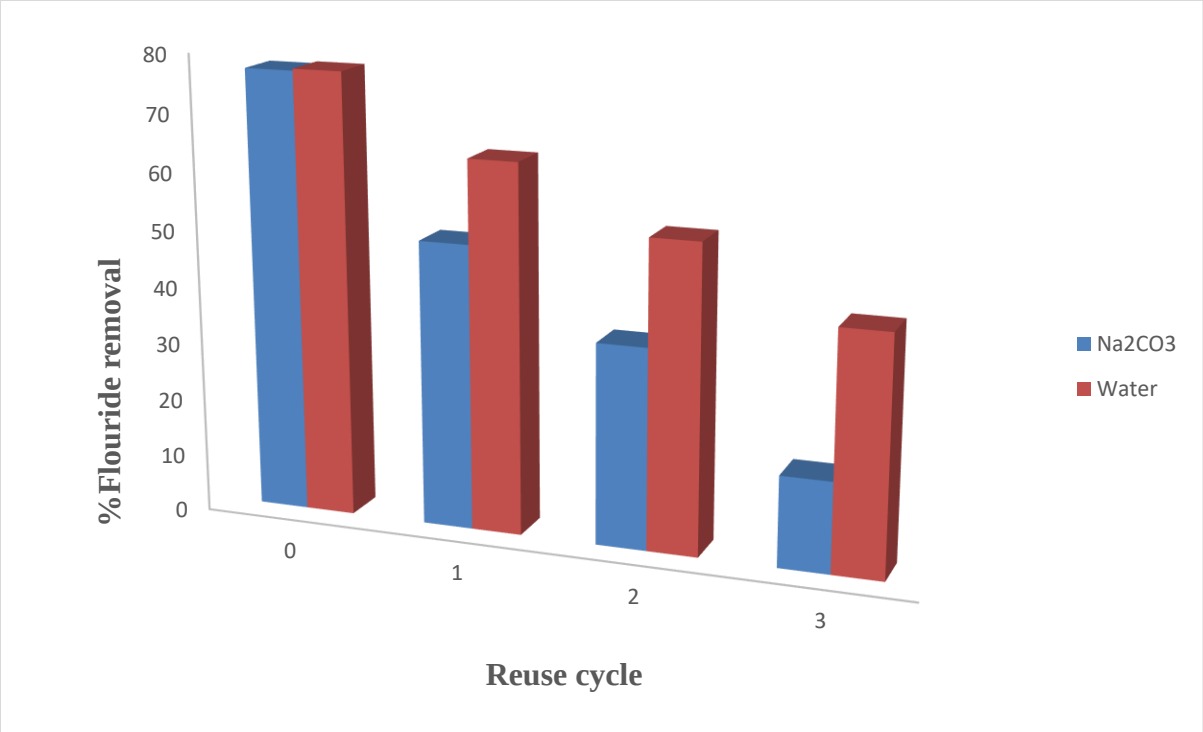

Fig. 8.15. Fluoride sorption by CECS@nHapAgMgO nanocomposite in successive regeneration cycles (10 mg/L initial F^-, sorbent dosage 0.3 g, 40 min contact time at 250 rpm).

8.6 Antibacterial studies of CECS@nHapAgMgO nanocomposite

The time-dependent results of the antibacterial activity of CECS@nHapAgMgO nanocomposite against gram-negative bacteria (*Escherichia coli* (ATCC 35218) and *Klebsiella pneumoniae* (ATCC-BAA-1705) and gram-positive bacteria (*S. aureus* (ATCC 33591) is summarised in Table 8.6 and Fig 8.16 (a)-(f)). The zone of inhibition and minimal inhibition concentration (MIC) was used to establish this claim. The toxicity of CECS@nHapAgMgO with time-based on the zone of inhibition was measured in the following order: *S. aureus* > *E. coli* > *K. pneumoniae* bacteria. The

increase in the zone of inhibition diameter after 48 h (Fig. 8.16 (b), (d) and (f)) may be as a result of the slow diffusion of the embedded AgMgO nanoparticles within the cell walls of the microbes, leading to more cell death. The lowest concentration at which the composite showed growth inhibition was recorded as the minimum inhibitory concentration (MIC). 16 µL of the CECS@nHapAgMgO nanocomposite (1000 µg/mL) was used for MIC analysis. 20 µg/mL was evaluated as the effective MIC concentration of CECS@nHapAgMgO nanocomposite capable to inhibit the growth of both *S. aureus* and *E. coli* compared to *K. pneumoniae* (10 µg/mL) (Fig. 8.17). Various studies have shown that the toxicity effects of nanomaterials depend on the type of bacterial strains, precursor concentration, methods of preparation, size, surface charges, and the capping and stability agents. Therefore, the probable mechanisms involved in CECS@nHapAgMgO antimicrobial potential may be due to the release and permeation of silver and MgO species through the cell membrane of the bacterial cells, thus disrupting the respiration functions and cell death (He *et al*., 2011; Mittal *et al*., 2017). In addition, the presence of the amine and hydroxyl functional groups in the peel extracts moieties and chitosan to some extent may have contributed to enzymatic functioning, oxidative stress and inactivation of the microbial DNA (Feng *et al*., 2000). This occurs when the positively charged chitosan particles in the composite interact with the negatively charged cell membranes, causing an increase in membrane permeability and eventually rupture and leakage of intracellular components (Qi *et al*., 2004). Thus, the antibacterial activities by the CECS@nHapAgMgO nanocomposite. The probable mechanism of CECS@nHapAgMgO nanocomposite inhibiting these pathogens is shown in Fig. 8. 18.

Table. 8.6. Inhibitory effect of synthesized CECS@nHapAgMgO nanocomposite

		Microorganisms		
		S. aureus (ATCC 33591)	***E. coli* (ATCC 35218)**	***K. pneumonia* *(ATCC-BAA-1705)***
Zone of inhibition (mm)				
24 h	Mean	10	10	8.5
	Std. Deviation	1.41	2.83	2.12
	Std error of mean	1	2	1.5
48 h	Mean	19.5	18	18.5
	Std. Deviation	0.71	1.41	4.95
	Std error of mean	0.5	1	3.5
	MIC (µg/mL)	20	20	10

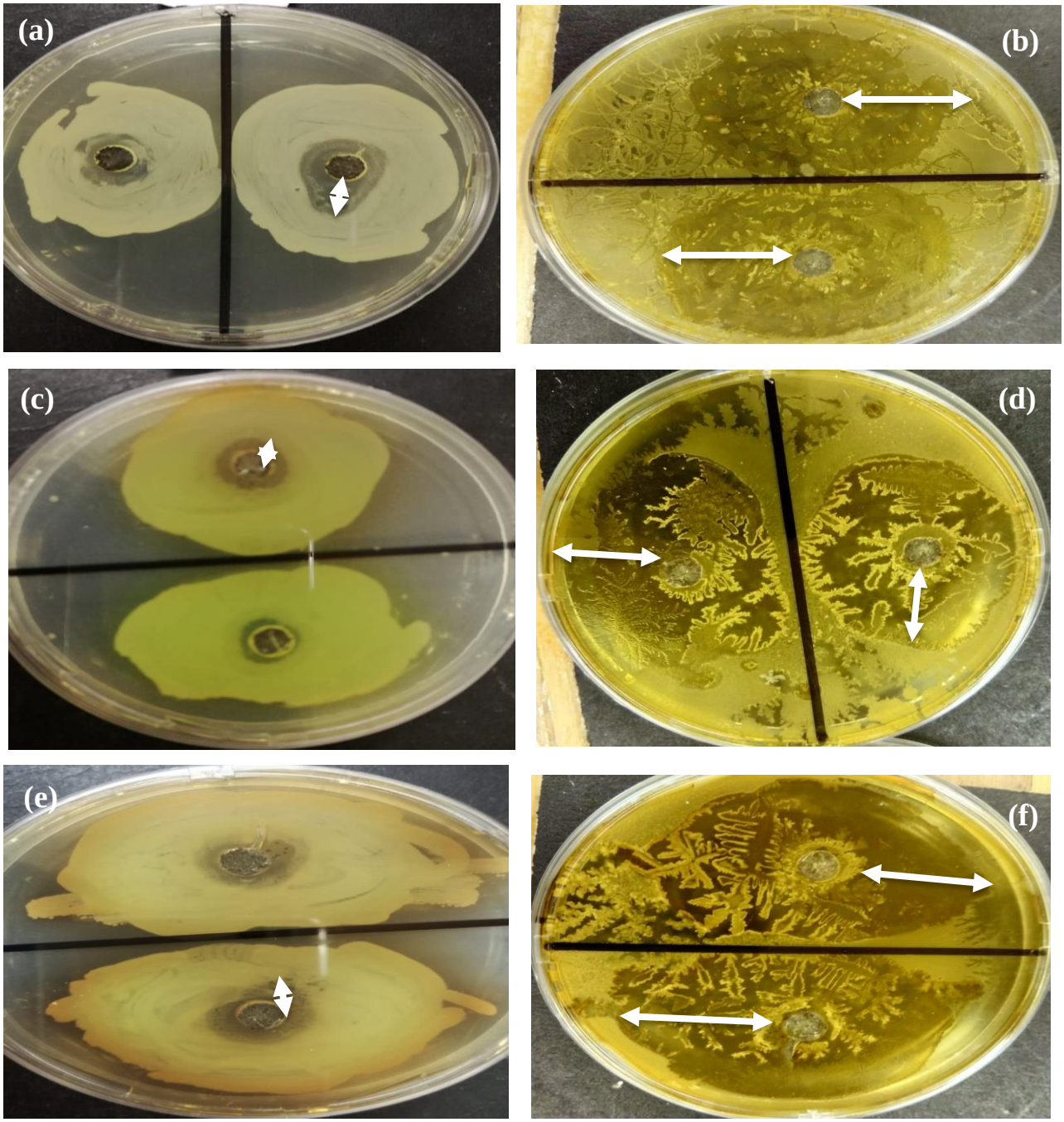

Fig. 8. 16. Inhibition zone photographs of the CECS@nHapAgMgO nanocomposites against bacteria *S. aureus* (a and b), *E. coli* (c and d) and *K. pneumoniae* (e and f) after 24 and 48 h respectively.

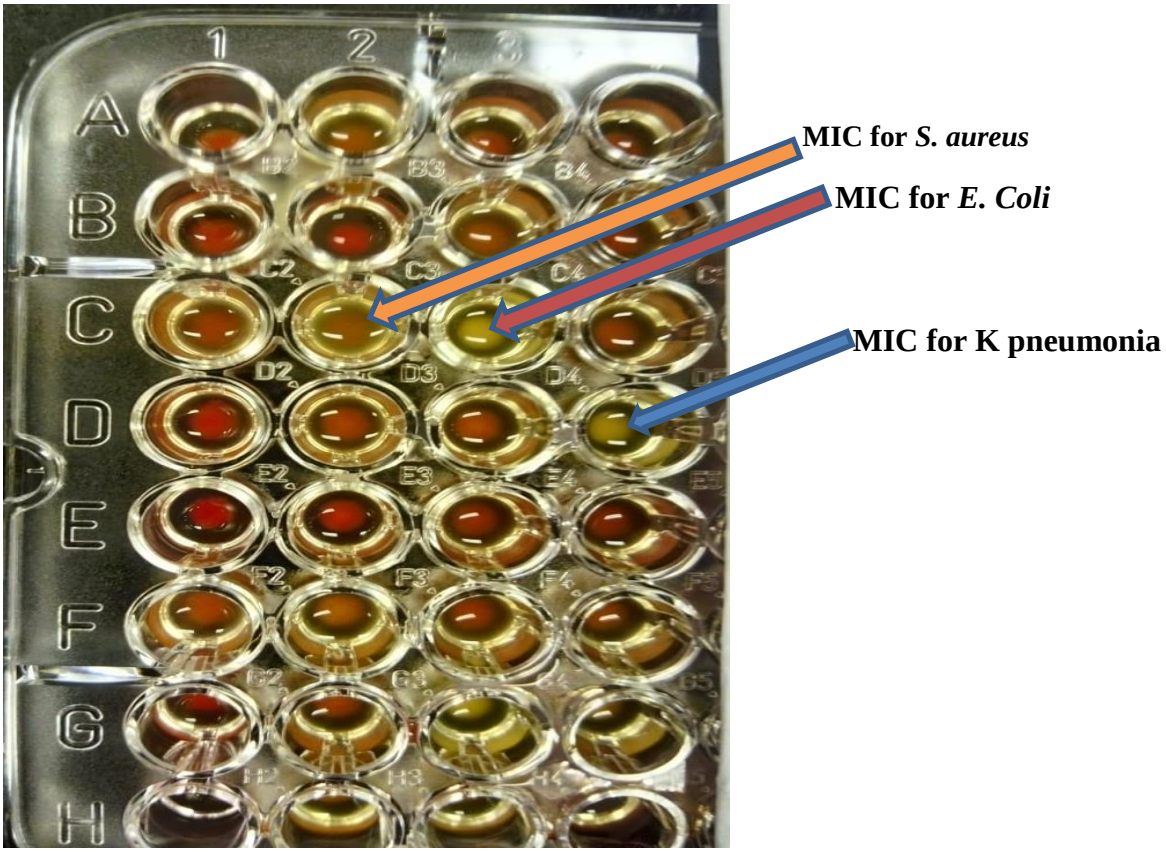

Fig. 8. 17. Representative images of 96 wells per agar disk (water (control (Column 1), *S. aureus* (Column 2), *E. coli* (Column 3) and *K. pneumoniae* (Column 4) bacteria) containing synthesized CECS@nHapAgMgO nanocomposite.

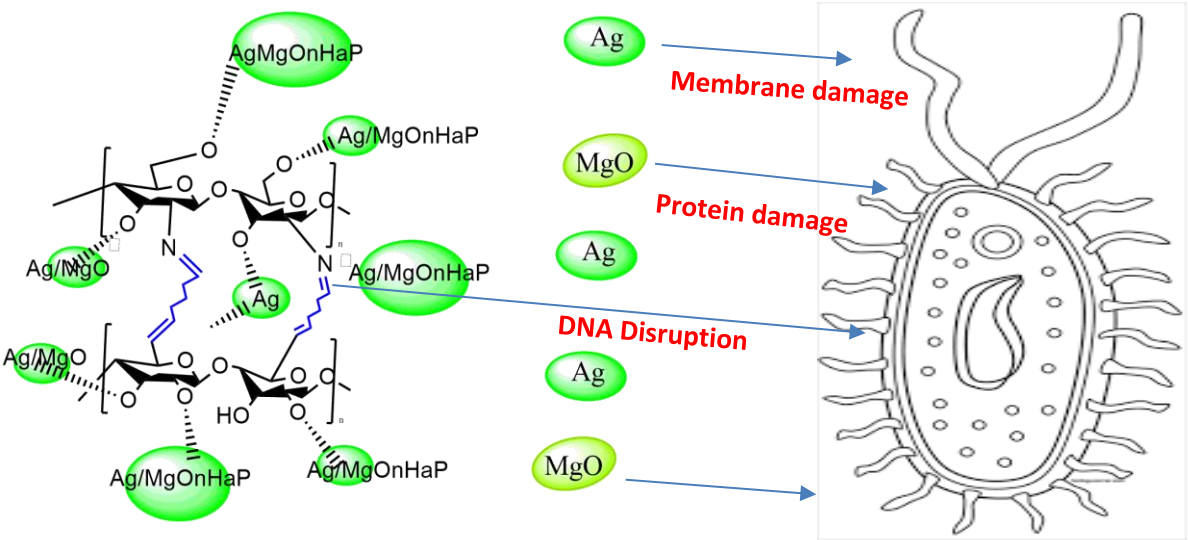

Fig. 8.18. Probable antimicrobial mechanism of CECS@nHapAgMgO nanocomposite

8.7. Field study

In this study, the applicability of the CECS@nHapAgMgO composite for fluoride and pathogens removal were evaluated in actual groundwater. The fluoride-contaminated groundwater (11.26 mg/L) was collected from a local village (Lephalale Municipality of Limpopo province, South Africa.) CECS@nHapAgMgO adsorbent dosage of 1 g/100 mL was used and the mixture was agitated at 250 rpm for 60 mins at room temperature. Table 8.7 shows the physicochemical parameters of groundwater before and after sorption process. CECS@nHapAgMgO successfully removed F^- below the WHO permissible limit of 1.5 mg/L in groundwater.

Table 8.7. Physicochemical parameters of Field trial results

Water quality parameter	Before treatment	After treatment	WHO guideline	SANS guideline
pH	7.21	7.22	6-9	5-9
EC (µS)	1415	483	<150	
Salinity (ppm)	732	232	-	-
TDS (mg/L)	1004	343	<600	<1000
F- (mg/L)	11.26	1.08	1.5	1-1.5
Br- (mg/L)	9.86	9.6	-	-

8.8 Comparison with other studies

The enhanced fluoride ion sorption capacity of the CECS@nHapAgMgO materials surpass the uptake properties of other reported sorbent materials of similar and natural compositions (Table 8.8). The structural modifications of the composite may have significantly increased the number of active binding sites at the surface CECS@nHapAgMgO for the fluoride uptake. The potential ability of simultaneously removing fluoride and pathogens from water show the significance of the study towards its applicability in point of use (POU) household scale.

Table 8.8 Comparison of different fluoride adsorption capacities by different sorbent materials.

Sorbent materials	F^- sorption capacity (mg/g)	Optimized condition	Microbial removal potential	Reference
HaP nanorods	1.49	3h. pH 7; 7g/L	Nil	Gao et al. 2009
nHap/chitosan composite	1.56	30 min; pH 3,	Nil	Sundaram et al., 2009
Synthestic Nanohydroxyapatite	0.49	pH 2, 0.5 g/25 mL	Nil	Sundaram et al., 2008
Sawdust raw	1.73	pH 6, 0.5 g/25 mL	Nil	Yadav et al., 2013
Zirconium impregnated cashew nut	1.83	pH 7	Nil	Alagumuthu et al2010
Magnesia–chitosan composite	11.24	pH 3.0–11.0	Nil	Sundaram et al., 2009
Ce (III) encapsulated chitosan polymer matrix	9	pH 7	Nil	Viswanathan et al., 2009
cellulose@hydroxyapatite nanocomposites	4.2	pH 6.5.	Nil	Yu et al., 2013
Ag/MgOnHaP	2.15	60 min; pH 6; 0.3g	Yes	Ayinde et al 2018
AgMgOnHaP@CSn	6.86	40 min; pH 7; 0.25	Yes	This study
CNF-AgMgOnHaP composite	8.71	10 min; pH 5; 0.25g	Yes	This study
CECS@nHapAgMgO	26.11	40 min; pH 5, 0.3 g	Yes	This study

8.9 Conclusion

Glutaraldehyde crosslinked cellulose/chitosan reinforced with hybrid nanocomposite (CECS@nHapAgMgO) was successfully synthesized with an improved morphology and surface properties for simultaneous removal of fluoride and pathogen in aqueous solutions. The initial rapid fluoride removal is presumably due to the instantaneous utilization of the most readily available binding functional groups active sites on the outer surface of CECS@nHapAgMgO by fluoride ions, and slower adsorption at the later stage may be due to a gradual diffusion of fluoride ions into the interior heterogenous porous surface of the adsorbent. The adsorption data for CECS@nHapAgMgO fitted well with pseudo-second-order and Freundlich models. The maximum fluoride adsorption capacities exhibited by CECS@nHapAgMgO nanocomposite is 26.11 mg/g at 0.3g/50 Ml. Optimum pH was established at 5 with a pHpzc of 7.27 at 40 min contact

time. The order of magnitude of the energy value obtained from the D-R and Temkin isotherms also suggests the involvement of physisorption process. Thermodynamic parameters established that the fluoride sorption process was exothermically and spontaneously inclined but decrease in the randomness at the sorbate-sorbent interface towards equilibrium. Evidence from FTIR, XPS suggested the reaction is more inclined towards chemisorption at a very short period. Moreover, the antimicrobial analysis revealed the order of inhibition in the following order: S. aureus > E. coli > K. pneumoniae bacteria. The adsorbent was effective in defluoridation of field groundwater at field pH (7.22) and can be easily regenerated with deionized water for reuse making it suitable for point of use defluoridation and pathogen removal device at the household level.

Conflicts of interest

The authors declare no conflicts of interest.

Acknowledgment

Authors would like to acknowledge financial support from USAID-PEER Cycle 6-Award No: AID-OAA-A-11-00012; National Research Foundation Grant No: 114726; University of Venda, South Africa (RPC grant Number: SES/17/ERM/03), Prof Gitari DHET Research incentive funds and Mintek, South Africa.

References

Abdul Khalil, H. P. S., Saurabh, C.K., Adnan, A.S., Fazita, M.N., Syakir, M.I., Davoudpour, Y., Rafatullah, M., Abdullah, C.K., Haafiz, M.K.M. and Dungani, R., 2016. A review on chitosan-cellulose blends and nanocellulose reinforced chitosan biocomposites: Properties and their applications. Carbohydrate polymers, 150, pp.216-226.

Adamson,A.W. A.P. Gast, Physical Chemistry of Surfaces, sixth ed., Wiley-Interscience, New York, 1997

Alagumuthu, G., Rajan, M., 2010b. Kinetic and equilibrium studies on fluoride removal by zirconium (iv) impregnated groundnut shell carbon. Hem. Ind. 64, 295–304.

Allan, G.G., Altman, L.C., Bensinger, R.E., Ghosh, D.K., Hirabayashi, Y., Neogi, A.N. and Neogi, S., 1984. Biomedical applications of chitin and chitosan. In Chitin, chitosan, and related enzymes (pp. 119-133). Academic Press.

Averbuch-Pouchot, M.T. and Guitel, J.C., 1976. Structure cristalline d'un tripolyphosphate acide mixte zinc–argent nonahydraté: Zn2Ag0, 62H0, 38P3O10. 9H2O. Acta Crystallographica Section B, 32(8), pp.2270-2274.

Ayinde WB, Gitari WM, Munkombwe M, Amidou S (2018a) Biosynthesis of Ultrasonically Modified Ag-MgO Nanocomposite and Its Potential for Antimicrobial Activity. J Nanotechnol 2018. https://doi.org/10.1155/2018/9537454

Balamurugan S, Ashna L, Parthiban P (2014) Synthesis of nanocrystalline MgO particles by combustion followed by annealing method using hexamine as a fuel. J Nano Tech 6:1–6. doi:10. 1155/2014/841803

Bhatnagar, A. and Sillanpää, M., 2009. Applications of chitin-and chitosan-derivatives for the detoxification of water and wastewater—a short review. Advances in colloid and Interface science, 152(1-2), pp.26-38.

Bomben, K.D., Moulder, J.F., Sobol, P.E. and Stickle, W.F., 1995. Handbook of X-ray photoelectron spectroscopy: a reference book of standard spectra for identification and interpretation of XPS data. Physical Electronics, Eden Prairie, MN.

Craver C, Carraher C (2000) Applied polymer science: 21st century. 1st edn. Elsevier Science.

Dąbrowski A (2001) Adsorption—from theory to practice. Adv Colloid Interface Sci 93(1-3),

Dhillon, A., Kumar, D., 2015. Development of a nanoporous adsorbent for the removal of health-hazardous fluoride ions from aqueous systems. J. Mater. Chem. 3 (8), 4215–4228.

Dubinin, M., Radushkevich, L., 1947. Equation of the characteristic curve of activated charcoal. Chem. Zentr. 1 (1), 875.

Fan, L., Zhang, Y., Luo, C., Lu, F., Qiu, H. and Sun, M., 2012. Synthesis and characterization of magnetic β-cyclodextrin–chitosan nanoparticles as nano-adsorbents for removal of methyl blue. International journal of biological macromolecules, 50(2), pp.444-450.

Fan, M., Dai, D. and Huang, B., 2012. Fourier transform infrared spectroscopy for natural fibres. In Fourier transform-materials analysis. InTech.

Feng, Q.L., Wu, J., Chen, G.Q., Cui, F.Z., Kim, T.N. and Kim, J.O., 2000. A mechanistic study of the antibacterial effect of silver ions on Escherichia coli and Staphylococcus aureus. Journal of biomedical materials research, 52(4), pp.662-668.

Fleet, M.E., Liu, X. and King, P.L., 2004. Accommodation of the carbonate ion in apatite: An FTIR and X-ray structure study of crystals synthesized at 2–4 GPa. American Mineralogist, 89(10), pp.1422-1432.

Gandhi, S., Abiramipriya, P., Pooja, N., Jeyakumari, J. J. L., Arasi, A. Y., Dhanalakshmi, V., Gopinathan, M. R. and Anbarasan, R., 2011. Synthesis and characterizations of nano sized MgO and its nano composite with poly(vinyl alcohol). Journal of Non-Crystalline Solids, 357, 181-185

Gao, S., Sun, R., Wei, Z.G., Zhao, H.Y., Li, H.X., Hu, F., 2009. Size-dependent defluoridation properties of synthetic hydroxyapatite. J. Fluorine Chem. 130, 550–556.

Grishkewich, N., Mohammed, N., Tang, J. and Tam, K.C., 2017. Recent advances in the application of cellulose nanocrystals. Current Opinion in Colloid & Interface Science, 29, pp.32-45.

He, D., Jones, A.M., Garg, S., Pham, A.N. and Waite, T.D., 2011. Silver nanoparticle− reactive oxygen species interactions: application of a charging− discharging model. The Journal of Physical Chemistry C, 115(13), pp.5461-5468.

Ho Y.S., Ng J.C.Y., McKay G., 2000. Kinetics of pollutant sorption by biosorbents: review. Sep Purif Methods; 29:189–232.

Ho, Y.S. and McKay, G., 1999. Pseudo-second order model for sorption processes. Process biochemistry, 34(5), pp.451-465.

Ho, Y.S., 2006. Review of second-order models for adsorption systems. Journal of hazardous materials, 136(3), pp.681-689.

Jagtap, S., Thakre, D., Wanjari, S., Kamble, S., Labhsetwar, N. and Rayalu, S., 2009. New modified chitosan-based adsorbent for defluoridation of water. Journal of Colloid and Interface Science, 332(2), pp.280-290.

Kalsi, P.S., 2007. Spectroscopy of organic compounds. New Age International.

Klemm, D., Heublein, B., Fink, H.P. and Bohn, A., 2005. Cellulose: fascinating biopolymer and sustainable raw material. Angewandte Chemie International Edition, 44(22), pp.3358-3393.

Koutsopoulos, S., 2002. Synthesis and characterization of hydroxyapatite crystals: a review study on the analytical methods. Journal of Biomedical Materials Research Part A, 62(4), pp.600-612.

Kunduru, K.R., Nazarkovsky, M., Farah, S., Pawar, R.P., Basu, A. and Domb, A.J., 2017. Nanotechnology for water purification: applications of nanotechnology methods in wastewater treatment. In Water Purification (pp. 33-74). Academic Press.

Kurita, K., 2006. Chitin and chitosan: functional biopolymers from marine crustaceans. Marine Biotechnology, 8(3), p.203.

Lagergren S., 1898. Zur Theorie der sogenannten adsorption geloster stoffe, K. Sven. Vetenskapsakad. Handl. 24 1–39.

LeChevallier, M.W. and Au, K.K., 2004. Water treatment and pathogen control. IWA publishing.

Loganathan, P., Vigneswaran, S., Kandasamy, J. and Naidu, R., 2013. Defluoridation of drinking water using adsorption processes. Journal of Hazardous materials, 248, pp.1-19.

Marchessault, R.H., Ravenelle, F. and Zhu, X.X. eds., 2006. Polysaccharides for drug delivery and pharmaceutical applications (No. 934). Amer Chemical Society.

Miretzky, P. and Cirelli, A.F., 2011. Fluoride removal from water by chitosan derivatives and composites: a review. Journal of Fluorine Chemistry, 132(4), pp.231-240.

Mittal, J., Jain, R. and Sharma, M.M., 2017. Phytofabrication of silver nanoparticles using aqueous leaf extract of Xanthium strumerium L. and their bactericidal efficacy. Advances in Natural Sciences: Nanoscience and Nanotechnology, 8(2), p.025011.

Modified Ag-MgO Nanocomposite and Its Potential for Antimicrobial Activity. J Nanotechnol 2018. https://doi.org/10.1155/2018/9537454

Mohamed, M. H.; Udoetok, I. A.; Wilson, L. D.; Headley, J. V. Fractionation Of Carboxylate Anions from Aqueous Solution Using Chitosan Cross-Linked Sorbent Materials. RSC Adv. 2015, 5, 82065−82077.

Mohapatra, M., Anand, S., Mishra, B.K., Giles, D.E. and Singh, P., 2009. Review of fluoride removal from drinking water. Journal of environmental management, 91(1), pp.67-77.

Muzzarelli, R.A., Boudrant, J., Meyer, D., Manno, N., DeMarchis, M. and Paoletti, M.G., 2012. Current views on fungal chitin/chitosan, human chitinases, food preservation, glucans, pectins

and inulin: A tribute to Henri Braconnot, precursor of the carbohydrate polymers science, on the chitin bicentennial. Carbohydrate polymers, 87(2), pp.995-1012.

Mumtaz, N., Pandey, G. and Labhasetwar, P.K., 2015. Global fluoride occurrence, available technologies for fluoride removal and electrolytic defluoridation: a review. Critical Reviews in Environmental Science and Technology, DOI: 10.1080/10643389.2015.1046768

Newberg, J.T., Starr, D.E., Yamamoto, S., Kaya, S., Kendelewicz, T., Mysak, E.R., Porsgaard, S., Salmeron, M.B., Brown Jr, G.E., Nilsson, A. and Bluhm, H., 2011. Formation of hydroxyl and water layers on MgO films studied with ambient pressure XPS. Surface Science, 605(1-2), pp.89-94.

Pandi, K. and Viswanathan, N., 2015. Enhanced defluoridation and facile separation of magnetic nano-hydroxyapatite/alginate composite. International journal of biological macromolecules, 80, pp.341-349.

Pelgrift, R.Y. and Friedman, A.J., 2013. Nanotechnology as a therapeutic tool to combat microbial resistance. Advanced drug delivery reviews, 65(13-14), pp.1803-1815.

Poinern, Gérrard Eddy Jai, Malay K. Ghosh, Yan-Jing Ng, Touma B. Iss,ShashiAnand, and Pritam Singh. (2011). Defluoridation behavior of nanostructured hydroxyapatite synthesized through an ultrasonic and microwave combined technique. Journal of Hazardous Materials 185. 29–37. pp.135-224.

Qi, L., Xu, Z., Jiang, X., Hu, C., Zou, X., 2004. Preparation and antibacterial activity of chitosan nanoparticles. Carbohydr. Res. 339, 2693–2700.

Qu, X., Alvarez, P.J.J., Li, Q., 2013. Applications of nanotechnology in water and wastewater treatment. Water Res. 47, 3931–3946.

Rojas, O.J. ed., 2016. Cellulose chemistry and properties: fibers, nanocelluloses and advanced materials (Vol. 271). Springer.

Rouxhet, P.G. and Genet, M.J., 2011. XPS analysis of bio-organic systems. Surface and Interface Analysis, 43(12), pp.1453-1470.

Samie, A., Obi, C.L., Bessong, P.O. and Namrita, L., 2005. Activity profiles of fourteen selected medicinal plants from Rural Venda communities in South Africa against fifteen clinical bacterial species. African journal of Biotechnology, 4(12).

Sundaram, C. S., Viswanathan, N., and Meenakshi, S. (2009). Defluoridation of water using magnesia/chitosan composite. Journal of Hazardous Materials, 163(2–3), 618–624.

Temkin, M.I., 1940. Kinetics of ammonia synthesis on promoted iron catalysts. Acta physiochim. URSS, 12, pp.327-356.

Tempkin, M., Pyzhev, V., 1940. Kinetics of ammonia synthesis on promoted iron catalyst. Acta Phys. Chim. USSR 12, 327.

Thakur, V.K. and Voicu, S.I., 2016. Recent advances in cellulose and chitosan based membranes for water purification: a concise review. Carbohydrate polymers, 146, pp.148-165.

Tian, Y., Wu, M., Liu, R., Wang, D., Lin, X., Liu, W., Ma, L., Li, Y. and Huang, Y., 2011. Modified native cellulose fibers—A novel efficient adsorbent for both fluoride and arsenic. Journal of hazardous materials, 185(1), pp.93-100.

Tran, H.N., You, S.J. and Chao, H.P., 2016. Thermodynamic parameters of cadmium adsorption onto orange peel calculated from various methods: a comparison study. Journal of Environmental Chemical Engineering, 4(3), pp.2671-2682.

Udoetok, I. A.; Dimmick, R. M.; Wilson, L. D.; Headley, J. V. Adsorption Properties of Cross-Linked Cellulose-Epichlorohydrin Polymers in Aqueous Solution. Carbohydr. Polym. 2016, 136, 329− 340.

UNESCO (2009): The United Nations World Water Development Report 3 - Water in a Changing World. UN Educ. Sci. Cult. Organ. Paris/New York: UNESCO/Berghahn Books.

Upadhyayula, V.K.K., Deng, S., Mitchell, M.C., Smith, G.B., 2009. Application of carbon nanotube technology for removal of contaminants in drinking water: a review. Sci. Total Environ. 408, 1–13.

Vijayaraghavan,K. T.V.N. Padmesh, K. Palanivelu, M. Velan, Biosorption of nickel(II) ions onto Sargassum wightii: application of two-parameter and three parameter isotherm models, J. Hazard. Mater. B133 (2006) 304–308.].

Viswanathan, N. and Meenakshi, S., 2009. Enhanced and selective fluoride sorption on Ce (III) encapsulated chitosan polymeric matrix. Journal of applied polymer science, 112(3), pp.1114-1121.

Wada, M., Heux, L. and Sugiyama, J., 2004. Polymorphism of cellulose I family: reinvestigation of cellulose IVI. Biomacromolecules, 5(4), pp.1385-1391.

Wang, X., Du, Y. and Liu, H., 2004. Preparation, characterization and antimicrobial activity of chitosan–Zn complex. Carbohydrate polymers, 56(1), pp.21-26.

Weber, W.J. and Morris, J.C., 1964. Equilibria and capacities for adsorption on carbon. Journal of the Sanitary Engineering Division, 90(3), pp.79-108.

WHO, Guidelines for drinking water quality, forth ed., World Health Organization, Geneva, 2011.

World Health Organization, 2016. Mortality and burden of disease from water and sanitation. Global Health Observatory (GHO) data.

WWAP (United Nations World Water Assessment Programme). (2015). The United Nations World Water Development Report 2015: Water for a Sustainable World. Paris, UNESCO.

Yadav, A.K., Abbassi, R., Gupta, A. and Dadashzadeh, M., 2013. Removal of fluoride from aqueous solution and groundwater by wheat straw, sawdust and activated bagasse carbon of sugarcane. Ecological engineering, 52, pp.211-218.

Yousef, R.I., El-Eswed, B., Al-Muhtaseb, A. 2011. Adsorption characteristics of natural xeolites as solid adsorbents for phenol removal from aqueous solution: Kinetics, mechanism, and thermodynamicss studies, Chem. Eng. J. 171, 1143-1149.

Yu X, Tong S, Ge M, Zuo J., 2013. Removal of fluoride from drinking water by cellulose@ hydroxyapatite nanocomposites. Carbohydrate polymers. Jan 30;92(1):269-75.

Zhou, X. and Zhou, X., 2014. The unit problem in the thermodynamic calculation of adsorption using the Langmuir equation. Chemical Engineering Communications, 201(11), pp.1459-1467.

CHAPTER NINE

CONCLUSION AND RECOMMENDATION

Shortage and contamination of global drinking water calls for the development of highly effective water purification techniques. Groundwater remains the most important source for drinking and other domestic needs in many rural communities of the world and South Africa. Waterborne epidemics associated with high fecal contamination pathway by pathogenic microbes and excessive fluoride-related diseases are a worldwide problem, that has endangered the quality of drinking water, despite the presence of other toxic contaminants in groundwater resources. The limitations of conventional water treatment methods and materials coupled with the view of severe effects of fluoride and microbial related diseases on human health have prompted the research community to pursue the discovering of a novel material with unusual properties. Hence, this research was motivated by this dangerous health risks incidental phenomenon associated with such contaminants in groundwater and proffer effective materials with vital functionalities in remediating this contaminant, especially at Point-Of-Use.

The thesis described the successful utilization of bio-based/agricultural waste materials in the development of a synergistic hybrid-biopolymeric loaded with metal metal-oxides nanocomposite in removing fluoride and pathogen from aqueous solution. This was done at laboratory scale using nanotechnological routes for environmental needs. The project analysis leads to the following conclusions:

- *Citrus paradisi* peel extract mediated methods yielded Ag and bi-layered Ag-MgO nanocomposite with increased reactivity and synergistic broad range antimicrobial action against water-borne pathogenic microbes.
- The use of biological material and environmentally benign reaction synthesis allowed the control of the nanoparticles size and stability and served as an alternative to the conventional chemical routes, which reduces its applicability. Thus making the nanoparticles as an effective nano-adsorbent for disinfecting of microbial species found in drinking water.
- Biosynthesized Ag-MgO nanomaterial was successfully incorporated into synthetic inorganic and natural bio-based polymeric materials aimed at increasing the fluoride adsorption capacity and improved antimicrobial activities.
- The Ag-MgOnHaP, AgMgOnHaP@CSn, CNF-AgMgOnHaP and CECS@nHapAgMgO nanocomposites removed fluoride ion with an adsorption capacity of 2.146, 6.86, 8.71 and 26.11 mg/g respectively.
- Optimal conditions between 10 – 60 mins, pH ranges of 5-7, dosage of 0.25-0.3 g/50mL across different operating sorption temperature were recorded in all the sorbent materials.

- Both chemisorption and physisorption reaction mechanisms were involved in all the synthesized nano-sorbents. Thus, indicating the combination of ion and ligand exchange, H-bonding as well as the structural modification through the introduction of more active functional groups for F^- uptake on the sorbent surface.
- The overall kinetic results indicated that the mechanisms not only depend on using the pseudo-second-order process but were also governed by mass transfer of the adsorbate molecules across all the developed nano-sorbents surfaces.
- The presence of other ions in groundwater did not significantly affect the defluoridation process. Moreover, the economic feasibility of the developed nano-sorbent materials was proved by its adsorption-desorption cycles of re-use.
- The successful surface functionalization synthesis of these improved surface area hybrid nano-sorbents supported by the different morphological techniques were found to be effective in creating more surface-active binding sites for fluoride adsorption and disinfection of waterborne pathogens from aqueous solution.
- The impregnated Ag-MgO nanoparticles were proven to be a significant contributor to the antimicrobial activities of all the synthesized nanosorbent materials.
- The combination of the polymeric materials with the nanoparticles greatly imparted its multi-functional properties for the high fluoride sorption and antimicrobial potency, which makes them suitable for use in drinking water treatment, especially in rural areas where minimum or no basic water facilities exist.
- Above all, the developed materials were established to possess superior fluoride adsorption capacity when compared to other reported sorbent materials.
- Lastly, the project/innovation will contribute to Sustainable Development Goals (SDG) 3 and 6, aimed at improving clean water supply and health of the communities and the world at large.

However, the following recommendations were made following the findings from this study:

- In order to increase the surface area to volume, greater selectivity, porosity, and mechanical stability of the polymers as well as size-exclusion mechanism without a large energy penalty of the microbes and fluoride ion for effective water treatment, a more effective and an enhanced multifunctional, multi-layer nanofibrous hybrid sorbent through electrospinning techniques should be considered for future work.
- More studies on the mode of actions and morphological changes in the original and treated bacteria leading to cell death through the influence of the nanocomposites should further be comprehensively evaluated for all classes of waterborne bacteria.
- Application of this advanced technology vis-à-vis another biomaterial to generate filter membrane towards efficient microbial removal and deflouridation is a great challenge worth looking into.
- Lastly, materials developed in the present study should be modeled, tested and fabricated at the point of use for fluoride and pathogen removal at the household level.

Contribution to knowledge

The study has contributed the following to the body of knowledge:

- Detailed surface modification/functionalization methods, as well as optimization of operating conditions, physicochemical, and morphological properties of the chitosan/cellulose/n-Hap/Ag-MgO nanocomposite towards pathogens removal and defluoridation in groundwater.
- Performances of chitosan/cellulose/n-Hap/Ag-MgO as sorbent media for defluoridation and other heavy metals removal on a laboratory scale as a baseline of technical feasibility.
- Optimized procedures for the regeneration of the F^- loaded adsorbents and their reusability potential using chitosan/cellulose/n-Hap/Ag-MgO
- The working principle, design, and surface effectiveness are projected to surpass traditional filtration system towards antimicrobial property whereby bacterial and other pathogens could be destructively oxidized producing safe and clean potable water.
- Design and operational parameters for Point-Of-Use household defluoridation unit using the chitosan/cellulose/n-Hap/Ag-MgO based adsorbents.

APPENDICES

Table 1A: Effect of contact time on fluoride adsorption onto Ag-MgOnHap composite

Time (min)	C_e (mg/g)	% F^- Removal	Q_e (mg/g)
10	3.63	67.30	1.66
20	3.01	72.88	1.80
30	2.54	77.12	1.90
40	2.24	79.82	1.97
50	2.19	80.27	1.98
60	1.78	83.96	2.07
90	1.56	85.95	2.12
120	1.44	87.03	2.15
150	1.43	87.12	2.15
180	1.4	87.39	2.15
200	1.38	87.57	2.16

Table 2A: Effect of adsorbent dosage on fluoride adsorption onto Ag-MgOnHap composite

Dosage (g)	C_e (mg/g)	% F^- Removal	Q_e (mg/g)
0.1	10.54	66.41	3.50
0.15	3.54	70.11	2.46
0.2	3.15	77.70	2.05
0.25	2.35	87.19	1.84
0.3	1.35	88.89	1.56
0.5	1.17	91.08	0.96
0.6	0.94	91.94	0.81
0.9	0.85	92.69	0.54
1	0.77	95.73	0.51

Table 3A: Effect of adsorbate conc. on fluoride adsorption onto Ag-MgOnHap composite

InitiaI Conc (mg/L)	Ce (mg/L)	% F^- Removal	qe (mg/g)
2	0.02	99.19	0.17
5	0.04	99.14	0.41
7	0.13	98.16	0.57
10	0.24	97.62	0.81
15	0.39	97.34	1.22
20	8.56	57.20	0.95
40	28.43	28.93	0.96
80	55.03	31.21	2.08

Table 4A: Effect of pH on fluoride sorption onto Ag-MgOnHap composite

pH	Ce (mg/L)	% Removal
4	4.60	56.36
5	5.57	47.15
6	3.25	69.17
7	3.20	69.64
8	4.77	54.74
10	5.56	47.25

Table 5A: Effect of contact time on fluoride adsorption onto AgMgOnHap@CSn composite

Time (min)	Ce (mg/L)	% F Removal	Qe (mg/g)
2	3.92	60.8	1.35
5	3.48	65.2	1.45
7	3.41	65.9	1.46
10	3.05	69.5	1.54
12	2.99	70.1	1.56
15	2.76	72.4	1.61
20	2.69	73.1	1.62
25	2.49	75.1	1.67
30	2.04	79.6	1.77
40	2.25	77.5	1.72
50	2.24	77.6	1.72
60	2.24	77.6	1.72

Table 6A: Effect of AgMgOnHap@CSn composite dosage on fluoride uptake

Dosage (g)	Ce (mg/L)	% F^- Removal
0.1	7.00	30.00
0.15	6.00	40.00
0.2	4.81	51.90
0.25	3.97	60.30
0.3	2.94	70.60
0.35	1.69	83.10

Table 7A: Variation of F^- sorption by AgMgOnHap@CSn with adsorbate concentration at 303 K

Initial F^- (mg/L)	Ce (mg/L)	% F Removal	Qe (mg/g)
5	1.85	63.00	0.63
7	2.75	60.67	0.85
10	4.33	56.73	1.14
12	5.75	52.08	1.25
15	7.21	51.93	1.56
20	8.17	59.17	2.37
40	13.73	65.68	5.26
80	45.97	42.54	6.81
100	78.69	21.31	4.26

Table 8A: Variation of F^- sorption by AgMgOnHap@CSn with adsorbate concentration at 313 K

Initial F^- (mg/L)	Ce (mg/L)	% F Removal	Qe (mg/g)
5	3.06	38.87	0.39
7	4.86	30.62	0.43
10	6.95	30.47	0.61
12	8.17	31.92	0.77
15	9.44	37.04	1.11
20	15.00	25.00	1.00
40	17.30	56.75	4.54
80	54.95	31.31	5.01
100	84.67	15.33	3.07

Table 9A: Variation of F^- sorption by AgMgOnHap@CSn with adsorbate concentration at 323K

Initial F^- (mg/L)	Ce (mg/L)	% F Removal	Qe (mg/g)
5	2.90	42.07	0.42
7	4.05	42.14	0.59
10	5.98	40.17	0.80
12	8.11	32.39	0.78
15	9.13	39.11	1.17
20	11.40	43.00	1.72
40	25.72	35.69	2.86
80	53.30	33.38	5.34
100	81.77	18.23	3.65

Table 10A: Effect of pH on fluoride sorption onto AgMgOnHap@CSn composite

pH	Ce (mg/L)	% F^- Removal
3	6.07	39.27
5	4.51	54.93
7	4.40	55.97
9	5.01	49.87
12	8.61	13.93

Table 11A: Effect of contact time on fluoride adsorption onto CNF-AgMgOnHap composite

Time (min)	Ce (mg/L)	% F Removal	Qe (mg/g)
2	1.63	83.67	1.86
5	1.06	89.40	1.99
7	1.03	89.70	1.99
10	0.69	93.08	2.07
12	0.51	94.94	2.11
15	0.33	96.67	2.15
20	0.161	98.39	2.19
30	0.23	97.73	2.17

Table 12A: Effect of CNF-AgMgOnHap composite dosage on fluoride adsorption

Dosage (g)	Ce (mg/L)	% F^- Removal
0.1	3.14	68.60
0.15	2.21	77.93
0.2	1.2	88.00
0.25	0.50	95.00
0.3	0.26	97.43
0.35	0.11	98.96

Table 13A: Effect of pH on fluoride sorption onto CNF-AgMgOnHap composite

pH	Ce (mg/L)	% F^- Removal
3	5.75	42.53
5	0.52	94.81
7	1.26	87.4
9	1.84	81.6
12	4.65	53.47

Table 14A: Variation of F^- sorption by CNF-AgMgOnHap with adsorbate concentration at 303K

Initial F^- (mg/L)	Ce (mg/L)	% F Removal	Qe (mg/g)
5	0.08	98.50	0.99
7	0.12	98.27	1.38
10	0.16	98.44	1.97
12	0.517	95.69	2.30
15	0.70	95.32	2.86
20	3.96	80.22	3.21
40	11.83	70.42	5.63
80	37.30	53.38	8.54
100	56.77	43.23	8.65

Table 15A: Variation of F^- sorption by CNF-AgMgOnHap with adsorbate concentration at 313K

Initial F- (mg/L)	Ce (mg/L)	% F Removal	Qe (mg/g)
5	0.07	98.59	0.99
7	0.13	98.15	1.37
10	0.31	96.91	1.94
12	0.69	94.17	2.26
15	0.90	94.00	2.82
20	4.07	79.67	3.19
40	12.57	68.58	5.49
80	40.37	49.54	7.93
100	61.60	38.40	7.68

Table 16A: Variation of F- sorption by CNF-AgMgOnHap with adsorbate concentration at 323K

Initial F- (mg/L)	Ce (mg/L)	% F Removal	Qe (mg/g)
5	0.07	98.53	0.99
7	0.07	99.06	1.39
10	0.13	98.75	1.975
12	0.36	96.99	2.33
15	0.52	96.51	2.90
20	5.08	74.58	2.98
40	14.1	64.75	5.18
80	42.67	46.67	7.47
100	61.11	38.89	7.78

Table 17A: Effect of contact time on fluoride adsorption onto CECS@nHapAgMgO composite

Time (min)	Ce (mg/L)	% F Removal	Qe (mg/g)
1	7.12	28.80	0.48
2	6.99	30.10	0.50
5	6.19	38.10	0.64
10	5.49	45.10	0.75
20	5.05	49.47	0.82
30	3.56	64.43	1.07
40	2.49	75.07	1.25
60	2.37	76.30	1.27
120	2.38	76.23	1.27
150	2.38	76.17	1.27

Table 18A: Effect of pH on fluoride sorption onto CECS@nHapAgMgO composite

pH	Ce (mg/L)	% F^- Removal
3	1.03	89.73
5	0.38	96.23
7	2.46	75.43
9	3.19	68.13
12	4.10	59.00

Table 19A: Variation of F^- sorption by CECS@nHapAgMgO with adsorbate concentration at 298K

Initial F^- (mg/L)	Ce (mg/L)	% F Removal	Qe (mg/g)
5	0.01	99.89	0.83
10	0.01	99.92	1.67
15	2.14	85.73	2.14
20	5.58	72.10	2.40
40	15.97	60.07	4.00
70	41.57	40.62	4.74
100	50.47	49.53	8.26
150	84.97	43.36	10.84

Table 20A: Variation of F- sorption by CECS@nHapAgMgO with adsorbate concentration at 303K

Initial F- (mg/L)	Ce (mg/L)	% F Removal	Qe (mg/g)
5	0.438	91.24	0.760
10	1.82	81.77	1.36
15	2.36	84.29	2.11
20	6.02	69.90	2.33
40	19.37	51.58	3.44
70	41.47	40.76	4.76
100	61.60	38.40	6.40
150	89.70	40.20	10.05

Table 21A: Variation of F^- sorption by CECS@nHapAgMgO with adsorbate concentration at 313K

Initial F- (mg/L)	Ce (mg/L)	% F Removal	Qe (mg/g)
5	0.40	92.07	0.77
10	1.48	85.2	1.42
15	2.04	86.42	2.16
20	5.36	73.22	2.44
40	20.10	49.75	3.32
70	42.60	39.14	4.57
100	67.70	32.30	5.38
150	90.03	39.98	9.99

Photographic Images of all as-prepared sorbent materials

Fig. 1A: Synthesized nanohydroxyapatite (nHaP)(Dried)

Fig. 2A: Ag/MgO nanoparticle modified nanohydroxyapatite (Ag-MgOnHaP)

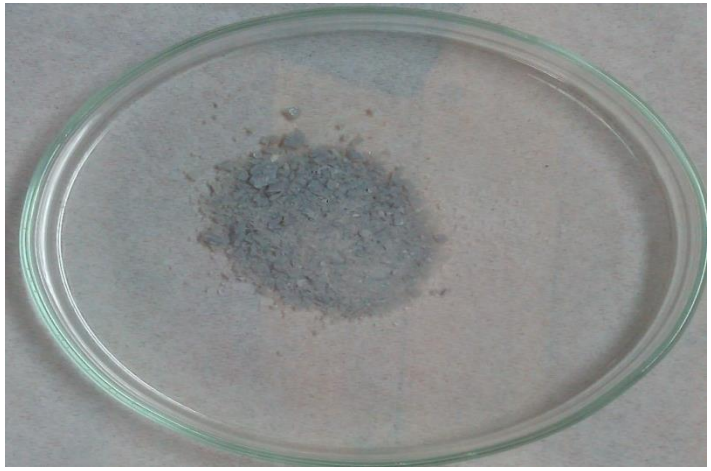

Fig. 3A: Dried Ag-MgOnHaP

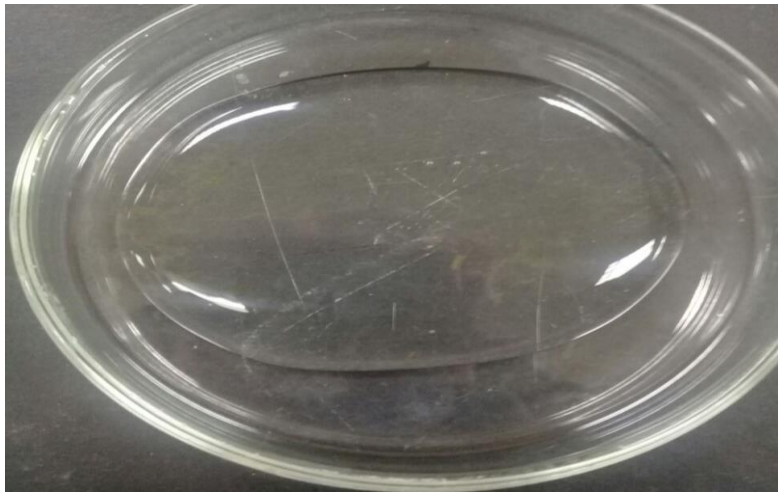

Fig. 4A: Chitosan slurry (CSn)

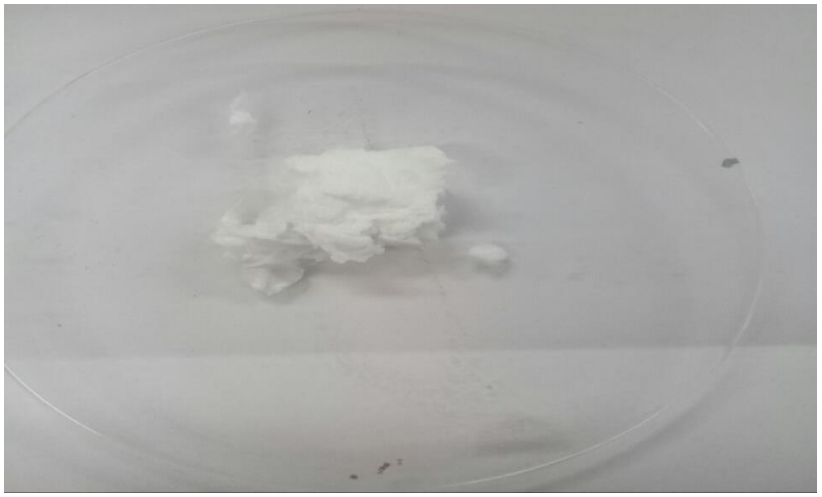

Fig. 5A: Dried Chitosan (CSn)

Fig. 6A: Chitosan embedded with AgMgO (CSn-AgMgO)

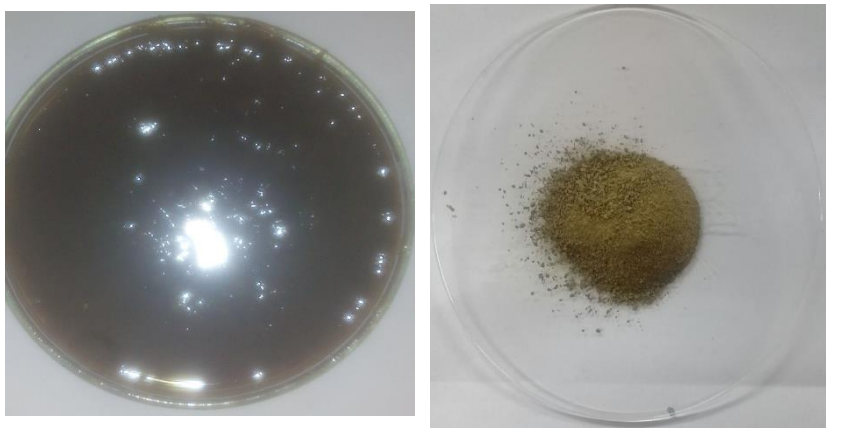

Fig. 7A: AgMgOnHaP@CSn nanocomposite (Before and after drying)

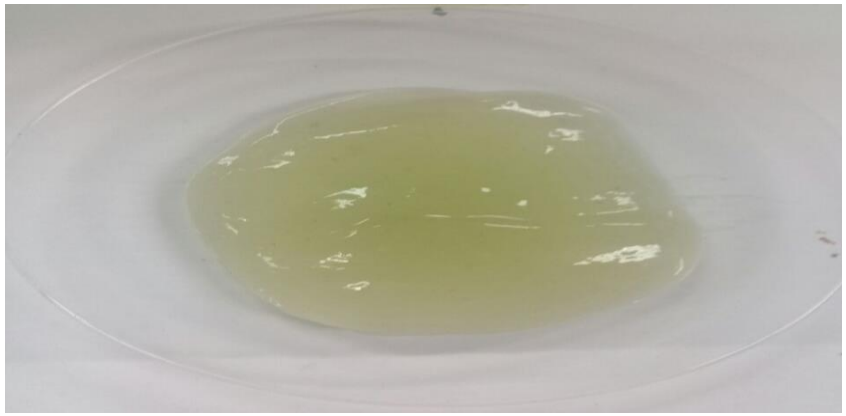

Fig. 8A: Cellulose nanofiber (CNF)slurry isolated from sawdust

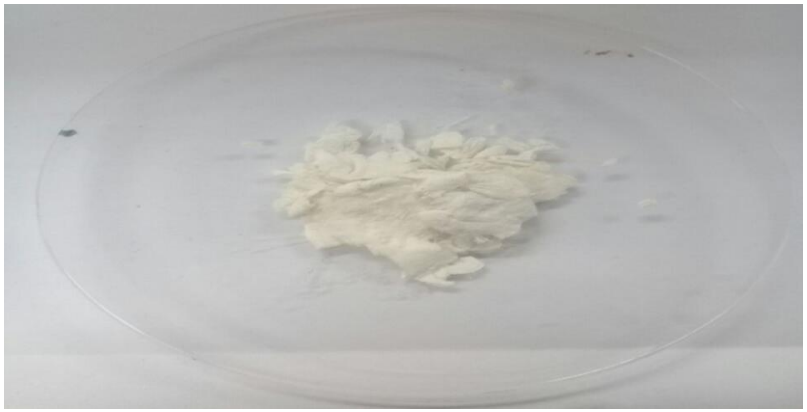

Fig. 9A: Dried cellulose nanofiber (CNF) slurry isolated from sawdust

Fig. 10A: Dried CNF impregnated with AgMgO (CNF-AgMgO)

Fig. 11A: CNF-AgMgOnHaP nanocomposite (Before and after drying)

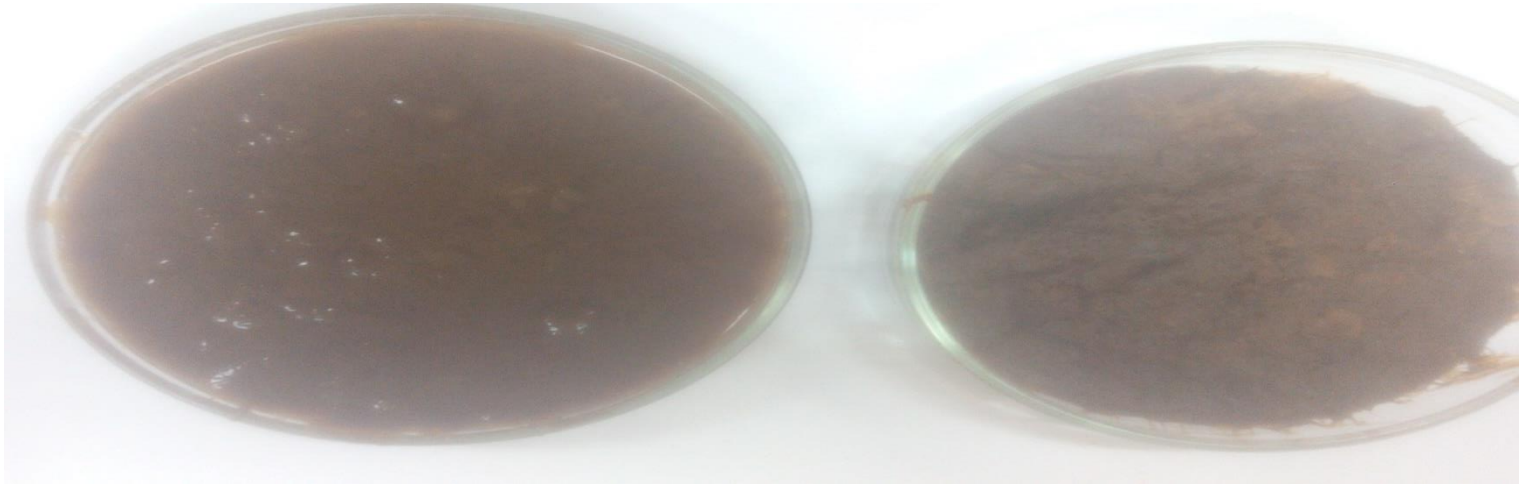

Fig. 12A: CECS@nHapAgMgO (Before drying)

Fig. 13A: Dried CECS@nHapAgMgO nanosorbent